A melt inclusion study of rhyolitic volcanics in the Bousquet Formation, Doyon-Bousquet-LaRonde district, Abitibi Subprovince, Québec: Insight into Archean magmatic processes

By
Daniel Joseph Meagher

A thesis submitted to Saint Mary's University, Halifax, Nova Scotia in partial fulfillment of the requirements for the Degree of Master of Science in Applied Science

Halifax, Nova Scotia

Approved: Dr. Jacob Hanley
Supervisor
Department of Geology
Saint Mary's University

Approved: Dr. Daniel Kontak
Supervisory Committee
Harquail School of Earth Sciences
Laurentian University

Approved: Dr. James Brenan
Supervisory Committee
Department of Earth and Environmental Sciences
Dalhousie University

Approved: Dr. Patrick Mercier-Langevin
Supervisory Committee
Geological Survey of Canada
Natural Resources Canada

Approved: Dr. Robert Singer
Supervisory Committee
Department of Chemistry
Saint Mary's University

December 22, 2020

Abstract

A melt inclusion study of rhyolitic volcanics in the Bousquet Formation, Doyon-Bousquet-LaRonde district, Abitibi Subprovince, Québec: Insight into Archean magmatic processes

By: Daniel Joseph Meagher

Silicate melt inclusions (SMI) from 2697 – 2699 Ma Bousquet rhyolites (Doyon-Bousquet-LaRonde district, Québec) were characterized to elucidate magmatic contributions to VMS deposit tenor in the region.

The key results are as follows: (i) Early rhyolite is of dominantly ocean ridge (tholeiitic) to transitional affinity, whereas later rhyolite has dominantly volcanic arc (calc-alkaline) affinity; (ii) SMI record a wide compositional range compared to host (bulk) rocks, reflecting extensive plagioclase fractionation at depth and inconsistent with TTG classifications previously proposed for the melts; (iii) Ore/accessory metal concentrations in SMI (e.g., Auavg = 33 to 120 ppb) are much higher than crustal abundances, and reflect pre-eruptive Bousquet Formation magma metal tenor; and (iv) melts were saturated in liquid CO_2 but undersaturated in H_2O at depth.

The study is one of only a few studies of SMI from Archean rocks and the first to present trace element/ore metal data for SMI of this age.

December 22, 2020

Acknowledgments

I would like to thank Dr. Jacob Hanley for all his time, assistance, and guidance throughout this thesis as my primary supervisor. His help and generosity are very much appreciated. I would also like to thank my committee members Dr. Daniel Kontak (Laurentian University), Dr. James Brenan (Dalhousie University), Dr. Patrick Mercier-Langevin (Geological Survey of Canada), and Dr. Robert Singer (Saint Mary's University) for their continued support throughout this thesis. I would like to specifically thank Dr. Zoltán Zajacz, Dr. Yana Fedortchouk, and their respective laboratory staff for all the time and patience they have dedicated to this project. I would like to thank Agnico Eagle Mines Limited and IAMGOLD Corporation for mine site and drill core access. I extend my gratitude to my friends and colleagues Dr. Mitchell Kerr, Kevin Neyedley, Fergus Tweedale, and Xiang Yang (Saint Mary's University) for their expertise and guidance with in-house analytical equipment and data collection. I would like to acknowledge all the help, support, and funding from the Targeted Geoscience Initiative-5 (Natural Resources Canada), without which much of this work would not be possible. A big thank you goes out to the Mineral Exploration Research Centre, McCallum Environmental Limited, and Dillon Consulting Limited for the internship opportunities. I would like to give special thanks to the Hanley lab group (MEOFL) members for their continued support throughout all stages of the thesis, including the essential afternoon brainstorming sessions at the Gorsebrook Pub. Finally, my family (Pat, Doug, Chris and Steph) are thanked for their immense support in my academic career and every other aspect of my life. I would not be where I am today without them.

Table of Contents

List of Figures

***In* Chapter 1**

***In* Chapter 2**

List of Tables

***In* Chapter 1**

***In* Chapter 2**

Chapter 1: Introduction

1.0 Structure and objectives of thesis

This study is comprised of three chapters: Chapter 1 offers a brief outline of the thesis structure, key objectives, and background on volcanogenic massive sulphide (VMS) deposits, a principle deposit type hosted within, and genetically linked to, the volcanic rocks in the study area. Chapter 2 investigates silicate melt inclusions in the Archean (2699–2697 Ma; Lafrance et al., 2003; Mercier-Langevin et al., 2007b) Bousquet Formation (Blake River Group, Abitibi Subprovince, Québec) volcanics and their potential links to Au-rich VMS deposits and other Au-rich deposit styles (e.g., sub-sea floor epithermal) in the region. Chapter 2 represents a stand-alone manuscript for submission to Contributions to Mineralogy and Petrology. The research presented in Chapter 2 is potentially critical in helping to explain the anomalously high Au content in VMS deposits of the Doyon-Bousquet-LaRonde (DBL) deposit camp and represents *the first* investigation of silicate melt inclusions in an Archean terrane. The overall incentive to conduct analysis of silicate melt inclusions in these rocks is the desire to determine the original ore and accessory metal tenor of the magmatic system. Where they are preserved in phenocryst quartz, their compositions may be largely unaffected by post-solidus processes (Schiano, 2003). Chapter 3 provides a summary of the key findings of Chapter 2 and outlines future work needed to resolve outstanding issues raised in this study.

The primary objective of this thesis was to investigate SMI in volcanics that may be genetically linked to Au-rich VMS deposits in the region. The investigation: (i) Evaluates the robustness of SMI preservation through petrography and chemical analysis in Bousquet

Formation volcanics; (ii) Constrains the metal and trace element chemistry of SMI trapped in different lithologies and at different times throughout the evolution of the volcanic stratigraphy, and evaluates processes that may have influenced metal enrichment (e.g., fractional crystallization); (iii) Evaluates the possible role of volatiles (either degassing from and originating in the magmas, or from wall rocks) in modifying the metal content of the crystallizing magmas; and (iv) Evaluates the magmatic fluid contribution to Au-rich VMS and possibly related systems through comparison of metal ratios and concentrations in regional ore deposits and silicate melt inclusions.

This study was funded by the Targeted Geoscience Initiative-5 (TGI-5; Natural Resources Canada) – a collaborative federal geoscience program that provides industry with the next generation of geoscience knowledge and innovative techniques, which will hopefully result in more effective targeting of buried mineral deposits (Natural Resources Canada, 2019). Although previous studies have suggested a link between the Mooshla Intrusive Complex, Bousquet volcanics, and regional deposits in the study area based on geochronology, mapping/field relations, petrography, and lithogeochemistry (see Chapter 2: Introduction), a silicate melt inclusion study is a novel approach to clarifying this link.

1.1 VMS deposits

Volcanogenic massive sulphide deposits are known historically as volcanic-associated, volcanic-hosted, and volcano-sedimentary-hosted massive sulphide deposits (Galley et al., 2007). They are major sources of Zn, Cu, Pb, Ag, and Au, and notable sources for Co, Sn, Se, Mn, Cd, In, Bi, Te, Ga, and Ge (Galley et al., 2007). Canada hosts close to 350 known VMS deposits, representing nearly half of the known deposits worldwide (~ 800; Galley et al., 2007). Due to extensive development and mining of these deposits, they have contributed to 27%, 49%, 20%, 40%, and 3% of Canada's Cu, Zn, Pb, Ag, and Au production, respectively (Galley et al., 2007).

These magmatic-hydrothermal deposits are as old as 3.4 Ga and are still actively forming at, or near, the seafloor in submarine volcanic environments by the discharge of evolved, high temperature, seawater-dominated hydrothermal fluids (Franklin et al., 1981, 2005; Lydon, 1984, 1988; Large et al., 2001a; Gibson et al., 2007; Galley et al., 2007). They are syngenetic, stratabound lens-like accumulations of polymetallic massive to semi-massive sulphide (Figure 1; Gibson et al., 2007). There are two geometrically distinct parts of the deposit: a massive sulphide lens that runs parallel to adjacent or underlying strata; and, sulphide-rich veins that cross-cut strata (i.e., stringer/stockwork zone) enveloped by altered footwall volcanics or sediments (i.e., alteration pipe; Figure 1; Gibson et al., 2007). This resulting geometry of VMS deposits is independent of their tectonic setting. They all contain the alteration pipe zone that underlies the ocean floor interface and contains a lens of massive sulphide ore composed primarily of pyrite, chalcopyrite, sphalerite, and sometimes galena (Figure 1; Yergeau et al., 2015). The pipe-like zone of disseminated

sulphides also contains extensive chloritic and sericitic alteration created by hot fluids that passed though the rock on its way to the ocean floor (Figure 2; Hannington et al., 1999; Huston, 2000; Dubé et al., 2007a; Gibson et al., 2007; Mercier-Langevin et al., 2011a).

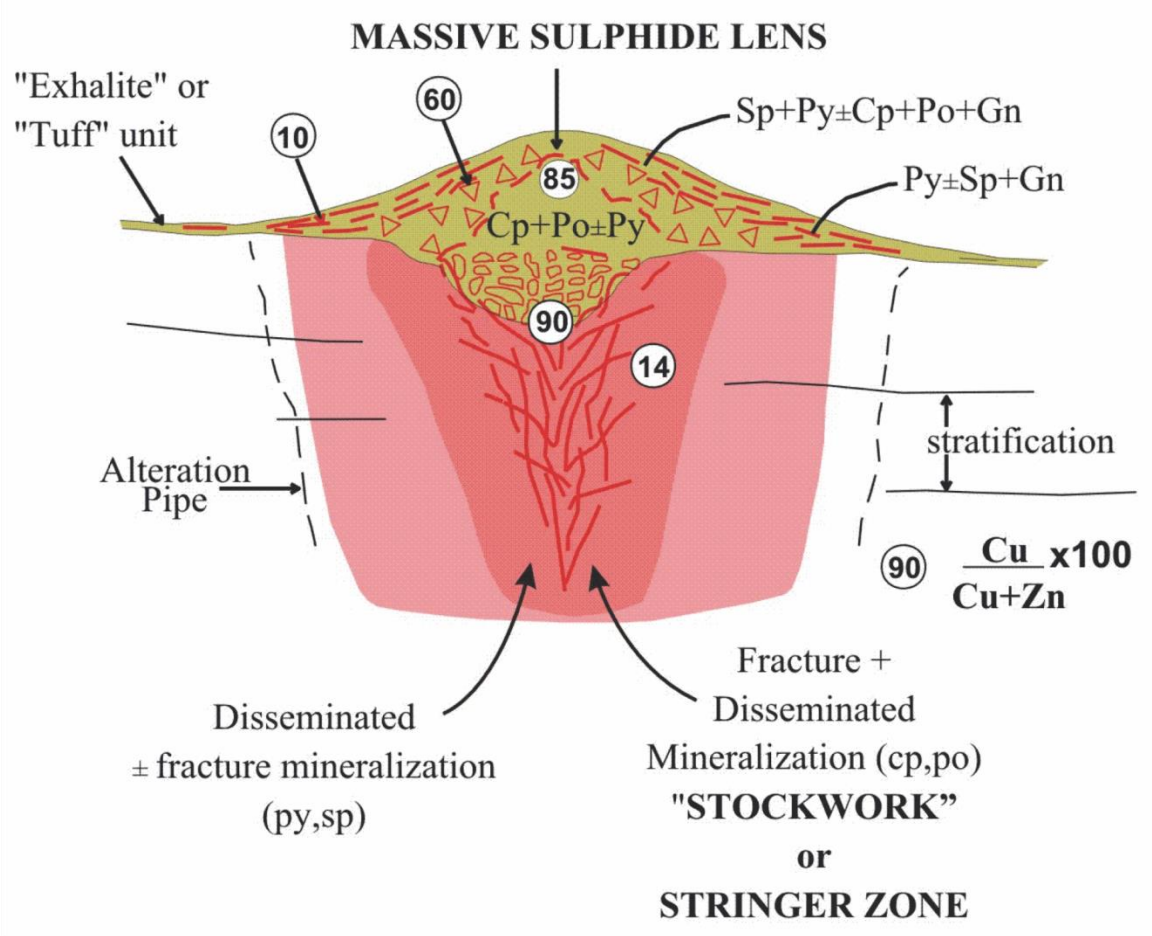

Figure 1: Volcanogenic massive sulphide deposit schematic (after Gibson et al., 2007). Contains a concordant semi-massive to massive sulphide lens containing exhalative deposits of ferruginous chemical sediments and pyrrhotite-pyrite-chalcopyrite-sphalerite-galena ore overlying a discordant stringer/stockwork sulphide zone enveloped by altered rocks (i.e., alteration pipe). Circled numbers represent metal zonation, with the higher numbers being Cu-rich and the lower numbers more Zn-rich. Py = pyrite, Cp = chalcopyrite, Po = pyrrhotite, Sp = sphalerite, and Gn = galena.

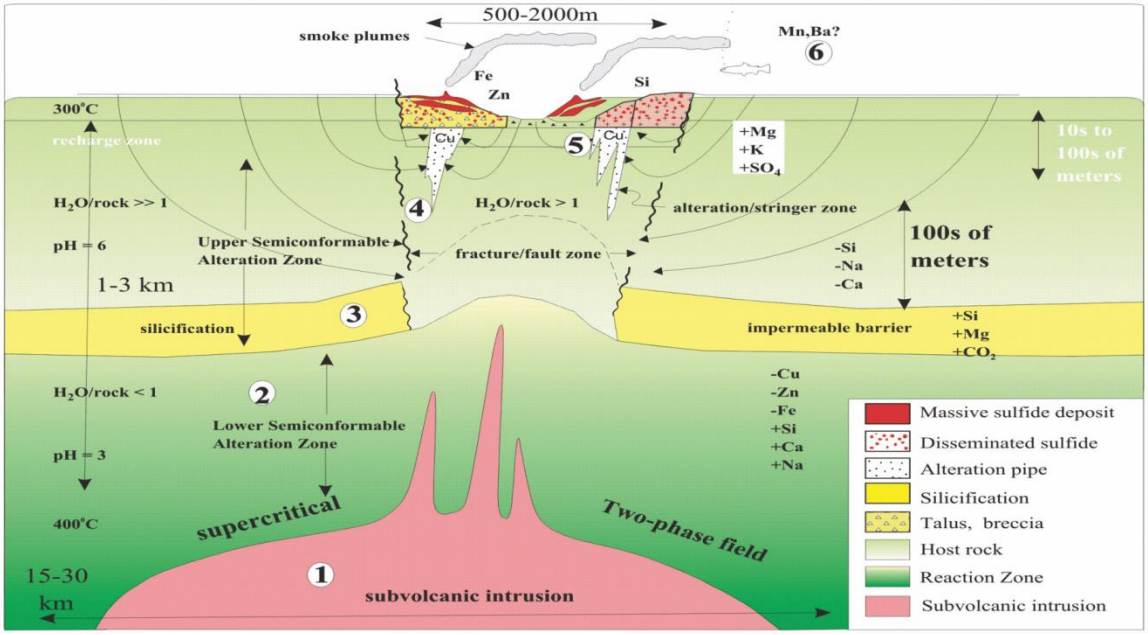

Figure 2: Illustrative relationships of subvolcanic intrusions, sub-seafloor alteration, synvolcanic faulting, and the formation of VMS deposits (after Gibson et al., 2007). See text for explanation of the six essential features (i.e., circled numbers in schematic).

There are six essential features for the formation of VMS hydrothermal systems (Figure 2; Franklin et al., 2005; Gibson et al., 2007). First, there needs to be a heat source, potentially from a synvolcanic intrusion, to initiate, drive and maintain the long duration, hot hydrothermal system (see #1 in Figure 2; Cathles, 1981; Cathles et al., 1997; Gibson et al., 2007). Most Precambrian VMS camps contain a large subvolcanic intrusion, typically of quartz diorite-tonalite-trondhjemite composition, that could have acted as a heat source (Galley, 2003). Second, there is a reaction zone where metals are leached by evolved seawater from volcanic and sedimentary strata (see #2 in Figure 2; Gibson et al., 2007). Third, there are large-scale, deep synvolcanic faults that act as conduits for the recharge and discharge of metal-rich hydrothermal fluids (see #3 in Figure 2; Gibson et al., 2007). Fourth, there are alteration zones in the hanging wall and footwall that formed when near surface strata reacted with mixed hydrothermal fluid and ambient seawater (see #4 in Figure 2; Gibson et al., 2007). Fifth, there is a massive sulphide deposit with a metal content refined by successive hydrothermal events (see #5 in Figure 2; Gibson et al., 2007). Sixth, there are distal exhalites that were formed by a hydrothermal contribution to background sedimentation (see #6 in Figure 2; Galley et al., 2007).

Volcanogenic massive sulphide deposits can be found in a variety of tectonic settings: Ophiolite-related obduction environments, oceanic spreading ridges, thickened oceanic crust, sedimented oceanic ridges and sedimented continental margin rifts, and many rifted arc settings such as nascent arcs, island arcs, fore-arc troughs, back-arc basins, intra-oceanic arc rifts, primitive volcanic arcs, mature volcanic arcs, and continental arcs (Figure 3; Ohmoto and Skinner, 1983; Swinden, 1991; Rona et al., 1993; Scott, 1997; Carvalho et

al., 1999; Galley and Koski, 1999; Goodfellow and Zierenberg, 1999; Perfit et al., 1999; Syme et al., 1999; Huston, 2000; Barrett et al., 2001; Piercey et al., 2001b; Dusel-Bacon et al., 2004; Hannington et al., 1995, 1999, 2005; Galley et al., 2007; Piercey, 2009; Shanks, 2012). The VMS deposits in the Noranda and DBL camps, for example, are similar to a modern primitive island arc or back-arc environment that was undergoing extension and rifting (Mercier-Langevin et al., 2007c; Gibson and Galley, 2007; Beaudoin et al., 2014). Some of the most economically important VMS districts (e.g., Bathurst, Finlayson Lake, Golden Grove, Bergslagen, Mount Windsor, and the Iberian Pyrite Belt) are contained within continental back-arc settings that are dominated by bimodal siliciclastic rocks ± iron formation (Allen et al., 1996; Carvalho et al., 1999; Doyle and McPhie, 2000; Piercey et al., 2001; Sharpe and Gemmell, 2002; van Staal et al., 2003; Galley et al., 2007). A large volcanic edifice within the Kermadec and Tonga-Fiji supracrustal tectonic zone of the western Pacific is a modern analogue of the inferred primitive rifted arc environment of economic VMS deposits such as the bimodal-mafic Kidd Creek VMS deposit (Barrie and Hannington, 1999; Gibson and Galley, 2007).

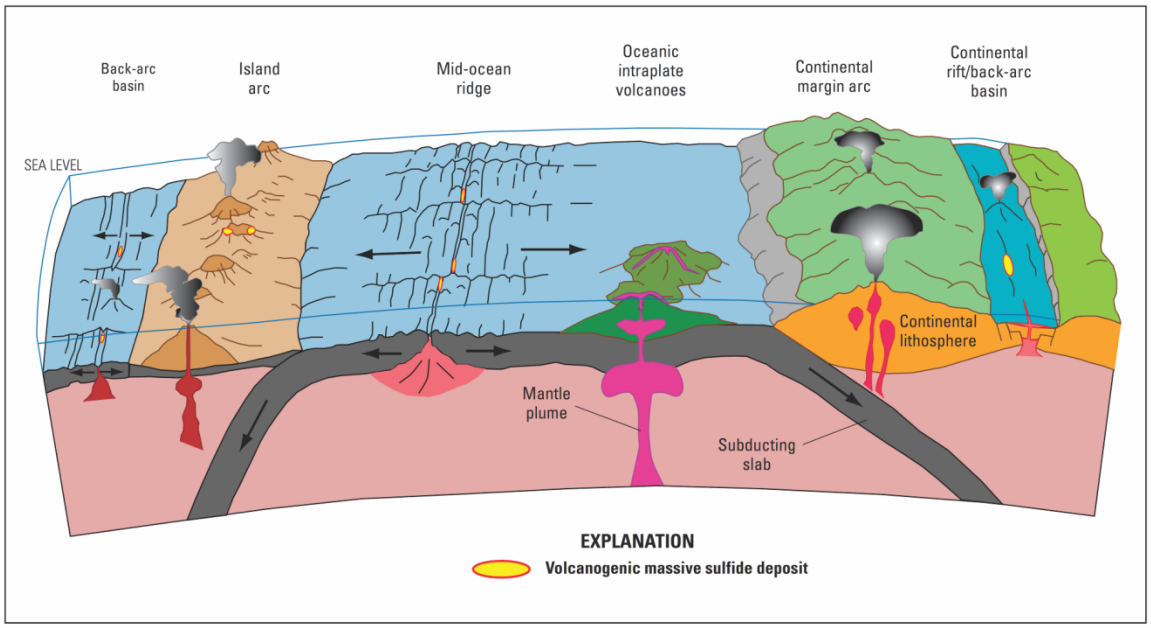

Figure 3: Large scale tectonic settings for the formation of VMS deposits. Settings include back-arc basin, island arc, mid-ocean ridge, and continental rift, with VMS deposits depicted by bright yellow dots (from Shanks, 2012).

In addition to large volcanic edifices, black smokers are also modern analogues for active VMS formation and are found in arc settings, and extensional zones and basins with volcanic activity along mid-ocean ridges (Hedenquist and Lowenstern, 1994). Many concepts of ore genesis have been supported by studies of these modern VMS systems (i.e., black smokers; Ohmoto and Skinner, 1983 and references therein; Hannington et al., 2005). Ore genesis models propose that fluids of black smokers originate from cold (2 ˚C), alkaline, oxidizing, and metal-deficient seawater, but when they vent through chimneys of black smokers, they are hot (250-400 ˚C), slightly acidic, reduced, and metal-charged (Ohmoto, 1996). The metal-rich fluids are discharged from the vent and rise like a plume into the overlying seawater, causing ore minerals to crystallize and settle on the seafloor (Solomon and Walshe, 1979; Ohmoto, 1996). The chimneys themselves are made up of an assortment of anhydrite, barite, and sulphides such as pyrite, pyrrhotite, chalcopyrite, and sphalerite, as well as gangue opaline silica. The hydrothermal fluids that reach chimneys of black smokers have changed from metal-deficient to metal-charged because they have circulated through and metasomatized the basaltic ocean crust and collected/mobilised metals along the way (Schiffman et al., 1987; Richardson et al., 1987; Barrie and Hannington, 1999; Yardley and Bodnar, 2014; Patten et al., 2016).

Regardless of how VMS deposits were formed, they are often simply classified by either base metal content (e.g., Hutchinson, 1973; Solomon, 1976; Franklin et al., 1981; Large, 1992), tectonic setting (e.g., Sawkins, 1976; Hutchinson, 1980), Au content (Poulsen and Hannington, 1996; Hannington et al., 1999; Huston, 2000), host rock textures (e.g., Morton and Franklin, 1987; Gibson, 1999), or host rock lithology (e.g., volcanic, volcano-

sedimentary, sedimentary divisions: Sangster and Scott, 1976; Barrie and Hannington, 1999; Galley et al., 2007). However, they can also be classified using five host rock composition: Mafic, mafic-siliciclastic, bimodal-mafic, bimodal-felsic, and felsic-siliciclastic (Figure 4; Barrie and Hannington, 1999; Franklin et al., 2005; Piercey, 2011). When the host rock composition classification scheme is used, VMS deposits of similar characteristics group together well and many ambiguities that arise when classifying based on metal content (e.g., both felsic- and mafic-dominant successions contain Cu-Zn deposits), tectonic setting (e.g., deposits with ambiguous oringins due to metamorphism), or age (e.g., many Phanerozoic Cu-Zn deposits are similar to Archean Cu-Zn deposits) are avoided (Barrie and Hannington, 1999). This host rock classification is based on the pre-altered rock before hydrothermal fluids circulated through the system providing ore-forming metals and creating alteration zones.

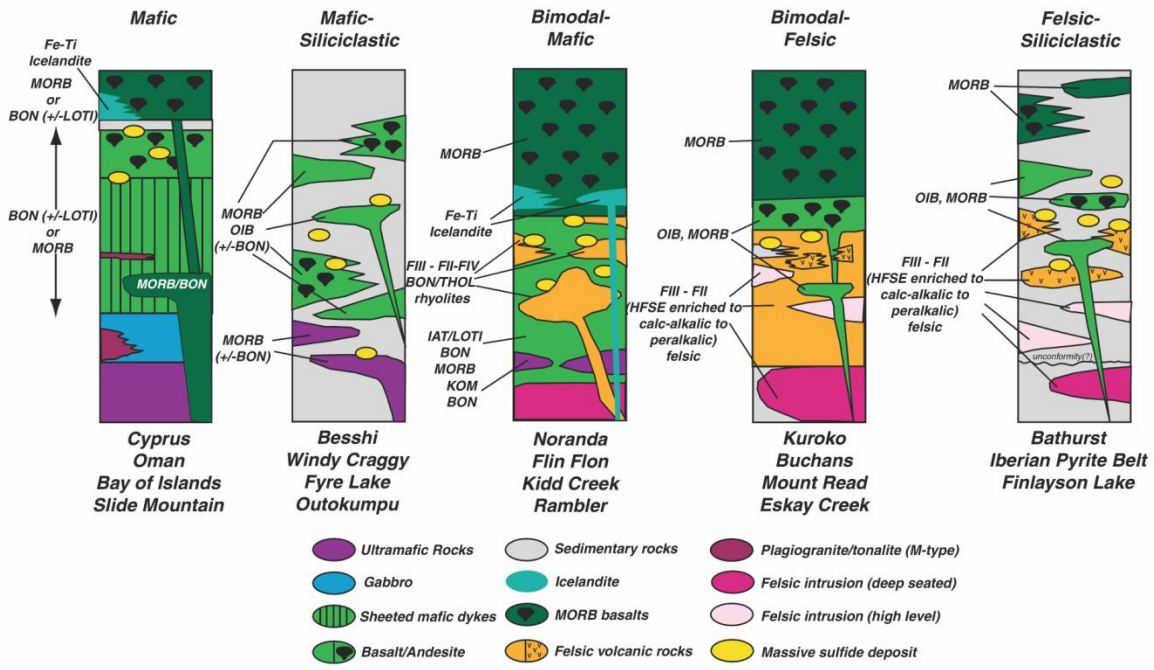

Figure 4: Stratigraphic relationships and potential petrochemical assemblages for different VMS deposit groups based on host rock composition (after Piercey, 2011). BON = boninite, HFSE = high field strength element, IAT = island arc tholeiites, KOM = komatiite, LOTI = low-Ti tholeiite, MORB = mid-ocean ridge basalt, OIB = ocean island basalt, THOL = tholeiite.

The hydrothermal alteration associated with VMS ore is dependant on the composition, architecture, and facies of the volcanic succession (Gibson et al., 1999; Large et al., 2001b; Doyle and Allen, 2003; Gibson et al., 2007; Shanks, 2012; Debreil et al., 2018). When VMS deposits are hosted by massive or pillowed lavas, they are typically characterized by sea floor exhalative sulphide mounds underlain by discordant alteration pipes and stockworks (Gibson et al., 1999; Debreil et al., 2018). In contrast, tabular sulphide bodies with broader alteration zones that can extend to the hanging wall develop in VMS deposits hosted by volcaniclastic-dominated successions (Gibson et al., 1999; Large et al., 2001b; Doyle and Allen, 2003; Gibson et al., 2007; Shanks, 2012; Debreil et al., 2018). Invaluable information on ore-forming processes (chemical and physical), as well as exploration guidelines, can be learned from studying hydrothermal alteration associated with VMS deposits (Çağatay, 1993; Shanks, 2012). For example, the Küre pyritic Cu orebodies in the western Black Sea region are associated with illite-mica + quartz zones that display rapid changes in the degree of feldspar alteration (Çağatay and Boyle, 1977; Çağatay, 1993). This rapid change indicates steep temperature changes and intensity of hydrothermal alteration, and can be implemented as directional vectors for drilling programs (Çağatay and Boyle, 1977; Çağatay, 1993).

There is a series of commonly recognized alteration zones in hydrothermal settings: potassic, argillic, phyllic, and propylitic (Sales and Meyer, 1948; Titley and Hicks, 1966; Meyer and Hemley, 1967; Meyer et al., 1968; Shanks, 2012). Each alteration zone has distinct mineralogy and a decrease in alteration intensity away from the vein or pluton, respectively (Shanks, 2012). Some of the above alteration zone classifications were

adopted by researchers for VMS deposits, but sericitic replaced phyllic and chloritic and advanced argillic were added as an alteration zone in subseafloor settings (Table 1; Sillitoe et al., 1996; Hannington et al., 1999; Shanks, 2012). There is an unmistakeable thermodynamic basis for the presence of the alteration assemblages associated with the aforementioned alteration zones (Hemley and Jones, 1964; Beane, 1994; Reed and Palandri, 2006; Shanks, 2012). The higher temperature and pressure mineral assemblages can be predicted for metamorphosed VMS deposits (Table 1; Bonnet and Corriveau, 2007; Shanks, 2012). The study of hydrothermal alteration mineral assemblages is an essential tool for pinpointing the origin of metallic elements in VMS deposits (Shanks, 2012). For example, combining the depletion of key elements in altered rocks with measured estimates of the rock volume can delimit possible sources of ore metals (Shanks, 2012).

Table 1: Diagnostic minerals in hydrothermally altered VMS deposits at different metamorphic grades.

Alteration type	Diagnostic minerals: unmetamorphosed deposits	Diagnostic minerals: greenschist facies	Diagnostic minerals: granulite facies
Advanced argillic	Kaolinite, alunite, opal, smectite	Kaolinite, pyrophyllite, andalusite, corundum, topaz	Sillimanite, kyanite, quartz
Argillic	Sericite, illite, smectite, pyrophyllite, opal	Sericite, illite, pyrophyllite	Sillimanite, kyanite, quartz, biotite, cordierite, garnet
Sericitic	Sericite, illite, opal	Sericite, illite, quartz	Biotite, K-feldspar, sillimanite, kyanite, quartz, cordierite, garnet
Chloritic	Chlorite, opal, quartz, sericite	Chlorite, quartz, sericite	Cordierite, orthopyroxene, orthoamphibole, phlogopite, sillimanite, kyanite
Carbonate propylitic	Carbonate (Fe, Mg), epidote, chlorite, sericite, feldspar	Carbonate (Fe, Mg), epidote, chlorite, sericite, feldspar	Carbonate, garnet, epidote, hornblende, diopside, orthopyroxene

The source of metal contributions in VMS deposits is open for debate. Huston et al. (2011) concluded that there is at least a small magmatic-hydrothermal contribution but that metal leaching of underlying rocks is well documented suggests that a magmatic-hydrothermal contribution is not necessary. However, some evidence, like disproportionately high magmatic SO_2, found through sulfur isotope systematics, indicates a significant magmatic-hydrothermal contribution (Huston et al., 2011). It is believed that volcanic rock of basaltic ocean crust is the main source of metals carried by the hydrothermal fluids escaping submarine vents. A large amount of metals are mobilised from the crust but only a small amount becomes trapped as VMS mineralization (Patten et al., 2016). Mass balance studies have demonstrated the geochemical connection between the fluids and volcanics by identifying similarities of the metal content of VMS deposits with that of their associated primary igneous rocks. For example, ophiolite-hosted Cu-Zn deposits, which are typified by the deposits of the Troodos Massif, Cyprus, leach metals from mafic volcanics that are characterized by much higher Cu and Zn contents than their felsic equivalents. However, sulfur is an element which is not sourced from the rock but rather it comes from the sulfate component of the cold ambient seawater that mixes with the hydrothermal fluids (Shanks, 2012). This metal source debate will be looked at in depth in Section 1.1.2 Magmatic contributions to VMS. The following section, however, will focus only on the setting and characteristics of the economically significant Au-rich VMS deposits.

1.1.1 Gold-rich VMS systems

Gold-rich VMS deposits are a subtype of both VMS and lode-Au deposits and can be found in belts and districts of all ages (Figure 5; Poulsen and Hannington, 1996; Hannington et al., 1999; Huston, 2000; Poulsen et al., 2000; Dubé et al., 2004, 2007a; Mercier-Langevin et al., 2011a). They are found in areas of high hydrothermal and tectonic activity in volcanic terranes represented by arc-, back-arc, or rifting-related seafloor environments (Figure 3; Dubé et al., 2007a; Mercier-Langevin et al., 2011a). They are located near major crustal-scale faults, like the Cadillac-Larder Lake fault in the DBL camp, and large subvolcanic intrusions in orogenic belts and greenstone belts (Dubé et al., 2007a). There can be a wide range in volume for these subvolcanic composite intrusions (e.g., intrusions related to the Archean Sturgeon Lake and Noranda, and Paleoproterozoic Snow Lake VMS camps range from 300 to 1,000 km^3; Galley, 2003). These structural blocks separate the Au deposits and the younger Cu-Zn VMS deposits of Noranda (Mercier-Langevin et al., 2011a). This exemplifies the fact that, in most cases, Au-rich VMS deposits are situated in recognizably different volcanic and/or structural settings than other types of VMS deposits in the same district (Mercier-Langevin et al., 2011a).

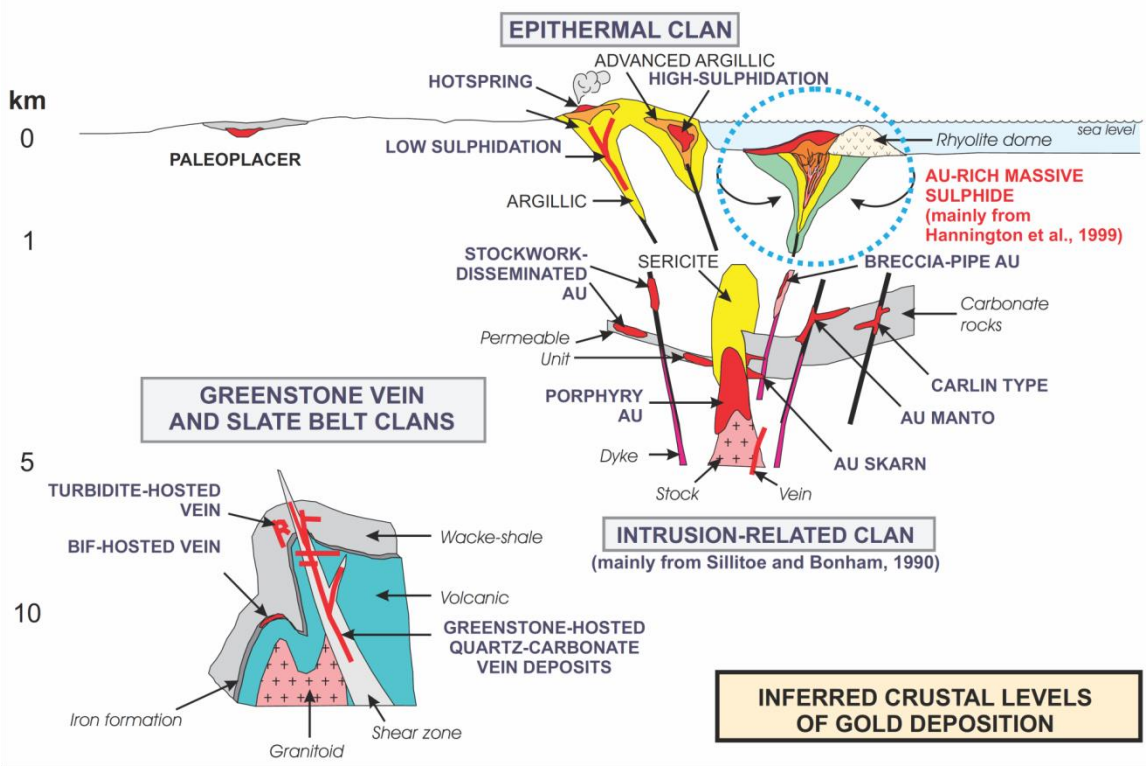

Figure 5: Schematic of the various types of Au deposits. Deposits at their inferred crustal levels of formation (Dubé et al., 2001; Poulsen et al., 2000; from Dubé et al., 2007a). BIF = banded iron formation.

Gold-rich VMS deposits have many of the same features as other VMS deposits, but form in volcanic environments that somewhat differ from that of other VMS deposits of their host district, and are sometimes hosted in transitional to calc-alkaline intermediate to felsic volcanic rocks which may suggest a fertile geodynamic setting and/or optimal timing of formation of the deposit (e.g., early arc rifting or rifting front; Hannington et al., 1999; Dubé et al., 2007b; Mercier-Langevin et al., 2011a; Beaudoin et al., 2014). The timing of these Au-rich deposits in some VMS districts could be directly related to the geodynamic evolution of the tectonic (i.e., arc-back-arc) setting and the corresponding magmatic characteristics (e.g., Macuchi Arc in Ecuador; Chiaradia et al., 2008; Baimak-type VMS deposits of the South Urals; Prokin and Buslaev, 1999; Herrington et al., 2005; Mercier-Langevin et al., 2011a).

Worldwide, Au-rich VMS deposits have a variety of host sequences, including: effusive volcanics, volcanoclastics, or epiclastic mafic to felsic rocks, and mixed volcanogenic sedimentary sequences such as terrigenous, pelagic, or chemical sedimentary rocks (Mercier-Langevin et al., 2007b). They occur in greenstone belts of all ages with greenschist to lower amphibolite metamorphism and are associated with subvolcanic intrusions and dyke-sill complexes in the presumed stratigraphy (Galley, 2003; Dubé et al., 2007a). It is common for the deposits to occur near intermediate to felsic volcanic centres, or adjacent to intermediate to felsic domes and basalt-andesite or clastic sediments (Figure 6; Dubé et al., 2007a). The volcanic successions that host Au-rich VMS deposits have, in general, a higher proportion of felsic rocks than mafic rocks (Barrie and Hannington, 1999; Hannington et al., 1999; Mercier-Langevin et al., 2007b). Similar to most VMS deposits,

Au-rich VMS deposits contain semimassive to massive, stratabound to locally discordant sulphide lenses that overlie stockwork feeder zones (Figure 6; Dubé et al., 2007a). Also, syntectonic sulphide veins can develop, and primary sulphide layering is rarely preserved in deformed deposits (Dubé et al., 2007a).

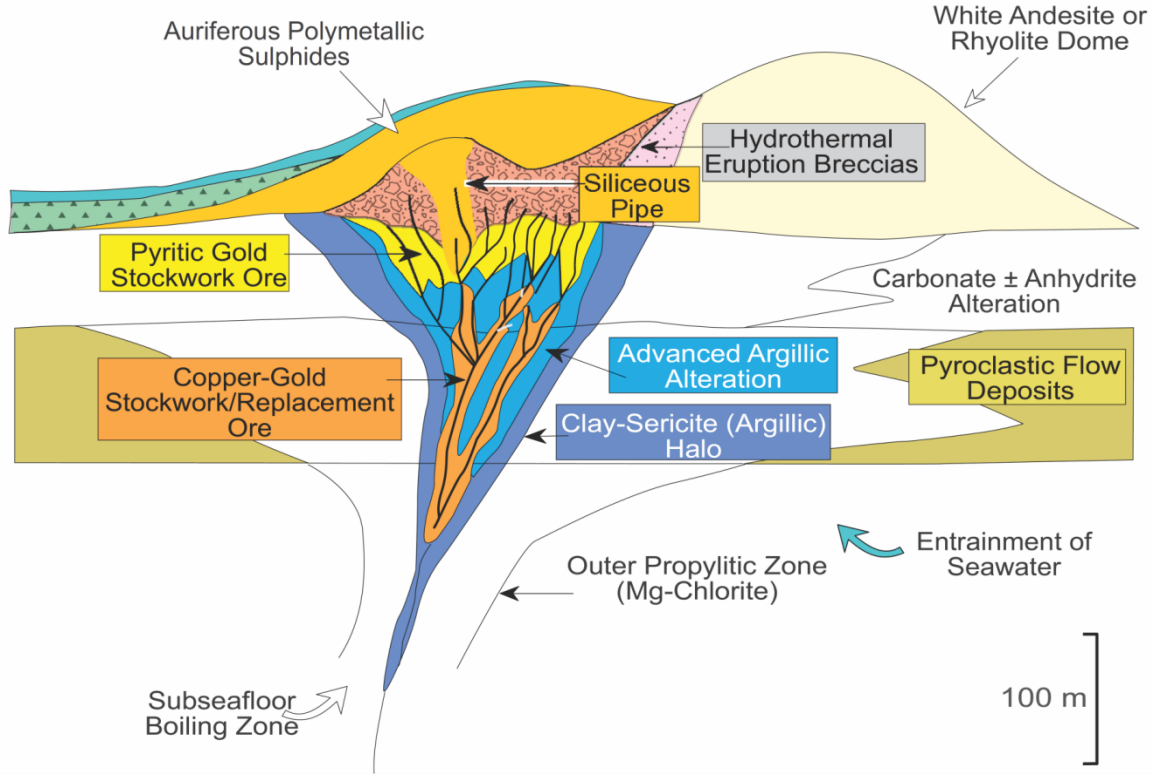

Figure 6: Schematic of Au-rich VMS system. Geological setting and hydrothermal alteration zones associated with an Au-rich VMS system (from Dubé et al., 2007a).

Ultimately, the main characteristic that sets Au-rich VMS apart from other VMS deposits is their anomalously high Au (Mercier-Langevin et al., 2011a). Mercier-Langevin et al. (2011a) analyzed Au grades and tonnages of 513 VMS deposits and concluded that deposits with 3.46 g/t Au and 31 t Au or more are considered Au-rich VMS. The Au content (in g/t) of an Au-rich VMS exceeds the associated combined Cu, Pb, and Zn grades (in weight percent; Hannington et al., 1999; Huston, 2000; Poulsen et al., 2000; Dubé et al., 2007a). The Archean Abitibi greenstone belt hosts some of the best examples of the most extensive Au mineralization in VMS deposits in the world, including the Horne (53 Mt of ore at 6.1 g/t Au or 328 t Au; Kerr and Mason, 1990), and Quemont (13.8 Mt of ore at 5.5 g/t Au or 76 t Au; Mercier-Langevin et al., 2011b) deposits of the Noranda camp (Mercier-Langevin et al., 2014).

In terms of mineralization, there is considerable debate regarding the synvolcanic versus syntectonic origin of Au-rich VMS deposits because the original mode of mineralization in ancient terranes has been obscured by deformation and metamorphism (Dubé et al., 2007a; Dubé et al, 2007b). There are two proposed genetic models for the mineralization of Au-rich VMS deposits (Dubé et al., 2007a). The first model is the syntectonic model which postulates that conventional syngenetic volcanic-hosted Au-poor, base metal-rich, VMS mineralization was overprinted during regional deformation and metamorphism by Au mineralizing fluids (Tourigny et al., 1989a, 1990; Marquis et al., 1990a,b,c; Yeats and Groves, 1998). The syn-deformational nature of Au mineralization is inferred by the location of deposits in highly deformed and metamorphosed sequences close to regional-scale faults, the existence of discordant sulphide veins, and ore zones that are locally

parallel to foliation (e.g., DBL district; Tourigny et al., 1989a; Marquis et al., 1990a, b, c; Dubé et al., 2007a) or that are transposed along discordant post-ore shear zones (or high-strain zone; e.g., Boliden; Allen et al., 1996; Bergman Weihed et al., 1996; Mercier-Langevin et al., 2013). The second model is the synvolcanic model which proposes that the Au-rich deposits are syngenetic VMS deposits characterized by anomalous fluid chemistry (with magmatic Au input) and/or deposits from a shallow-water to subaerial volcanic setting analogous to epithermal conditions in which boiling may have had a major impact on the fluid chemistry (Poulsen and Hannington, 1996; Hannington et al., 1996; Sillitoe et al., 1996; Huston, 2000; Dubé at al., 2007a). The fluid would have had high Au content relative to base metals, and the Au would have precipitated due to a rapid change in pH and a decrease in temperature (Poulsen and Hannington, 1996; Dubé et al., 2007a).

The above models can be simplified into four potential processes that explain the enrichment of Au and related elements (i.e., As, Sb, Se, and Te): (i) boiling in the subseafloor of a shallow water environment; this changes the fluid chemistry and creates a Au-rich gaseous fluid (Urabe et al., 1987; Huston and Large, 1989; Butterfield et al., 1990; Poulsen and Hannington, 1996; Hannington et al., 1999; Patten et al., 2016); (ii) VMS formation in areas with originally high Au concentrations such as back-arc settings or mantle plumes (Huston, 2000; Moss et al., 2001; Pitcairn, 2011; Webber et al., 2013; Patten et al., 2016); (iii) magmatic input from a source such as a shallow sub-seafloor intrusion (Urabe et al., 1987; Stanton, 1990; Sillitoe et al., 1996; Patten et al., 2016); and (iv) late mineralization overprinting due to regional metamorphism (Dubé et al., 2007a; Patten et al., 2016).

Host rocks can become enriched in Au for several reasons: the partial melting of a residual mantle containing Au-enriched magmatic sulphide to form boninites, and suppression of sulphide and oxide fractionation which isolates Au in alkaline, high f_{O2} magmatic systems leading to various hydrothermal processes (Hamlyn et al., 1985; McInnes and Cameron, 1994; Barrie and Hannington, 1999). Primary depositional controls and subsequent tectonic modification and remobilization have produced an uneven Au distribution in the host rocks of Au-rich VMS deposits (Dubé et al., 2007a). Elongated sulphide orebodies in VMS deposits represent macroscale evidence of ductile redistribution and remobilization of orebodies (Rickard and Zweifel, 1975; Gaal, 1977; Gilligan and Marshall, 1987; Belkabir and Hubert, 1995). The sulphide mineralogy of Au-bearing ores are typically more complex than in Au-poor VMS and contain pyrite, chalcopyrite, sphalerite, pyrrhotite, and galena, with minor minerals such as bornite, tennantite, sulphosalts, arsenopyrite, mawsonite, and tellurides (Hannington et al., 1999; Dubé et al., 2007a). The ores are dominated by Au, Ag, and Cu or Zn with locally high concentrations of As, Sb, Bi, Pb, Se, Te, and Hg (Dubé et al., 2007a). Deposits with the Au-Cu association generally have advanced argillic alteration, like the LaRonde Penna and Bousquet 2-Dumagami deposits in the DBL mining district (Dubé et al., 2007a). High-sulfidation conditions like those in some epithermal environments are deduced from the metamorphosed advanced argillic and more discrete massive silicic alteration assemblages (Dubé et al., 2007a).

Gold-rich VMS deposits will often have advanced argillic-style alteration which is symptomatic of an environment with acidic, relatively oxidized, and sulfur-rich fluids of

magmatic origin and are comparable to fluids in the upper parts of volcanoes (Hedenquist and Lowenstern, 1994; Sillitoe et al., 1996). These Au-rich deposits also have intense silicification (and their metamorphosed equivalents) that appear strata-bound to semi-conformable; sometimes they will also contain K-feldspar-bearing footwall alteration assemblages that contrast with the sericite- and chlorite-dominated alteration facies typical of most VMS deposits (Sillitoe et al., 1996; Hannington et al., 1999; Huston, 2000; Dubé et al., 2007a; Mercier-Langevin et al., 2011a; Beaudoin et al., 2014). This style of alteration differs from the pipe-like, strongly focused, sericite- and chlorite dominated alteration assemblages ordinarily found in most VMS deposits (Beaudoin et al., 2014). Gold-poor VMS deposits can also exhibit zones of argillic or aluminous alteration (e.g., Mattabi deposit in Sturgeon Lake, Ontario, Canada; Franklin et al., 1975; Undu deposit in Fiji; Colley and Rice, 1975; Sillitoe et al., 1996; some Kuroko deposits; Marumo, 1989); however, a high percentage of the most Au-rich VMS deposits have this style of alteration (Mercier-Langevin et al., 2011a).

There is evidence that the aluminous ore zone alteration assemblage of the LaRonde Penna deposit was once an advanced argillic hydrothermal alteration zone formed in a submarine environment but was subsequently metamorphosed (Dubé et al., 2007b; Beaudoin et al., 2014). If the advanced argillic alteration was indeed formed in a submarine setting, then there was most likely a direct magmatic input into the hydrothermal system rather than it forming from steam-heated or weathering processes (Dubé et al., 2007b; Mercier-Langevin et al., 2007b; Beaudoin et al., 2014). The next section will focus on magmatic contributions to ore-forming processes in VMS deposits.

1.1.2 Magmatic contributions to VMS

Many researchers have shown that base and precious metals in ancient VMS deposits can come from the leaching of deep footwall rocks by evolved seawater in high-temperature zones (Franklin et al., 1981; Yang and Scott, 1996; Gibson et al., 2007). However, research has also shown the possibility of magmatic contributions to the ore-forming fluid because of the spatial association of massive sulphides with ancient and modern sea-floor volcanic rocks (Stanton, 1994; Fenner, 1933; Urabe and Marumo, 1991; De Ronde, 1995; Franklin et al., 1981; Rona and Scott, 1993; Yang and Scott, 1996). For this reason, there is a level of uncertainty regarding the source of metals in VMS deposits (De Ronde, 1995; Yang and Scott, 2002; Gibson et al., 2007). The leaching of rocks by evolved seawater can be best understood by recognizing and defining high temperature reaction zones; whereas, the direct or indirect magmatic contribution to VMS deposits can be understood through studying behaviour patterns of metals and sulphur during partial melting, magmatic fractionation, and submarine volcanic evolution (Gibson et al., 2007). Depending how evolved and volatile-rich the associated magmas are, it is likely that metals are sourced from both the leaching of rocks by seawater and magmatic fluids in varying amounts (Figure 7; Gibson et al., 2007; Mercier-Langevin et al., 2007b).

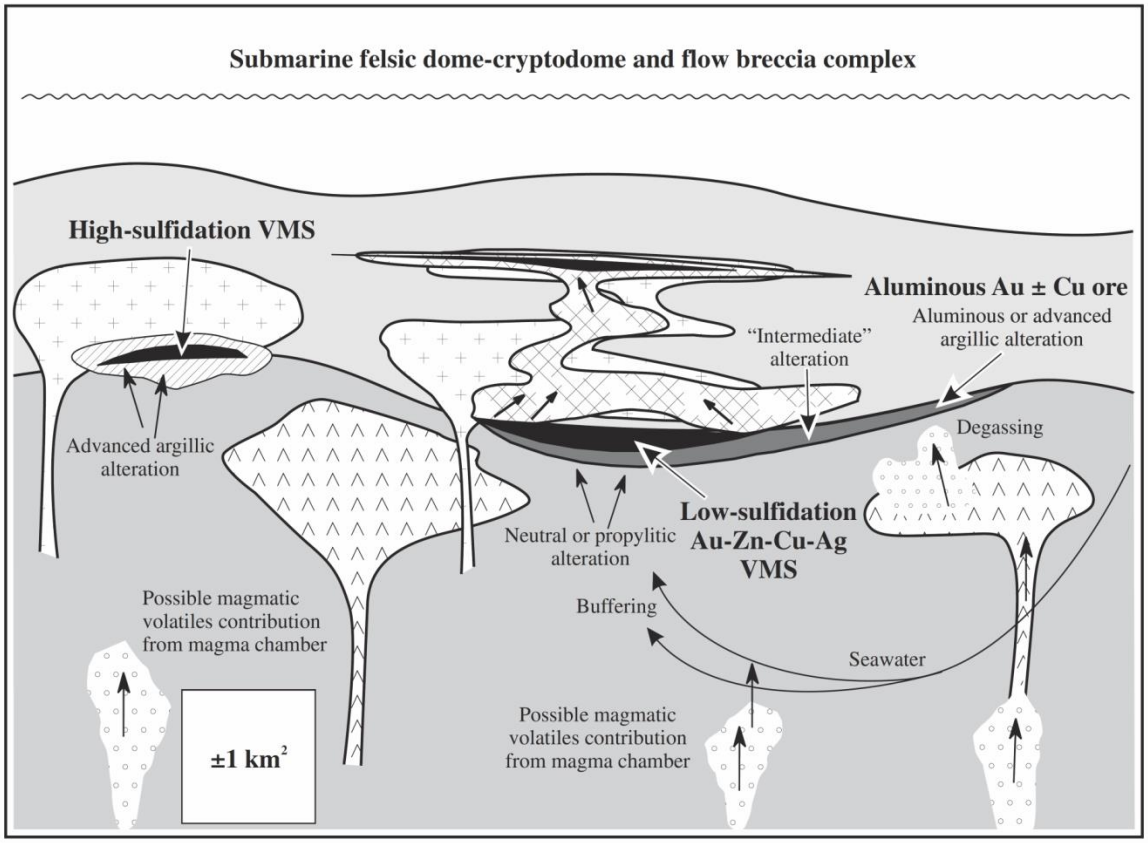

Figure 7: Model showing the environment for the formation of high- and low-sulfidation VMS deposits in a sub-marine felsic dome-cryptodome and flow breccia complex. The depicted volcanic architecture is a simplified version of the LaRonde-Bousquet 2 Au-rich VMS complex, Doyon-Bousquet-LaRonde mining camp, Quebec. The schematic shows that, in response to evolving local geology, mineralization styles can steadily evolve (spatially and temporally) from Au-Cu-Zn-Ag-Pb ore with neutral pH, to transitional, to acidic advanced argillic alteration with Au ± Cu ore. Importantly, the variability of seawater and magmatic volatile (degassing) contributions to the mineralizing hydrothermal fluids and its subsequent buffering controls what metal assemblages are transported to the ore (from Mercier-Langevin et al., 2007b).

To demonstrate the role seawater plays in the formation of VMS deposits, researchers have compared geochemical and geological characteristics of early VMS deposits to those of modern hydrothermal systems on the seafloor (Vearncombe et al., 1995; Jamieson et al., 2012). For example, sulphur isotope systematics of modern hydrothermal systems has shown that most of the sulphate in seawater precipitates as anhydrite as the downwelling fluid reaches higher temperatures (Alt, 1995; Jamieson et al., 2012). When the downwelling fluid reaches the base of the high-temperature upwelling zone, what is left of the sulphate reacts with the Fe^{2+}-bearing wall rock minerals (Shanks et al., 1981; Jamieson et al., 2012). At this point, the remaining sulphur is reduced and precipitates as sulphide minerals (i.e., ore minerals) at or near the seafloor surface after it has been mixed with sulphide leached from the volcanic host rock and ascended as hot fluid to mix with cold local seawater (Woodruff and Shanks, 1988; Jamieson et al., 2012). Not only does the reduced sulphur mix with sulphide leached from the volcanic host rock, but it also mixes with directly degassed magmatic sulphur (Herzig et al., 1998).

The magmatic contribution of metals to a VMS system is possible if three conditions are met: (i) there is an evolving magmatic system that exsolves volatiles with a fluid phase; (ii) there is an enrichment of ore metals in the exsolved fluid phase; and (iii) the enriched fluid separates and mixes with the sea-water convective system (Yang and Scott, 1996). The study of SMI in phenocrysts of fresh rocks can reveal information about the first two conditions because SMI are snapshots of the metal and volatile characteristics of pre-eruptive magmas at high pressure-temperature (PT) conditions (Roedder, 1984; Yang and Scott, 1996; Créon et al., 2018). Yang and Scott (1996) have demonstrated the potential

for magmatic contributions to submarine hydrothermal systems through the study of SMI in felsic volcanics dredged from the eastern Manus basin offshore of Papua New Guinea (Taylor et al., 1991). It is known that currently active volcanic systems, like those in the Manus basin, contain magmas that release magmatic fluids capable of carrying ore metals and volatiles when depressurized (Fenner, 1933; Roedder, 1984; Stanton, 1994; De Ronde, 1995; Hedenquist and Lowenstern, 1994; Yang and Scott, 1996). The volcanic rocks of the Manus basin host Cu-Zn-Pb-Ag-Au polymetallic sulphide deposits and represent a modern analogue of the hydrothermal environment that produced VMS deposits in the ancient geological record (Binns and Scott, 1993; Scott and Binns, 1995; Yang and Scott, 1996). The SMI of these volcanics were trapped in phenocrysts that formed early in the andesite-basaltic magma and contained metal- and CO_2-rich volatile phases (Yang and Scott, 1996). Together, these characteristics indicate that metals could have been transported by high-temperature fluids in the pre-erupted magma of the Manus basin and suggest that similar submarine magmatic-hydrothermal systems, like those that formed ancient VMS deposits, would exhibit the same processes (Ballhaus et al., 1994; Fleet and Wu, 1995; Stoiber and Rose, 1974; Taran et al., 1995; Yang and Scott, 1996).

Magmatic devolatilization could be the mechanism of subvolcanic intrusive complexes that produces hot fluids with enrichments of ore metals, S, and other volatiles, and supplies them to spatially associated seafloor deposits (Galley, 1996; Brauhart et al., 1998; Galley et al., 2003; Yang and Scott, 2003; Galley et al., 2007; Ioannou et al., 2007; Huston et al., 2011; Galley and Lafrance, 2014). For devolatilization to be effective in developing large ore deposits there would have to be appropriate temperature, pressure and redox conditions

for maintaining large concentrations of Cl and ore-forming metals in solution until a fluid phase is generated, the presence of hydrous magmas for production of a satisfactory vapour phase, and the sequestration of both metals and ligands in appropriate concentrations (Giggenbach, 1996; Christenson, 2000; Von Damm, 2000; Lilley et al., 2003; De Ronde et al., 2005; Galley and Lafrance, 2014). Due to its intricate evolution, the MIC, for example, may have had a suitable environment to trap metals and the ligands appropriate for their complexion and transportation to the subvolcanic depositional environment (Galley and Lafrance, 2014). Evidence of the in situ devolatilization process in subvolcanic intrusive complexes includes, but is not limited to, extensive alteration zones and miarolitic cavities associated with aplite dyke swarms, like those that formed during crystallization of the xenolith-rich tonalite magma chamber of the MIC-associated Mouska and Doyon stages (Audétat and Pettke, 2003; Galley and Lafrance, 2014).

In many cases, metal-rich magmatic volatiles can be supplied to precious metal-rich (e.g. Au) VMS systems (Lydon, 1996; Sillitoe et al., 1996; Hannington et al., 1999; Piercey, 2011). There is evidence suggesting this connection, including aluminous alteration assemblages, precious metal (Au-Ag) enrichment, fluid inclusions with high salinity and magmatic halogens, and suites of elements (e.g., Hg, Bi, Sb, and Ba) associated with epithermal deposits in the mineralization and alteration zones of the VMS systems (Sillitoe et al., 1996; Hannington et al., 1999; Roth et al., 1999; Sherlock et al., 1999; Dubé et al., 2007b; Mercier-Langevin et al., 2007b; Piercey, 2011). The shallow-level (i.e., less than 3-4 km depth) subvolcanic intrusions potentially provide the metals, fluids, and volatiles to precious metal-rich VMS systems, with deeper heat (i.e., ~10 km depth) being

the major driver for hydrothermal circulation on a larger, geodynamic scale (Figure 7; Piercey, 2011). The deeper heat source is typically a subvolcanic composite intrusion which, for exploration purposes, is important to dileneate because it establishes the location of thermal corridors that lead to significant VMS mineralization (Galley, 2003).

The large-scale fluid flow of these systems creates extensive (i.e., many kilometers of strike length) semi-conformable zones of hydrothermal alteration that intensifies into zones of discordant alteration in the footwall and hanging wall of individual deposits; they are discordant to regional metamorphic isograds (Figure 8; Galley, 1993; Hannington et al., 2003; Galley et al., 2007; Shanks, 2012). Some of these alteration zones, such as advanced argillic alteration zones associated with subaerial high-sulfidation hydrothermal systems (e.g., Arribas, 1995), are characterized by a direct contribution of magmatic fluids and meteoric fluid mixing (Hedenquist and Lowenstern, 1994; Beaudoin et al., 2014). Additionally, aluminous alteration zones, like those of the LaRonde Penna deposit, are interpreted to represent the metamorphosed equivalent of advanced argillic alteration zones and may also have contributions of magmatic fluids (Hedenquist and Lowenstern, 1994; Dubé et al., 2007b; Beaudoin et al., 2014). In a mineralogical context, a direct magmatic input can be inferred by the presence of uncommon alteration assemblages (e.g., advanced argillic, aluminous, strongly siliceous, or K-feldspar alteration; Hannington et al., 1999; Mercier-Langevin et al., 2011a). For example, the cone site of the Brothers hydrothermal system in the Southern Kermadec Arc has an advances argillic alteration assemblage of illite + amorphous silica + natroalunite + pyrite + native S, which is a common assemblage for subaerial magmatic hydrothermal systems (Arribas, 1995; De Ronde et al., 2005).

Geochemically, magmatic contributions to hydrothermal fluids can be inferred by specific trace element signatures; especially, those signatures with enrichments of chalcophile elements, like in fumarolic gas condensates from andesitic volcanoes (e.g., Au-Ag-As-Sb ± Bi-Hg-Te; Hannington et al., 1999; Huston, 2000; Halbach et al., 2003; Glasby et al., 2004; Glasby et al., 2008; Mercier-Langevin et al., 2011a).

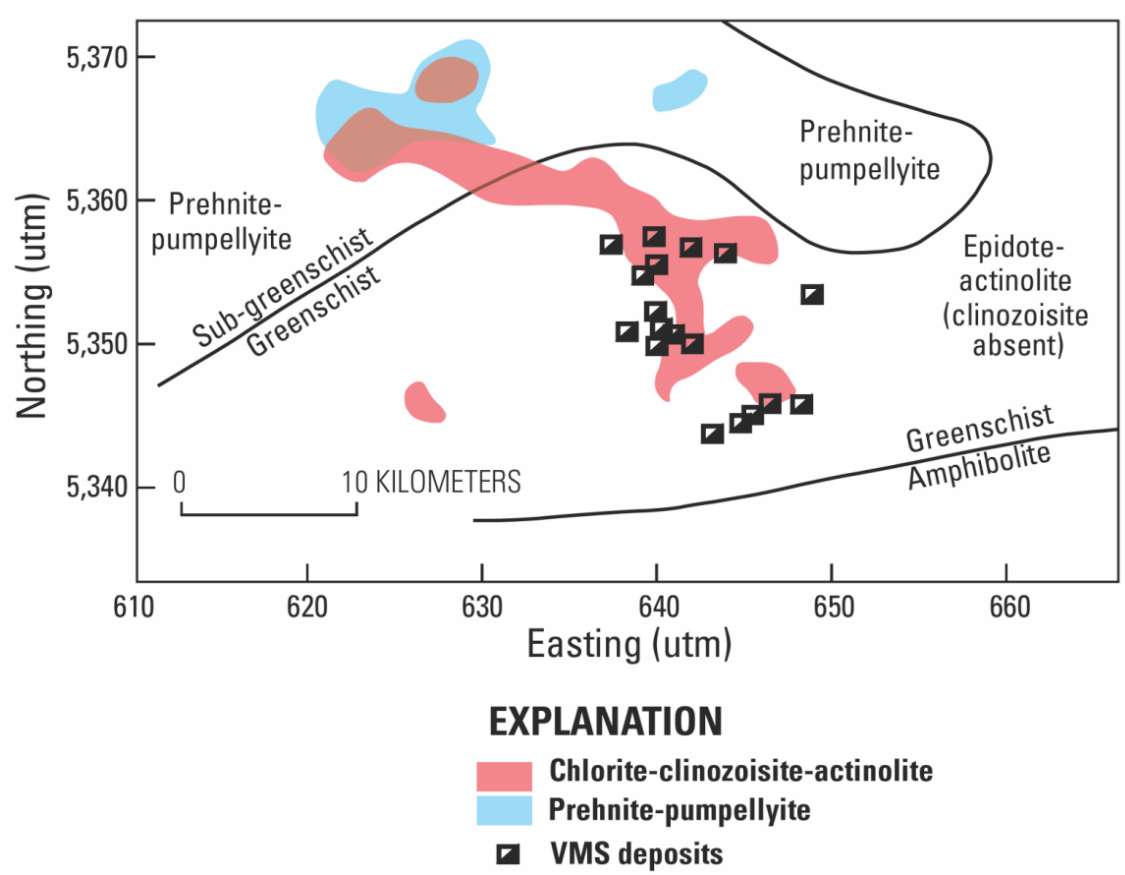

Figure 8: Example of the aerial extent of alteration zoning in VMS deposits. Semi-conformable alteration zones of the Blake River Group (Noranda volcanic complex, western Abitibi Subprovince, Ontario) that have a discordant geometry to the region's metamorphic isograds (Hannington et al., 2003; from Shanks, 2012).

1.2 List of acronyms and abbreviations

The following table summarizes acronyms and abbreviations that are commonly used throughout the thesis (following page):

Table 2: List of acronyms and abbreviations used throughout this thesis

Acronym/abbreviation	Meaning
alm	almandine
aln	allanite
ank	ankerite
ann	annite
BIF	banded iron formation
BON	boninite
BSE	back-scattered electron
bt	biotite
cal	calcite
CCD	charge-coupled device
ccp	chalcopyrite
chl	chlorite
CL	cathodoluminescence
cn	chondrite
cp	chalcopyrite
DBL	Doyon-Bousquet-LaRonde
EDS	energy dispersive spectroscopy
ep	epidote
flinc	fluid inclusion
fO2	oxygen fugacity
fsp	feldspar
Ga	giga-annum
gn	galena
grt	garnet
HCL	hot cathodoluminescence
HFSE	high field strength element(s)
HREE	heavy rare earth elements
IAT	island arc tholeiites
ilm	ilmenite
iron ox	iron oxide
KOM	komatiite
LA-ICP-MS	laser ablation inductively-coupled mass spectrometer
leu	leucoxene

LILE	large ion lithophile elements
LOTI	Low-Ti tholeiite
LREE	light rare earth elements
LRM	laser Raman microscopy
Ma	mega-annum
MHC	molybdenum-halfnium-carbide (vessel)
MIC	Mooshla Intrusive Complex
mnz	monazite
MORB	mid-ocean ridge basalt
ms	muscovite
Mt	million metric tons
NWR	New Wave Research (laser manufacturer)
OIB	ocean island basalt
phl	phlogopite
pl	plagioclase
po	pyrrhotite
PPL	plane polarized transmitted light
py	pyrite
QFP	quartz feldspar porphyry
qtz	quartz
REE	rare-earth element
rt	rutile
sd	siderite
SDD	silicon drift detector
SEM	scanning electron microscope
SILLS	Signal Integration for Leeds Laser System
SMI	silicate melt inclusion
sp	sphalerite
SRM	standard reference material
sul	sulphide
TGI-5	Targeted Geoscience Initiative-5
THOL	tholeiite
VMS	volcanogenic massive sulphide
zrn	zircon

Chapter 2: A melt inclusion study of rhyolitic volcanics in the Bousquet Formation, Doyon-Bousquet-LaRonde district, Abitibi Subprovince, Québec: Insight into Archean magmatic processes

Daniel Meagher*[1], Jacob Hanley[1], Kevin Neyedley[1], Zoltán Zajacz[2], Alexandra Tsay[2], and Patrick Mercier-Langevin[3].
[1]*Department of Geology, Saint Mary's University, Halifax, Nova Scotia, Canada*
[2]*Department of Earth Science, University of Toronto, Toronto, Ontario, Canada*
[3]*Natural Resources Canada, Geological Survey of Canada, Québec, Québec, Canada*
*corresponding author email address: daniel.meagher32@gmail.com

Number of pages: 222
Number of Figures: 35
Number of tables: 11 in text (3 in Appendices)
For submission to Contributions to Mineralogy and Petrology

Abstract

Silicate melt inclusions (SMI) in rhyolitic volcanic rocks in the ~2699 – 2697 Ma Bousquet Formation, Blake River Group (Doyon-Bousquet-LaRonde mining camp, Abitibi Subprovince, Québec) were studied using a variety of methods (petrography, microthermometry, high P-T homogenization, laser Raman microspectroscopy, SEM-EDS, SEM-CL, hot-CL, LA-ICP-MS). The main objectives of the study are to determine if the volcanic rocks preserve evidence of the original metal tenor of the magmas in SMI, and to examine the links between the metal contents and chemistry/volatile content of these melts and anomalously high Au content in some VMS deposits of the DBL deposit camp. The study is one of only a few studies of SMI from Archean age rocks and the first to present trace element/ore metal data for SMI of this age.

Diamond drill core was collected at the Westwood Mine and the LaRonde Penna Mine, while surface samples were collected near these mines, the Mooshla B deposit, and the Doyon Mine. Petrographic observations indicated that most units within the Bousquet Formation, except unit 4.2, contain SMI. However, only a few lithologies were appropriate for detailed study. The appropriate lithologies (i.e., units 2.0 and 5.3) contain locally large phenocrysts that were not pervasively fractured and SMI that were not chemically modified. Silicate melt inclusions of primary origin were characterized from magmatic quartz phenocrysts of units 2.0 [quartz feldspar porphyry (QFP) rhyolite sills] and 5.3 (QFP rhyolite flows). Data reported for SMI are for inclusions that are recrystallized but occur away from fractures and areas of alteration-dissolution-reprecipitation of the host phenocryst, as indicated by cathodoluminescence imaging, and do not show evidence of post-entrapment decrepitation. The SMI have a similar mineralogy to hourglass inclusions (physically connected to surrounding matrix), but can be differentiated from these on the basis of: (i) the hourglass inclusions are always completely crystallized (no glass) and contain secondary (metamorphic, alteration) minerals not found in SMI; (ii) the hourglass inclusions often appear to be still tied to an embayment of matrix material that protrudes into the quartz phenocryst but that extends below the inclusion out of the plane of focus; (iii) the hourglass inclusions are often highly irregular in shape and their contained crystals penetrate into the inclusion walls, whereas commonly (but not always) SMI are smaller and rounded/subrounded with smoother walls. Homogenized SMI show that co-entrapment of an immiscible carbonic fluid (CO_2-dominant) occurred, indicating that the melt was saturated in CO_2 at the time of entrapment in the phenocrysts.

Based on SEM analyses of homogenized SMI, the contained melts are rhyolitic. Trace element dissemination based on LA-ICP-MS data indicate that unit 2.0 SMI are of ocean ridge (ORG) or within plate (WPG; anorogenic) tectonic settings whereas unit 5.3 SMI are consistent with a syn-collision (syn-COLG) or volcanic arc (VAG) classification. However, no SMI have trace element (Sr-Y-La-Yb) characteristics consistent with Archean tonalite-trondhjemite-granodiorite (TTG), suggesting significant compositional modification (e.g., possibly due to crustal contamination) prior to entrapment relative to equivalent intrusive units of the Mooshla Intrusive Complex (MIC). Even though the bulk compositions of the SMI and bulk rocks are similar, the range in major and trace elements is much wider in the SMI. Comparative analysis of apatite, SMI, and bulk rock data shows: (i) At depth, prior to eruption-emplacement, the SMI and coeval apatite record the crystallization of significant amounts of plagioclase (An = 10 – 30%), K-feldspar, and apatite; (ii) The concentrations of Au, Cu, As, Sn, Sb, Bi, and Pb are up to two orders of magnitude higher in SMI than in bulk rocks; (iii) Major and trace data for the SMI reflect significant differentiation of the rhyolite (at least 70 – 75%) over its entrapment history indicating a prolonged phenocryst residence at depth in a rhyolitic magma chamber; and (iv) Metal concentrations in bulk rocks in this setting are not representative of the composition of the original magmatic liquids.

The presence of CO_2 in SMI of the Bousquet rhyolites, due to their advanced age, suggests that any SMI trapped in a magmatic system may potentially have CO_2 as a saturated phase. Unlike typical porphyry, which have natural fractionation degassing, the Bousquet magmatic system continuously received CO_2-bearing fluids from an external

source, became CO_2 saturated, and underwent constant fractionation iterations with degassing causing early removal of metal-bearing H_2O fluids. The source of CO_2 trapped in the SMI could have been organic matter or carbonates in wall rocks hosting the rhyolitic magma at depth. However, the oldest sedimentary rocks in the area belong to the Cadillac Group (<2689 Ma) which are younger and overly the Blake River Group.

Ore metal contents in the SMI of units 5.3 and 2.0 are potentially minimum values, suggested by the presence of co-entrapped carbonic liquid and very low water content in the inclusions. Immiscible or exsolving fluid phases likely disturbed the original metal contents of the SMI which is seen in the lack of correlation between very strongly incompatible elements (e.g., Cs) and ore metals in SMI. Ore metal ratios in the SMI are conserved even in the presence of saturated volatiles, as seen in the overlapping of selected metal ratios of the SMI and the LaRonde Penna deposit ore bodies. The overlap indicates that the volcanic rocks have had some direct influence, through active degassing or passive leaching, on the metals of the LaRonde Penna VMS deposits.

The SMI of unit 5.3 have a range of 6 ppb Au (1st quartile) to 159 ppb Au (3rd quartile; n = 10) while unit 2.0 SMI have a range of 5 ppb Au (1st quartile) to 24 ppb Au (3rd quartile; n = 14); at these Au concentrations, a *minimum* of 0.5 – 15 km^3 and 4 – 19 km^3 of rhyolitic magma would be required, respectively, to source the Au in the LaRonde Penna VMS deposits through leaching or devolatilization. A conservative estimate of the volume of the Upper Member of the Bousquet Formation is approximately ~7.5 km^3. Therefore, it is not unreasonable that with a correction for efficiency, the rhyolitic units of the Bousquet Formation provided magmatic Au to the VMS deposits.

2.0 Introduction

It is well known that a prerequisite for the evolution of volcanogenic massive sulfide (VMS) deposits is the presence of a synvolcanic magmatic system which initiates and drives subseafloor convective hydrothermal systems (Campbell et al., 1981; Cathles, 1981; Lydon, 1996; Brauhart et al., 1998; Barrie et al., 1999; Galley, 2003; Galley et al., 2003; Franklin et al., 2005; Baker, 2009; Galley and Lafrance, 2014). Many researchers have suggested that volatiles and metals of magmatic origin contribute directly to the ore-forming fluid of VMS systems, especially in Au-rich VMS deposits, stressing the spatial and temporal association of mineralization with ancient and modern sea-floor volcanic rocks (Fenner, 1933; Franklin et al., 1981; Urabe, 1987; Sawkins, 1990; Urabe and Marumo, 1991; Rona and Scott, 1993; Stanton, 1994; De Ronde, 1995; Sillitoe et al., 1996; Yang and Scott, 1996; Hannington et al., 1999; Hannington et al., 2005; Mercier-Langevin et al., 2007c). A magmatic contribution of metals to a VMS system is possible if three conditions are met: (i) there is an evolving metal-rich magmatic system that exsolves volatiles; (ii) there is an enrichment of ore metals in the exsolved volatile phase; and (iii) the metal enriched volatiles mix into the seawater convective system (Yang and Scott, 1996). Evidence for magmatic devolatilization of subvolcanic intrusive complexes as a process to enrich metals, S and other volatiles species in VMS systems has been extensively discussed (Galley, 1996; Brauhart et al., 1998; Galley et al., 2003; Yang and Scott, 2003; Galley et al., 2007; Ioannou et al., 2007; Huston et al., 2011; Piercey, 2011; Galley and Lafrance, 2014). Evidence for the in-situ devolatilization process in VMS-coeval subvolcanic intrusive complexes includes, but is not limited to, the presence of extensive alteration zones and miarolitic cavities associated with aplite dyke swarms. Evidence that

devolatilization has led to the delivery of metal-bearing magmatic volatiles to VMS systems includes the following features in mineralized and hydrothermally altered zones: (i) aluminous alteration assemblages (i.e., metamorphosed equivalent of advanced argillic assemblages); (ii) potassic alteration; (iii) enrichment in precious metals (Au-Ag); (iv) high salinity fluid inclusions and magmatic halogens; and (v) other element suites (e.g., As, Hg, Bi, Sb) typically associated with porphyry-epithermal deposits (Hedenquist and Lowenstern, 1994; Arribas, 1995; Sillitoe et al., 1996; Hannington et al., 1999; Roth et al., 1999; Sherlock et al., 1999; Halbach et al., 2003; Glasby et al., 2004, 2008; Dubé et al., 2007b; Mercier-Langevin et al., 2007b, 2011a; Piercey, 2011; Beaudoin et al., 2014).

In the DBL mining district, Abitibi Subprovince, Québec, a prolific period of Au-enriched VMS deposit formation was synchronous with the eruption/emplacement of the Bousquet Formation volcanics (2699–2697 Ma; Lafrance et al., 2003; Mercier-Langevin et al., 2007b; Mercier-Langevin et al., 2017), Blake River Group (ca. 2704 – 2695 Ma). Whereas the geological relationships between mineralization and volcanism are well documented, strongly suggesting a genetic link (e.g., Mercier-Langevin et al., 2007a, b; Galley and Lafrance, 2014), the metal endowment of the original magmas and their potential to supply ore and accessory metals and volatiles to the seafloor or subseafloor hydrothermal systems are unconstrained. In particular, the upper member of the Bousquet Formation, which hosts the majority of the Au-rich VMS deposits in the DBL camp (i.e., LaRonde Penna deposit: 59 Mt at 4.3 g/t Au, 8.1 Moz Au; Mercier-Langevin et al., 2007c; Bousquet 2-Dumagami deposit: 15.5 Mt at 7.3 g/t Au, 3.6 Moz Au; Mercier-Langevin et al., 2007c, 2009; Westwood deposit: 14.2 Mt at 7.6 g/t Au, 3.5 Moz Au; Mercier-Langevin

et al., 2009; and Bousquet 1 deposit: 7.5 Mt at 5.3 g/t Au, 1.3 Moz Au; Mercier-Langevin et al., 2009), is a strong candidate for contributing both metals and volatiles to the Au-rich VMS deposits. In particular, the unit 5.3 QFP rhyolite may have been especially important as a causative magma since it hosts the 20 North lens hanging wall of the LaRonde Penna deposit.

Previous studies (Valiant and Hutchinson, 1982; Guha et al., 1983; Gaudreau, 1986; Langshur, 1990; Marquis et al., 1990; Savoie et al., 1991; Trudel et al., 1992; Belkabir and Hubert, 1995; Tremblay et al., 1995; Gosselin, 1998; Lafrance et al., 2003a, 2005; Dubé et al., 2004, 2007a-b, 2014; Mercier-Langevin et al., 2004, 2007a-d, 2009, 2011a; Mercier-Langevin, 2005; Galley and Lafrance, 2007, 2014; Wright-Holfeld et al., 2010, 2011; Beaudoin et al., 2014; Yergeau, 2015; Yergeau et al., 2015) have suggested a genetic link between the MIC, Bousquet Formation volcanics, and regional deposits in the area, based on ore metal distributions, geochronology, mapping/field relations, petrography, and lithogeochemistry. Specific lines of evidence include: (i) crude metal zoning (Cu-Zn-Pb-Ag-Au), despite metamorphic recrystallization and deformation which is still evident in the massive sulphide lenses, demonstrating primary synvolcanic mineralization (Mercier-Langevin, 2005; Dubé et al., 2004, 2007a); (ii) U-Pb geochronology revealing that, in less than ~2 Ma, the volcanic and intrusive rocks of the Bousquet Formation and MIC were emplaced/erupted; crosscutting relationships and the relative timing of deformation and metamorphism suggest that ore-forming hydrothermal systems were linked to the magmatism, with VMS ores more or less coeval with volcanism (Dubé et al., 2014; Yergeau et al., 2015); (iii) petrography and lithogeochemistry indicating correlations of different volcanic and alteration facies with Au enrichment (Mercier-Langevin et al.,

2017); (iv) The occurrence of Au-enriched sulphide-rich clasts in debris flows that occur stratigraphically above massive sulphide lenses in the LaRonde Penna deposit, implying that there was pre-deformation Au-rich VMS mineralization (Mercier-Langevin, 2005; Dubé et al., 2007a); (v) The observation of little or no Au mineralization between stacked Au-rich ore lenses within the volcanic succession (Mercier-Langevin et al., 2017); and (vi) The observation of a primary distribution of Au and Cu preserved in highly strained lenses along synvolcanic faults (Mercier-Langevin et al., 2017).

In general, past studies indicate that Au, along with other metals (Cu-Zn-Ag-Pb) were mainly introduced as primary components of the ore bodies in the DBL camp (Dubé et al., 2004; Mercier-Langevin et al., 2004; Mercier-Langevin, 2005; Galley and Pilote, 2002; Galley and Lafrance, 2007; Lafrance et al., 2003a, b, c, 2005). For example, Au-Cu-Zn-Ag-Pb mineralization at the LaRonde Penna deposit is suggested to have formed from near-neutral, seawater-dominated hydrothermal fluids with possibly direct magmatic contributions responsible for the Au ± Cu endowment of the ore and advanced argillic alteration (now aluminous alteration; Dubé et al., 2007; Mercier-Langevin et al., 2007b, c). However, although less deformed parts of the volcanic sequence have been studied (e.g., the LaRonde Penna deposit), the extent of deformation, metamorphism and alteration severely limits the ability to accurately constrain ore paragenesis and primary features (e.g., original mineral assemblages and metal tenor; Tourigny et al., 1989a; Mercier-Langevin et al., 2007a, b, d). Such deformation and metamorphic events modify the metal chemistry of bulk rocks thereby masking evidence of metal enrichment, degassing, fluid-melt partitioning, and the extent of magmatic fractionation and their relationship to ore metal tenor (Ikramuddin et al., 1975; Hannington et al., 1986; Marshall and Gilligan, 1987, 1993;

Larocque et al., 1993; Marshall et al., 2000). In the DBL camp, the overlapping nature of multiphase deformation, regional metamorphic episodes, and magmatism is a fundamentally limiting issue when evaluating the causative links between magmatic activity and Au metallogenesis (Galley and Lafrance, 2014).

The Bousquet Formation volcanics at the LaRonde Penna mine, occurring to the east of the MIC, provide a rare opportunity in an Archean terrane to study the petrography and chemical composition of silicate melt inclusions (SMI) to develop first order constraints concerning the potential for a direct magmatic contribution to the district's Au-rich VMS deposits. Ore lenses of the LaRonde Penna Au-rich VMS deposit are hosted by the 2698 ± 0.8 Ma upper member of the Bousquet Formation (Mercier-Langevin et al., 2007b, 2017), contemporaneous with a prolific period of Au-rich VMS formation in the Blake River Group (McNicoll et al., 2014; Mercier-Langevin et al., 2017). The age relationship between the host upper member of the Bousquet Formation and the LaRonde Penna deposit suggests a viable correlation between the petrogenetic evolution of this volcanic assemblage and enrichment in Au (Mercier-Langevin et al., 2007c, 2011c, 2017).

The analysis of SMI preserved in phenocryst quartz and other relatively robust igneous minerals (e.g., apatite, titanite, zircon) provides a means to determine the original metal tenor and volatile of the magmatic system and its potential to supply ore metals to the hydrothermal system. The compositions of SMI may be largely unaffected by post-solidus processes, and may also preserve magmatic liquid compositions that predate magmatic-hydrothermal processes such as differentiation, degassing and leaching of metals (e.g., Roedder, 1979; Kamenetsky et al., 1999; Audétat et al., 2000; Danyushevsky et al., 2002; Rapien et al., 2003; Schiano, 2003; Student and Bodnar, 2004; Halter et al., 2005; Audétat

and Pettke, 2006; Zajacz et al., 2008; Lerchbaumer and Audétat, 2013; Zhang and Audétat, 2018). Specifically, integrating petrographic studies with geochemical analysis of the SMI allows the temporal evolution of melt composition to be evaluated at different stages in the magmatic-hydrothermal evolution of a mineralizing environment, as shown in many studies (e.g., Sobolev and Shimizu, 1993; Nielsen et al., 1995; Gurenko et al., 1996; Sobolev and Chaussidon, 1996; Sobolev, 1996; Kamenetsky et al., 1997; Kamenetsky et al., 1999; Métrich et al., 1999; Audétat et al., 2000; Sobolev et al., 2000; Rapien et al., 2003; Student and Bodnar, 2004; Halter et al., 2005; Audétat and Pettke, 2006; Zajacz et al., 2008; Lerchbaumer and Audétat, 2013; Zhang and Audétat, 2018).

In this study, quartz phenocryst-hosted SMI in two rhyolitic units of the lower and upper members of the Bousquet Formation were characterized using a variety of microanalytical techniques (scanning electron microscopy-backscattered electron [SEM-BSE] imaging, SEM-energy dispersive spectroscopy [EDS], cathodoluminescence [CL], laser Raman microspectroscopy [LRM], laser ablation-inductively coupled plasma-mass spectrometry [LA-ICPMS], and preliminary microthermometry/homogenization experiments) in order to provide a detailed mineralogical and geochemical description of the SMI, including ore and accessory metal chemistry. Together, the data gathered provide new constraints on the chemical evolution of the magmatic-hydrothermal systems in the district. Specific objectives addressed include: (i) An evaluation of the robustness of SMI preservation through petrography and chemical analysis; (ii) Constraining the metal and trace element chemistry of SMI and evaluating processes that may influence metal enrichment; (iii) A preliminary evaluation of the presence and role of volatiles in magma evolution; and (iv) A preliminary evaluation of the magmatic fluid contribution to Au-rich VMS.

The present study is one of only a few investigations of SMI in Archean-age terranes (e.g., McDonough and Ireland, 1993; Shimizu et al., 2001; Chupin et al., 2006; Berry et al., 2008). These studies of Archean SMI focus exclusively on komatiitic olivine phenocrysts which are typically fractured and replaced by serpentine and entrap melts during the rapid growth of spinifex olivine (Kamenetsky et al., 2010). A lack of studies in Archean terranes may stem partially from the assumption of a lack of SMI preservation (extensive modification) but these are unfounded concerns since polyphase deformation, metamorphism, and uplift can equally impact younger terranes. The current study offers a new approach to Archean melt inclusion investigations, focusing on quartz phenocrysts as hosts to SMI.

2.1 Geological Setting

2.1.1 Deposit overview

Deposits of the DBL mining camp ,discovered and developed 50 km east of the Noranda district, have been mined since the 1930s and contain Au ± Cu-Zn-Ag-Pb ores which contain more than 28 Moz of Au combined, making the camp one of the most Au-rich mineralized districts in Canada, and one of the world's largest Au districts hosted in Archean-age rocks (Lafrance et al., 2003; Gibson and Galley, 2007; Mercier-Langevin et al., 2007a, 2009, 2011b; Mercier-Langevin et al., 2011b; Galley and Lafrance, 2014).

There are three main Au ± Cu-Zn-Ag deposit types in the camp: (i) Au-rich VMS deposits (*LaRonde Penna, Bousquet 2-Dumagami, Bousquet 1, Westwood, Ellison, and Warrenmac deposits*; total ≈ 12.3 Moz Au); (ii) epizonal "intrusion-related" Au-Cu

sulphide-rich vein systems (*Doyon deposit*; total ≈ 5.7 Moz Au); and (iii) shear zone-hosted, orogenic (remobilized), Au-Cu sulphide-rich veins (*Mouska, Mic Mac, and Mooshla deposits*; total ≈ 7.6 Moz Au; Mercier-Langevin et al., 2007a, 2009; Galley and Lafrance, 2014; Yergeau, 2015). The third type (shear zone-hosted) shares characteristics with ore types 1 and 2 and could be transposed and/or remobilized epizonal intrusion-related Au-Cu vein systems or Au-rich VMS (Mercier-Langevin et al., 2007a). The shear zone-hosted deposit has a quartz-sulphide vein type that resembles that of the epizonal intrusion-related Au-Cu deposits (e.g., Doyon deposit; Mercier-Langevin et al., 2007a). Specifically, the veins contain 75 vol% sulphides (pyrrhotite and chalcopyrite are dominant, with minor pyrite), the quartz is greyish, and there are trace amounts of magnetite, ilmenite, electrum, and tellurides of Ag and Pb (Belkabir and Hubert, 1995; Mercier-Langevin et al., 2007a). Together, all the deposits in the camp make it the sixth largest Au district in the Superior Province with a total past production, current reserves, and estimated resources of 790.1 t Au (Mercier-Langevin et al., 2020). The present study focuses on the Au-rich VMS deposits of the DBL camp which contains two world-class deposits (i.e., LaRonde Penna and Bousquet 2) with production, reserves, resources, and metal ratios shown in Table 1.

Table 1: Total production, reserves, and resources[1] at the end of 2013 (December 31, 2013) for the Doyon-Bousquet-LaRonde mining camp

Deposit type	Mine name	Year	Cummulative production								Total metal budget (in situ)					
			Tonnage (Mt)	Au (g/t) prod.	Au (g/t) in situ	Au (t) prod.	Au (t) in situ	Ag (t) prod.	Cu (t) prod.	Zn (t) prod.	Tonnage (Mt)	Au (g/t)	Au (t)	Ag (t)	Cu (t)	Zn (t)
Au-rich volcanogenic massive (±semimassive) sulfide lenses, and Au-rich sulfide veins, stockworks and disseminations																
	Dumagami	1988-1999	7.33	6.28	6.84	46.01	50.12	85.79	34,196	4,994	7.33	6.84	50.11	143	48,854	8,323
	LaRonde Penna[2]	2000-	32.43	2.81	3.11	91.21	100.96	1,584.62	80,542	733,732	71.33	3.91	279.21	2,903	204,479	1,386,061
	Bousquet 2	1990-2002, 2007	8.22	8.11	8.56	66.64	70.31	0.42	45,804	20	10.31	7.95	81.99		54,411	
	Bousquet 1	1978-1996	7.45	5.3	5.7	39.49	42.45				22.68	3.47	78.65			
	Ellison										1.69	4.56	7.71			
	Total VMS DBL		55.43	5.63	6.05	243.35	263.84	1670.83	160,542	738,746	113.34	5.35	497.67	3046	307,744	1,394,384

Deposit type	Deposit/Unit	Metal ratios			
		Sb/Bi ratio (ave ± 1 std dev)	Au/As ratio (ave ± 1 std dev)	Cu/As ratio (ave ± 1 std dev)	Cu/Au ratio (ave ± 1 std dev)
Au-rich volcanogenic massive (±semimassive) sulfide lenses, and Au-rich sulfide veins, stockworks and disseminations					
	LaRonde (Zn-rich 20N lens)[3]	48.4 ± 48.9	0.0085 ± 0.012	9.72 ± 21.34	1449.97 ± 2265.68
	LaRonde (Zn-rich 20S lens)[3]	3.35 ± 8.43	0.036 ± 0.039	11.43 ± 12.41	750.57 ± 589.08
	LaRonde (Au-rich, aluminous 20N lens)[3]	0.10 ± 0.019	0.030 ± 0.015	24.90 ± 18.66	1369.21 ± 1251.36
	Doyon[4]	4.91 ± 9.01	0.64 ± 0.51	136.23 ± 177.45	145.37 ± 121.24
	Westwood[4]	23.19 ± 18.01	1.02 ± 2.02	62.66 ± 146.84	222.06 ± 224.58
	Mouska[4]	4.25 ± 6.33	3.38 ± 5.59	337.77 ± 314.42	3172.34 ± 7566.53
	unit 2.0 SMI	2.14 ± 1.56	0.0035 ± 0.0034	13.62 ± 30.60	1270.63 ± 2846.97
	unit 5.3 SMI	6.91 ± 9.93	0.045 ± 0.00	0.16 ± 0.019	4.00 ± 0.00

Note: Modified from Mercier-Langevin et al., 2017.

1. Global gold endowment figures (total metal budget in situ) include total historical production (in situ) plus current reserves and resources data taken from public sources and are for comparison purposes only; refer to Iamgold and Agnico Eagle Mines websites for details.
2. Current producers.
3. Reference: Dubé et al., 2003.
4. Reference: GSC, unpublished.

2.1.2 Regional geology

The DBL mining camp's regional geology and geologic setting of its contained mineral deposits have been described in Gunning (1941), Fillion et al. (1977), Valiant and Hutchinson (1982), Marquis et al. (1990b), Trudel et al. (1992), Lafrance et al. (2003, 2005), Mercier-Langevin et al. (2004, 2007a, 2011b), and Yergeau (2015). The DBL mining camp is within the eastern- and upper part of the Blake River Group (ca. 2704 – 2695 Ma; McNicoll et al., 2014), which is the youngest volcanic-dominated group in the Archean Abitibi greenstone belt between the Lac Parfouru fault to the north and the Cadillac-Larder fault zone to the south (Ayer et al., 2002; Lafrance et al., 2005; Mercier-Langevin et al., 2007a, b; McNicoll et al., 2014). The DBL mining camp is a ~10 km long east-west-striking, southerly younging homoclinal succession of Blake River Group tholeiitic, transitional, and calc-alkaline submarine volcanic rocks (Lafrance et al., 2003a; Mercier-Langevin et al., 2007d). The base of the Blake River Group volcanics (i.e., the Hébécourt Formation) is in thrust contact with the sedimentary rocks of the younger Kewagama Group (≤2686 ± 4 Ma; Davis, 2002) to the north along the Lac Parfouru fault, and is disconformably overlain by siliciclastic strata and minor iron formation of the Cadillac Group to the south (≤2689 Ma ± 2 Ma in the LaRonde Penna mine area: Mercier-Langevin et al., 2007a, and ≤2687.4 ± 1.2 Ma in the Doyon mine area: Lafrance et al., 2005; Mercier-Langevin et al., 2007b, d; Galley and Lafrance, 2014).

The Blake River Group is divided into the Hébécourt Formation in the north and the Bousquet Formation in the south (Lafrance et al., 2003a). The base of the Hébécourt Formation is primarily tholeiitic pillowed to massive aphyric to glomeroporphyritic

tholeiitic basalt flows and sills (Lafrance et al., 2003). Its upper contact is intruded by QFP rhyolite sills of unit 2.0 of the Bousquet Formation (Lafrance et al., 2003). More emphasis will be on the Bousquet Formation because it is the focus of this study; it overlies the Hébécourt Formation, consists of a volcanic succession that is more geochemically evolved and fractionated than the basalt and andesite of the Hébécourt Formation, and has a composition of transitional tholeiitic at the base (i.e., north) to calc-alkaline at the top (i.e., south; Lafrance et al., 2003a; Mercier-Langevin et al., 2007b, d; Galley and Lafrance, 2014). It is divided into two members: the lower member (unit 2.0, 2698.6 ± 1.5 Ma, Lafrance et al., 2003; unit 4.2, 2698.3 ± 0.9 Ma, Lafrance et al., 2005) and the upper member (unit 5.2, 2698.3 ± 0.8 Ma, Mercier-Langevin et al., 2007b; unit 5.3, 2697.8 ± 1 Ma, Mercier-Langevin et al., 2007b; unit 5.5, 2697.5 ± 1.1 Ma, McNicoll et al., 2014).

Strong deformational and metamorphic events are seen in the Bousquet Formation, with at least three phases of deformation that account for the present geometry of the camp (Langshur, 1990; Savoie et al., 1991; Belkabir and Hubert, 1995; Mercier-Langevin et al., 2007b). A weak, moderately inclined northeast-southwest foliation (S_1) defines the first phase of deformation (D_1) which is responsible for the regional folding of the Blake River Group (Hubert et al., 1984; Mercier-Langevin et al., 2007b; Yergeau, 2015). A strong, overprinting, and penentrative east-west schistosity (regional S_2) with shear planes and faults that dip steeply to the south represents the second and main deformation phase (D_2) in the DBL area (Mercier-Langevin et al., 2007b; Galley and Lafrance, 2014). The second deformational event (D_2) caused intense flattening, stretching, folding, and shearing of primary features in most deposits (e.g., Bousquet deposit: Tourigny et al., 1989b; Bousquet

2-Dumagami deposit: Tourigny et al., 1993; Marquis et al., 1990b; Doyon deposit: Savoie et al., 1991). Dextral transpressive brittle-ductile faults related to the third phase of deformation (D_3) overprint D_2 (Yergeau, 2015). In a regional metamorphic context, the Blake River Group has a prograde upper greenschist-lower amphibolite-facies episode associated with the main deformational phase (D_2), and an overprinting phase associated with retrograde greenschist metamorphic facies (Dimroth et al., 1983a, b; Tourigny et al., 1989a; Marquis et al., 1990a; Powell et al., 1995; Lafrance et al., 2003; Mercier-Langevin, 2005; Dubé et al., 2007b). Unoriented porphyroblasts of actinolite and biotite in the MIC suggest peak metamorphism is late to post-D_2 (Marquis et al., 1990b; Belkabir and Hubert, 1995; Dubé et al., 2004; Mercier-Langevin, 2005).

2.1.3 Lower Member of the Bousquet Formation

The Bousquet Formation volcanics are sub-divided into a lower member and an upper member (Figure 1; Galley and Lafrance, 2014). The lower member is older than the upper member and is predominantly composed of tholeiitic to transitional, mafic to felsic pillows and flows, and its units are laterally extensive (Stone, 1990; Lafrance et al., 2003a; Mercier-Langevin et al., 2007a, b, 2008; Yergeau et al., 2015). It can be up to 600m thick and is characterized in the western DBL camp by a glomeroporphyritic dacite unit overlying intermediate scoriaceous tuffs and tuff breccia units with mainly basaltic to andesitic fragments (unit 3.3; Mercier-Langevin et al., 2008). The lowest stratigraphic unit (unit 2.0; 2698.6 ± 1.5 Ma; Lafrance et al., 2003) is comprised of porphyritic (quartz and feldspar), tholeiitic, rhyolite sills that intrude the older Hébécourt Formation (Figures 1 and 2; Lafrance et al., 2003a). These sills can have up to 35 vol % blue quartz and feldspar

phenocrysts (<1.5 mm) in a sericitized matrix (Mercier-Langevin et al., 2007c). Unit 2.0 rhyolite is distinct from other units of the Bousquet formation because it has high Si and Zr contents and an elevated Zr/TiO_2 ratio (Mercier-Langevin et al., 2009). Unit 2.0 consists of meter-thick sills of unit 2.1 in the Hébécourt basalt (Figures 1 and 2).

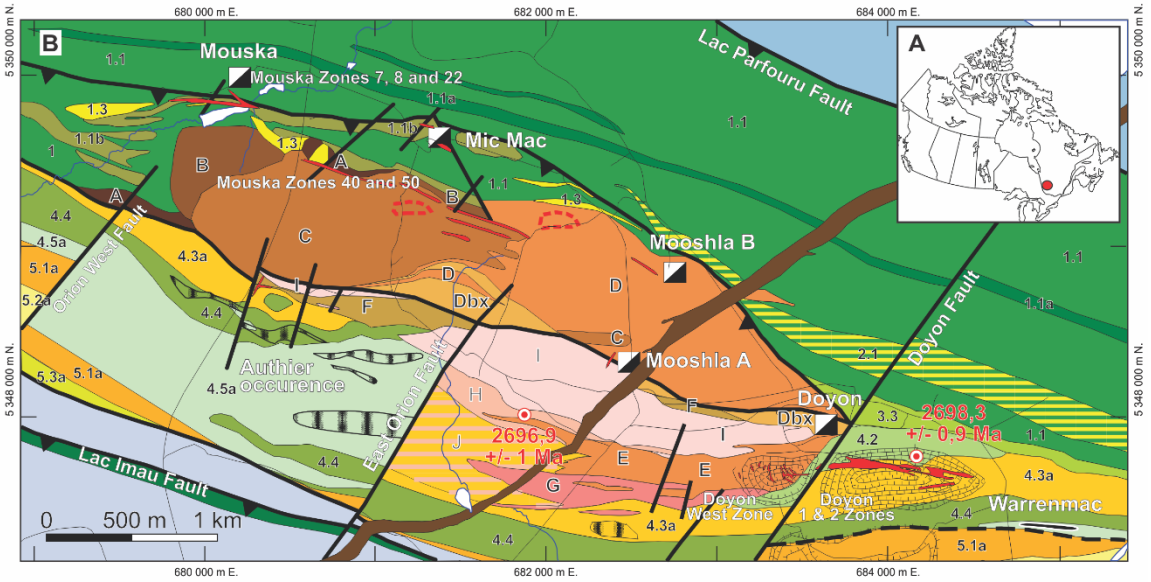

Intrusive rocks

- Proterozoic diabase

Mooshla intrusive complex

Doyon stage

- I — Aphyric to quartz porphyritic trondhjemite
- J — Interlayered Phase H and I in Unit 4.3a
- H — Plagioclase-quartz porphyritic trondhjemite
- G — Plagioclase porphyritic tonalite
- F — Plagioclase-horneblende porphyritic tonalite

Mouskla stage

- E — "Doyon quartz diorite": pendant of Dbx
- Dbx — Xenolith-rich tonalite: Phase D hangingwall contact
- D — Tonalite
- C — Quartz diorite
- B — Layered gabbro
- A — Aphyric/ feldspar porphyritic diorite

Sedimentary rocks

- Cadillac sedimentary rocks
- Kewagama sedimentary rocks

Volcanic rocks

Bousquet Formation

Upper Bousquet

- 5.3a — Bousquet-Ferris QFP rhyolite
- 5.2a — Doyon rhyodacite-rhyolite
- 5.1a — Doyon dacite-rhyodacite

Lower Bousquet

- 4.5a — **Warrenmac rhyodacite** Rhyodacitic schist
- 4.4 — **Bousquet heterogeneous unit** Basaltic to andesitic schist
- 4.3a — **Doyon mine felsic Unit** Dacitic to rhyolitic schist
- 4.2 — **Doyon glomeroporphyritic dacite**
- 3.3 — **Bousquet scoriaceous tuff** Andesite and dacite
- 2.1 — **Bousquet felsic sills swarm** Rhyolite

Hébécourt Formation

- 1.3 — Rhyolite
- 1.1b — Magnetite-rich basalt and basaltic andesite
- 1.1a — Glomerporphyritic basalt and basaltic andesite
- 1.1 — Basalt and basaltic andesite flows

Mineralization

- Gold mine
- Gold lens
- Anomalous gold zone
- Massives sulfides zone
- Massives sulfides horizon
- VMS stringer mineralization
- Open Pit

Figure 1 (previous page): Location and geological map of the DBL mining camp. (A) Simplified map of Canada showing the location of the DBL mining camp in Rouyn-Noranda, Quebec. Location is indicated by the red dot. (**B)** Geological map of the MIC, Bousquet Formation volcanics, and associated ore deposits (modified from Galley and Lafrance, 2014). Note: Although this map does not list unit 2.0, it is the most straightforward representation in the literature of the relationship between intrusives and volcanics in the DBL camp; therefore, unit 2.0 is represented by unit 2.1 on the map because unit 2.0 is simply a collection of meter-thick sills of unit 2.1.

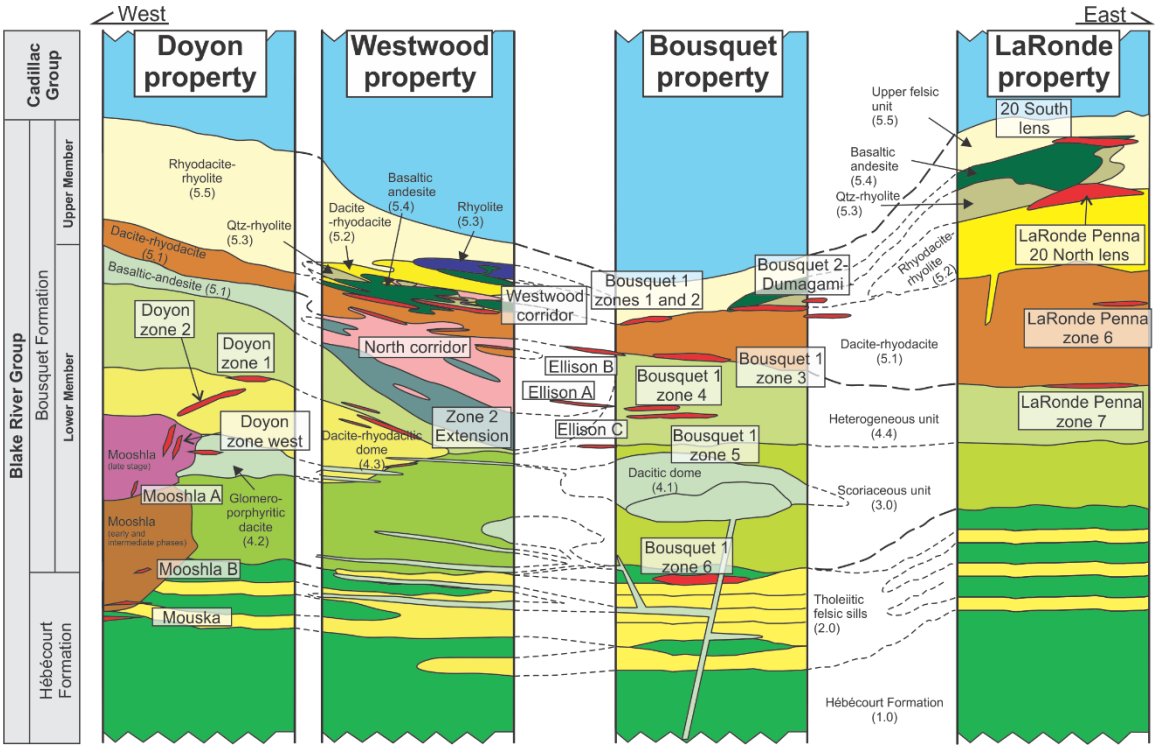

Figure 2: Stratigraphic columns of the DBL mining camp. Stratigraphy of the DBL mining camp depicting the stratigraphic setting of the principal ore lenses in the Doyon, Westwood, Bousquet 1, and LaRonde regions. The ore lenses are not to scale. The Bousquet Formation is divided into a lower member of tholeiitic to transitional composition and an upper member of transitional to calc-alkaline composition. Unit 2.1 is not shown here but is depicted by unit 2.0 which is a collection of meter-thick sills of unit 2.1 (from Yergeau et al., 2015; modified from Lafrance et al., 2003a).

Stratigraphically higher is unit 3.1 (intermediate tuff breccia to lapilli tuff) and unit 3.2 which is comprised of fragmental feldspar-phyric basalt and/or andesite with a fine-grained matrix of chl + ep + cb + ser (Mercier-Langevin et al., 2007b, c, 2008). At the Westwood-Warrenmac Corridor, unit 3.2 overlies the tholeiitic felsic rocks of unit 2.0 and can be composed of mafic to intermediate banded lapilli tuffs with some amygdular fragments (Figure 2; Mercier-Langevin et al., 2009). Rocks of unit 3.2 are characterized by negative Nb-Ta and Zr-Hf anomalies and slightly enriched HFSE and LREE patterns (Mercier-Langevin et al., 2009). Overlying unit 3.2 is unit 3.3, which is comprised of scoriaceous tuffs with highly altered and brecciated tholeiitic andesitic to dacitic tuffs dominated by scoriaceous fragments (Figures 1 and 2; Mercier-Langevin et al., 2007b, c, 2009). Amygdules are filled with epidote and carbonate and, sometimes, by quartz and feldspar. This unit is either of a pyroclastic or an autoclastic origin (Mercier-Langevin et al., 2007c). This unit is less differentiated than the underlying units; there is enrichment in LREE and depletion in HREE compared to the Hébécourt Formation, so these andesitic rocks were not generated by simple fractional crystallization of the tholeiitic magma reservoir inferred for the Hébécourt Formation (Mercier-Langevin et al., 2007c). Mercier-Langevin et al. (2007c) proposed several partial melting scenarios combined with fractional crystallization of amphibole ± plagioclase at midcrustal levels that could have produced the tholeiitic to transitional, mafic to intermediate rocks of units 3.3 and 4.4.

Overlying the intermediate scoriaceous tuffs and tuff breccias of unit 3.3 is unit 4.2 (2698.3 ± 0.9 Ma; Lafrance et al., 2005), which is a dacite glomeroporphyritic volcaniclastic unit (Figures 1 and 2; Lafrance et al., 2005; Wright-Holfeld et al., 2010;

Galley and Lafrance, 2014; Yergeau et al., 2015). Above unit 4.2 is unit 4.3, which is a dacitic to rhyolitic schist characterized by aphanitic rhyodacitic sills and dykes that can be up to 200m thick and is of transitional to calc-alkaline magmatic affinity (Figures 1 and 2; Mercier-Langevin et al., 2009; Wright-Holfeld et al., 2010; Galley and Lafrance, 2014; Yergeau et al., 2015). It is a highly deformed sericite-altered schist which does not allow for the identification of primary volcanic features (Savoie et al., 1990; Lafrance et al., 2003a). There are intensely bleached intervals in unit 4.3 associated with quartz-carbonate veins and an abundance of pyrite (Wright-Holfeld et al., 2010).

Finally, unit 4.4 is a heterogeneous unit comprised of microporphyritic (5–40 vol % feldspar phenocrysts) basalt and andesite with a fine-grained granoblastic matrix of act + fsp + ep + chl + qtz + cb + bt + ser + leu + py (Figures 1 and 2; Mercier-Langevin et al., 2007b, c, 2008, 2009; Wright-Holfeld, 2010; Galley and Lafrance, 2014; Yergeau et al., 2015). It is more homogeneous in the LaRonde Penna mine area where it is in sheared-contact with unit 5.1 (Mercier-Langevin et al., 2007c). This homogeneous portion of unit 4.4 is mainly highly altered tholeiitic to transitional, glomeroporphyritic to massive textured, pillowed, and brecciated flows of basalt and andesite (Mercier-Langevin et al., 2007c).

2.1.4 Upper Member of the Bousquet Formation

The upper member (2698.3 ± 0.8 Ma - 2697.5 ± 1.1 Ma; McNicoll et al., 2014) is younger than the lower member and is comprised of units 5.1 to 5.5 (Figures 1 and 2; Mercier-Langevin et al., 2007c). The lithology of the upper member is primarily

transitional to calc-alkaline, intermediate (i.e., basaltic andesite, andesite) to felsic (i.e., dacite, rhyodacite, rhyolite) flows, lobes, and flow breccias (Figures 1 and 2; Lafrance et al., 2003a; Dubé et al., 2007b; Mercier-Langevin et al., 2007a, b, c, d, 2009; Wright-Holfeld et al., 2010; Yergeau et al., 2015). The felsic units of the upper member are laterally restricted and are made up of coalesced flows, unlike the lower member units which are laterally extensive (Figure 2; Stone, 1990; Lafrance et al., 2003a; Mercier-Langevin et al., 2007b). The lowest stratigraphic unit (unit 5.1) is comprised of dacite-rhyodacite, andesitic to Ti-rich dacitic sills (Figures 1 and 2; Mercier-Langevin et al., 2007b, c, 2009; Wright-Holfeld et al., 2010; Yergeau et al., 2015). These sills are 5 to 25 m thick and have feldspar-microporphyritic and amygdaloidal textures with minor volcaniclastics (Mercier-Langevin et al., 2007c). Additionally, there are massive, pillowed, amygdaloidal, and feldspar-phyritic flows that are up to 50 m thick (Mercier-Langevin et al., 2007c). These successions also contain hyaloclastites (crystal tuffs) mixed with polymictic volcaniclastic beds that have small scale (mm to cm) quartz and carbonate-filled amygdules and less than 10 vol % feldspar microphenocrysts in a recrystallized matrix (Mercier-Langevin et al., 2007c). There are 2- to 10-m-thick sills with feldspar-microporphyritic and amygdaloidal textures emplaced within a dacite-rhyodacite subunit (i.e., Unit 5.1b-d; Mercier-Langevin et al., 2007c). Subunits labelled with an “a” are found proximal to the MIC (e.g., Doyon Mine and Westwood Deposit), while subunits labelled with a “b” are found distal to the MIC (e.g., LaRonde Penna Mine). Finally, Unit 5.1 contains a 25- to 150-m thick sequence of massive, microporphyritic (feldspar and quartz) domes with lobes and flow breccia (Mercier-Langevin et al., 2007c).

The second oldest unit is unit 5.2 (2698.3 ± 0.8 Ma; Lafrance et al., 2005; Mercier-Langevin et al., 2007b), which is a rhyodacite-rhyolite volcaniclastic unit comprised of feldspar-dominated microporphyritic volcanic rocks (Figures 1 and 2; Mercier-Langevin et al., 2007b, c, 2009; Yergeau et al., 2015). This unit was not significantly fractionated by magmatic processes and has a chemically homogenous protolith, as indicated by a constant Zr/TiO_2 ratio of 290 (Mercier-Langevin et al., 2007c). There are subunits of unit 5.2; those labelled with an "a" are found proximal to the MIC (e.g., Doyon Mine and Westwood Deposit), while subunits labelled with a "b" are found distal to the MIC (e.g., LaRonde Penna Mine). Following unit 5.2 in the volcanic sequence is unit 5.3 (2697.8 ± 1 Ma; Mercier-Langevin et al., 2007b), which is a calc-alkaline, feldspar- and quartz-phyric rhyolite comprised of massive and brecciated autoclastic flows, domes, and tuffaceous rhyolite (Figures 1 and 2; Mercier-Langevin et al., 2007b, c, 2009; Wright-Holfeld et al., 2010; Yergeau et al., 2015). It overlies and intrudes unit 5.2 and contains fine-grained volcaniclastic beds (crystal tuffs) in a quartz and feldspar matrix with sericite alteration (Mercier-Langevin et al., 2007c). The phyric texture contains 5-15 vol %, 1-2 mm rounded and partially resorbed blue quartz microphenocrysts and 7-15 vol %, 1-2 mm zoned plagioclase microphenocrysts (Mercier-Langevin et al., 2007c).

Overlying unit 5.3 is unit 5.4, which is a basaltic andesite unit comprised of a sills and dikes complex with feldspar-dominant microporphyritic and fine-grained amygdaloidal facies (Figure 2; Mercier-Langevin et al., 2007b, c, 2009; Wright-Holfeld, 2010). There are a few narrow glomeroporphyritic sills that are only very locally developed (Mercier-Langevin et al., 2007c). The porphyritic textures can be seen in the hanging wall of the

Bousquet 2-Dumagami deposit which contains andesite with up to 15 vol % plagioclase phenocrysts (Dubé et al., 2014). Finally, unit 5.5 (2697.5 ± 1.1 Ma; McNicoll et al., 2014) is the upper felsic unit and is comprised of quartz and feldspar microporphyritic rhyodacite to rhyolite (5-20 vol % albite microphenocrysts; recrystallized matrix), and fine-grained volcaniclastics with massive domes, lobes, and autoclastic flow breccia (Figure 2; Lafrance et al., 2003a; Mercier-Langevin et al., 2007b, c, 2009; Wright-Holfeld et al., 2010; Yergeau et al., 2015). In the LaRonde Penna mine area, these lobes and breccias overly unit 5.3 and are intruded by unit 5.4 (Figure 2; Lafrance et al., 2003a).

2.1.5 Mooshla Intrusive Complex

The polyphase Mooshla synvolcanic intrusion occurs along the contact between the Hébécourt and Bousquet Formations in the western portion of the DBL camp and has an oval geometry of roughly 4 x 2 km (Figure 1; Valliant and Hutchinson, 1982; Gaudreau, 1986; Langshur, 1990; Galley and Lafrance, 2014). The MIC is grouped into two distinct stages of formation: (i) Mouska stage (2698.5 ± 0.5; McNicoll et al., 2014) consisting of five intrusive phases (phases A - E) ranging from gabbro to tonalite; and (ii) Doyon stage (2696.9 ± 1 Ma; Lafrance et al., 2005) comprising four intrusive phases (phases F-I) ranging from tonalite to trondhjemite typical of Archean TTG (Galley and Lafrance, 2014).

Galley and Lafrance (2014) distinguished each intrusive phase by chemical composition, variable intrusion style, and by distinctive overprinting relationships. The Mouska stage intrusive phases were emplaced along the contact of the Hébécourt Formation and the lower member of Bousquet Formation (Langshur, 1990; Galley and

Lafrance, 2007; Galley and Lafrance, 2014). The geochemical characteristics of the intrusives are consistent with those of the Bousquet Formation volcanics, implying a synvolcanic timing and coeval relationship for the intrusive complex. This agrees with the U-Pb zircon geochronology of Lafrance et al. (2005) and McNicoll et al. (2014), and with the findings of Langshur (1990) and Belkabir (1995). There is also a similarity in their Ta versus Yb and Nb versus Yb values (see Fig. 11B, C of Galley and Lafrance, 2014) and between their primitive mantle-normalized trace element profiles (see Fig. 9A, C of Galley and Lafrance, 2014). The tholeiitic to transitional affinity of the Mouska stage (i.e., gabbros, quartz diorites, and tonalites) is consistent with the affinity of the lower Bousquet Formation (i.e., basalt to rhyodacite suite; Lafrance et al., 2003). The U-Pb dating, described in McNicoll et al. (2014), found an age of 2698.5 ± 0.4 Ma for the phase C, which shows that the Mouska stage is synchronous with some of the units of the lower Bousquet Formation. The transitional to calc-alkaline Doyon stage (i.e., porphyries and trondhjemites) is geochemically compatible with the upper Bousquet Formation (i.e., dacites and rhyodacites; Lafrance et al., 2003). The U-Pb dating, described in Lafrance et al. (2005) and in McNicoll et al. (2014), produced an age of 2696.9 ± 1 Ma for the phase H which distinctly establishes that the Doyon stage is synchronous with the felsic volcanic units of the upper Bousquet Formation (2698−2697 Ma; Lafrance et al., 2005; Mercier-Langevin et al., 2007a, 2011a; McNicoll et al., 2014).

There are overlapping trace element compositional fields between the MIC and the mafic, intermediate, and felsic extrusive units, suggesting similar tectonic settings (Galley and Lafrance, 2014). Additionally, there are aplite/rhyolite dikes similar in trace element

composition to unit 5.3 that crosscut the phase D tonalite in the eastern part of the MIC (see Figs. 9, 11 of Galley and Lafrance, 2014). The Mouska stage and the lower Bousquet Formation are crosscut by the Doyon stage phases which is contemporaneous and possibly comagmatic with the upper member (Langshur, 1990; Lafrance et al., 2003; Galley and Lafrance, 2007, 2014; Mercier-Langevin et al., 2007a). All of the above data from the literature indicate that the MIC is both temporally and spatially related to the period of upper Blake River Group arc-style volcanism, which developed during early stages of oceanic arc rifting (Mercier-Langevin et al., 2007b, 2011; Galley and Lafrance, 2014).

The MIC hosts the Mooshla A and B Au deposits and portions of the Doyon and Mouska Au-Cu deposits (Galley and Lafrance, 2007, 2014; Mercier-Langevin et al., 2007a; Dubé et al., 2014). The pluton is associated with hydrothermal events that formed these ore bodies and the Mic Mac deposit ore body which is hosted in the Hébécourt Formation (Mercier-Langevin et al., 2007a). Both Mouska and Mic Mac deposits are shear-hosted Au deposits (Lafrance et al., 2003a; Mercier-Langevin et al., 2007a, 2009, 2011b; Galley and Lafrance, 2014; Yergeau, 2015). The Mic Mac deposit has a synvolcanic and pre-intrusive VMS-style mineralization, while the Mouska deposit has a late "early-intrusive"-stage VMS and sulphide-rich vein-type mineralization (Belkabir et al., 2004; Galley and Lafrance, 2007; Mercier-Langevin et al., 2007a). The Doyon and Mooshla A deposits have a syn 'late-intrusive'-stage quartz and sulphide vein-type mineralization, while the Mooshla B deposit has a post-intrusion or syndeformation quartz ± tourmaline-carbonate-sulphide vein-type mineralization (Belkabir et al., 2004; Galley and Lafrance, 2007; Mercier-Langevin et al., 2007a).

2.1.6 Gold-enriched VMS deposits of the DBL camp

The upper member of the Bousquet Formation hosts most of the Au-rich VMS lenses of the DBL camp at the LaRonde Penna, Bousquet 2-Dumagami, Bousquet 1 and Westwood deposits (Dubé et al., 2007; Mercier-Langevin et al., 2007a, 2009; Wright-Holfeld et al., 2010, 2011; Galley and Lafrance, 2014). In general, the LaRonde Penna deposit is predominantly associated with thick footwall volcaniclastic rocks of the Upper Member of the Bousquet Formation (Mercier-Langevin et al., 2007b; Mercier-Langevin et al., 2011a). It is made up of four stacked massive sulphide lenses and has two main ore zones (20 North and 20 South; Dubé et al., 2007a, b; Mercier-Langevin et al., 2007a, b; Dubé et al., 2014). The 20 North and 20 South ore zones are sheetlike, massive to semi-massive polymetallic sulphide lenses and stringer zones (Dubé et al., 2007b). A majority of the 20 North lens hanging wall is comprised of feldspar- and quartz-phyric rhyolite of unit 5.3 (Dubé et al., 2007a; Mercier-Langevin et al., 2007c). Its footwall is made up of rhyodacite-rhyolite feldspar-phyric flow breccia, and rhyolitic domes/cryptodomes of unit 5.2, with an alteration assemblage of quartz-biotite-garnet-muscovite (Dubé et al., 2007a; Mercier-Langevin et al., 2007c). There is an abundance of unit 5.2 rhyodacitic clasts in the 20 North ore zone which indicates that the sulphide lens formed, at least in part, through replacement of this unit (Dubé et al., 2007b; Mercier-Langevin et al., 2007a).

The 20 South ore body at the LaRonde Penna Mine is an 8- to 10-m-thick Au- and Zn-rich sulphide lens and stringer zone that was emplaced toward the top of unit 5.4 (Dubé et al., 2007a, b, 2014). It is primarily hosted in rhyodacitic volcanic flow-breccia of unit 5.5 and basaltic andesite sills of unit 5.4 (Dubé et al., 2007a, b, 2014; Mercier-Langevin et al.,

2007c). The hanging wall is comprised of unit 5.5 in the east and unit 5.4 in the centre of the deposit, while units 5.5 and 5.3 are in its footwall (Dubé et al., 2007a, b, 2014; Mercier-Langevin et al., 2007c). The hanging wall and footwall have plagioclase-quartz-rutile and/or anatase-titanite-biotite ± chlorite alteration (Dubé et al., 2007b). Dubé et al. (2007b) proposed that the hanging-wall basaltic andesite of unit 5.4 could have been a thermal barrier that isolated the ore-forming fluid from cold seawater and helped to focus hydrothermal fluid flow.

The Bousquet 2-Dumagami deposit contains stacked, deformed, and transposed semi-massive to massive pyrite-rich lenses, breccia zones, and associated sulphide veins and stringer zones (Dubé et al., 2014). It has three ore zones: The Massive Hangingwall zone, the Massive Footwall zone, and Zone 5 (Tourigny et al., 1993; Dubé et al., 2014). Many ore zones occur at or near blue quartz-phyric rhyolitic flows and sills of unit 5.3 (hanging wall) and dacitic to rhyodacitic volcaniclastic rocks of unit 5.1 (footwall; Dubé et al., 2014). The Massive Hangingwall zone is the main ore zone at the Bousquet 2 mine (Dubé et al., 2014). It is an Au-Ag-Cu-Zn sheet-like, semi-massive to massive, pyrite-rich sulphide lens intermixed with vein and breccia zones, with a pyrite-sphalerite ± chalcopyrite ± bornite ± galena ore assemblage (Dubé et al., 2014). The ore zone contains unit 5.5 which is in contact with the overlying greywacke of the Cadillac Group (Marquis et al., 1990a; Savoie et al., 1991; Trudel et al., 1992; Teasdale et al., 1996; Dubé et al., 2004, 2007b, 2014). This contact is delineated by a centimeter to several decimeters thick, semi-massive, deformed, and brecciated pyrrhotite-rich horizon with local weakly anomalous Zn values (Marquis et al., 1990a; Savoie et al., 1991; Trudel et al., 1992;

Teasdale et al., 1996; Dubé et al., 2004, 2007b, 2014). The Massive Footwall zone is another semi-massive to disseminated pyrite-rich auriferous zone at the Bousquet 2 mine (Dubé et al., 2014). It is composed of breccias and stringer zones including, or mixed with, massive pyrite veins and lenses (Dubé et al., 2014). Finally, Zone 5 is the main ore zone at the Dumagami mine and is equivalent to the Massive Hangingwall zone at Bousquet 2 (Dubé et al., 2014). It consists of massive pyrite and massive sphalerite-galena bodies, with the presence of chalcopyrite and/or bornite being a reliable indication of economic Au grades (Marquis et al., 1990a; Dubé et al., 2014).

The Westwood deposit contains two Au-rich VMS lenses: The North corridor and the Westwood-Warrenmac corridor (Mercier-Langevin et al., 2009; Wright-Holfeld et al., 2010, Yergeau et al., 2015). The intermediate to felsic upper member of the Bousquet Formation volcanics hosts the ore-zones of these corridors (Mercier-Langevin et al., 2009; Wright-Holfeld et al., 2010; Yergeau et al., 2015). The North corridor ore-zone is hosted in tholeiitic to transitional andesite of unit 5.1, whereas ore zones in the Westwood-Warrenmac Corridor are hosted in transitional to calc-alkaline dacite-rhyodacite of unit 5.1 (Mercier-Langevin et al., 2009; Wright-Holfeld et al., 2010; Yergeau et al., 2015). The Westwood-Warrenmac Corridor is significantly sheared and its associated hydrothermal system overprinted the North corridor (Mercier-Langevin et al., 2009; Wright-Holfeld et al., 2010). Both corridors have widespread quartz-chlorite-sericite alteration and proximal Mn-garnet alteration (Mercier-Langevin et al., 2009; Wright-Holfeld et al., 2010).

The Westwood-Warrenmac Corridor is one of two major Au-rich sulphide vein, stockwork- and VMS lens dissemination-style deposits in the DBL camp; the Bousquet 1

deposit also shows this type of mineralization (Valliant and Hutchinson, 1982; Tourigny et al., 1993; Lafrance et al., 2003a; Mercier-Langevin et al., 2007a; Yergeau, 2015; Yergeau et al., 2015; Boily-Auclair et al., 2020). The five ore zones (1 to 5, from south to north) of the Bousquet 1 deposit are stratiform volcanic-sedimentary exhalative pyritic bodies and subconformable sulphidic veins (Valliant and Hutchinson, 1982; Tourigny et al., 1988; Mercier-Langevin et al., 2007a). Eighty percent of the ore is in Zone 3 which is found at the contact between the lower and upper members of the Bousquet Formation (Mercier-Langevin et al., 2007a).

2.2 Sampling and analytical methods

2.2.1 Sample collection and preparation

Representative samples of each volcanic unit were collected from outcrop and drill core in the Westwood and LaRonde Penna mine site areas. Outcrop samples were taken distal to VMS lenses (Figure 3) to obtain the freshest examples of the various units as possible. Distal alteration assemblages include fine-grained biotite and quartz with local zones of intense muscovite alteration, whereas proximal alteration assemblages contain quartz, Mn-garnet, biotite, and muscovite (Mercier-Langevin et al., 2017). Sampling was conducted on various surface outcrops, on 3 drill holes from the LaRonde Penna Mine and 7 drill holes from the Westwood Mine (Table 2). These drill holes were selected for detailed sampling as they represent an almost complete stratigraphic column through the entire Bousquet Formation providing the opportunity to examine the melt inclusion record in all volcanic units. The sampling strategy for drill core was to obtain representative lithologies

but also to target the units that contained ideal host phases for SMI (e.g., units containing quartz phenocrysts; Audétat and Pettke, 2003). A total of 67 samples were collected from 12 different volcanic units spanning the upper and lower Bousquet formations. All samples were cut and processed into polished thin sections (30 μm) at Vancouver Petrographics Limited, and following petrographic observations by optical microscope, a sub-set of samples were made into double-polished thick sections (150 μm) for detailed SMI analysis.

Table 2: Description of sample lithologies

Unit	# of samples collected	[1]Location of samples	Lithology	Lithofacies	Inferred volcanic setting	Description of SMI, flincs, and host minerals
2.0	1 surface sample 7 drill core samples	Surface sample: 682,731 m E. 5,349,061 m N. Drill hole - LaRonde - 3215-166: 2,866.93m (elevation) 5,501.48 (UTM-E) 3,324.37 (UTM-N) Drill hole - LaRonde - 3086-29: 4,150.33m (elevation) 8,335.41 (UTM-E) 3,327.20 (UTM-N)	Quartz- and feldspar-phyric rhyolite (QFP rhyolite)	Porphyritic (quartz and feldspar), tholeiitic, rhyolite sills that intrude the Hébécourt Formation; ≤35 vol% blue quartz micro-phenocrysts and angular feldspar phenocrysts in a sericitized matrix; high Si and Zr contents and an elevated Zr/TiO_2 ratio (Lafrance et al., 2003; Mercier-Langevin et al., 2007b, c, 2009; Yergeau et al., 2015).	Intrusive (shallow sill and dike complex)	Poor to very good quality, well preserved, abundant, and large (19 - 61 µm) SMI hosted in phenocrystic quartz; CO_2-rich fluid inclusion trails that are sometimes coeval with SMI.
3.2	1 surface sample 1 drill core sample	Surface sample: 690,121 m E. 5,347,621 m N. Drill hole - LaRonde - 3215-161: 2,867.03m (elevation) 5,517.48 (UTM-E) 3,305.70 (UTM-N)	Basalt and andesite	Fragmental feldspar-phyric basalt and andesite with a fine-grained matrix of chl + ep + cb + ser; mafic to intermediate banded lapilli tuffs with some amygdular fragments; negative Nb-Ta and Zr-Hf anomalies and slightly enriched HFSE and LREE patterns (Mercier-Langevin et al., 2007b, c, 2008, 2009).	Extrusive (volcaniclastic beds)	Small (5 - 8 µm) and moderate quality but sparse SMI hosted in amphibole; not enough to acquire large data set.
3.3	6 drill core samples	Drill hole - LaRonde - 3215-161: 2,867.03m (elevation) 5,517.48 (UTM-E) 3,305.70 (UTM-N) Drill hole - Westwood - R17628: *3,402.709m (elevation) *14,686.086 *6,409.472	Andesite and dacite	Tholeiitic to transitional, mafic to intermediate scoriaceous tuffs; contains highly altered and brecciated tholeiitic andesitic to dacitic tuffs dominated by scoriaceous fragments; amygdules are filled with ep + cb + qtz + fs.; enrichment in LREE and depletion in HREE compared to the Hébécourt Formation (Mercier-Langevin et al., 2007b, c, 2009).	Effusive (flow breccias; either of a pyroclastic or an autoclastic origin)	Small (4 - 6 µm) and poor to moderate quality SMI with opaque phases hosted in deformed matrix quartz; single phase fluid inclusions and an abundance of rutile crystals in matrix quartz.
4.2	2 surface samples	Surface sample: 684,177 m E. 5,343,566 m N. Surface sample: 683,991 m E. 5,347,830 m N.	Dacite	Dacite glomeroporphyritic volcaniclastic unit (Lafrance et al., 2005; Wright-Holfeld et al., 2010; Galley and Lafrance, 2014; Yergeau et al., 2015).	Extrusive (volcaniclastic beds)	No SMI found.
4.3	6 drill core samples	Drill hole - Westwood - R17721: *3,933.19m (elevation) *14,069.29 *6,455.53 Drill hole - Westwood - R17678: *3,933.05m (elevation) *14,069.55 *6,455.60	Dacitic to rhyolitic rock	Transitional to calc-alkaline, dacitic to rhyolitic rock; aphanitic rhyodacitic sills and dykes that can be up to 200m thick; highly deformed and sericite-altered; intensely bleached intervals associated with quartz-carbonate veins and an abundance of pyrite (Savoie et al., 1990; Lafrance et al., 2003; Mercier-Langevin et al., 2009; Wright-Holfeld et al., 2010; Galley and Lafrance, 2014; Yergeau et al., 2015).	Intrusive (shallow sill and dike complex)	Small (4 - 8 µm), poor to good quality SMI hosted in phenocrystic blue (Ti-rich) quartz; quartz is very fractured; abundant fluid inclusion (~1 - 4 um) trails along and crosscutting quartz grain boundaries.
4.4	1 surface sample 6 drill core samples	Surface sample: 690,143 m E. 5,347,462 m N. Drill hole - LaRonde - 3215-161: 2,867.03m (elevation) 5,517.48 (UTM-E) 3,305.70 (UTM-N) Drill hole - LaRonde - 3215-166: 2,866.93m (elevation) 5,501.48 (UTM-E) 3,324.37 (UTM-N) Drill hole - Westwood - R17721: *3,933.19m (elevation) *14,069.29 *6,455.53 Drill hole - Westwood - R17688: *3,936.069m (elevation) *13,972.727 *6,470.195 Drill hole - Westwood - R17707: *3,403.669m (elevation) *14,621.815 *6,300.298	Basaltic to andesitic rock	Heterogeneous unit comprised of microporphyritic (5 – 40 vol % feldspar phenocrysts) basalt and andesite with a fine-grained granoblastic matrix of act + fsp + ep + chl + qtz + cb + bt + ser + leucoxene + py (Mercier-Langevin et al., 2007b, c, 2008, 2009; Wright-Holfeld, 2010; Beaudoin et al., 2014; Galley and Lafrance, 2014; Yergeau et al., 2015).	Effusive (pillows and flow breccia)	Small (ave = 4 µm) moderate quality SMI hosted in matrix quartz; some samples did not have SMI; fluid inclusions trails in matrix quartz; good quality SMI hosted in hornblende; poor quality SMI hosted in feldspar; very altered sample - not good for SMI analysis.

1. UTM83 - Zone 17
*Westwood system - Not UTM

Table 2 (continued): Description of sample lithologies

Unit	# of samples collected	[1]Location of samples	Lithology	Lithofacies	Inferred volcanic setting	Description of SMI, flincs, and host minerals
5.1	1 surface sample 4 drill core samples	Surface sample: 690,145 m E. 5,347,396 m N. Drill hole - LaRonde - 3215-161: 2,867.03m (elevation) 5,517.48 (UTM-E) 3,305.70 (UTM-N) Drill hole - Westwood - R14665: *4,797.30m (elevation) *14,446.82 *6,473.69	Dacite to rhyodacite	Dacite-rhyodacite, andesitic to Ti-rich dacitic sills (5 to 25 m thick); massive, pillowed, amygdaloidal, and feldspar (≤10%)-phyritic flows (≤50 m thick) with minor volcaniclastics (hyaloclastites; Dubé et al., 2007b, 2014; Mercier-Langevin et al., 2007b, c, 2009; Wright-Holfeld et al., 2010; Beaudoin et al., 2014; Yergeau et al., 2015).	Intrusive (dikes + sills) and extrusive (domes and volcaniclastic beds)	Medium (5 - 10 μm) poor to good quality SMI hosted in matrix quartz; abundant single and two phase fluid inclusions (1 - 3 μm) clustered in quartz; some necked CO_2 fluid inclusions in quartz; abundance of rutile needles in quartz.
5.2	1 surface sample 2 drill core samples	Surface sample: 690,707 m E. 5,347,272 m N. Drill hole - LaRonde - 3215-161: 2,867.03m (elevation) 5,517.48 (UTM-E) 3,305.70 (UTM-N) Drill hole - Westwood - R14665: *4,797.30m (elevation) *14,446.82 *6,473.69	Rhyodacite to rhyolite	Rhyodacite-rhyolite volcaniclastic; feldspar-dominated microporphyry (Dubé et al., 2007b; Mercier-Langevin et al., 2007b, c, 2009; Beaudoin et al., 2014; Yergeau et al., 2015).	Extrusive (volcaniclastic beds)	Abundant quartz grains in the groundmass but rarely any SMI (ave = 5 μm) ; lots of mineral inclusions in quartz.
5.3	2 surface samples 8 drill core samples	Surface sample: 684,732 m E. 5,347,148 m N. Surface sample: 690,711 m E. 5,347,200 m N. Drill hole - LaRonde - 3215-161: 2,867.03m (elevation) 5,517.48 (UTM-E) 3,305.70 (UTM-N) Drill hole - Westwood - R14665: *4,797.30m (elevation) *14,446.82 *6,473.69	Quartz- and feldspar-phyric rhyolite (QFP rhyolite)	Massive and brecciated feldspar and quartz-phyric flows, domes, and flow breccia (block and lapilli) with fine-grained volcaniclastics (crystal tuffs); 5-15 vol %, 1-2 mm rounded and partially resorbed blue quartz microphenocrysts and 7 to 15 vol %, 1-2 mm zoned plagioclase microphenocrysts, in a sericitized quartz and feldspar matrix (Mercier-Langevin et al., 2007b).	Intrusive (dikes + sills) and extrusive (domes and volcaniclastic beds)	Very good quality, large (30 - 39 μm) SMI hosted in phenocrystic quartz with abundant rutile needles; poor quality SMI hosted in feldspar and matrix quartz; many mineral inclusions in matrix and phenocrystic quartz; small fluid inclusions in large altered feldspar phenocrysts.
5.4	1 drill core sample	Drill hole - Westwood - R14665: *4,797.30m (elevation) *14,446.82 *6,473.69	Basaltic andesite	Massive sills and dikes complex with microporphyritic to glomeroporphyritic facies (base: ≥10 vol %, 1-10 mm zoned plagioclase phenocrysts in a crystalline matrix of feldspar laths and biotite-hornblende) and fine-grained amygdaloidal facies (top: ≤20 vol %, 1-10 mm coalesced quartz amygdules in a very fine grained matrix; Mercier-Langevin et al., 2007b).	Intrusive (shallow sill and dike complex)	Sample is very altered and only SMI (5 - 8 μm) found were recrystallized in amphibole.
5.5	3 drill core samples	Drill hole - LaRonde - 3215-161: 2,867.03m (elevation) 5,517.48 (UTM-E) 3,305.70 (UTM-N)	Quartz- and feldspar-phyric rhyodacite to dacite	Massive domes and flow breccia (block and lapilli) with fine-grained volcaniclastics (crystal tuffs); 5-20 vol % albite microphenocrysts in a recrystallized quartz and feldspar matrix (Mercier-Langevin et al., 2007b).	Effusive (domes and flow breccia)	Moderate quality, medium size (ave = 10 μm) SMI hosted in matrix quartz and altered phenocrystic feldspar; matrix quartz is metamorphosed and has many mineral inclusions.

1. UTM83 - Zone 17
*Westwood system - Not UTM

2.2.2 SMI petrography

Petrography characterization and mapping/selection of SMI for further analysis were conducted initially on polished thin sections, followed by double-polished thick sections. Petrographic analysis of SMI constituted the basis for all other analytical techniques carried out and described below, and involved characterizing and classifying the SMI present using the melt inclusion assemblage (MIA) method (cf. Goldstein, 2003; Bodnar and Student, 2006). The appearance and distribution of the SMI, and the relative timing of their entrapment in each volcanic unit was established, where possible. Maps of SMI distribution were created to aid in selecting individual SMI for analytical work and providing constraints on the overall origin of the inclusions, when combined with other imaging (e.g., BSE, CL) methods. Subsets of SMI were selected based on the following criteria: (i). The abundance and size of SMI in host phenocrysts; (ii) the degree of preservation of SMI (e.g., away from fractures in, and near the edges of, phenocrysts; absence of decrepitation halos); (iii) samples in which host matrix was the least altered and deformed relative to other samples of the same unit; (iv) differentiating accidentally-trapped mineral inclusions and SMI visibly contaminated by those minerals from uncontaminated SMI; and (v) differentiating partially enclosed (‘hourglass”) inclusions from completely enclosed SMI. Mainly, the prevailing limitations were the abundance of SMI and the presence of quartz phenocrysts. Other volcanic samples had plagioclase phenocrysts with SMI, for example, but the grains were highly altered and contain cleavage planes that promote the incursion of metamorphic fluids.

2.2.3 SMI microthermometry

Preliminary SMI microthermometry was carried out at Saint Mary's University's Department of Geology on a Linkam Scientific Instruments TS1500 heating stage with sapphire heating plates, mounted on an Olympus BX41 with a Q-Imaging color video camera to provide real-time video and capture capability for heating experiments. The melting points of pure Ag (961.8°C), Au (1064°C), and Cu (1085°C) (Alfa Aesar Inc.) were determined during repeated heating experiments at a heating rate of 6°C/min, and compared to known values to create a calibration curve to correct future measurement temperatures. Heating rates during measurements were cycled between 10°C/min and 30°C/min, with Ar gas (40 mL/min) pumped through the stage sample chamber to prevent oxidation of SMI during heating. The uncertainty associated with temperature measurements is ± 2°C based on monitoring stage stability during cycled melting/freezing of a pure Ag standard at a heating rate of 6^{o}C/min.

2.2.4 Confocal laser Raman microspectroscopy

Confocal laser Raman microspectroscopy (LRM) was performed at the Department of Geology, Saint Mary's University, Halifax, Nova Scotia, to determine the volatile composition of glass and fluid bubbles in homogenized SMI (from both "high P-T piston cylinder" and "MHC cold-seal pressure vessel" methods), and to assess the crystallinity of homogenized SMI. Analyses were performed using a Horiba Jobin-Yvon LabRam HR instrument (Saint Mary's University) equipped with a 100 mW (at source), 532 nm Nd-YAG diode laser (Laser Quantum) and a Synapse CCD detector (Horiba Jobin-Yvon). Pure silicon was used as a frequency calibration standard and analyses were performed using a

20 to 40 µm confocal hole diameter, depending on inclusion/bubble size and inclusion depth, selected to maximize resolution at depth. A 600 grooves/mm grating (spectral resolution of approximately ± 2 cm^{-1}) was used during spectrum collection. Spectra were collected by accumulating three, 50-60 s acquisitions at 100% laser power (~2.15 mW at sample surface through a 100x long working length objective). The method was used to detect the presence of volatile phases (e.g., H_2O, CO_2, N_2, CH_4, H_2S) and glass that cannot be identified by optical petrography or microthermometry.

2.2.5 Scanning electron microscope-energy dispersive spectroscopy (SEM-EDS), back-scattered electron (BSE), and cathodoluminescence (CL) analysis

Mineral identification and major/minor element analyses were performed on quartz phenocrysts, exposed SMI (homogenized and unhomogenized), and general volcanic rock unit mineral assemblages using a TESCAN MIRA 3 LMU Variable Pressure Schottky Field Emission SEM (Saint Mary's University, Halifax, Nova Scotia, Canada). The SEM is equipped with a back-scattered electron (BSE) detector, energy dispersive spectroscopy (EDS), and cathodoluminescence (CL) functionality. The BSE detector can provide qualitative elemental/phase information about the sample being analysed. For EDS, a solid-state, 80 mm^2 X-max Oxford Instruments EDS detector was used. The EDS system utilized silicon drift detector (SDD) technology to analyse characteristic X-rays emissions and provided semi quantitative elemental information for exposed SMI that were homogenized by high P-T experiments (see below). A beam voltage of 20 kV and an approximate working distance of 17-20 mm was used for all analyses. Images were acquired using a

Gatan miniCL imaging system that measures cathodoluminescence photons in the UV, visible, near infrared and ultraviolet regime (wavelength range: 185 - 850 nm).

2.2.6 Laser ablation-inductively coupled plasma-mass spectrometry (LA-ICP-MS)

Trace element concentrations in unhomogenized SMI and accessory apatite (occurring as inclusions in quartz), and the Ti content of phenocryst quartz were determined by LA-ICP-MS at the Magmatic and Ore-Forming Processes Research Laboratory at the University of Toronto. This method is favored as it samples the entire volume of the SMI (or included apatite grain) but does not require homogenization of the SMI prior to analysis to acquire quantitative compositional information (Halter et al., 2002a, b; Halter and Pettke, 2004). The set up consisted of a New Wave Research (NWR) 193UC ArF Excimer laser ablation system attached to an Agilent 7900 quadrupole mass spectrometer. Silicate melt inclusions were ablated through stepwise increase of the ablation pit diameter (10-100 μm) such that the final pit size was slightly larger than the maximum inclusion dimension. After collecting ~50s of background signal with the laser turned off, the inclusions required 10 to 30 s of ablation time to collect the melt inclusion + host quartz signal. The instrument was tuned to maximum sensitivity while maintaining robust plasma conditions (U≈Th on NIST SRM610) and low oxide and doubly charge ion production rates (ThO/Th < 0.3%; Mass 21/42 < 0.3%). Helium was used as a carrier gas at a flow rate of 1.0 L/min.

Dwell times for all isotopes in all sample types (apatite, quartz, SMI) were 10 ms, except for ^{197}Au and ^{107}Ag for SMI analyses for which dwell times were set at 50 ms. Interference corrections for $^{91}Zr^{16}O$ on ^{107}Ag, and $^{181}Ta^{16}O$ on ^{197}Au were performed manually, based

on determination of oxide production rates using in-house zircon and rutile standards, respectively, and subtracting corresponding contributions (count rate basis) from Zr and Ta occurring in the SMI. Host corrections for the SMI routinely reduced 30.7 ± 22.4% of the total ^{107}Ag signals and 4.0 ± 3.8% of the total ^{197}Au signals. Table 3 lists detailed instrument operation conditions and data reduction parameters for SMI analyses. Data were acquired in time-resolved signal mode, displayed as a signal intensity versus time plot with progressive analysis. Analyses of up to ~30 unknowns (i.e., SMI, apatite, quartz) were bracketed by 2 standard analyses at the beginning and the end of each analysis block to enable drift correction during data reduction. SMI and apatite grain measurements produced a mixed transient signal with the host quartz. Increased counts of elements such as P (for apatite) and Al (for SMI), and decreased counts of Si were used to distinguish the start and end of SMI ablation from background host quartz during signal selection. While quartz-host only measurements were obtained, host quartz signal intervals in SMI and apatite inclusion measurements were also quantified as additional quartz analyses for Ti thermometry. The Ti concentrations were implemented into the equations of the Ti-in-quartz thermometer from Thomas et al. (2010).

Table 3: LA-ICP-MS instrument and data acquisition parameters for SMI

NWR 193UC ArF excimer laser ablation system	
Output Energy	150 mJ
Energy Density on sample	~7 -10 J/cm^2
Repition Rate	5 - 10 Hz
Pit Size	Between 16 and 90 µm
Ablation Cell Volume	100 x 100 mm
Cell Gas Flow (He)	~1 L/min
Agilent 7900 quadrupole MS	
Auxiliary gas flow	1.03 l/min Ar
RF power	1500 V
Detector Mode	Dual 8 orders of magnitude linear dynamic range
Quadrupole Settline Time	2 ms
ThO/Th	0.15-0.3 %
Mass 21/42	0.15-0.3 %
U/Th	~1.09-1.14
Data acquisition parameters	
Sweeps per reading	1
Reading per replicate	200 - 300
Replicates	1
Dwell time per isotope	10 ms, except for Ag (107) 50 ms and Au (197) 200 ms dwell times on shortened analyte menu for SMI
Points per peak	1 per measurement
External Standard	NIST610
Interference corrections	$^{91}Zr^{16}O$ on ^{107}Ag (using zircon) and $^{181}Ta^{16}O$ on ^{197}Au (using rutile)
Isotopes Analyzed	Li (7), Na (23), Mg (25), Al (27), Si (29), P (31), K (39), Ca (44), Sc (45), Ti (47), V (51), Cr (53), Mn (55), Fe (56), Co (59), Ni (62), Cu (65), Zn (66), Ga (71), Ge (72), As (75), Rb (85), Sr (88), Y (89), Zr (90), Nb (93), Mo (95), Ag (107), In (115), Sn (118), Sb (121), Te (125), Cs (133), Ba (137), La (139), Ce (140), Pr (141), Nd (146), Sm (147), Eu (153), Gd (157), Tb (159), Dy (163), Ho (165), Er (166), Tm (169), Yb (172), Lu (175), Hf (178), Ta (181), W (182), Au (197), Pb (208), Bi (209), Th (232), U (238)

The compositions of SMI, apatite inclusions, and host quartz in the phenocrysts were quantified using the software SILLS (Guillong et al., 2008). This involved deconvoluting the mixed SMI or apatite + host quartz signal from the host only signal after calculation of background corrected count rates for each isotope, and quantification of inclusion and host compositions. The standard reference material (SRM) NIST610 silicate glass was used for the calibration of analyte sensitivities for SMI, apatite, and quartz analyses. Internal standard values of 70 wt% SiO_2, 55 wt% CaO (ideal), and 99.99 wt% SiO_2 were applied for SMI, apatite, and quartz quantification, respectively. Other constraints used for the SMI quantification were 95 wt% total oxides and 5 wt% H_2O (laser Raman analyses of homogenized SMI indicated low quantities of H_2O; therefore, 5 wt% H_2O is likely an overestimate). It should be noted that whereas a fixed value of 70 wt% for SiO_2 was used for SMI quantification, analysis of homogenized SMI (via internally-heated pressure vessel; see below) by SEM-EDS showed that SMI compositions were slightly higher in unit 2.0 (~74 - 79 wt% SiO_2) on an anhydrous basis. Recalculation of the LA-ICP-MS data shows that this introduces a maximum of a ~9% (relative) underestimate of trace element concentrations in the SMI reported (e.g., at 70% SiO_2, a value of 30 ppm Rb; at 79% SiO_2 a value of 34 ppm Rb).

2.2.7 Hot cathodoluminescence (HCL) imaging of quartz

Hot cathodoluminescence (HCL) emission imaging was performed on polished thin sections of select volcanic units (i.e., 2.0, 4.3, and 5.3) to provide textural information for discrete quartz generations and quartz growth zones. Hot cathodoluminescence analysis was performed using a Lumic HC4-LM hot-cathode cathodoluminescence microscope at Saint Mary's University, Halifax, Nova Scotia, Canada. The cathodoluminescence microscope is coupled to a Olympus BXFM focusing mount with images captured by a Kappa DX40C peltier cooled camera operated using the DX40C-285FW software package. An acceleration voltage between 9.5 - 11.5 kV, a beam current of 0.25 mA, a filament current of 2.3 A, a deflection of 10 V and a focus of 5.5 V were used during analysis.

2.2.8 High pressure-temperature piston cylinder analysis of quartz

Three high PT piston cylinder experiments were performed on quartz grain aliquots from sample 711-7200-U5.3 (unit 5.3) at the Dalhousie University High Pressure Laboratory. Each experiment had a 5 mm diameter, 0.127 mm wall thickness, Pt capsule containing aluminum oxide powder, and 6 quartz grains that were roughly 0.25 mm in diameter. The capsules were welded using the 'ash-can' design and a Lampert PUK 3 welder in micro mode with output power at 20% (Sneeringer and Watson, 1985; Zhang et al., 2015). The capsules were placed in ¾ inch assemblies containing an Al_2O_3 tube with thermocouple and disk, a crushable MgO tube, a graphite furnace, a prefractured Pyrex sleeve, and an NaCl sleeve (Zhang et al., 2015). The Pyrex sleeves were prefractured at 600˚C to achieve a stable initial pressurization (Tropper and Manning, 2007). The assemblies containing capsules were stored at 110˚C for >12 hours in a vacuum oven and

then placed in a piston-cylinder apparatus for various time, temperature, and pressure conditions.

Experiment #1 ran for 72 hours and was set at a temperature and pressure of 900˚C and 3 kbar, respectively. Experiment #2 ran for 120 hours and was set at a temperature and pressure of 950˚C and 5 kbar, respectively. Experiment #3 ran for 72 hours and was set at a temperature and pressure of 950˚C and 3 kbar, respectively. A Eurotherm controller with a W95Re5-W74Re26 thermocouple was used to monitor the temperatures. A spinel thermometer was used to establish a thermal gradient of ± 20˚C within the capsule (Watson et al., 2002). All runs used N_2 flow to prevent thermocouple oxidation (Walter and Presnall, 1994). Temperatures of 900 - 950°C were chosen to exceed the SMI trapping temperature of ~800°C (established by Ti-in-quartz thermometry – see Section 2.3.6). Overheating the sample provided the extra thermodynamic drive to homogenize the SMI. The same overheating principle was applied to the molybdenum-hafnium-carbide (MHC) cold-seal pressure vessel analytical technique (see Section 2.2.9).

2.2.9 Molybdenum hafnium carbide (MHC) cold-seal pressure vessel

All experiments were performed at 950 ± 10˚C and 1500 ± 50 bar on surface samples 711-7200-U5.3 (unit 5.3) and 731-9061-U2.0 (unit 2.0) in an externally-heated rapid quench MHC cold-seal pressure vessel assembly at the Magmatic and Ore-Forming Processes Research Laboratory at the University of Toronto. Argon was used as a pressure medium and the pressure was monitored throughout the experiment using a factory calibrated digital pressure transducer. Each experiment had a 5 mm ⌀, 0.127 mm wall

thickness, Pt capsule containing aluminum oxide powder, and 6 - 8 quartz grains that were roughly 0.25 mm in diameter. The capsules were welded using the 'ash-can' design (Sneeringer and Watson, 1985) and a Lampert PUK 3 welder in micro mode with output power at 20% (Zhang et al. 2015).

2.2.10 Host bulk rock analysis

Drill core samples were sent to the Ontario Geological Survey (GeoLabs) in Sudbury, Ontario for whole rock analyses. Major element and loss of ignition (LOI) 44 determined by X-ray fluorescence spectrometry (XRF). The sample powders underwent LOI determinations, and were then fused with a borate flux to produce a glass disk. Trace elements were analyzed by inductively-coupled plasma mass spectrometry (ICP-MS) after closed vessel, four acid (HF-HCl-HNO3-HClO4) digestion. Relative analytical uncertainties are within ± 5 % for all major elements and ± 3 % for most trace elements.

2.3 Results

2.3.1 Petrography of host volcanic rocks

Twelve units/subunits of the Bousquet Formation were collected from diamond drill core at the Westwood Mine and the LaRonde Penna Mine, and from outcrop near these mines, the Mooshla B deposit, and the Doyon Mine (Figures 3 - 5; Table 2). In this study, rock type classifications and descriptions are based on field and laboratory observations, and from past studies (i.e., Mercier-Langevin et al., 2007b, c, 2008, 2009; Wright-Holfeld et al., 2010; Galley and LaFrance, 2014; Yergeau et al., 2015). Outcrop-scale (surface and

underground) and hand-sample scale (from polished slabs of diamond drill core) features of the volcanic units of the Bousquet Formation are shown in Figures 4 and 5. Of importance to note in the context of an SMI study is that these images show volcanic rocks exhibiting variable degrees of strain and hydrothermal alteration (Figures 4 and 5). While deformation and alteration do not preclude a rock unit from SMI studies, it was noted during sampling as it may impact the preservation of both SMI and their host mineral phases (c.f., Student and Bodnar, 2004). Additionally, the presence and abundance of coarse-grained phenocryst phases (quartz, feldspars, pyroxene) as potential host phases for SMI are highly variable within units, and with some units showing far higher abundance whereas others are devoid of these (Figures 4 and 5).

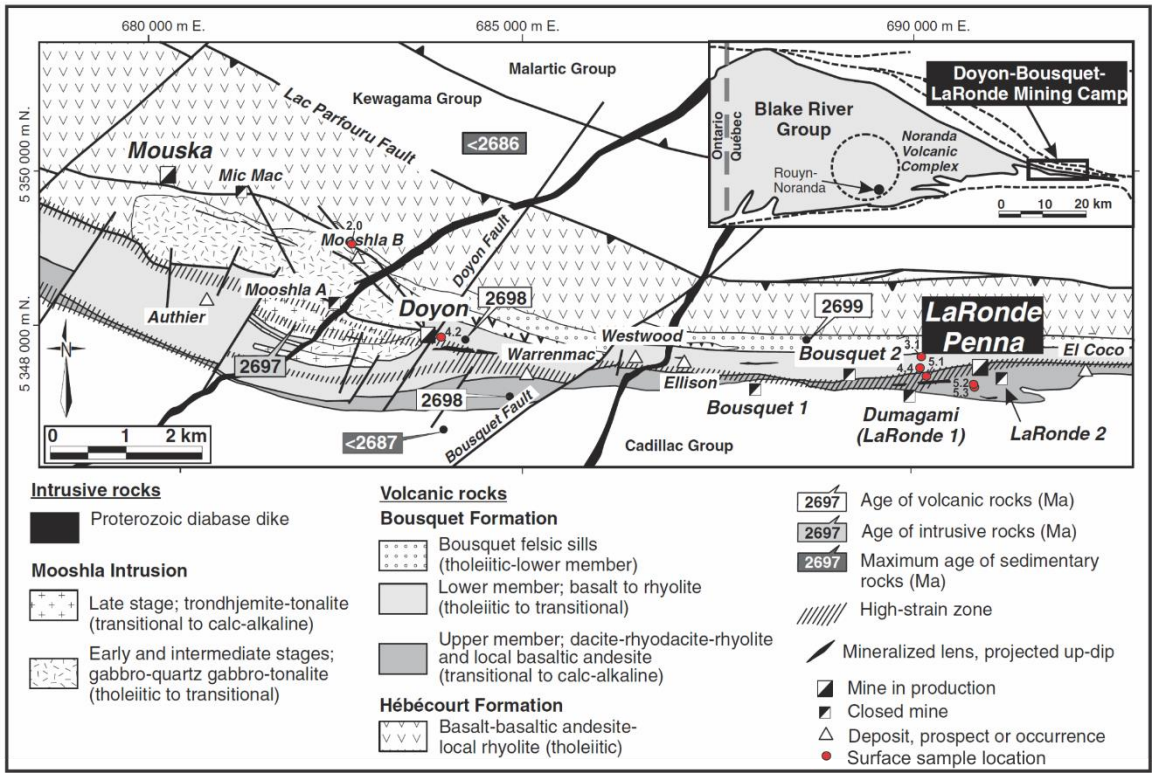

Figure 3: Sample location map of the DBL mining camp showing the LaRonde Penna mine and other mines, and major bedrock lithologies and structures. Inset shows the location of the more detailed map. Red dots show the locations of samples collected from outcrops and are labelled with their corresponding unit. The location of drill holes from which samples were obtained are not shown but are summarized in Table 2 (modified from Mercier-Langevin et al., 2007b).

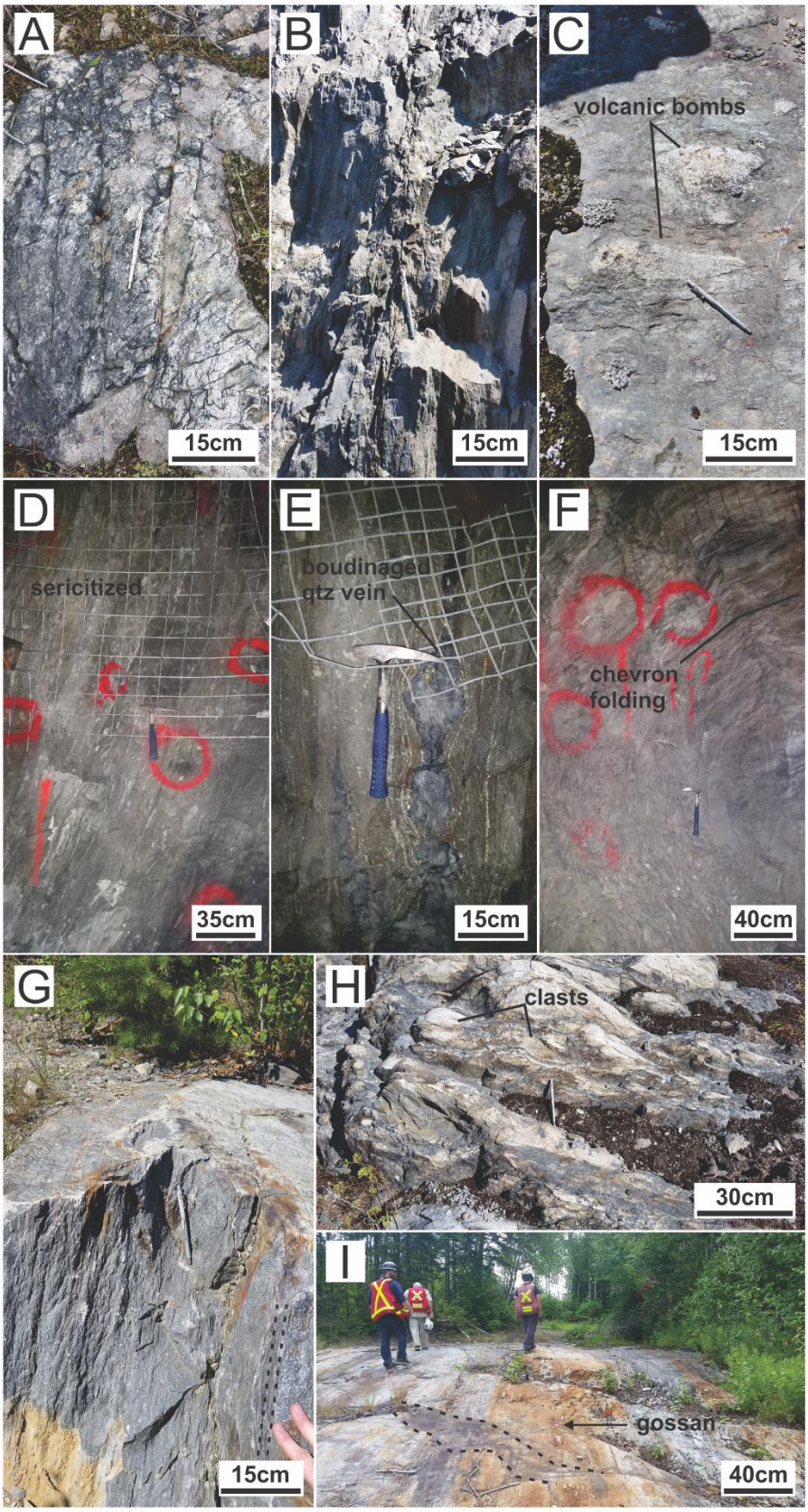
A
15cm
B
15cm
C
volcanic bombs
15cm
D
sericitized
35cm
E
boudinaged
qtz vein
15cm
F
chevron
folding
40cm
G
15cm
H
clasts
30cm
I
gossan
40cm

Figure 4 (previous page): Photographs of the Bousquet Formation volcanics in outcrop and underground at the Westwood Mine. (A) Unit 2.0 tholeiitic QFP rhyolite sill; (**B)** Unit 3.2 basalt with quartz amygdules; (**C)** Unit 4.2 scoriaceous tuff; lapilli blocky tuff with qtz + ep amygdules as part of alteration rims of volcanic bombs; (**D)** Variably sericitized, deformed Unit 4.3 dacite to rhyolite; (**E)** Unit 4.3 boudinaged quartz vein in mineralized (sulfidic) dacite to rhyolite; (**F)** Unit 4.4 heterogenous volcanic (basalt to andesite) with late chevron folding (post-mineralization); (**G)** Unit 5.1 foliated (dashed lines follow foliation plane), fine-grained rhyodacitic sill. (**H)** Flow breccia with unit 5.2 rhyodacitic-rhyolitic feldspar-rich microporphyry clasts; and (**I)** Unit 5.4 basaltic andesite dyke (dashed outline) crosscutting layered, mineralized (note gossan) unit 5.2 rhyodacite-rhyolite volcaniclastic.

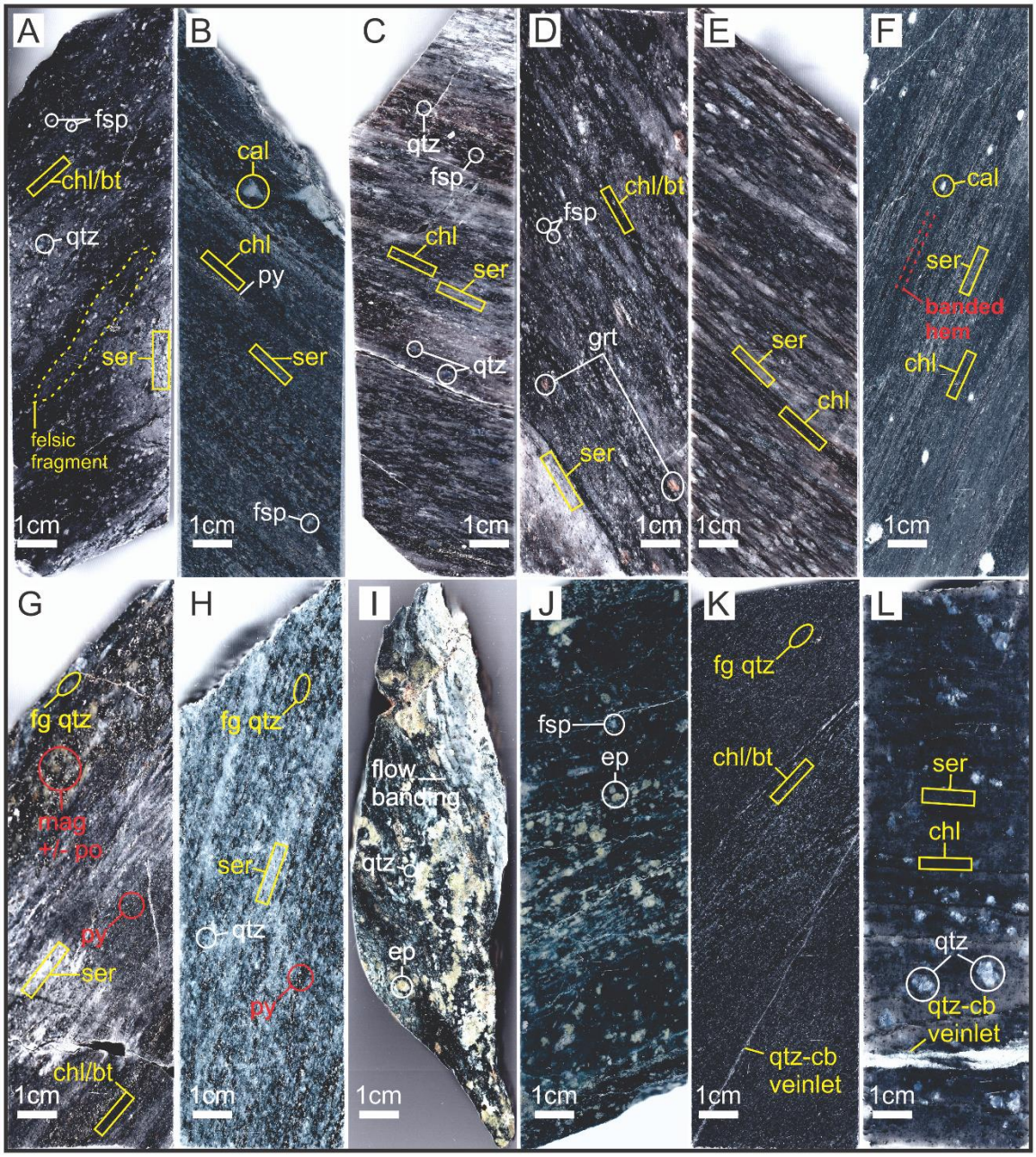
A
fsp
chl/bt
qtz
ser
felsic fragment
1cm
B
cal
chl
py
ser
fsp
1cm
C
qtz
fsp
chl
ser
qtz
1cm
D
fsp
chl/bt
grt
ser
1cm
E
ser
chl
1cm
F
cal
ser
banded hem
chl
1cm
G
fg qtz
mag +/- po
py
ser
chl/bt
1cm
H
fg qtz
ser
qtz
py
1cm
I
flow banding
qtz
ep
1cm
J
fsp
ep
1cm
K
fg qtz
chl/bt
qtz-cb veinlet
1cm
L
ser
chl
qtz
qtz-cb veinlet
1cm

Figure 5 (previous page): Representative images of polished slabs/drill core samples of the Bousquet Formation volcanic units, arranged from youngest (A) to oldest (L). **(A)** Unit 5.5 rhyodacitic-dacitic quartz feldspar porphyry (QFP); **(B)** Unit 5.4 basalt-andesitic basalt; (**C)** Unit 5.3 rhyolitic QFP; **(D)** Unit 5.2b rhyodacite-rhyolite; **(E)** Unit 5.2a Doyon rhyodacite-rhyolite; **(F)** Unit 5.1ac dacite-rhyodacite; **(G)** Unit 4.4 basalt to andesite; **(H)** Unit 4.3 Doyon dacite-rhyolite; **(I)** Unit 4.2 glomeroporphyritic dacite; **(J)** Unit 3.3 andesitic-dacitic scoriaceous tuff; **(K)** Unit 3.2 basalt; **(L)** Unit 2.0 QFP rhyolite. Note: White text = phenocrysts and amygdules, yellow text = alteration minerals, red text = mineralization, bt = biotite, cal = calcite, cb = carbonate, chl = chlorite, ep = epidote, fsp = feldspar, grt = garnet, mag = magnetite, po = pyrrhotite, py = pyrite, qtz = quartz, ser = sericite.

Commonly, the volcanic rocks in the mine domain are very sulfide rich. However, the core intervals and surface samples chosen for this study are not from significantly mineralized areas as those may be too hydrothermally altered to preserve melts in phenocrysts. The main features of the sampled lithologies are summarized below, based on petrographic observations:

- Unit 5.5 - Pale to medium grey, rhyodacitic-dacitic quartz feldspar porphyry (QFP) that is silicified (Figures 5A and 6A). The samples contain quartz and plagioclase phenocrysts (up to 1 mm) concentrated in pale grey, deformed felsic lithic fragments (Figures 5A and 6A). Muscovite and intergrown medium to pale grey sericitic and chloritic/biotite alteration patches occur through the groundmass (Figures 5A and 6A). The felsic fragments often show more sericite alteration than the matrix (Figure 5A). The samples of this unit are unmineralized to locally weakly pyrite/pyrrhotite-mineralized; generally, sulphides occur in fine-grained, mm to cm sized clusters and fine- to medium-grained, disseminated blebs.
- Unit 5.4 - Basalt to andesitic basalt containing feldspar and clinopyroxene phenocrysts, showing absent to very weak schistosity, and very weak chloritization and sericitization (Figures 5B and 6B). There are isolated patches of calcite in the matrix and bands (mm - cm) of pyrite (Figures 5B and 6B).
- Unit 5.3 - Very pale grey to pale greenish-grey, non-mineralized QFP rhyolites with locally pale blue quartz phenocrysts (Figures 5C and 6C). They have pervasive, streaky, greenish-grey sericitic alteration in the matrix and are silicified (Figures

5C and 6C). Calcite veinlets, biotite and muscovite also occur in the groundmass (Figures 5C and 6C).

- Unit 5.2b (i.e., subunit of 5.2 from the LaRonde Penna Mine which is distinct from subunit 5.2a occurring at the Doyon Mine and Westwood deposit) - Rhyodacite to rhyolite (Figures 5D and 6D). They are silicified with dark grey chloritic + biotite/white mica banding (mm – cm) occurring in a paler grey sericite altered matrix (Figures 5D and 6D). This unit has recrystallized quartz phenocrysts, quartz-carbonate veinlets (mm – cm), metamorphic garnet, and is non- to weakly pyrite mineralized (Figures 5D and 6D).
- Unit 5.2a - Unmineralized to weakly pyrite-mineralized, rhyodacitic to rhyolitic rocks with weak schistosity and alkali feldspar phenocrysts. The matrix shows dark chloritic, siliceous and white mica banding, and pale grey sericitic alteration (Figures 5E and 6E).
- Unit 5.1ac (i.e., subunit of 5.1 that is found at the Doyon Mine is distinct from subunit 5.1b found at the LaRonde Penna Mine) - Dacite to rhyodacite (Figures 5F and 6F). They are unmineralized unit hematitic banding, a weak schistosity, and alternating bands of sericitic and chloritized matrix. They have dispersed crystals of calcite (Figures 5F and 6F).

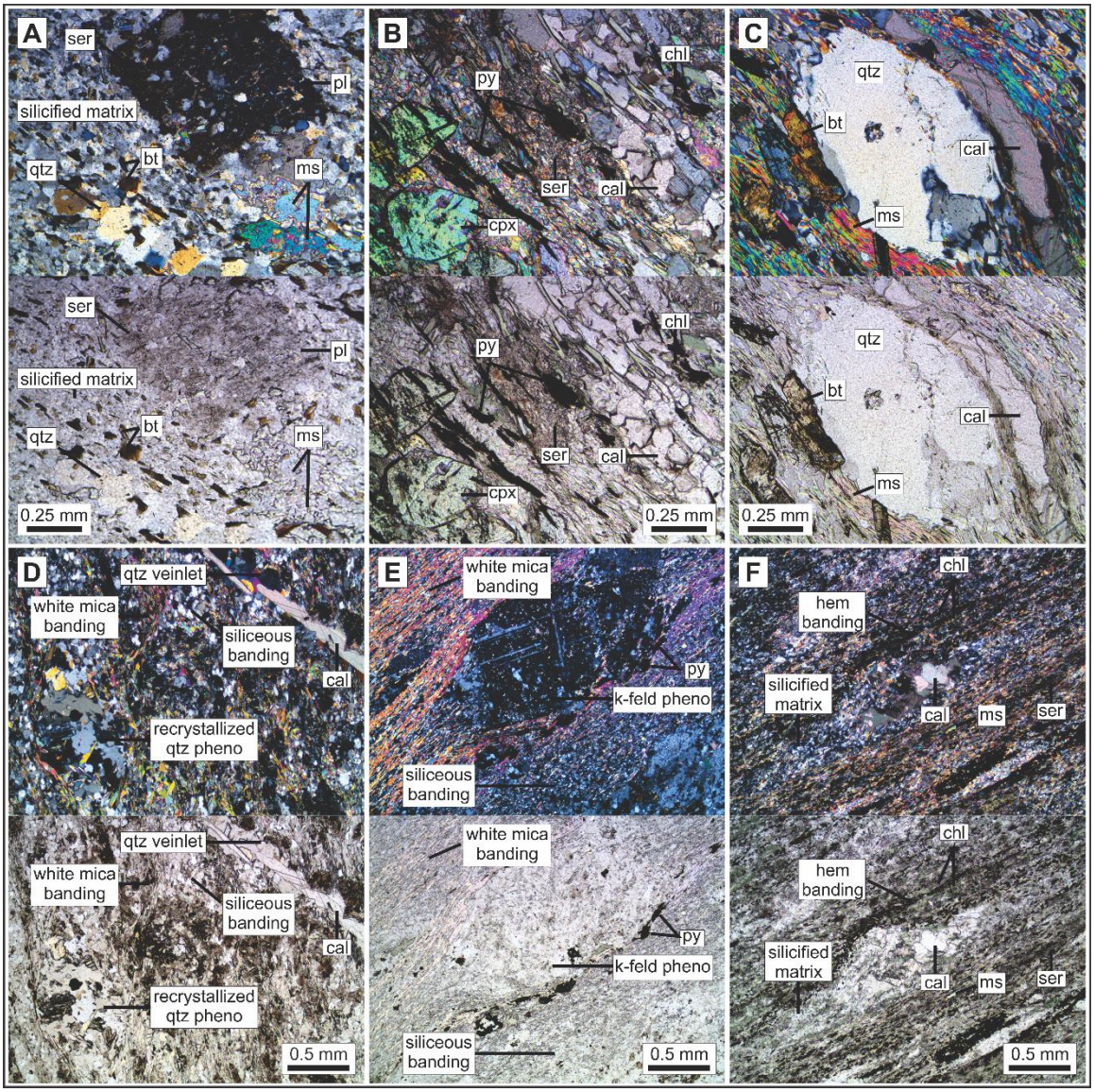
A
ser
pl
silicified matrix
qtz
bt
ms
ser
pl
silicified matrix
qtz
bt
ms
0.25 mm
B
chl
py
ser
cal
cpx
chl
py
ser
cal
cpx
0.25 mm
C
qtz
bt
cal
ms
qtz
bt
cal
ms
0.25 mm
D
qtz veinlet
white mica banding
siliceous banding
cal
recrystallized qtz pheno
qtz veinlet
white mica banding
siliceous banding
cal
recrystallized qtz pheno
0.5 mm
E
white mica banding
py
k-feld pheno
siliceous banding
white mica banding
py
k-feld pheno
siliceous banding
0.5 mm
F
chl
hem banding
silicified matrix
cal
ms
ser
chl
hem banding
silicified matrix
cal
ms
ser
0.5 mm

Figure 6 (previous page): Petrography of the upper member Bousquet Formation volcanics. All samples shown in XPL and PPL. **(A)** Unit 5.5 rhyodacitic-dacitic QFP containing sericite, plagioclase, quartz, biotite, muscovite, and a silicified matrix. **(B)** Unit 5.4 phenocrystic basalt-andesitic basalt with clinopyroxene crystals in an inequigranular matrix of opaques (pyrite?), chlorite, sericite, and calcite. **(C)** Unit 5.3 non-mineralized QFP rhyolite with quartz phenocrysts in a fine-grained matrix of muscovite and biotite, with calcite veinlets. **(D)** Unit 5.2b rhyodacite-rhyolite with recrystallized quartz phenocrysts in a microcrystalline matrix of banded mica and quartz; contains quartz-carbonate veinlets. **(E)** Unit 5.2a unmineralized to weakly pyrite mineralized rhyodacite-rhyolite with potassium feldspar phenocrysts in a mica and siliceous banded matrix. **(F)** Unit 5.1ac unmineralized dacite-rhyodacite with hematitic banding, a weak schistosity, alternating bands of sericite, chlorite, and muscovite, and dispersed crystals of alteration calcite. Note: bt = biotite, cal = calcite, chl = chlorite, cpx = clinopyroxene, hem = hematite, k-feld = potassium feldspar; ms = muscovite, pl = plagioclase, ppl = plane polarized light, py = pyrite, qtz = quartz, ser = sericite, xpl = cross polarized light

- Unit 4.4 - Pyrite-mineralized andesites, with chlorite and biotite altered groundmass, and diffuse pale grey sericitic banding (mm – cm; Figures 5G and 7A). This unit is silicified (Figures 5G and 7A). Locally the samples are magnetic due to very fine-grained magnetite or pyrrhotite (Figure 5G). Weak to moderate pyrite mineralization occurs as fine to medium-grained disseminations, clusters, and bands (mm – cm; Figures 5G and 7A). The samples also contain muscovite, clinopyroxene, and garnet (Figure 7A).
- Unit 4.3 - Dacite to rhyolite with a schistose to massive texture (Figures 5H and 7B). They contain disseminated pyrite, bands of pale grey sericitic alteration, and are pervasively silicified. The groundmass contains plagioclase, muscovite, chlorite, and blue-grey quartz phenocrysts (Figures 5H and 7B).
- Unit 4.2 - Glomeroporphyritic dacites showing primary flow banding, quartz-epidote amygdules, chloritic alteration, and a silicified groundmass (Figures 5I and 7C).
- Unit 3.3 - Andesitic to dacitic scoriaceous tuffs with sericite-altered feldspar phenocrysts in an altered, amphibole-rich groundmass containing epidote amygdules and chlorite (Figures 5J and 7D).
- Unit 3.2 - Fine-grained basalts with banded (mm – cm) to massive textures (Figures 5K and 7E). The samples are chlorite- and biotite-altered with weak to moderate silicification (Figures 5K and 7E). The unit is non-mineralized and contains white quartz-carbonate veinlets (5-10%; mm – cm; Figures 5K and 7E).
- Unit 2.0 - Rhyolitic with a weak schistosity, intense silicification, and contain muscovite and biotite in the groundmass (Figures 5L and 7F). The unit contain

abundant blue-grey quartz and feldspar phenocrysts (i.e., QFP; Figures 5L and 7F). The unit also shows very weak chloritization and sericitization in the groundmass and late quartz-carbonate veinlets (Figures 5L and 7F).

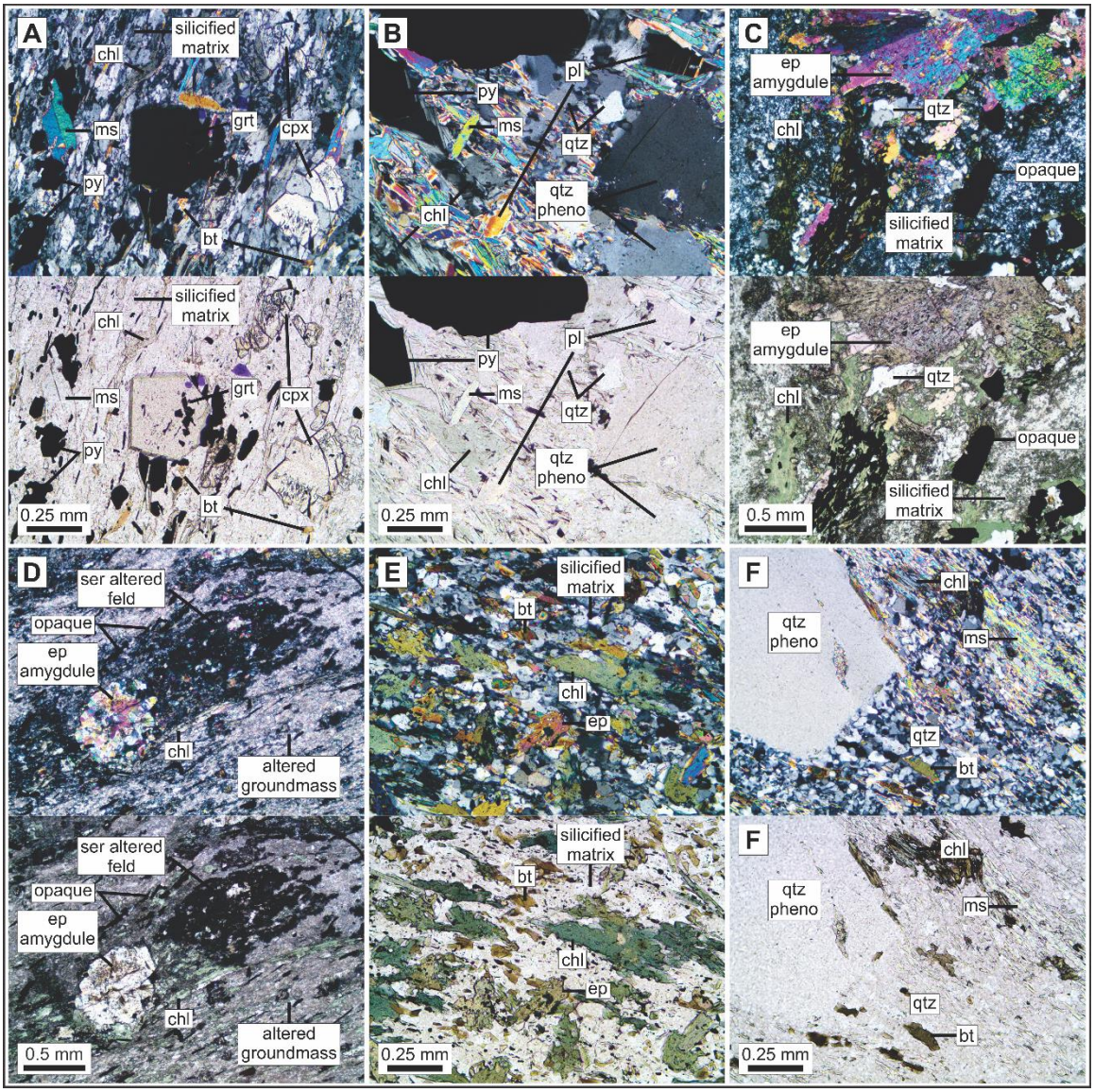
A
silicified matrix
chl
ms
grt
cpx
py
bt
B
pl
py
ms
qtz
qtz pheno
chl
C
ep amygdule
qtz
chl
opaque
silicified matrix
silicified matrix
chl
ms
grt
cpx
py
bt
0.25 mm
pl
py
ms
qtz
qtz pheno
chl
0.25 mm
ep amygdule
qtz
chl
opaque
silicified matrix
0.5 mm
D
ser altered feld
opaque
ep amygdule
chl
altered groundmass
ser altered feld
opaque
ep amygdule
chl
altered groundmass
0.5 mm
E
silicified matrix
bt
chl
ep
silicified matrix
bt
chl
ep
0.25 mm
F
chl
qtz pheno
ms
qtz
bt
F
chl
qtz pheno
ms
qtz
bt
0.25 mm

Figure 7 (previous page): Petrography of the lower member Bousquet Formation volcanics. All samples shown in XPL and PPL. **(A)** Unit 4.4 silicified andesite with an inequigranular matrix of chlorite, muscovite, biotite, clinopyroxene, garnet, and pyrite. **(B)** Unit 4.3 pyrite mineralized dacite-rhyolite with phenocrysts of quartz in a fine-grained matrix of muscovite, chlorite, plagioclase, and quartz. **(C)** Unit 4.2 glomeroporphyritic dacite with primary flow banding in a silicified microcrystalline matrix, with epidote-quartz amygdules, and chlorite alteration. **(D)** Unit 3.3 andesitic-dacitic scoriaceous tuff with sericite-altered feldspar phenocrysts in an altered, amphibole-rich groundmass with epidote amygdules and chlorite. **(E)** Unit 3.2 fine-grained basalt with banded (mm – cm) to massive textures containing chlorite- and biotite-alteration with weak to moderate silicification. **(F)** Unit 2.0 rhyolite with a weak schistosity, chloritization and sericitization, a strong silicification, and contains muscovite + biotite in the groundmass; contains abundant quartz and feldspar (not shown) phenocrysts, and late quartz-carbonate veinlets. Note: bt = biotite, cal = calcite, chl = chlorite, cpx = clinopyroxene, ep = epidote, grt = garnet, hem = hematite, ms = muscovite, pheno = phenocryst, pl = plagioclase, ppl = plane polarized light, py = pyrite, qtz = quartz, ser = sericite, xpl = cross polarized light

2.3.2 Petrography of silicate melt inclusions and other included phases

Silicate melt inclusions are rare and difficult to identify in all units of the Bousquet Formation. Units 2.0, 4.3, 4.4, and 5.3 were suitable for SMI analysis, whereas all other units were not suitable because they were completely altered, had no suitable host minerals, and/or no SMI were observed. Phenocrysts (rather than matrix minerals) host the largest and most easily optically-discernable inclusions used for SMI investigations (Figure 8A - L). Notably, unit 2.0 has large (0.25 – 0.75 cm) abundant (10 - 15%) blueish-grey (Ti-rich) quartz phenocrysts in rhyolitic sills (Figure 5L), unit 4.3 has abundant (15 - 20%) blueish quartz phenocrysts in dacitic to rhyolitic schists (Figure 5H), unit 4.4 has abundant (10 – 25%) hornblende crystals in basaltic to andesitic schists (Figure 5G), and unit 5.3 has abundant (5 – 10%) quartz phenocrysts in rhyolite (Figure 5C). Units 2.0 (QFP rhyolitic sills; Yergeau et al., 2015), 4.3 (rhyodacitic sills and dykes; Yergeau et al., 2015), and 5.3 (QFP rhyolitic flow; Mercier-Langevin et al., 2007b) were the only volcanics found to contain viable SMI (see Section 2.2.2 – SMI petrography for SMI selection criteria). A complete list of samples containing viable SMI for microanalytical study is presented in Table 4.

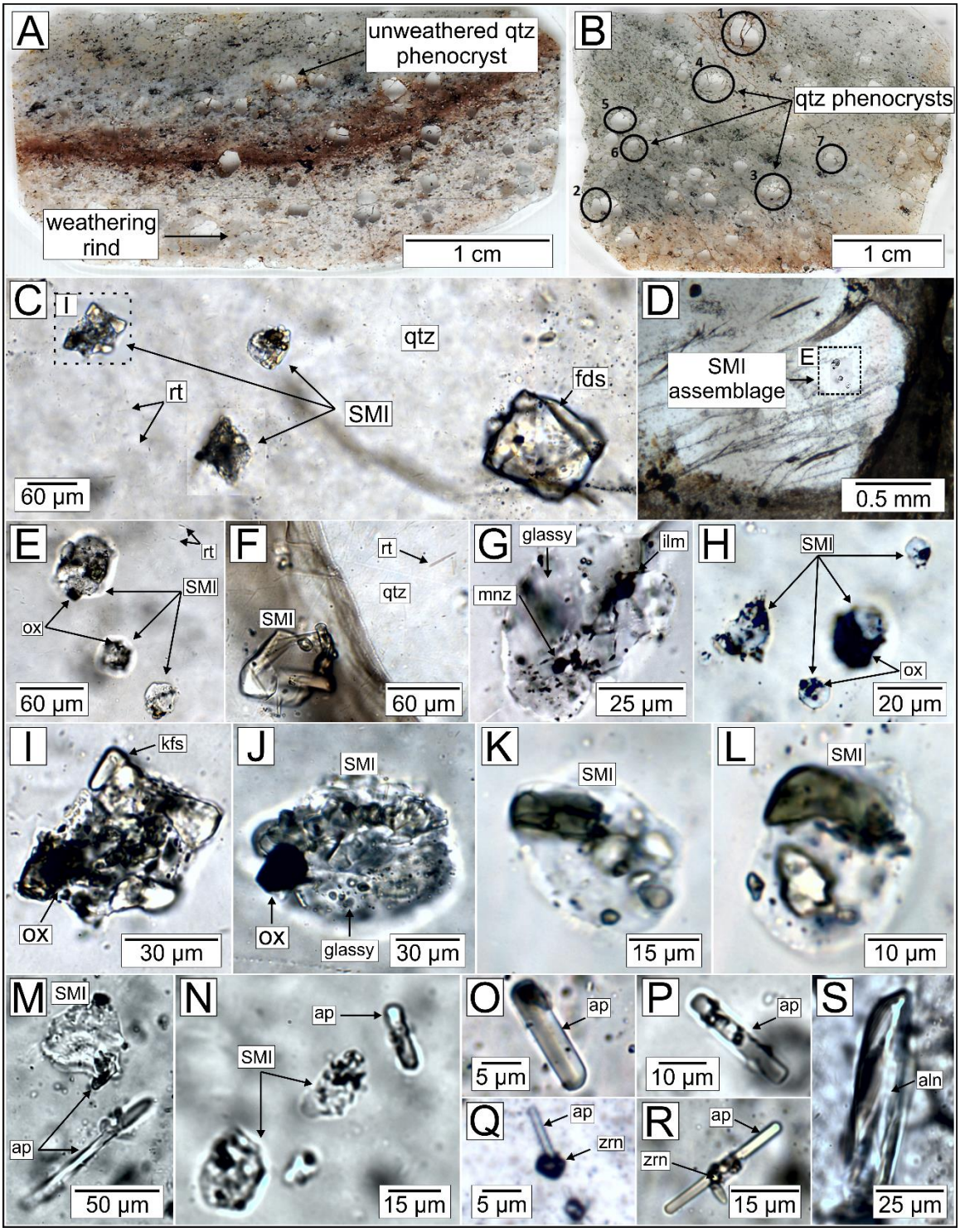
A
unweathered qtz phenocryst
weathering rind
1 cm
B
qtz phenocrysts
1 cm
C
I
qtz
rt
SMI
fds
60 µm
D
SMI assemblage
E
0.5 mm
E
rt
SMI
ox
60 µm
F
rt
qtz
SMI
60 µm
G
glassy
ilm
mnz
25 µm
H
SMI
ox
20 µm
I
kfs
ox
30 µm
J
SMI
ox
glassy
30 µm
K
SMI
15 µm
L
SMI
10 µm
M
SMI
ap
50 µm
N
ap
SMI
15 µm
O
ap
5 µm
P
ap
10 µm
S
aln
25 µm
Q
ap
zrn
5 µm
R
ap
zrn
15 µm

Figure 8 (previous page): Representative photomicrographs of SMI hosted in quartz from units 2.0 and 5.3 of the Bousquet Formation. All images taken in transmitted PPL. (**A**) Thin section of partially weathered rhyolite from a unit 2.0 surface sample. (**B**) Thin section of rhyolite from a unit 2.0 surface sample showing abundant phenocrystic quartz; circled grains contain melt inclusions. **(C)** Recrystallized assemblage of three SMI and an accidentally trapped K-feldspar grain in a rutile-included quartz phenocryst. **(D)** SMI assemblage containing 3 inclusions; dashed area is enlarged in frame (E). **(E)** Partially recrystallized SMI assemblage [enlarged view from (D)]. included rutile needles are shown in the upper right corner of the frame. (**F)** Large, partially recrystallized SMI and included rutile grains in a quartz phenocryst. **(G)** A partly recrystallized SMI containing monazite and ilmenite daughter phases. Part of the inclusion is glassy. **(H)** Assemblage of 4 SMI containing opaque oxide daughter phases; the large opaque phase in the inclusion in the center right of the image is likely an accidentally trapped phase. **(I)** Recrystallized SMI containing oxide and K-feldspar daughter phases. Enlarged image of inclusion shown in (C). **(J)** Recrystallized SMI with a glassy area near the bottom of the inclusion and a large oxide grain, possibly accidentally trapped. (**K-L)** Two SMI from a single assemblage showing consistent daughter phase mineralogy; both have greenish phases (mica or amphibole), clear translucent phases (glass, K-feldspar or quartz), yellowish high relief phases (unknown), and small dark phases (oxides) in similar phase proportions. (**M-N)** SMI co-entrapped with apatite (both in the SMI and in quartz, adjacent to the SMI; apatite is considered an accidentally trapped phase saturated at the time of SMI enclosure). (**O-R)** Apatite and zircon grains included in quartz phenocrysts. (**S)** Allanite grain included in a quartz phenocryst. Note: aln = allanite, ap = apatite, ilm = ilmenite, kfs = K-feldspar, mnz = monazite, ox = oxide, qtz = quartz, rt = rutile, SMI = silicate melt inclusion, zrn = zircon.

Table 4: Summary of SMI selected for LA-ICP-MS analysis

Sample	Unit	# of qtz phenos with viable SMI	# of SMI reported in final data set	Ave diameter of SMI (μm)	Description of SMI
3086-29-177	2.0	3	5	37	Medium size, glassy, and sparse; n = 4 (type I); and n = 1 (type II).
3086-29-188.5	2.0	7	14	29	Medium size, moderate amount of crystallized phases, and sparse; n = 4 (type I); and n = 10 (type II).
3086-29-218	2.0	5	8	30	Medium size, glassy, and sparse; n = 7 (type I); and n = 1 (type II).
3086-29-278	2.0	4	7	19	Small size, glassy, and sparse; n = 4 (type I); and n = 2 (type II).
3086-29-282	2.0	4	11	47	Large size, moderate amounts of crystallized phases, and abundant; n = 4 (type I); and n = 7 (type II).
3215-166-79.3	2.0	5	12	61	Very large size, moderate amount of crystallized phases, and abundant; n = 5 (type I); and n = 7 (type II).
3215-166-131.8	2.0	10	17	38	Medium size, moderate amount of crystallized phases, and sparse; n = 9 (type I); and n = 8 (type II).
731-9061-U2.0	2.0	11	25	30	Medium size, glassy, and abundant; n = 25 (type I).
3215-161-493	5.3	10	33	30	Medium size, moderate amounts of crystallized phases, and abundant; n = 12 (type I); and n = 20 (type II).
711-7200-U5.3	5.3	4	16	39	Large size, glassy, and abundant; n = 15 (type I); and n = 1 (type II).

The SMI are categorized into three types based on petrographic observations at room T (Figure 9). *Type I* inclusions are SMI with a transparent, isotropic, and amorphous glassy proportion, or devitrified glass proportion (composed of tiny crystallites of K-feldspar, quartz, and other daughter phases) dominating the inclusion volume (>50 vol%) with lesser daughter mineral phases (<50 vol%; see SEM results below; Figure 9A & D; Table 5; Frezzotti, 2001). Through SEM-BSE, optical petrography, and LA-ICP-MS, daughter mineral phases encountered routinely include apatite (Figure 8M – R), zircon (Figure 8Q), K-feldspar (Figures 10H & J, and 11N & O), calcic plagioclase (An = 10 – 30%; Figure 10G and I), ilmenite (Figures 10G and I, and 11N), oxides (Figure 8H – J), biotite (Figure 10G – J), and muscovite (Figure 10H and J). Importantly, the muscovite in SMI is a low-Mg and -Fe variety as compared to muscovite in the matrix and hourglass inclusions. *Type II* inclusions are SMI with a glassy proportion of <50 vol% and daughter phases dominating the inclusion volume (>50 vol%; Figure 9B & D; Table 5). Types I and II inclusions are desirable for analysis/interpretation relevant to characterizing melt chemistry because they are interpreted to represent true melt inclusions (isolated from source magma at the time of quartz growth). However, sometimes types I and II inclusions contain accidentally trapped solids (e.g., K-feldspar, calcic plagioclase, muscovite, biotite, zircon, apatite, ilmenite) and, based on evaluation of the LA-ICP-MS compositional data (see below; images of all SMI selected for LA-ICP-MS analyses are shown in Appendix 1), were excluded from the final dataset because their bulk compositions do not reflect the true composition of the melt. Similarly, *Type III* inclusions (Figure 9C - D; Table 5) are not true SMI but rather "hourglass"-style inclusions (Anderson, 1991) that have been exposed in cross-section during thin section preparation in such a way that they appear to be completely included.

However, they were never isolated from their surroundings and thus were prone to chemical/mineralogical modification. Units 2.0 and 5.3 contain all three types of inclusions along with co-entrapped accessory minerals (Figure 8). Petrographically, types I/II inclusions were distinguished from accidentally trapped mineral inclusions and type III inclusions (truncated hourglass inclusions) using four criteria: (i) Type III inclusions are always completely crystallized (no glass) and contain secondary (metamorphic, alteration) minerals not found in type I/II SMI (ankerite, Mg-rich siderite, calcite, magnetite, and sulphides; see SEM results below; Figure 9C; Table 5); (ii) Type III inclusions are often spatially related or directly connected to an embayment of matrix material (i.e., hourglass inclusion) that protrudes into the quartz phenocryst but that extends below the inclusion out of the plane of focus (Figure 9D); (iii) Type III inclusions are often highly irregular in shape and their contained crystals that penetrate into the inclusion walls, whereas commonly (but not always) type I/II inclusions are smaller and rounded/subrounded with smoother walls; and (iv) Accidentally trapped minerals occur in types I/II/III inclusions and in host quartz (free of recrystallized melt); they preserve some original euhedral crystal shape (i.e., of a single crystal), and have distinct petrographic features including contraction “gaps” along their host walls (cavity in quartz), and/or penetration into the walls of the inclusion that otherwise shows smooth edges bounding its contents and variable grain sizes and proportions that are not consistent from inclusion to inclusion.

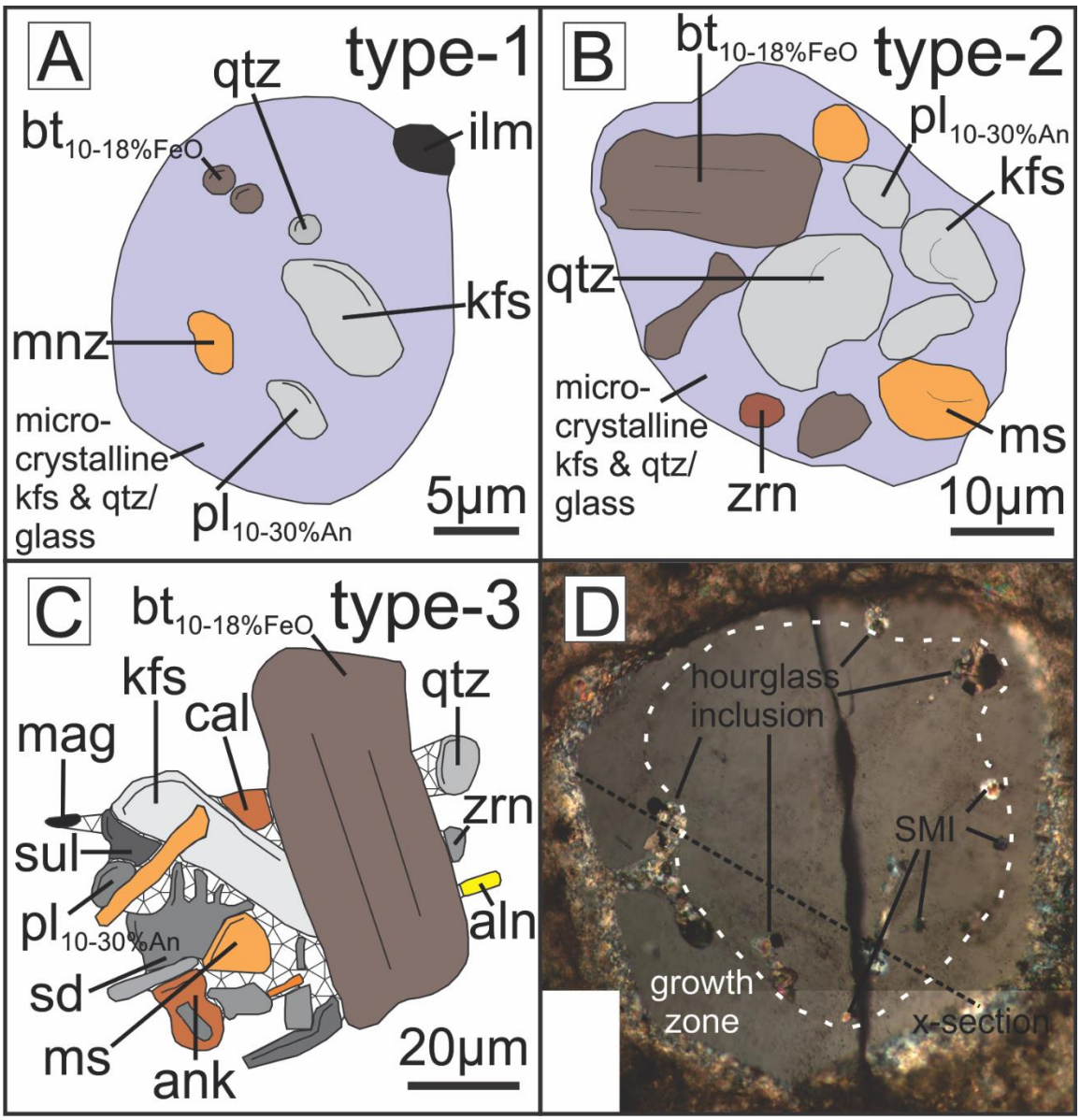
A
type-1
qtz
bt10-18%FeO
ilm
kfs
mnz
micro-
crystalline
kfs & qtz/
glass
pl10-30%An
5µm
B
bt10-18%FeO
type-2
pl10-30%An
kfs
qtz
micro-
crystalline
kfs & qtz/
glass
zrn
ms
10µm
C
bt10-18%FeO
type-3
kfs
cal
qtz
mag
zrn
sul
aln
pl10-30%An
sd
ms
ank
20µm
D
hourglass
inclusion
SMI
growth
zone
x-section

Figure 9 (previous page): Schematic differentiating idealized examples of three inclusion types recognized in the Bousquet volcanics. All mineral phases shown in the inclusions were identified consistently by SEM-EDS but do not necessarily represent all minerals present in the inclusions as some could not be identified based on EDS analyses owing to their size or ambiguous composition. Mineral phases are not to scale. **(A)** Sketch of a type I SMI with an amorphous microcrystalline fsp + qtz body and few crystallized phases (bt ± pl ± kfs ± ilm ± mnz). **(B)** Sketch of a type II SMI with an amorphous microcrystalline fsp + qtz body and a moderate number of crystallized phases (ms ± bt ± kfs ± zrn). **(C)** Sketch of a composite type III inclusion that contains crystallized matrix minerals (ms ± qtz ± bt(ann) ± kfs ± aln ± cal ± sul ± ank ± mag (Fe-oxides) ± pl ± sd (Mg-rich) ± zrn). Types I and II inclusions are true SMI, whereas Type III inclusions represent partly included melt (now altered, mineralized, and not having a bulk composition representative of the liquid) along embayments in the host phenocryst (hourglass inclusions). **(D)** A cross polarized light image of a quartz phenocryst showing examples of hourglass inclusions and types of SMI along a growth zone; if a cross section was taken through the neck of the hourglass inclusion (dashed line), it would have the appearance of a recrystallized SMI. Note: aln = allanite, ank = ankerite, ann = annite, bt = biotite, cal = calcite, ilm = ilmenite, kfs = potassium feldspar, mag = magnetite, mnz = monazite, ms = muscovite, pl = plagioclase, sd = siderite, sul = sulphide, zrn = zircon.

Table 5: Mineral phases in inclusions and groundmass of units 2.0 and 5.3

	Unit 2.0			Unit 5.3		
Mineral	Type-I/II	Type-III	Groundmass	Type-I/II	Type-III	Groundmass
quartz	✓	✓	✓	✓	✓	✓
alkali feldspar	✓	✓		✓	✓	✓
plagioclase	✓		✓			
muscovite	✓	✓	✓			✓
biotite	✓		✓		✓	✓
annite		✓				
sericite			✓			✓
chlorite			✓			✓
ankerite		✓				
calcite		✓	✓			
Mg-rich siderite		✓				
sulphides		✓				
chalcopyrite			✓			
garnet			✓			
allanite			✓			
apatite			✓			✓
magnetite		✓				
epidote			✓			
ilmenite	✓		✓	✓		✓
monazite				✓		
zircon	✓	✓	✓			

Note: Data based on ~300 SEM-EDS spot analyses of minerals in exposed inclusions or groundmass on polished thin section surfaces

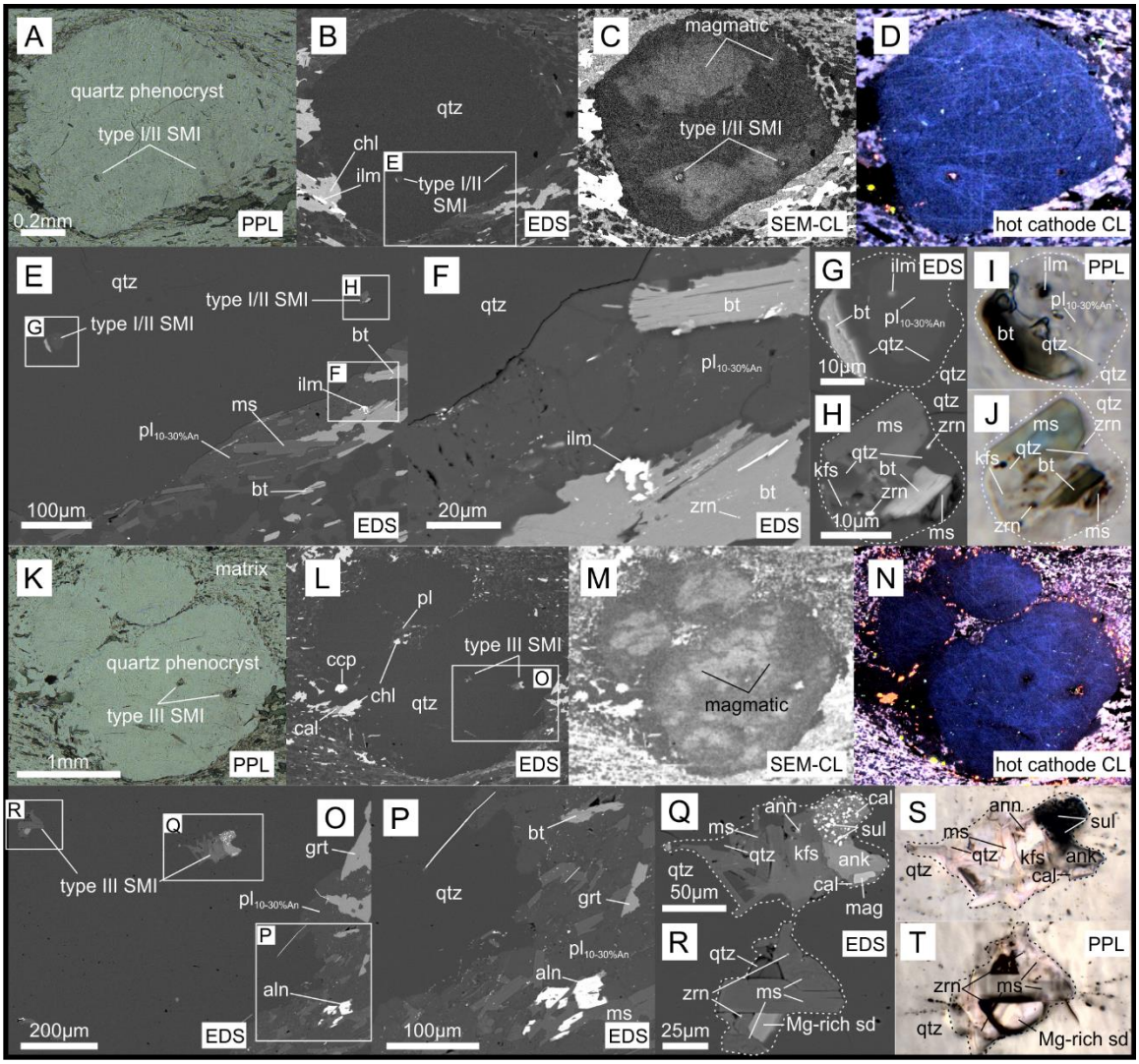
A
quartz phenocryst
type I/II SMI
0.2mm
PPL
B
qtz
chl
ilm
E
type I/II SMI
EDS
C
magmatic
type I/II SMI
SEM-CL
D
hot cathode CL
E
qtz
type I/II SMI
H
G
type I/II SMI
bt
F
ilm
ms
pl10-30%An
bt
100µm
EDS
F
qtz
bt
pl10-30%An
ilm
20µm
zrn
bt
EDS
G
ilm
EDS
bt
pl10-30%An
qtz
10µm
qtz
I
ilm
PPL
pl10-30%An
bt
qtz
qtz
H
qtz
ms
zrn
qtz
kfs
bt
zrn
10µm
ms
J
qtz
ms
zrn
qtz
kfs
bt
zrn
ms
K
matrix
quartz phenocryst
type III SMI
1mm
PPL
L
pl
type III SMI
ccp
O
chl
qtz
cal
EDS
M
magmatic
SEM-CL
N
hot cathode CL
R
type III SMI
Q
pl10-30%An
O
grt
P
aln
200µm
EDS
P
bt
qtz
grt
pl10-30%An
aln
ms
100µm
EDS
Q
ms
ann
cal
sul
qtz
qtz
kfs
ank
cal
50µm
mag
EDS
R
qtz
zrn
ms
25µm
Mg-rich sd
S
ann
ms
sul
qtz
kfs
ank
qtz
cal
T
PPL
zrn
ms
qtz
Mg-rich sd

Figure 10 (previous page): Mineralogy and petrographic characteristics of inclusions in unit 2.0. Photomicrographs are in transmitted PPL, or from SEM-BSE, SEM-CL, and hot cathode CL imaging. (**A**) PPL image of a quartz phenocryst with two exposed SMI. (**B**) SEM-BSE image showing matrix mineralogy (ilm + chl) and two exposed SMI. (**C-D)** SEM-CL and hot CL images showing light grey/intense blue (i.e., magmatic) and dark grey/dull blue (i.e., metamorphic) zones. Note the halos around exposed SMI. (**E**) SEM-BSE image showing detailed matrix mineralogy (ilm + bt + ms +pl) and two exposed SMI. (**F)** SEM-BSE image showing detailed matrix mineralogy (ilm + bt + pl). **(G-J)** SEM-BSE and PPL images showing detailed SMI composition (ilm + bt + ms + kfs + pl + zrn). (**K**) PPL image of a quartz phenocryst with two exposed hourglass inclusions. (**L**) SEM-BSE image showing matrix mineralogy (chl + pl + cal + ccp) and two exposed hourglass inclusions. (**M-N**) SEM-CL and hot CL images showing light grey/intense blue (i.e., magmatic) and dark grey/dull blue (i.e., metamorphic) zones. Note the presence of halos around the two exposed hourglass inclusions. (**O**) SEM-BSE image showing detailed matrix mineralogy (pl + grt + + aln) and two exposed hourglass inclusions. (**P)** SEM-BSE image showing detailed matrix mineralogy (bt + pl + grt + aln). (**Q-T)** SEM-BSE and PPL images showing detailed hourglass inclusion mineralogy (qtz + ms + ann + kfs + cal + ank + mag + sul + Mg-rich sd + zrn). Note: aln = allanite, ank = ankerite, ann = annite, bt = biotite, cal = calcite, ccp = chalcopyrite, chl = chlorite, grt = garnet, ilm = ilmenite, kfs = potassium feldspar, mag = magnetite, Mg-rich sd = magnesium-rich siderite, ms = muscovite, pl = plagioclase, qtz = quartz, SMI = silicate melt inclusion, sul = sulphide, zrn = zircon.

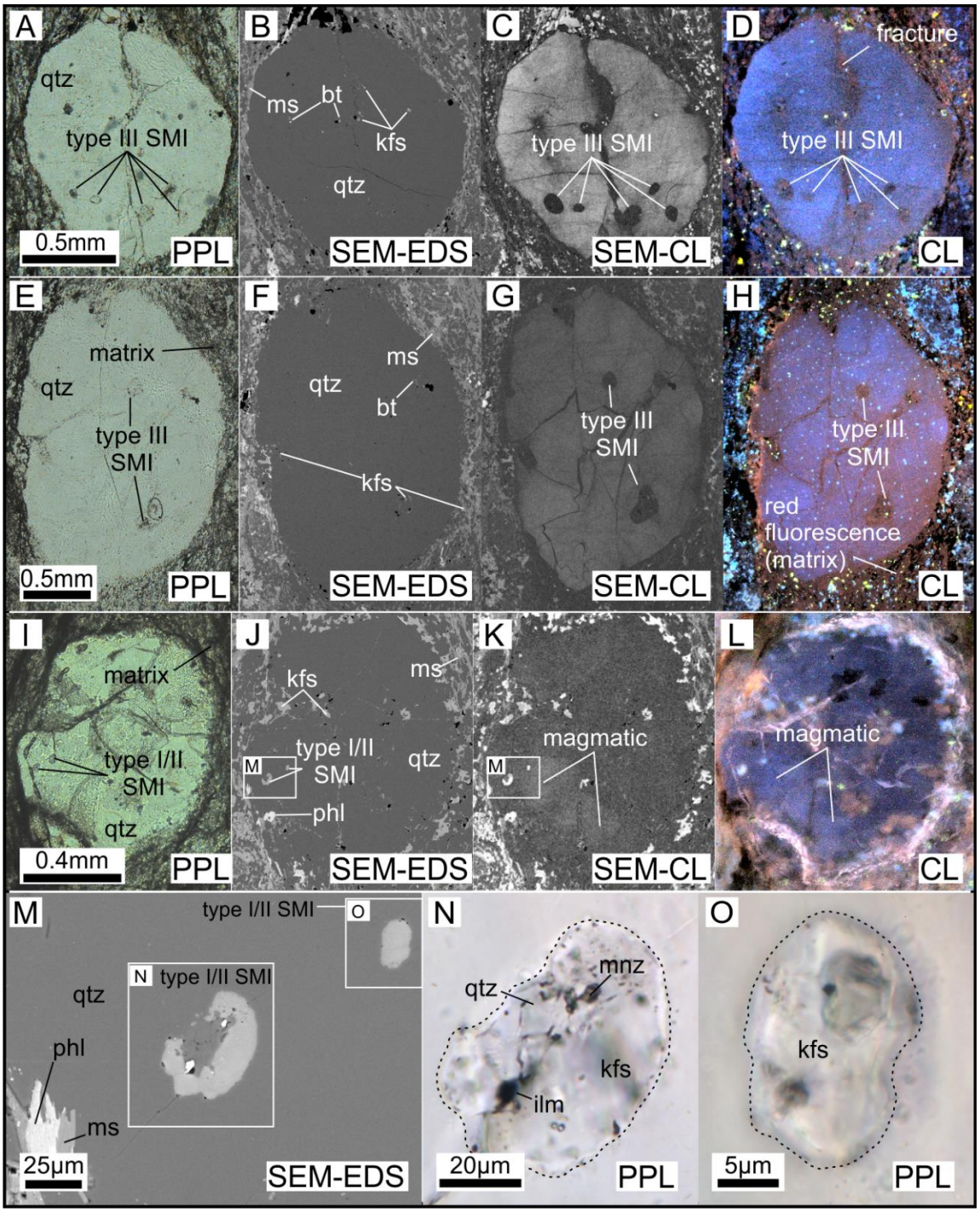
A
qtz
type III SMI
0.5mm
PPL
B
ms
bt
kfs
qtz
SEM-EDS
C
type III SMI
SEM-CL
D
fracture
type III SMI
CL
E
matrix
qtz
type III SMI
0.5mm
PPL
F
ms
qtz
bt
kfs
SEM-EDS
G
type III SMI
SEM-CL
H
type III SMI
red fluorescence (matrix)
CL
I
matrix
type I/II SMI
qtz
0.4mm
PPL
J
kfs
ms
type I/II SMI
qtz
M
phl
SEM-EDS
K
magmatic
M
SEM-CL
L
magmatic
CL
M
type I/II SMI
O
N
type I/II SMI
qtz
phl
ms
25µm
SEM-EDS
N
mnz
qtz
kfs
ilm
20µm
PPL
O
kfs
5µm
PPL

Figure 11 (previous page): Petrographic mosaic of unit 5.3 quartz phenocrysts. Microphotographs captured with PPL, SEM-BSE, SEM-CL, and hot CL. (**A-B**) PPL and SEM-BSE images of a quartz phenocryst showing hourglass inclusion mineralogy (bt ± kfs) and matrix mineralogy (ms). (**C**) SEM-CL image showing dark circles that represent hourglass inclusions. (**D**) Hot CL image showing mostly an intense blue colour (i.e., magmatic) and minor amounts of a brownish-red colour (i.e., metamorphic). The brownish-red colour is found in a medial fracture and blebs of hourglass inclusions. (**E-F**) PPL and SEM-BSE images of a quartz phenocryst showing hourglass inclusion mineralogy (bt ± kfs) and matrix mineralogy (ms ± kfs). (**G**) SEM-CL image showing dark circles that represent hourglass inclusions. (**H**) Hot CL image showing a reddish blue coloration, which indicates some hydrothermal and metamorphic influence. (**I-J**) PPL and SEM-BSE images of a quartz phenocryst with two exposed SMI; images show SMI mineralogy (kfs), fracture-fill mineralogy (kfs), and matrix mineralogy (kfs ± phl ± ms). (**K-L**) SEM-CL and hot CL images showing light grey/intense blue (i.e., magmatic) and dark grey/dull blue (i.e., metamorphic) zones. (**M**) SEM-BSE image showing detailed matrix mineralogy (ms ± phl) and two SMI (ilm ± mnz ± kfs). (**N-O)** PPL image showing detailed SMI composition (ilm ± mnz ± kfs). Note: bt = biotite, ilm = ilmenite, kfs = potassium feldspar, mnz = monazite, ms = muscovite, phl = phlogopite, qtz = quartz.

Importantly, types I/II/III inclusions are associated with growth zones within quartz phenocrysts suggesting a primary origin (Figure 9D). Differentiation of type I/II from type III inclusions is further resolved with a combination of plane-polarized light, SEM-BSE, SEM-CL, and hot cathode CL (HCL) images collected for ~50 quartz phenocrysts from 15 thin sections of units 2.0 and 5.3 (Figures 10, 11, and 12). The type I/II SMI included in the final dataset are enclosed within light grey (SEM-CL) and intense blue (HCL) "remnant" zones of magmatic quartz (Figures 10C – D, and 11J - L). The type I/II SMI found outside of these zones in darker grey, or less intense blue "altered" quartz were eliminated from the dataset because modification of the host may have leaked and/or changed their physical/chemical composition. Type III inclusions occur within dark grey (SEM-CL) and dull blue or red (hot CL) zones reflecting local alteration of the primary quartz host (Figures 10M – N, and 11C, D, G, and H). Rarely, quartz phenocrysts that contained SMI showed primary zoning in the CL images (Figure 12G and H).

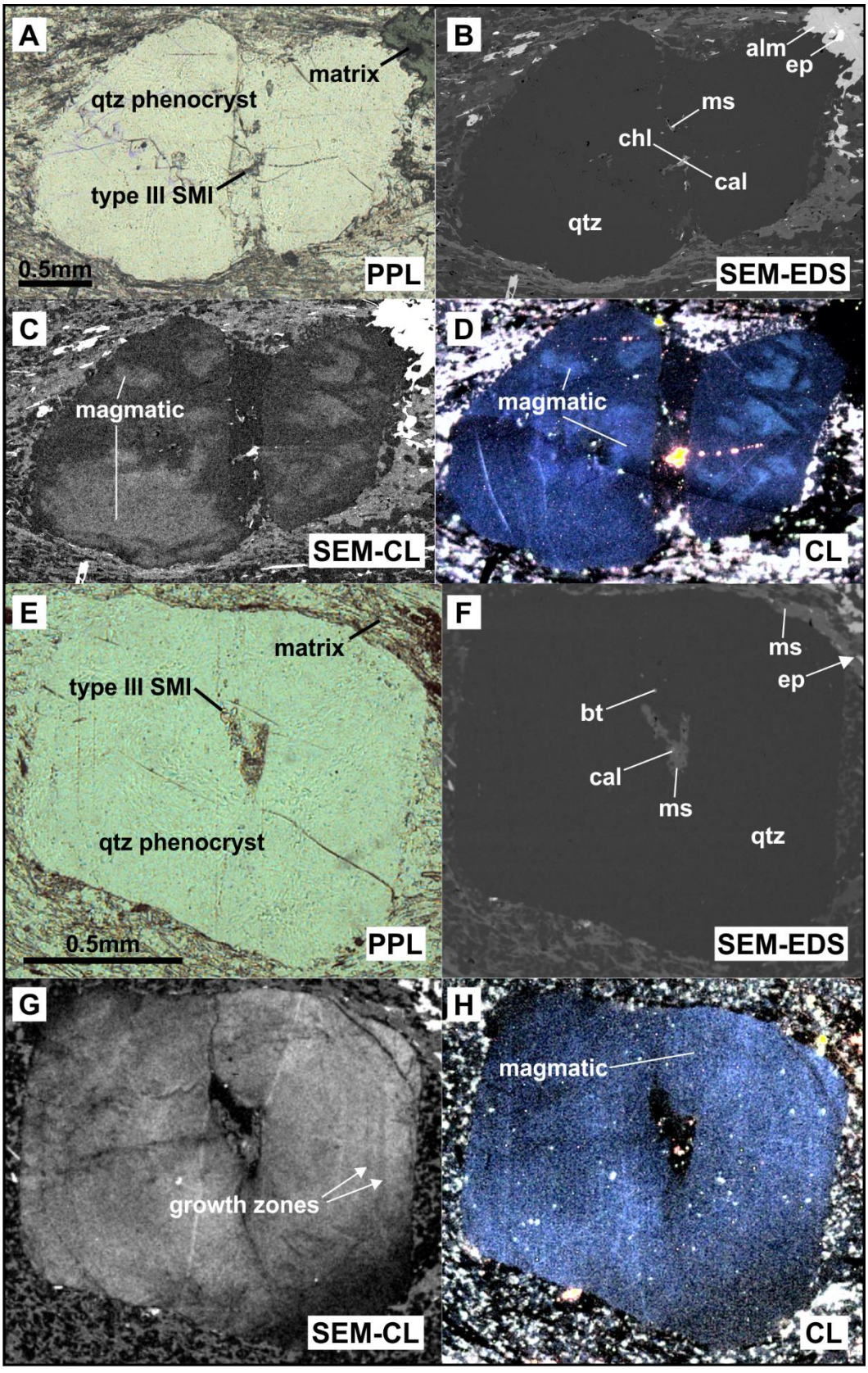
A
matrix
qtz phenocryst
type III SMI
0.5mm
PPL
B
alm
ep
ms
chl
cal
qtz
SEM-EDS
C
magmatic
SEM-CL
D
magmatic
CL
E
matrix
type III SMI
qtz phenocryst
0.5mm
PPL
F
ms
ep
bt
cal
ms
qtz
SEM-EDS
G
growth zones
SEM-CL
H
magmatic
CL

Figure 12 (previous page): Petrographic mosaic of unit 2.0 quartz phenocrysts. Microphotographs captured with PPL, SEM-BSE, SEM-CL, and hot CL. **(A)** PPL image of a quartz phenocryst with an hourglass inclusion. **(B)** SEM-BSE image showing hourglass inclusion mineralogy (chl ± ms ± cal) and matrix mineralogy (alm ± ep). **(C & D)** SEM-CL and hot CL images showing light grey/intense blue (i.e., magmatic) and dark grey/dull blue (i.e., metamorphic) zones. **(E)** PPL image of a quartz phenocryst with an hourglass inclusion. **(F)** SEM-BSE image showing hourglass inclusion mineralogy (bt ± ms ± cal) and matrix mineralogy (ms ± ep). **(G)** SEM-CL image showing contrasting shades of light and dark grey, indicating primary growth zoning. **(H)** Hot CL image showing an intense blue (i.e., magmatic origin). Note: alm = almandine, bt = biotite, cal = calcite, chl = chlorite, ep = epidote, ms = muscovite, qtz = quartz.

2.3.3 Composition of SMI

The major and trace element composition of the quartz-hosted SMI was obtained by LA-ICP-MS in order to provide constraints on the composition of the magmatic reservoir where the melts were trapped, including its ore and accessory metal tenor. Figure 13 shows representative transient LA-ICP-MS signals from SMI ablations as well as other phases (e.g., accidentally trapped mineral grains) to illustrate the characteristics of different signal types. Typical melt inclusion signals, free of accidentally trapped mineral phases, had count rates rise and fall gradually with a dome-like signal-time distribution that is synchronous for many major and trace elements (Figure 13A - B, and G - P). Metal isotope signals tend to increase and decrease together and generally follow other isotopes tied to the recrystallized melt phase. For example, ^{209}Bi, ^{121}Sb, and ^{107}Ag show a distinctive dome shape in Figure 13O – P. However, metal isotope count rates may also be somewhat "decoupled" from other elements (Figure 13A – B, and I – J). Melt inclusions with reported Au had unambiguously higher count rates for ^{197}Au than the background and host quartz. For example, the SMI shown in Figure 13N had an average of 64.4 cps ^{197}Au over the SMI + host signal interval, whereas background/host only had an average of 9.2 cps ^{197}Au. Occasionally, isolated metal-bearing phases (Cu + As + Bi + Ag) were observed in the SMI signals that are not "melt-dissolved" metals but accidentally trapped sulphide particles (Figure 13G – H). These inclusion signals, when quantified, yield unrealistically high metal concentrations

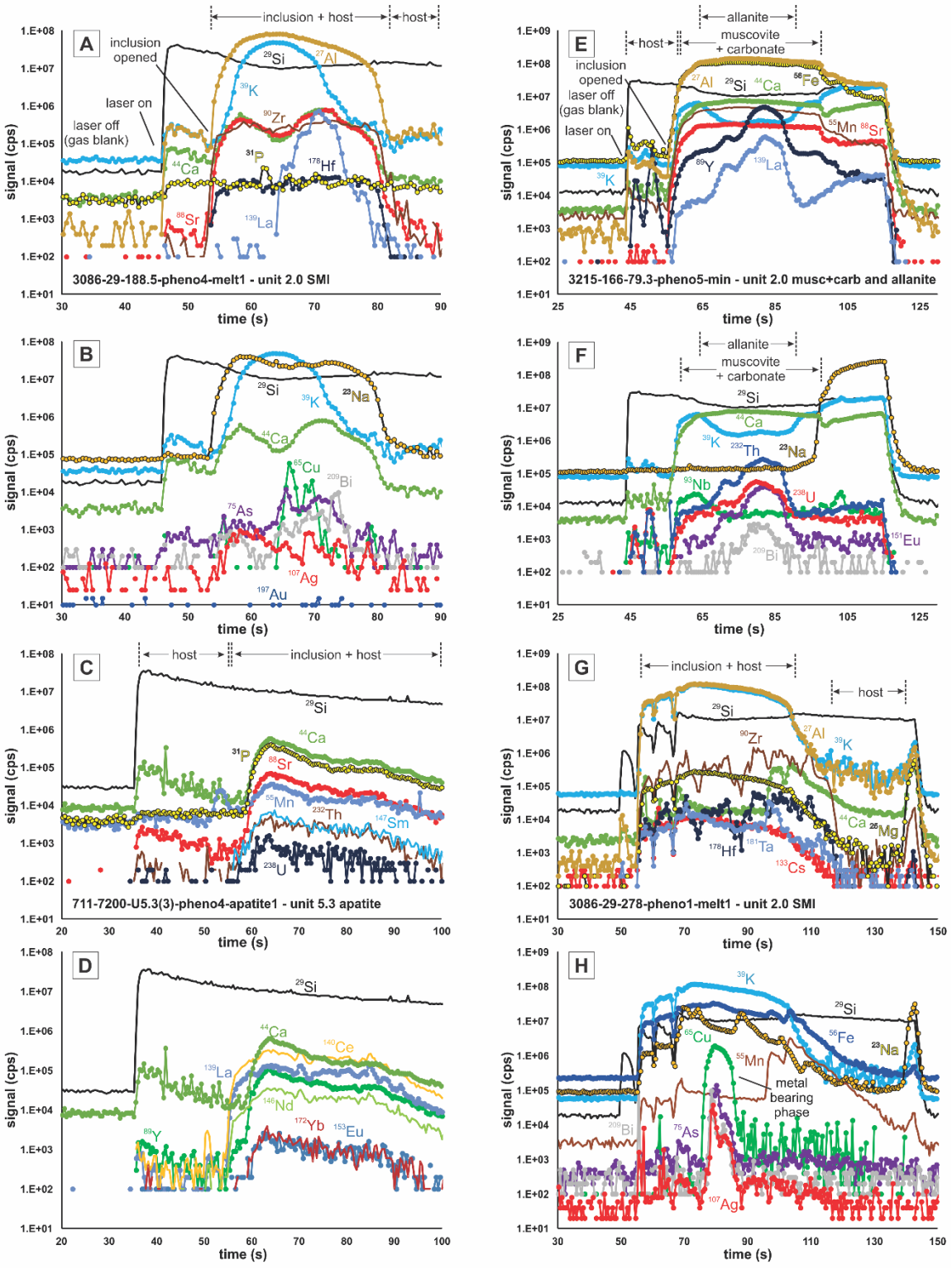
A
inclusion + host
host
inclusion opened
laser on
laser off (gas blank)
29Si
27Al
39K
90Zr
31P
44Ca
178Hf
88Sr
139La
3086-29-188.5-pheno4-melt1 - unit 2.0 SMI
B
29Si
39K
23Na
44Ca
65Cu
209Bi
75As
107Ag
197Au
C
host
inclusion + host
29Si
44Ca
31P
88Sr
55Mn
232Th
147Sm
238U
711-7200-U5.3(3)-pheno4-apatite1 - unit 5.3 apatite
D
29Si
44Ca
140Ce
139La
146Nd
172Yb
153Eu
89Y
E
allanite
host
muscovite + carbonate
inclusion opened
laser off (gas blank)
laser on
27Al
29Si
44Ca
56Fe
55Mn
88Sr
89Y
139La
39K
3215-166-79.3-pheno5-min - unit 2.0 musc+carb and allanite
F
allanite
muscovite + carbonate
29Si
44Ca
39K
232Th
23Na
93Nb
238U
151Eu
209Bi
G
inclusion + host
host
29Si
90Zr
27Al
39K
44Ca
26Mg
178Hf
181Ta
133Cs
3086-29-278-pheno1-melt1 - unit 2.0 SMI
H
39K
29Si
65Cu
56Fe
23Na
55Mn
metal bearing phase
209Bi
75As
107Ag
signal (cps)
time (s)

Figure 13 (previous page): Representative LA-ICP-MS signals of SMI, mineral inclusions, and melt with accidentally trapped minerals. (A-B) Elemental concentrations in counts per second (cps) of a quartz phenocryst-hosted SMI of unit 2.0. Laser is off and a background (gas blank) signal is collected from 30-45 seconds; laser is on from 45-90 seconds; and the SMI is ablated from 52-82 seconds. The SMI is represented by decreased counts of ^{29}Si and increased counts of ^{27}Al, ^{39}K, ^{44}Ca, ^{88}Sr, ^{90}Zr, ^{107}Ag, and ^{178}Hf. This is a good, typical, melt signal of a completely buried SMI and it does not display a stepwise opening. It has a nice dome shape in general but with a distinction between different phases in the inclusion. Note the ^{65}Cu, ^{75}As, ^{139}La, and ^{209}Bi bearing phase from 65-80 seconds. **(C-D)** Elemental concentrations in cps of a quartz phenocryst-hosted apatite grain of unit 5.3. Laser is off and a background signal is collected from 20-35 seconds; laser is on from 35-100 seconds; and the apatite grain is ablated from 60-100 seconds. This is not an SMI but was included as an important signal because of its relevance to subsection 2.2.3 of the results. Note that the end of the apatite signal is not shown because it continued down to the glass slide contact which compressed the curves and distorted the image. The apatite grain is represented by increased counts of ^{31}P, ^{44}Ca, ^{55}Mn, ^{88}Sr, ^{139}La, ^{140}Ce, ^{146}Nd, ^{147}Sm, ^{153}Eu, ^{172}Yb, ^{232}Th, and ^{238}U. **(E-F)** Elemental concentrations in cps of a polymineral inclusion in a quartz phenocryst of unit 2.0. Laser is off and a background signal is collected from 25-45 seconds; laser is on from 45-115 seconds; and the host inclusion is ablated from 55-95 seconds. The high ^{56}Fe, ^{27}Al, ^{44}Ca, ^{55}Mn, ^{88}Sr and lack of ^{23}Na suggests this is not plagioclase but rather muscovite + carbonate together with a small allanite in the center. Note the allanite phase that contains elevated ^{89}Y, ^{139}La, ^{151}Eu, ^{209}Bi, ^{232}Th, and ^{238}U from 55-85 seconds. **(G-H)** Elemental concentrations in cps of a quartz phenocryst-hosted SMI of unit 2.0. Laser is off and a background signal is collected from 30-45 seconds; laser is on from 45-145 seconds; and the SMI is ablated from 55-110 seconds. The SMI is represented by decreased counts of ^{29}Si and increased counts of ^{23}Na, ^{25}Mg, ^{27}Al, ^{39}K, ^{56}Fe, ^{133}Cs, ^{178}Hf, and ^{181}Ta. Note the accidentally trapped metal-rich phase (alloy or mineral). that contains elevated ^{65}Cu, ^{75}As, ^{107}Ag, and ^{209}Bi from 75-90 seconds. Areas of spectra with metal-bearing phases were not included in the quantification of SMI composition. Note: Most LA-ICP-MS spectra have a step-like feature that is caused by the shifting of the aperture size of the laser. As the aperture increases in size, the laser is blocked briefly and causing a drop in element counts.

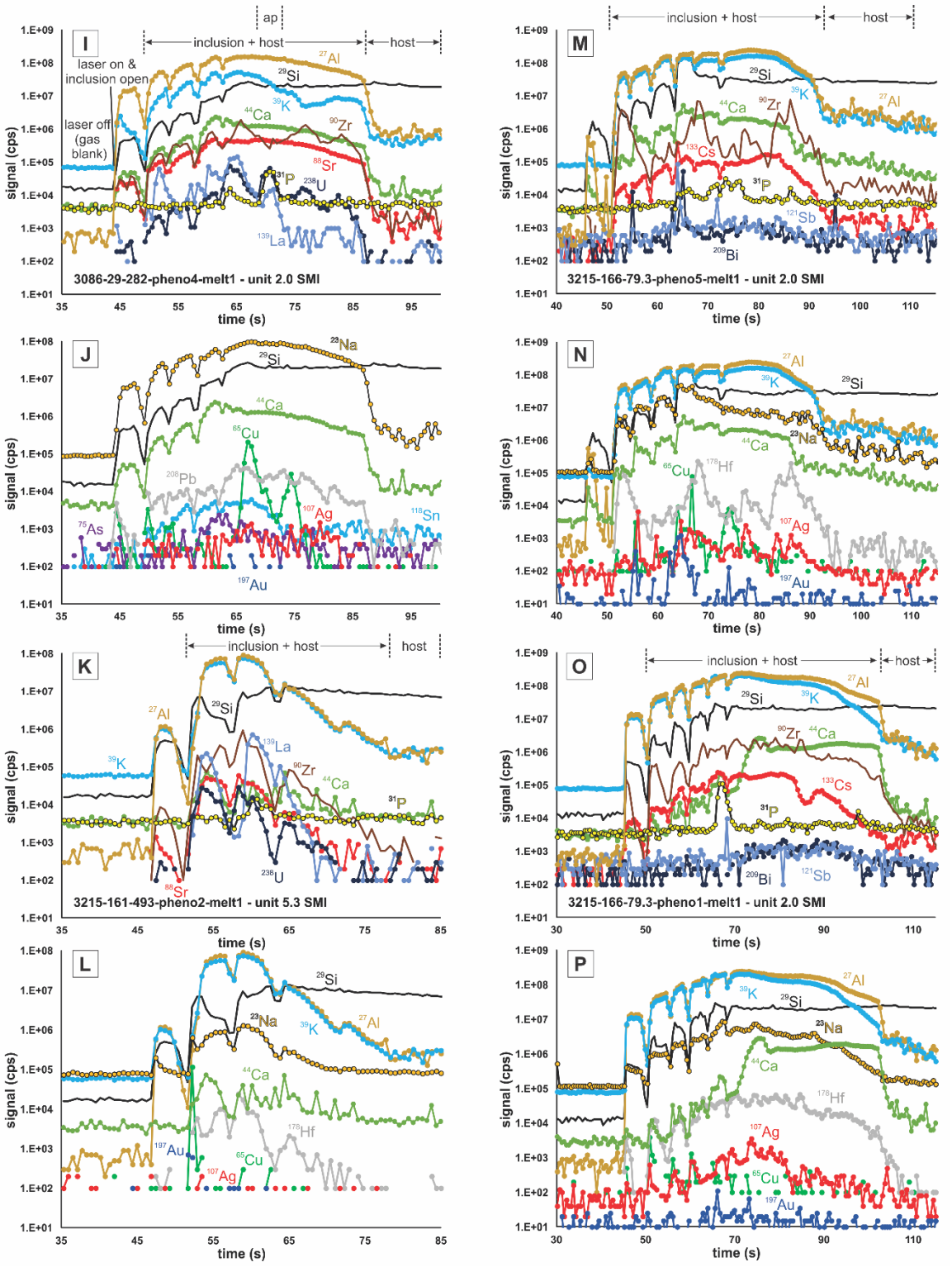
I
ap
inclusion + host
host
laser on & inclusion open
laser off (gas blank)
27Al
29Si
39K
44Ca
90Zr
88Sr
31P
238U
139La
3086-29-282-pheno4-melt1 - unit 2.0 SMI
signal (cps)
time (s)
J
23Na
29Si
44Ca
65Cu
208Pb
107Ag
118Sn
75As
197Au
K
inclusion + host
host
27Al
29Si
39K
139La
90Zr
44Ca
31P
88Sr
238U
3215-161-493-pheno2-melt1 - unit 5.3 SMI
L
29Si
23Na
39K
27Al
44Ca
178Hf
197Au
107Ag
65Cu
M
inclusion + host
host
29Si
39K
27Al
44Ca
90Zr
133Cs
31P
121Sb
209Bi
3215-166-79.3-pheno5-melt1 - unit 2.0 SMI
N
27Al
39K
29Si
23Na
44Ca
65Cu
178Hf
107Ag
197Au
O
inclusion + host
host
27Al
29Si
39K
90Zr
44Ca
133Cs
31P
209Bi
121Sb
3215-166-79.3-pheno1-melt1 - unit 2.0 SMI
P
27Al
39K
29Si
23Na
44Ca
178Hf
107Ag
65Cu
197Au

Figure 13 continued (previous page): Representative LA-ICP-MS signals of SMI, mineral inclusions, and melt with accidentally trapped minerals. (I-J) Elemental concentrations in counts per second (cps) of a quartz phenocryst-hosted SMI of unit 2.0. Laser is off and a background (gas blank) signal is collected from 35-45 seconds; laser is on from 45-100 seconds; and the SMI is ablated from 52-90 seconds. The SMI is represented by decreased counts of ^{29}Si and increased counts of ^{23}Na, ^{27}Al, ^{39}K, ^{44}Ca, ^{75}As, ^{88}Sr, ^{90}Zr, ^{107}Ag, ^{118}Sn, ^{139}La, ^{208}Pb, and ^{238}U. Note the ^{65}Cu-bearing phase from 65-75 seconds and ^{31}P, ^{139}La, and ^{238}U spikes from 70-75 seconds, representing an included apatite grain. (**K-L)** Elemental concentrations in cps of a quartz phenocryst-hosted SMI of unit 5.3. Laser is off and a background signal is collected from 35-45 seconds; laser is on from 45-85 seconds; and the SMI is ablated from 52-75 seconds. The SMI is represented by decreased counts of ^{29}Si and increased counts of ^{23}Na, ^{27}Al, ^{39}K, ^{88}Sr, ^{90}Zr, ^{139}La, ^{178}Hf and ^{238}U. Note the elevated ^{197}Au value which correlates with ^{65}Cu but not ^{107}Ag; therefore, it is not accidentally trapped electrum. (**M-N)** Elemental concentrations in cps of a quartz phenocryst-hosted SMI of unit 2.0. Laser is off and a background signal is collected from 40-45 seconds; laser is on from 45-105 seconds; and the SMI is ablated from 50-95 seconds. The SMI is represented by decreased counts of ^{29}Si and increased counts of ^{23}Na, ^{27}Al, ^{39}K, ^{44}Ca, ^{90}Zr, ^{133}Cs, and ^{178}Hf. Note the elevated metals, including ^{65}Cu, ^{107}Ag, ^{121}Sb, ^{197}Au, and ^{209}Bi. (**O-P)** Elemental concentrations in cps of a quartz phenocryst-hosted SMI of unit 2.0. Laser is off and a background signal is collected from 30-45 seconds; laser is on from 45-115 seconds; and the SMI is ablated from 52-105 seconds. The SMI is represented by decreased counts of ^{29}Si and increased counts of ^{23}Na, ^{27}Al, ^{39}K, ^{44}Ca, ^{90}Zr, ^{133}Cs, and ^{178}Hf. Note trapped apatite (^{31}P spike) and the elevated metals, including ^{65}Cu, ^{107}Ag, ^{121}Sb, ^{197}Au, and ^{209}Bi. Note: Most LA-ICP-MS spectra have a step-like feature that is caused by the shifting of the aperture size of the laser. As the aperture increases in size, the laser is blocked briefly and causing a drop in element counts.

Signals representing included mineral phases (either monomineralic or polymineralic aggregates), or accidental entrapment of mineral phases with or without co-entrapped melt, were rejected from the final data set. These were recognized in signals by their flat intensity profiles for many major and trace elements (Figure 13E – F), or irregular humps in the transient signals for elements in the accidental phase that synchronously increased and decreased in measured isotope intensity, not corresponding to the intensity of elements in the true melt fraction (Figure 13E – F). Sometimes minerals accidentally trapped in melt inclusions dominate the signal. Hourglass inclusions, and inclusions containing large, accidentally trapped mineral phases were identified by anomalously high count rates for certain isotopes (^{44}Ca = calcite; ^{56}Fe = magnetite; ^{56}Fe, ^{25}Mg, ^{44}Ca = siderite, ankerite; ^{47}Ti, ^{93}Nb, ^{56}Fe = oxides; ^{44}Ca, ^{23}Na, ^{27}Al = plagioclase; ^{44}Ca, some REE = apatite or allanite; ^{90}Zr, ^{178}Hf = zircon; ^{85}Rb, ^{137}Ba, ^{27}Al = K-feldspar; and ^{208}Pb, ^{75}As, ^{107}Ag, ^{118}Sn, ^{182}W = oxides or sulfides).

The final data set for SMI from unit 2.0 (n = 99) reflects a data filtering process that significantly reduced the ranges in specific major and trace element concentrations (TiO_2, Al_2O_3, CaO, Na_2O, B, Rb, Ba, HFSE, REE, Mo, Sn, W, and Pb; Figure 14). Filtering (i.e., removing inclusions from the data set) was justified on examination of signals/quantified values that demonstrated the presence of mineral inclusions that were not part of the crystallized melt (i.e., accidentally trapped phases). The same data filtering process resulted in a final data set for unit 5.3 (n = 49) with a reduction in error bar ranges in a box-whisker plot for a variety of elements (TiO_2, $Al2O_3$, FeO, MnO, MgO, CaO, Cs, Rb, Ba, Nb, Zr, Hf, Ce, Lu, As, Ag, Sn, W, and Pb; Figure 15).

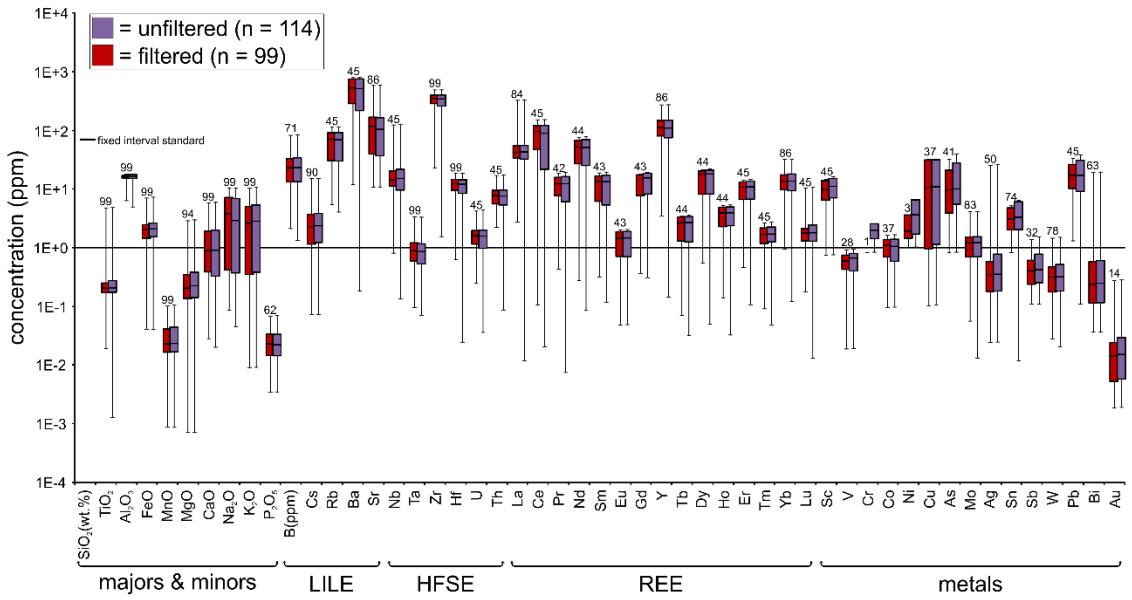

Figure 14: Box-whisker plot of unit 2.0 (filtered vs unfiltered). Box-whisker plot with the 1st and 3rd quartile ranges, averages, and error bars of major and minor oxides, LILE, HFSE, REE, and metals of unit 2.0 SMI. Concentrations of oxides and elements were collected by LA-ICP-MS. Purple boxes show the unfiltered data set (n = 114) while red boxes show the filtered data set (n = 99). Numbers above each box and whisker represent the number of filtered SMI analyses for each corresponding element or oxide. Note the reduction in error bar ranges for TiO_2, Al_2O_3, CaO, Na_2O, B, Rb, Ba, HFSE, REE, Mo, Sn, W, and Pb.

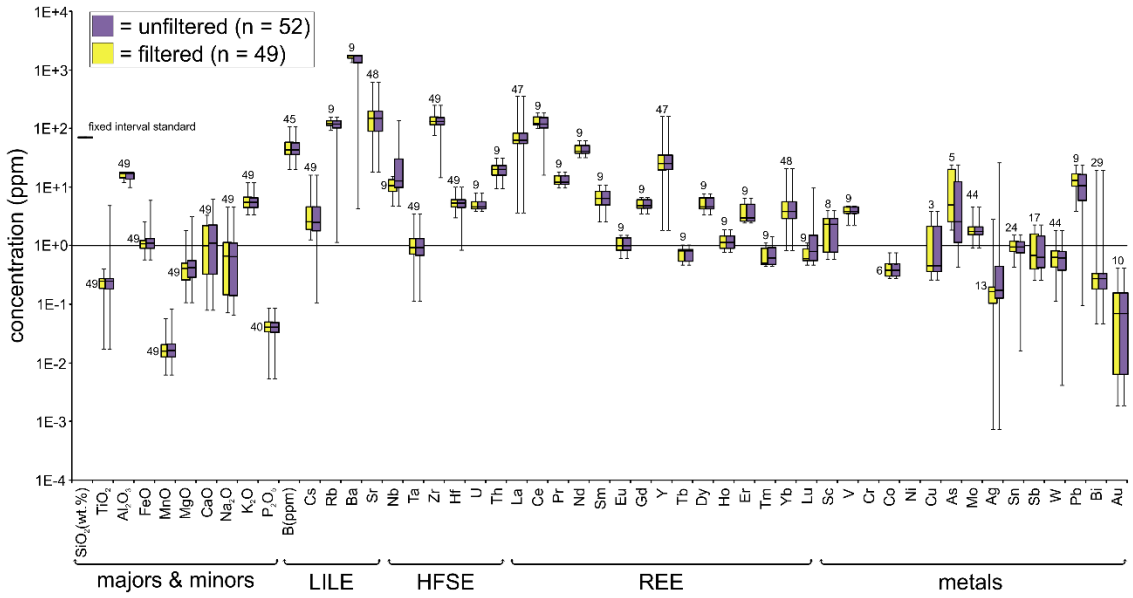

Figure 15: Box-whisker plot of unit 5.3 SMI (filtered vs unfiltered). Box-whisker plot with the 1st and 3rd quartile ranges, averages, and error bars of major and minor oxides, LILE, HFSE, REE, and metals of unit 5.3 SMI. Concentrations of oxides and elements were collected by LA-ICP-MS. Purple boxes show the unfiltered data set (n = 52) while yellow boxes show the filtered data set (n = 49). Numbers above each box and whisker represent the number of filtered SMI analyses for each corresponding element or oxide. Note the reduction in error bar ranges for TiO_2, Al_2O_3, FeO, MnO, MgO, CaO, Cs, Rb, Ba, Nb, Zr, Hf, Ce, Lu, As, Ag, Sn, W, and Pb.

Bulk rock data (Table 6) was also obtained for the host rhyolites and compared to the SMI data for units 2.0 (Figure 16; Table 7) and 5.3 (Figure 17; Table 7) in order to determine if: (i) post entrapment processes modified the bulk magma and/or rock composition (e.g., by continued fractionation/differentiation, degassing, alteration, and metamorphism); and (ii) whether the bulk rock analyses can be used as a reliable proxy for magma metal tenor. Quantification of major, minor, and trace elements in SMI of units 2.0 and 5.3 included the ore metals Au-Ag-Cu-Mo-Sn-Sb-W (Table 7).

Table 6: Bulk rock analyses of units 2.0 and 5.3 of the Bousquet Formation

	Unit 2.0						Unit 5.3	
Element	3086-29-177	3086-29-218	3086-29-278	3086-29-282	3215-166-79	3215-166-131	3215-161-493	711-7200
SiO_2 (wt%)	74.79	76.38	76.04	74.11	80.49	76.37	72.37	78.84
TiO_2	0.17	0.24	0.26	0.25	0.12	0.18	0.2	0.23
Al_2O_3	11.97	11.94	12.56	12.01	11.5	12.33	14.88	12.27
FeO	2.35	2.65	2.56	2.24	1.66	3.27	2.22	0.89
MnO	0.064	0.057	0.041	0.061	0.032	0.094	0.052	0.015
MgO	0.88	0.39	0.35	0.45	0.35	0.78	1.46	0.48
CaO	2.54	1.87	1.65	3.65	1.95	1.53	1.7	0.20
Na_2O	2.81	4.19	4.96	1.92	0.83	3.2	0.93	3.13
K_2O	2.14	1.14	0.95	2.09	2.41	1.2	3.83	3.44
P_2O_5	0.02	0.037	0.043	0.04	0.01	0.021	0.037	0.077
Total LOI	2.85	1.33	1.19	2.92	1.29	1.16	2.08	1.24
B(ppm)	n.a.	n.a.	n.a.	n.a.	n.a.	n.a.	n.a.	n.a.
Cs	2.47	1.19	0.82	1.49	12.81	4.14	2.33	1.48
Rb	48.86	27.42	19.34	40.45	49.81	29.61	33.57	92.51
Ba	433.3	197	281.8	274.3	328	211.7	1095.1	909
Sr	71.8	51.8	48.2	48.6	74.3	89.6	82.2	190.8
Nb	11.76	13.10	13.01	13.22	15.54	13.38	13.24	10.49
Ta	0.73	0.83	0.83	0.82	0.91	0.71	1.08	0.82
Zr	233	238	235	240	286	247	136	112
Hf	6.39	6.58	6.66	6.76	7.74	5.92	3.65	2.91
U	0.97	0.94	0.94	0.91	0.80	0.79	3.19	2.16
Th	3.76	3.79	3.66	3.52	3.60	2.74	10.68	9.19
La	23	28.5	31.5	22.3	21.1	19.9	39	27.7
Ce	52.37	61.21	73.26	50.04	49.22	45.09	75.76	50.49
Pr	7.03	8.20	9.75	6.77	6.70	6.29	8.22	5.30
Nd	30.06	35.58	41.49	29.14	28.8	27.8	27.41	17.48
Sm	7.14	8.49	9.63	6.84	7.08	6.79	4.03	2.70
Eu	1.11	1.37	1.58	1.20	1.59	1.12	0.79	0.55
Gd	7.91	9.04	9.62	7.75	8.62	7.56	3.09	2.56
Y	51.32	60.26	53.36	51.77	53.72	53.74	18.66	26.13
Tb	1.33	1.47	1.56	1.31	1.49	1.26	0.47	0.45
Dy	8.857	9.73	9.64	8.54	9.91	8.2	2.97	3.3
Ho	1.91	2.11	2.06	1.88	2.08	1.75	0.63	0.83
Er	5.90	6.64	6.32	5.85	6.52	5.39	2.08	2.89
Tm	0.89	1.01	0.96	0.89	1.00	0.80	0.33	0.52
Yb	6.21	6.98	6.60	6.32	7.04	5.64	2.37	3.87
Lu	0.96	1.08	1.03	0.99	1.08	0.86	0.40	0.68
Sc	8.4	7.6	7.5	7.4	8.6	10.2	2.5	4.7
V	2.9	6.4	7.6	7.2	<0.8	<0.8	12	19.2
Cr	42	43	39	23	21	27	18	10
Co	1.36	1.67	1.59	1.7	0.32	1.01	5.11	0.86
Ni	1.1	1.6	1	1.3	1	1.5	6.9	1.6
Cu	3.1	1.8	1.7	2.2	1.4	12.8	6.1	3.6
As	0.7	<0.7	<0.7	<0.7	<0.7	<0.7	1.6	0.7
Mo	2.04	2.4	2.16	1.29	1.03	4.06	5.84	0.58
Ag	<0.2	<0.2	<0.2	<0.2	<0.2	<0.2	<0.2	<0.2
Sn	2.07	1.48	1.61	1.6	1.96	2.37	0.78	0.74
Sb	0.07	0.04	<0.04	<0.04	<0.04	0.04	0.07	0.09
W	0.16	0.21	0.34	0.18	0.78	0.18	0.4	0.58
Pb	1.85	2.3	1.82	2	2.58	4.14	26.9	5.93
Bi	<0.02	<0.02	<0.02	<0.02	<0.02	0.04	0.03	0.06
Au	<0.002	<0.002	<0.002	<0.002	<0.002	<0.002	0.002	<0.002

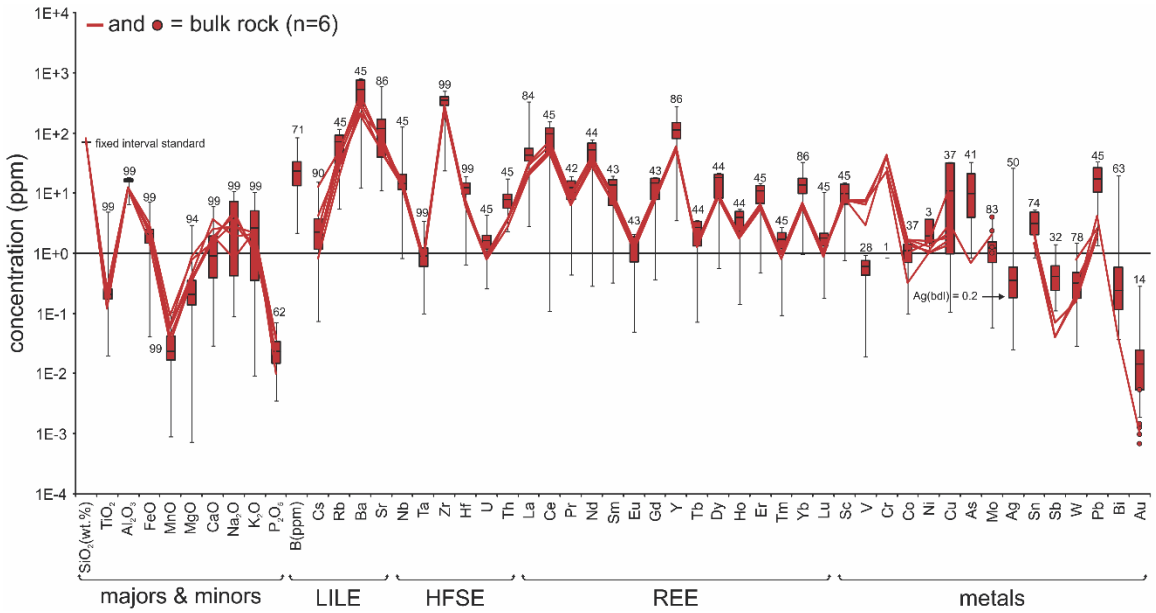

Figure 16: Box-whisker plot of unit 2.0 SMI and bulk rocks major and trace element concentrations. Shown are the 1st and 3rd quartile ranges, averages, and error bars of major and minor oxides, LILE, HFSE, REE, and metals of unit 2.0 SMI (n = 99). Concentrations of oxides and elements were collected by LA-ICP-MS. Numbers above each box-whisker represent the number of SMI analyses for each corresponding element or oxide. Bulk rock data (n = 6) overlay the box-whisker symbols for comparison and were collected from six corresponding SMI-bearing samples. Only the SMI values for V are significantly lower than the bulk rock values. Many SMI values are higher than the bulk rock values, including Zr, Hf, U, Th, La, Y, Er, Yb, As, Sb, Pb, Bi, and Au. All bulk rock Ag values were below detection limit (bdl = 0.2 ppm).

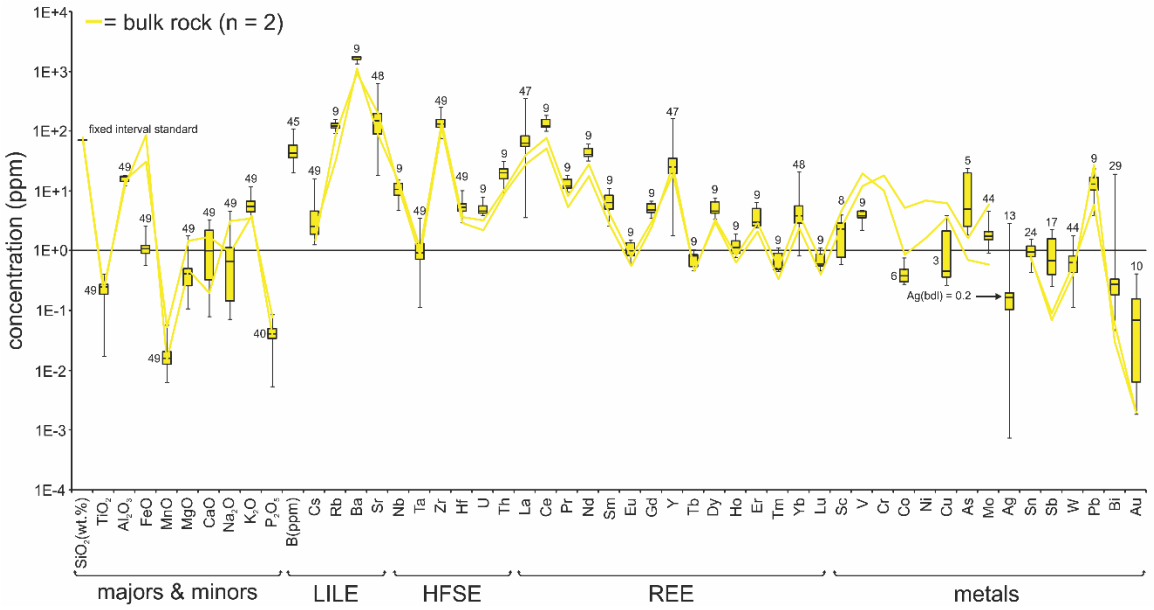

Figure 17: Box-whisker plot of unit 5.3 SMI and bulk rocks major and trace element concentrations. Shown are the 1st and 3rd quartile ranges, averages, and error bars of major and minor oxides, LILE, HFSE, REE, and metals of unit 5.3 SMI (n = 49). Concentrations of oxides and elements were collected by LA-ICP-MS. Numbers above each box-whisker represent the number of SMI analyses for each corresponding element or oxide. Bulk rock data (n = 2) overlay the box-whisker symbols for comparison and were collected from two corresponding SMI-bearing samples. Several SMI values are lower than the bulk rock values, including FeO, Na_2O, Sc, V, Co, and Cu. Many SMI values are higher than the bulk rock values, including K_2O, U, Th, La, Ce, Nd, Gd, Dy, As, Sb, Bi, and Au. All bulk rock Ag values were below detection limit (bdl = 0.2 ppm).

Table 7: Compositions of units 2.0 and 5.3 SMI analyses

	Unit 2.0 SMI			Unit 5.3 SMI		
	average	range	n	average	range	n
TiO_2 (wt%)	0.2	0.02 - 1.89	99	0.2	0.02 - 0.40	49
Al_2O_3	16.2	6.5 - 19.2	99	16.3	12.2 - 18.6	49
FeO	2.2	0.04 - 6.3	99	1.1	0.6 - 2.6	49
MnO	0.03	0.001 - 0.17	99	0.02	0.006 - 0.058	49
MgO	0.3	0.001 - 1.36	94	0.5	0.1 - 1.8	49
CaO	1.4	0.03 - 14.8	99	1.3	0.08 - 3.31	49
Na_2O	3.9	0.09 - 9.6	99	1.0	0.07 - 4.63	49
K_2O	2.7	0.01 - 6.3	99	6.5	3.5 - 12.1	49
P_2O_5	0.03	0.003 - 0.3	62	0.04	0.005 - 0.085	40
B (ppm)	27.3	2.2 - 188	71	49.5	20.6 - 108	45
Cs	3.2	0.1 - 16	90	3.5	1.3 - 16.2	49
Rb	66	6 - 150	45	125	93.4 - 160	9
Ba	579	12 - 1884	45	1634	1334 - 1787	9
Sr	130	11 - 502	86	180	18.2 - 627	48
Nb	15.8	0.8 - 36	45	10.7	4.7 - 15.2	9
Ta	1.0	0.1 - 8.4	99	1.1	0.1 - 3.5	49
Zr	354	24 - 1318	99	140	76 - 255	49
Hf	12.6	0.6 - 40	99	5.6	3.1 - 10.3	49
U	1.6	0.3 - 3.6	45	5.2	3.9 - 8.0	9
Th	7.8	2.3 - 20.4	45	20.4	9.5 - 31.4	9
La	42.8	2.8 - 129	84	76.7	3.6 - 356	47
Ce	89.2	0.1 - 250	45	137	101 - 184	9
Pr	11.9	0.4 - 35.7	43	13.7	9.7 - 18.6	9
Nd	49.9	0.3 - 140	44	45.0	32 - 62	9
Sm	12.7	0.3 - 38.7	43	6.8	2.6 - 11.1	9
Eu	1.3	0.05 - 3.07	43	1.1	0.6 - 1.5	9
Gd	14.0	0.4 - 43.8	43	5.1	3.5 - 6.8	9
Y	114	3.5 - 273	86	29.3	2 - 164	47
Tb	2.4	0.1 - 7.4	44	0.8	0.5 - 1.0	9
Dy	16.4	0.6 - 46.9	44	5.3	3.5 - 7.8	9
Ho	3.7	0.1 - 11.3	44	1.3	0.8 - 1.9	9
Er	10.5	0.5 - 27.4	45	3.9	2.5 - 6.4	9
Tm	1.6	0.1 - 3.3	45	0.7	0.4 - 1.1	9
Yb	13.8	1.0 - 28.8	86	4.4	0.8 - 20.7	48
Lu	1.7	0.2 - 3.1	45	0.7	0.5 - 1.1	9
Sc	11.7	0.8 - 51.9	45	2.1	0.6 - 4.0	8
V	1.0	0.1 - 11.4	27	3.9	2.3 - 4.8	9
Cr	0.8	0.8 - 0.8	1	< 7.8a	N/A	1
Co	1.1	0.1 - 2.3	37	0.4	0.3 - 0.8	6
Ni	2.8	1.0 - 5.4	3	< 14.4a	N/A	1
Cu	22.0	0.1 - 167	35	1.5	0.3 - 3.9	3
As	18.0	0.9 - 113	41	10.7	1.8 - 24.1	5
Mo	1.2	0.1 - 3.4	83	1.8	0.9 - 4.7	44
Ag	1.1	0.02 - 16.1	50	0.4	0.001 - 2.87	13
Sn	4.4	0.9 - 28.4	74	1.0	0.4 - 1.6	24
Sb	0.6	0.1 - 3.9	32	1.0	0.3 - 2.3	17
W	0.4	0.03 - 3.1	78	0.6	0.1 - 1.8	44
Pb	27.3	1.3 - 207	45	13.5	3.9 - 24.0	9
Bi	1.3	0.04 - 42.3	63	0.3	0.05 - 0.78	20
Au	0.033	0.002 - 0.27	14	0.120	0.002 - 0.415	10

[xx]Represents measured isotope; data is not only for the indicated isotopebut for the total element.

[a]Lowest detection limit for specified element.

Note: Anomalously high Cu values of unit 2.0 (n = 2) are not counted as they are due to the presence of metal rich accidentally trapped phases.

Notably, there are large ranges in unit 2.0 SMI concentrations (up to two orders of magnitude) of B, Cs, REE, Sc, V, Cu, As, Mo, Ag, W, Bi and Au (Figure 16), and many elements have higher concentrations in unit 2.0 SMI than in the bulk rock analyses (Zr, Hf, U, Th, La, Y, Er, Yb, As, Sn, Sb, Pb, Bi, and Au; Figure 16). However, bulk rock concentrations of Cs, Sr, Nb, Ta, Sc, Co, Ni, Cu, Mo, and W are equal, or show similar ranges to those in the SMI (Figure 16). Concentrations of V and Cr in unit 2.0 SMI are lower than the bulk rock (Figure 16). All bulk rock Ag values are below detection limit (i.e., bdl = 0.2 ppm; Figure 16).

Almost all elements measured in unit 5.3 SMI have concentration ranges of less than one order of magnitude, except for La, Y, Ag, Bi, and Au which have ranges of up to two orders of magnitude (Figure 17). The following groups of elements and metals for unit 5.3 have higher concentrations in SMI than bulk rock: REE, As, Sn, Sb, Bi, and Au (Figure 17). Concentrations of major and minor oxides (with the exception of FeO), LILE, HFSE, Mo, W, and Pb are equal, or show similar ranges, in the SMI compared to bulk rock (Figure 17). Concentrations of Sc, V, Co, and Cu for unit 5.3 SMI are lower than the bulk rock (Figure 17). All bulk rock Ag values are below detection limit (i.e., bdl = 0.2 ppm; Figure 16).

2.3.4 Composition of quartz-hosted accessory apatite

Apatite was analyzed because it is an abundant co-entrapped phase, and it was straightforward to also analyze to gain additional information about the magmatic reservoir. Apatite is a common mineral phase identified in SMI (as an accidentally trapped

phase, showing variable phase proportions) and was identified by transient “spikes” in Ca, P, LREE, and U isotope count rates within, but distinct (offset) from, the melt signal (Figure 13I - J, and O - P). The Ca signal from apatite small grains can be obscured by the Ca within the melt fraction, whereas P is present in the melt fraction at much lower concentration so P was used as an identifier for accidental apatite inclusions. Quartz phenocryst-hosted apatite grains, free of melt, were also identified as isolated grains in the vicinity of SMI and recognized in LA-ICPMS signals by coincident, increased count rates in Ca, P, Mn, Sr, REE, U and Th (Figure 13C - D). Table 8 summarizes LA-ICPMS analyses of the apatite included in quartz (free of melt), providing data that is relevant to the interpretation of the source and evolution of the silicate melt which is unambiguously coeval, based on the observations of co-entrapment (Figure 8M – R). Note that some anomalously high Ti values in the apatite data are due to small needles of rutile included in the analytical volume. Other less common accessory minerals identified as accidentally-trapped phases, also relevant to petrogenetic modelling, are allanite and zircon (Figures 8Q – S, and 13E - F).

Table 8: LA-ICP-MS analyses of trace elements in quartz-hosted apatite inclusions, Bousquet Formation

Sample	^{47}Ti(ppm)	^{56}Fe	^{55}Mn	^{59}Co	^{62}Ni	^{65}Cu	^{75}As	^{88}Sr	^{89}Y	^{90}Zr	^{137}Ba	^{139}La	^{140}Ce	^{141}Pr	^{146}Nd	^{147}Sm	^{153}Eu	^{157}Gd	^{159}Tb	^{163}Dy	^{165}Ho	^{166}Er	^{169}Tm	^{172}Yb	^{175}Lu	^{208}Pb	^{232}Th	^{238}U	Sum REE
unit 5.3																													
711-7200...																													
...(2)-p2-ap1	<202	<2955	396	<26.5	<1893	<109	<544	1170	2351	<11.6	<51.6	210	918	175	1123	291	27.6	351	50.0	376	88.7	193	35.0	166	19.7	33.8	71.8	10.5	3974
...(2)-p3-ap1	304	5907	660	<1.60	<97.7	<4.45	<29.4	1009	1606	35.7	149	1691	4087	528	2167	369	42.0	367	51.1	342	65.9	180	24.6	143	18.7	42.9	43.3	14.2	10024
...(2)-p4-ap1	<6.73	2076	1109	<0.81	<49.4	411	43.7	839	790	<0.18	<1.63	1817	4414	556	2389	426	40.3	336	39.7	190	34.2	79.5	9.42	53.7	7.14	12.7	41.6	<0.13	10351
...(3)-p1-ap1	<83.9	2272	1418	<11.2	<716	29.1	<168	622	602	125	313	763	1916	212	897	131	21.6	121	15.9	99.2	24.3	65.1	6.02	46.6	7.47	63.1	18.1	7.80	4310
...(3)-p2-ap1	<25.2	5288	644	<4.24	<233	27.2	<58.9	1291	1081	23.9	74.0	872	2150	283	1231	275	25.5	234	34.0	200	42.1	105	13.1	84.3	11.0	219	30.3	8.13	5526
...(3)-p3-ap1	<4.75	4511	919	<0.70	<37.1	3.68	37.4	1104	1833	67.3	<1.11	2608	6127	742	2877	504	50.0	424	54.9	325	64.2	174	22.1	124	16.1	78.4	224	11.8	14057
...(3)-p4-ap1	<13.7	5402	661	<2.32	<116	<6.35	<25.8	1023	1403	31.4	119	2181	4958	615	2465	416	39.2	349	44.4	258	53.1	139	18.2	107	15.8	40.3	51.3	10.3	11614
...(3)-p6-ap1	<20.4	<153	597	4.62	<177	34.6	<32.7	919	984	0.80	26.9	402	1336	198	1074	234	22.9	240	29.8	168	37.1	93.0	11.7	80.6	9.72	68.9	22.6	6.40	3905
...(3)-p5-ap1	986	2033	513	<5.18	<253	35.9	<53.1	1410	1281	8.03	147	1771	4564	630	2523	432	23.2	382	41.8	248	49.4	124	15.0	83.6	12.4	101	42.4	9.86	10858
...(3)-p7-ap1	2319	7327	559	<2.72	<125	48.2	<26.7	963	1315	<0.84	508	163	527	91.6	494	147	14.0	219	31.6	199	42.9	112	13.7	79.3	9.08	30.4	10.6	2.32	2111
3215-161-493...																													
...(7)-p2-ap1	<6.88	1801	321	<0.93	<47.7	<2.80	<12.4	172	1195	2.16	<2.81	118	336	68.9	469	198	18.9	254	36.9	232	50.7	134	19.5	119	14.4	45.2	27.3	8.00	2033
...(7)-p1-ap1	1933	19197	677	1.16	<11.1	<0.55	45.8	298	1156	88.9	895	2422	5763	713	2858	447	42.5	341	43.3	241	48.3	145	23.6	172	23.2	40.9	56.9	21.9	13239
unit 2.0																													
731-9061-u2...																													
...(4)-p3-ap1	n.a.	7482	652	0.338	<11.3	2.18	21.7	232	5666	n.a.	<0.41	978	3123	577	3436	1107	100	1436	205	1221	235	600	67.3	359	44.3	4.83	16.9	4.49	13283
...(4)-pB-ap1	2733	3211	519	1.04	<37.2	6.70	20.3	268	7112	<0.31	174	1014	3875	668	3882	1298	112	1811	249	1527	300	777	91.2	476	57.7	17.4	28.0	7.89	15888
...(4)-pB-ap2	1057	<393	238	<4.99	<236	<12.6	<47.6	345	10107	39.9	23.2	1554	5266	973	5918	1881	160	2580	362	2130	417	1058	118	638	85.0	<4.95	44.0	9.30	22781
...(4)-pC-ap1	553	3250	492	<5.28	<265	<11.9	<55.4	855	10865	186	<9.10	1651	5776	1092	6710	2169	172	2837	411	2469	479	1192	129	676	100	21.9	47.7	9.75	25452
...(4)-pE-ap1	621	31207	919	4.58	<15.1	82.2	32.7	463	7349	40.6	327	1339	4252	762	4489	1406	119	1834	267	1627	307	778	84.0	455	57.1	11.9	34.5	7.00	17508
...(4)-pF-ap2	97.8	1036	611	<1.01	<46.4	<2.95	26.6	240	8656	33.0	22.4	1206	3867	710	4327	1351	112	1891	270	1693	332	896	104	533	70.2	9.75	26.2	6.26	17092
...(4)-pF-ap1	<6.28	3177	622	1.99	<62.8	13.9	31.4	292	8209	45.7	120	1319	4280	789	4734	1466	112	2043	283	1707	330	856	92.5	477	60.7	9.69	27.2	5.06	18267
...(3)-p1-ap1	<1.45	724	600	<0.21	<10.7	<0.56	22.1	183	5950	9.76	14.4	994	3153	577	3438	1115	96.1	1427	203	1247	237	621	71.1	387	47.6	4.25	15.7	3.97	13411
...(3)-p2-ap1	2244	<268	<35.0	<4.28	<200	<10.3	<36.2	195	7548	31.4	<7.08	697	2417	443	2540	926	83.7	1513	240	1466	289	730	77.3	402	48.9	<3.54	13.0	5.15	11635
...(3)-p3-ap1	<1.79	497	395	<0.31	<14.5	5.83	17.9	269	5553	15.5	7.68	887	2875	523	3167	1056	78.3	1370	196	1167	221	561	61.7	320	38.5	6.46	13.0	3.25	12326
...(3)-p3-ap2	<1.20	1024	413	<0.22	<9.40	0.87	25.7	279	7066	22.9	3.03	1119	3576	673	4076	1350	102	1772	252	1513	287	721	78.7	408	50.2	8.84	19.2	4.51	15726
...(3)-p3-ap3	773	6192	445	<1.57	<66.5	<3.89	25.2	369	7403	25.0	63.0	1023	3166	590	3346	1094	95.3	1537	226	1477	286	777	87.5	475	59.0	23.2	13.7	5.89	14012
...(3)-p4-ap1	<38.5	1065	375	<6.76	<309	<18.1	<52.0	438	6517	10.9	92.9	454	1985	416	2851	1155	92.4	1644	233	1375	259	657	77.7	404	44.6	21.0	14.6	3.29	11414
...(3)-p5-ap1	<27.2	2411	217	<4.77	<219	<11.2	<32.9	385	8094	36.8	375	1113	4012	746	4546	1418	97.8	1936	281	1659	312	794	91.3	478	56.0	7.41	34.8	7.34	17259
...(3)-p6-ap1	<10.9	<89.7	281	<1.80	<79.4	<4.70	18.4	239	4810	9.94	<3.66	693	2304	416	2500	829	67.6	1068	165	962	192	500	57.6	305	41.5	3.77	15.6	2.64	9935
...(3)-p7-ap1	<23.7	5212	799	<3.98	<184	34.6	31.1	353	6205	16.3	<2.14	828	2724	505	3162	1048	80.1	1437	208	1275	240	638	74.6	382	52.3	4.98	19.1	4.60	12444
3086-29-278...																													
...pA-ap1	140	4274	433	<3.17	<180	10.9	<66.6	125	3321	4.76	203	282	1252	262	1702	587	30.9	810	117	744	147	388	44.2	230	26.0	10.7	13.3	2.77	6505
...pB-ap1	173	958	410	0.220	<11.1	<0.46	37.9	74.4	3756	26.8	103	300	1225	260	1703	627	41.7	914	139	866	175	454	50.7	290	37.2	52.8	10.1	3.49	6944
...pD-ap1	856	2037	568	<16.79	<1002	43.5	<243	92.8	2762	47.9	244	162	786	148	1146	432	18.8	719	87.7	500	119	279	35.9	197	26.9	17.0	9.18	<2.40	4570
...pE-ap1	5554	<256	234	<2.89	<147	<9.01	<45.1	63.7	2618	<0.65	<5.18	287	952	154	1080	386	20.0	577	84.4	558	114	326	40.6	225	29.4	<2.93	11.4	1.49	4749
3086-29-282.7...																													
...pA-ap1	<49.7	<355	456	<7.04	<371	<18.5	<64.5	34.6	3535	2.94	<6.87	343	1375	265	1689	619	27.1	760	110	622	138	343	41.3	245	32.1	<4.39	10.6	1.94	6498
...pB-ap1	2097	144	541	<2.00	<103	108	17.9	42.8	3163	64.8	<2.67	381	1184	201	1216	414	20.8	610	86.5	552	113	304	35.0	198	27.6	4.94	8.00	2.58	5256
3086-29-188.5...																													
...p10-ap1	n.a.	957	763	<0.96	<59.8	<5.42	<29.4	195	1511	n.a.	24.1	170	719	146	1036	406	15.6	531	80.8	491	89.8	211	23.0	124	15.1	41.9	7.20	1.92	3977
...p10-ap2	n.a.	7070	1261	<0.76	<47.0	<3.99	74.6	214	3244	n.a.	24.3	1118	3536	577	3228	915	66.6	1071	156	930	184	471	52.6	294	36.6	53.4	17.4	5.96	12477
...p11-ap1	n.a.	2970	534	<0.76	<47.1	<4.50	40.0	258	3318	n.a.	25.7	850	2484	433	2495	743	44.0	959	140	882	170	457	49.9	283	35.5	73.6	17.0	3.82	9885
...p12-ap1	n.a.	776	593	0.180	3.03784	<0.33	10.5	496	3092	n.a.	53.9	274	1014	203	1364	522	33.5	786	122	770	154	396	44.8	241	30.1	9.57	10.9	3.19	5834
...p13-ap1	n.a.	2365	499	<0.21	<20.0	2.29	42.9	212	2920	n.a.	100	1185	3552	570	3127	822	42.9	927	131	759	143	362	42.1	203	33.2	78.3	14.6	3.95	11768

2.3.5 Composition of rehomogenized SMI

The goal of homogenization experiments was to characterize the volatile chemistry of the melt, to assess homogenization temperature as it relates to minimum entrapment T, and to determine the SiO_2 content of the melt as an internal standard for LA-ICP-MS data reduction. Three different homogenization approaches were applied: (i) 1 atm heating stage brought to a maximum temperature of 1345°C at a heating rate of 10 - 30°C/min; (ii) three high pressure-temperature piston cylinder experiments (Experiment 1: t = 72 hours, T = 900˚C; and P = 3 kbar; Experiment 2: t = 120 hours, T = 950˚C and P = 5 kbar; Experiment 3: t = 72 hours, T = 950˚C, and P = 3 kbar); and (iii) one rapid quench MHC cold-seal pressure vessel experiment at 950˚C and 1500 bar for 36 hours.

Initial homogenization experiments using a high T microthermometric stage were performed on a phenocrystic quartz hosted SMI. This showed a first phase change (onset of melting) at ~692°C (Figure 18D) with a mottled appearance distinct at ~785°C consistent with an increase of the silicate liquid proportion in the inclusion (Figure 18E). Microfractures began to develop in the quartz host at 1345°C and melting of the quartz in the inclusion wall between 1050˚C and 1345˚C was observed with no closure of the bubble, precluding determination of the homogenization T (Figure 18G - I). Interestingly, the inclusion selected for measurement also contained a distinct, and volumetrically significant, CO_2 phase (L_{CO2} + V_{CO2}) at room T (Figure 18A).

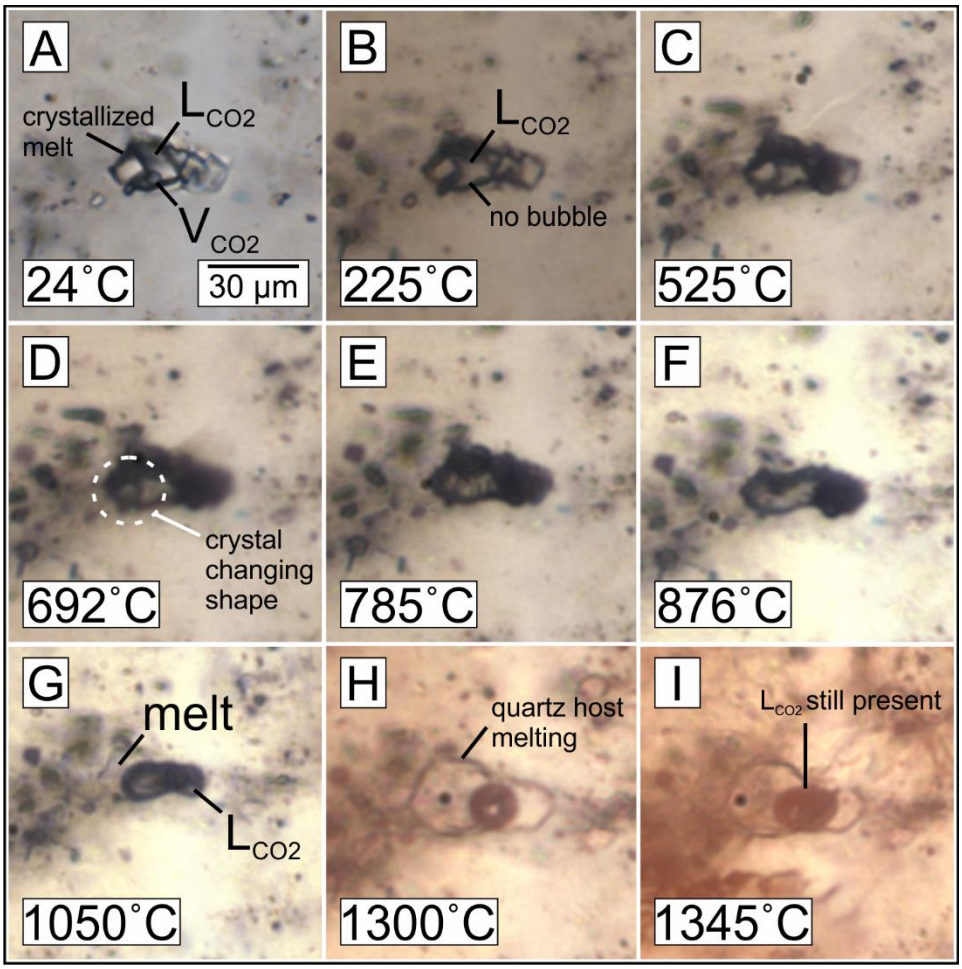

Figure 18: Microthermometry of Bousquet Formation SMI. Plane polarized light microphotographs of a unit 4.3 quartz-hosted SMI during progressive heating stages. **(A)** There is liquid CO_2 and a vapour CO_2 bubble at 24°C in a crystallized melt inclusion. **(B - D)** Progressive heating resulting in the SMI undergoing a phase change at 692°C; the phase (white dotted circle) became darker and changed shape; this was the first sign of melting in the inclusion. **(E - F)** A mottled texture appeared at 785°C, indicating an increase in liquid present in the inclusion. **(G)** Separation of a CO_2 phase from the liquid melt. **(H - I)** At 1330°C, the quartz host began to melt as is evidenced by the expansion of the SMI cavity; subsequent micro fractures developed in the quartz host making it difficult to calculate the total homogenization of the inclusion.

The final T before terminating the experiment (1345°C) is far too high for homogenization of a hydrous granitic SMI (Bodnar and Student, 2006), suggesting that water must have been lost from the melt during heating by diffusion or through microcracks (Student and Bodnar, 1996; Bodnar and Student, 2006), and/or that the CO_2 phase was heterogeneously trapped with melt. If related to water loss, the melting temperature of the inclusion would increase because water lowers the solidus and liquidus. In addition, the isochoric nature of the inclusion was lost because fractures formed and the host melted (i.e., the inclusion volume changed, and the bubble got larger). The larger bubble required a higher T to force it to shrink. This process of melting, fracturing, and bubble expansion feeds back on itself and the homogenization T is never reached (see Figure 18H). Alternatively, if the CO_2 is accidentally trapped as an immiscible phase in the SMI, it cannot dissolve entirely in the melt because it has a saturated (free) volatile phase and not an original melt component, so no realistic amount of heating will homogenize this CO_2 phase.

After the initial microthermometric heating experiment on unit 4.3 SMI to observe melting behavior, alternative homogenization methods (piston cylinder, and MHC pressure vessel) were used that prevent decrepitation and volatile loss (Student and Bodnar, 1996; Bodnar and Student, 2006) with the focus on units 2.0 and 5.3 because they were also the units that produced substantial LA-ICP-MS compositional data sets (Appendix 2). Inclusions in quartz phenocrysts, hand-picked from unit 2.0 and unit 5.3 were recovered from high P-T experimental capsules and analyzed by laser Raman microspectroscopy. The heated phenocrysts contained numerous homogenized SMI suitable for analysis,

containing a transparent (glassy) to translucent (finely crystalline, devitrified?) solid phase and bubble/s (maximum ~ 5 μm diameter) at room T (Figure 19). The glassy portion of the homogenized SMI had very low H_2O contents (Figure 19A). The bubble phases vary in total bubble phase proportion from inclusion to inclusion, showed commonly two phases within them, a liquid phase, and a vapour phase that exhibited Brownian motion. Laser Raman microspectroscopy confirmed that the bubbles in the SMI of both units contained CO_2 liquid and CO_2 vapour (Figure 19B). Representative Raman spectra of the vapour phases in homogenized SMI (by piston cylinder) show characteristic peaks for CO_2 and minor CO_3^{-2}, N_2, and CH_4 (Figure 19B), while spectra of the homogenized glass show absent or low magnitude peaks of water bands (Figure 19C). The distribution of some species/compounds contained within a homogenized SMI are shown in Figure 20.

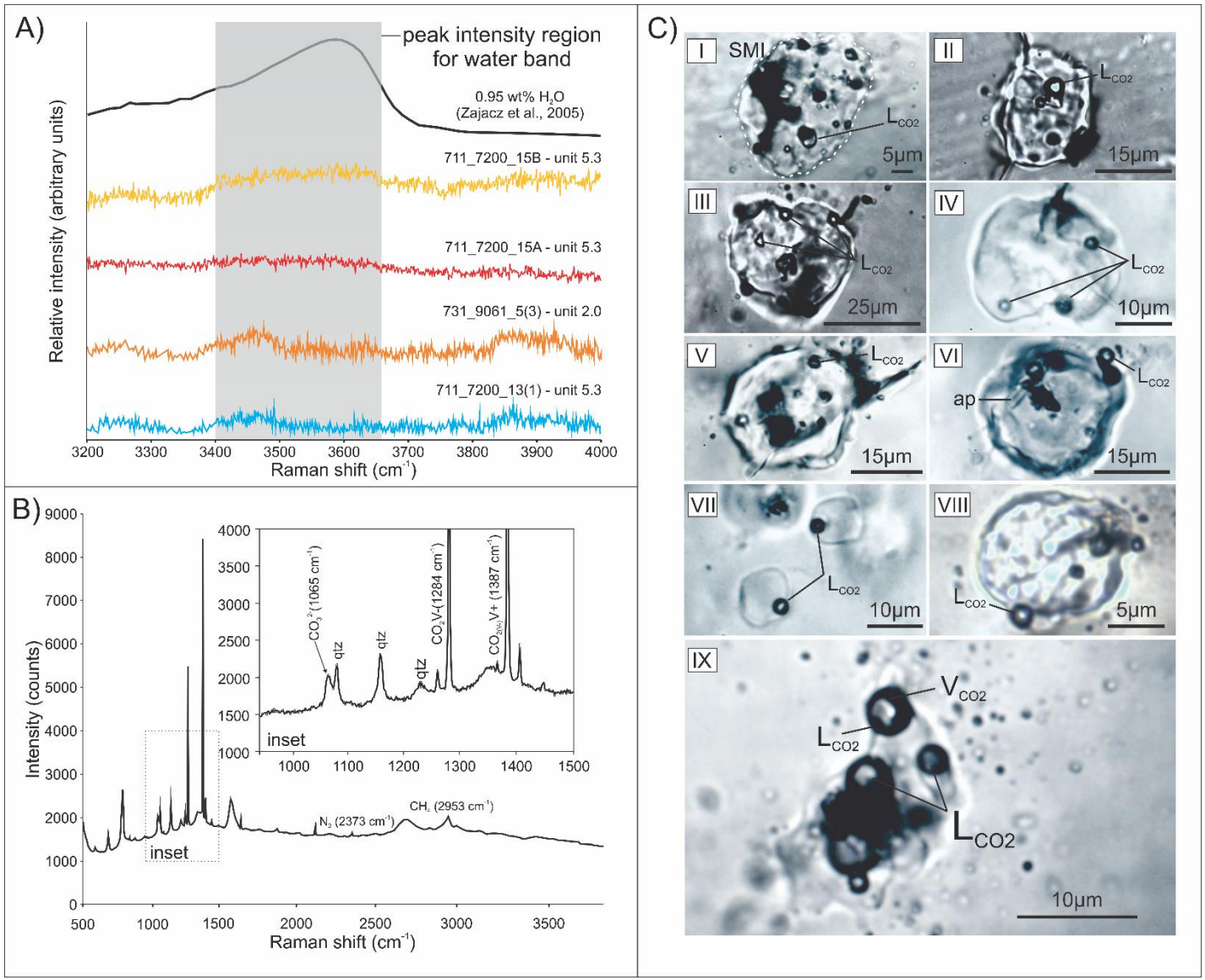
A)
peak intensity region for water band
0.95 wt% H2O (Zajacz et al., 2005)
711_7200_15B - unit 5.3
711_7200_15A - unit 5.3
731_9061_5(3) - unit 2.0
711_7200_13(1) - unit 5.3
Relative intensity (arbitrary units)
Raman shift (cm-1)
B)
Intensity (counts)
inset
CO3 2-(1065 cm-1)
qtz
qtz
qtz
CO2V-(1284 cm-1)
CO2V+ (1387 cm-1)
N2 (2373 cm-1)
CHx (2953 cm-1)
Raman shift (cm-1)
C)
I SMI
LCO2
5μm
II
LCO2
15μm
III
LCO2
25μm
IV
LCO2
10μm
V
LCO2
15μm
VI
ap
LCO2
15μm
VII
LCO2
10μm
VIII
LCO2
5μm
IX
VCO2
LCO2
LCO2
10μm

Figure 19 (previous page): Petrography and Raman spectra of CO_2-rich and H_2O-poor homogenized SMI of the Bousquet rhyolites. Raman spectra of bubbles and glass or devitrified glass from homogenized SMI of Bousquet volcanics. Intensity measured in counts and Raman shift in cm^{-1}. **(A)** Baseline corrected Raman spectra from units 2.0 and 5.3 SMI displaying water band peak areas. Water peak with 0.95 wt% H_2O is from Zajacz et al. (2005). Spectra 711_7200_15A and B are from analyzed glass of the homogenized SMI in Figure 20. **(B)** Raman spectrum displaying peaks of quartz and CO_2. **(C-I to C-IX)** Transmitted PPL images of partially homogenized quartz-hosted SMI from the unit 5.3 surface sample; bubbles contain CO_2 liquid (L_{CO2}) and vapour (V_{CO2}) as determined by laser Raman spectroscopy.

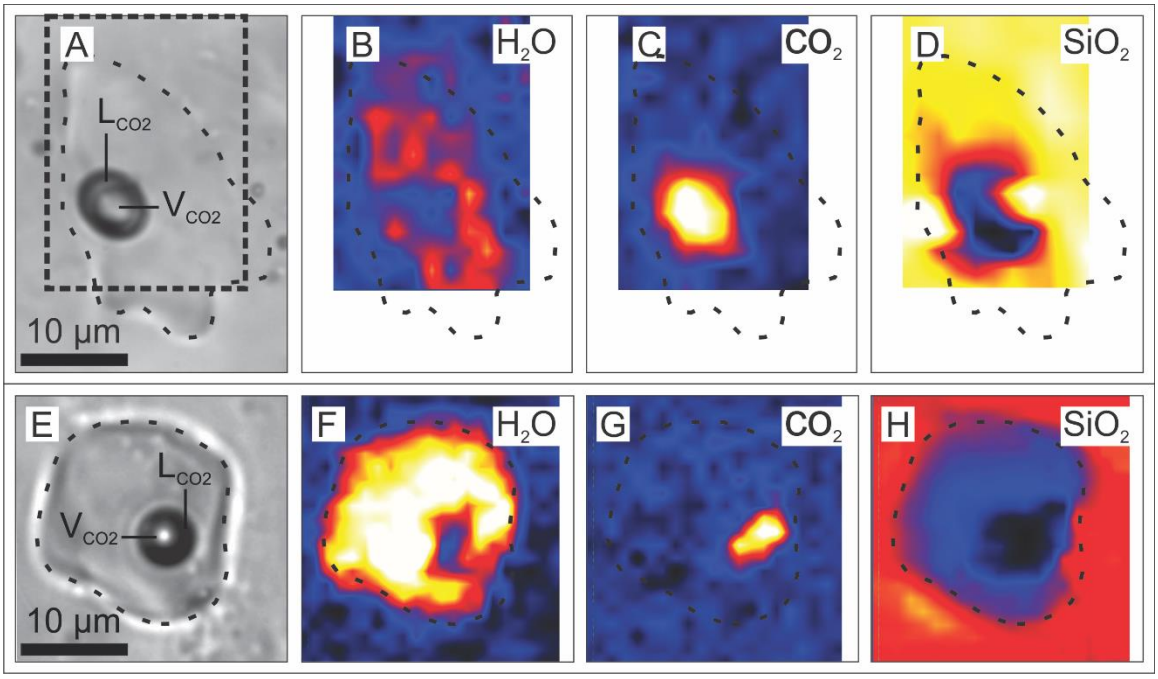

Figure 20 (previous page): Raman maps of a homogenized SMI from unit 5.3. The mapped areas for H_2O, CO_2, SiO_2 are based on intensity ranges 3450-3650 cm^{-1}, 1385-1390 cm^{-1}, and 450-475 cm^{-1}, respectively. **(A)** PPL image of a homogenized SMI with a large liquid and vapour CO_2 bubble in glass. **(B - D)** Intensity distribution of H_2O, CO_2, and SiO_2 in the homogenized SMI and surrounding host quartz. **(E)** PPL image of a homogenized SMI with a large liquid and vapour CO_2 bubble in glass. **(F - H)** Intensity distribution of H_2O, CO_2, and SiO_2 in the homogenized SMI and surrounding host quartz.

Homogenized SMI analyses (from MHC pressure vessel experiments) for unit 2.0 can be found in Table 9. Compositional data for SMI from unit 2.0 bracket the SiO_2 content between 79.2 and 74.6 wt% (Table 9). Assuming that this compositional range may still slightly overreport SiO_2 due to incorporation of excess silica from the host quartz, and loss of some H_2O, the LA-ICP-MS data (Appendix 2) were reduced using an internal standard value of 70 wt% SiO_2. The worst-case scenario in terms of uncertainty of this assumption is that the trace element LA-ICP-MS data are within ~10% relative of their true values. To illustrate the difference in calculated trace element values based on the chosen internal standard for LA-ICP-MS (i.e., 70 wt% SiO_2) and a higher value of internal standard of 79.2 wt% SiO_2, calculations were done in SILLS at each value. For example, in inclusion 7 in sample 711-7200-U5.3 (phenocryst 4; Appendix 2B), at 70 wt% SiO_2 the calculated concentrations of Mo and Au are 1.15 and 0.15 ppm, respectively; using a value of 79.2 wt% SiO_2 concentrations of Mo and Au are 1.3 and 0.17 ppm, respectively.

Table 9: SEM-EDS analyses of homogenized SMI from unit 2.0 (T = 950˚C and P = 1500 bar, 36 hours)

Component	731-9061-1(U2.0)	731-9061-4(U2.0)	731-9061-5(U2.0)	731-9061-6(U2.0)	731-9061-9(U2.0)	731-9061-12(U2.0)
SiO_2(wt%)	79.18	74.58	77.83	77.19	77.66	78.64
Al_2O_3	11.15	14.35	11.90	10.54	11.61	11.08
CaO	0.35	0.57	0.21	0.32	0.54	0.54
FeO	0.95	1.21	bdl	2.40	1.77	1.65
MgO	0.26	bdl	0.20	0.20	bdl	bdl
Na_2O	2.96	4.66	3.60	3.35	4.32	4.29
K_2O	4.65	4.63	4.90	5.44	3.43	3.56
Cl	0.50	0.02	1.36	0.55	0.71	0.34
Total	100	100.02	100	99.99	100.04	100.1

Note: bdl = below detection limit.

The water bands in the Raman spectra from homogenized SMI (via MHC pressure vessel) in units 2.0 and 5.3 have maximum peak intensities that are an order of magnitude or lower than in hydrous (2.5 – 5 wt% H_2O) melt inclusions reported in felsic systems (Zajacz et al., 2005) and in some inclusions, no water peak was recognized at ~3500 cm^{-1}. A semi-quantitative estimate of the water content of the SMI of units 2.0 and 5.3 using the approach of Zajacz et al., (2005) indicates << 0.5 wt% H_2O (C. Dalzell, communication, 2020). Consequently, whereas the water content (5%) originally applied to the LA-ICP-MS calculations is too high, determining an internal standard value (SiO_2 wt%) from homogenized SMI using SEM-EDS (rather than by EEMP) was appropriate considering not only how small the inclusions are, but also the similarity anticipated between anhydrous (SEM) and hydrous (EMP by difference) composition determination. (Figure 19C).

Many SMI contained refractory mineral phases that did not melt completely in larger inclusions. For example, Fe was commonly under-reported due to the presence of Fe-oxide phases along inner walls of the inclusions that were not included in spot analyses of the glass. (Table 9). Because it is likely that only some of the quartz that had precipitated naturally along the wall of the SMI was remelted back into the SMI during homogenization, it was initially thought that the rastering approach (i.e., including quartz host slightly beyond the boundary of the SMI) would ensure all quartz grown along the wall of the cavity would be included in the analytical volume. However, rastered and area analyses of SMI by SEM-EDS over-reported silica because the analytical volumes included minor quartz host surrounding the SMI. This led to other elements being under-reported. Consequently,

spot analyses were used, and it should be noted that SiO_2 is probably slightly overreported in the homogenized inclusions.

2.3.6 Titanium in host quartz

Quartz phenocrysts are saturated in rutile (Figure 8C, E, and F). Thus, the Ti content has the potential to provide a constraint on the temperature of entrapment of quartz, confirming the T of entrapment from piston cylinder and MHC vessel of at least 900˚C at 3 kbar (piston cylinder, run time = 72 hours) and 950 ± 10˚C at 1500 ± 50 bar (MHC, run time = 36 hours). Concentrations of Ti in quartz phenocrysts from units 2.0, 4.3, and 5.3 were measured by LA-ICP-MS (Table 10; Appendix 3A, B, and C). The Ti values are not contaminated by rutile grains because the final concentrations obtained for each unit had narrow ranges indicating the laser beam was not hitting large rutile needles, but rather the quartz itself. Concentrations were implemented into the equations of the Ti-in-quartz thermometer from Thomas et al. (2010). The activity of Ti was assumed to be 1 based on the presence of rutile in the quartz. However, the rutile may have been exsolved from the quartz; thus, it was not saturated when the quartz crystallized. Therefore, additional calculations with a Ti activity of 0.7 (due to saturated ilmenite in SMI) were completed and presented in a PT diagram (see Section 2.4.7). Pressures used for the T calculation are based on robust barometry for the MIC rocks (Neyedley et al., 2021). The calculations yielded T values consistent with crystallizing conditions for the MIC Phases B and C (i.e., 6.5 – 13.5 kbar) which were established through Ti-in-zircon and Ti-in-quartz thermometry (Neyedley et al., 2021). This P constraint assumes that the phenocrysts of quartz grew in the same magma chamber as the MIC zircons. Unit 5.3 quartz phenocrysts (n = 83) have

an average Ti concentration of 113 ppm (1σ = 21.8 ppm) corresponding to a crystallization temperature of 686˚C (1σ = 25.6˚C) at 6.5 kbar and 848˚C (1σ = 29.9˚C) at 13.5 kbar and $a_{TiO2} = 1$; unit 4.3 quartz phenocrysts (n = 39) have an average Ti concentration of 268 ppm (1σ = 79.8 ppm) corresponding to a crystallization temperature of 785˚C (1σ = 36.5˚C) at 6.5 kbar and 964˚C (1σ = 42.7˚C) at 13.5 kbar and $a_{TiO2} = 1$; and unit 2.0 quartz phenocrysts (n = 182) have an average Ti concentration of 83.4 ppm (1σ = 21.3 ppm) corresponding to a crystallization temperature of 653˚C (1σ = 33.2˚C) at 6.5 kbar and 809˚C (1σ = 38.8˚C) at 13.5 kbar and $a_{TiO2} = 1$ (Table 10). The Ti concentrations of unit 4.3 are highly variable with a 1σ of 79.8 ppm, which could mean the quartz has been altered so the data was omitted from tables dan figures.

Table 10: Summarized LA-ICP-MS analyses of titanium in quartz.

	Titanium (ppm)			T (°C) at 6.5 kbar		T (°C) at 13.5 kbar	
	Average	1σ	n	Average	1σ	Average	1σ
Unit 2.0	83.4	21.3	182	653	33.2	809	38.8
Unit 5.3	113	21.8	83	686	25.6	848	29.9

Note: $a_{TiO2} = 1$

2.4 Discussion

2.4.1 Preservation and origin of SMI

Quartz phenocrysts in unit 2.0 (rhyolitic sills) and 5.3 (quartz rhyolite flow) contain the only unambiguous and well-preserved (based on petrographic characteristics) SMI of the Bousquet Formation volcanics (Figure 8C - L). The SMI are associated with growth zones (observed rarely; Figures 8D and 12G), so they have been trapped in the growing quartz phenocrysts at any number of stages (e.g., in the staging magma chamber at depth, as they rose through the crust, and/or as the magmas were extruded as flows or injected as subvolcanic sills/dykes). However, the SMI analyzed are tied to growth zones not in the outermost rims of the phenocrysts (Figure 9D), and therefore, they are interpreted to have been trapped considerably earlier than actual host flow or sill emplacement, prior to eruption (cf. Anderson et al., 2000). The SMI analyzed are well preserved, showing no physical signs of being impacted by deformation, decrepitation, or alteration. They are recrystallized or partly recrystallized due to post-entrapment slow cooling and devitrification (Frezzotti, 2001; Figure 8K - L), but show no decrepitation haloes or radial cracks, contain primary igneous daughter minerals, and occur in remnant magmatic quartz domains in the phenocrysts, based on CL analysis (Figures 10C and 11K).

The SMI are not secondary in origin because they cluster in assemblages in the centre of phenocrysts (Figure 8D) and/or along growth zones (Figure 9D) away from the edges of phenocrysts, rather than in cross-cutting trails along healed fractures near the edge of the grains (Roedder, 1984; Frezzotti, 2001; Abersteiner et al., 2019). Hot CL and SEM-CL

was conducted on quartz phenocrysts from unit 2.0 (Figures 10C – D, M - N, 12C – D, and G - H) and unit 5.3 (Figure 11C – D, G – H, and K – L) to confirm if the quartz retained magmatic compositional provenance or if it was recrystallized and overprinted by a metamorphic event. Bodnar and Student (2006) note that SMI can be altered through chemical diffusion during post-solidus processes. For example, it is possible for H and H_2O to diffuse out of the SMI, while trace elements simultaneously enter the inclusion from the surroundings (Bodnar and Student, 2006).

Cathodoluminescence imaging can be used to assess the extent of recrystallization, resorption, dissolution, and reprecipitation as well as solid state diffusion related chemical changes in quartz (Götze et al., 2001). The intensity and colour of CL fluorescence in quartz are proportional to the concentration of Ti which correlates with the temperature of crystallization in quartz containing rutile (Wark and Spear, 2005; Rusk et al., 2006; Spear and Wark, 2009). Visible CL luminescence colours in magmatic quartz are long-lived, deep violet to blue, whereas greenschist to amphibolite facies metamorphic quartz is generally brown-red (Götze et al., 2001). Phenocrysts from units 2.0 and 5.3 show distinct blue CL luminescence in the core of the phenocrysts confirming that the quartz is magmatic (Figures 10D & N, 11D, H, & L, and 12D & H).

The hot CL images of quartz phenocrysts indicate that most of the quartz grains have not been pervasively altered and preserve remnant magmatic domains (Figure 11D & L). Some phenocrysts have large isolated fractures that show the red CL coloration (characteristic of metamorphism; e.g., Figure 11A – D). These areas of re-equilibrated quartz tend to occur as extensive networks of rimming and fractures on/through magmatic

quartz domains. There are rare cases of dark stringers or zones cut across bright areas of quartz grains (Figure 12D). The compositional boundaries between light CL and dark CL areas are sharp. Some phenocrysts are quite damaged and show CL patterns with mottling and corroded edges (Figures 10C, M, and 12C); in some cases, there are only small light grey spots remaining (Figure 11K). It is clear that the quartz phenocrysts have been recrystallized and hydrothermally modified in the areas that have mottling patterns and corroded edges (Figure 12C - D; Frelinger et al., 2015). These features, likely formed at sub-solidus conditions associated with hydrothermal alteration and would affect the composition of proximal SMI (Bodnar and Student, 2006). Smaller quartz phenocrysts may be more easily altered/recrystallized. Overall, the CL luminescence (blue, red, and non-luminescent quartz) in the samples indicate at least two different generations of quartz.

Most phenocrysts that host SMI do not show primary zoning (Figure 12G and H) and where observed it is weakly visible suggesting that the phenocrysts were in equilibrium with their host melt during prolonged crystallization. Primary zoning is related to varying abundances of lattice defects or activator ions and may represent trace element variations on the parts per million scale (Watt et al., 1997; Götze, 2012). The phenocrysts in this study may have crystallized slowly enough to allow trace elements that are cathodoluminescence activators to diffuse evenly in the crystal. This is important because it suggests that P-T conditions were stable, and residence times were long for the phenocrysts during their growth, and supports the idea that the SMI were trapped at depth rather than during transit/emplacement/eruption (Matthews et al., 2012). Alternatively, lack of primary zoning could be the consequence of metamorphism (Sittner and Götze, 2018). If the

phenocrysts were heated back up in a metamorphic environment to amphibolite grade conditions, the CL-activating elements that show primary zoning could have redistributed evenly throughout the grains destroying the primary zoning. However, hot CL images indicate that most quartz phenocrysts still carry the characteristic deep, long-lived blue of magmatic quartz (Figures 10 D, N, 11D, L, and 12D, H,) as opposed to the purple to reddish-brown colour of metamorphic quartz (Figure 11H).

Generally, the phenocrysts containing analyzed SMI do not show an abundance of secondary features, like "spider" dissolution-reprecipitation fractures or extensive rimming/creeping replacement that would suggest a pervasive incursion of hydrothermal fluids (Rusk et al., 2008a; Rusk et al., 2008b; Frelinger et al., 2015). This strengthens the argument that the SMI analyzed are unmodified and isolated from the external surroundings after entrapment (Schiano, 2003).

The majority of unit 5.3 phenocrysts incorporated melt and partially crystallized melt to form type III (hourglass) inclusions (Figure 11C and G), and some phenocrysts have areas of reddish CL luminescence or are non luminescent suggesting alteration/re-equilibration to some extent (Figure 11H). Type III (hourglass) inclusions have very dark (non-luminescent) SEM-CL characteristics (Figure 11A - C and E - G). However, analyzed SMI occur within the fresh parts of the phenocrysts, as shown by the corresponding grey scale SEM-CL images and hot CL images (Figures 10C – D, and 11I - L). The majority of SMI have thin, dark haloes (in SEM-CL) around their edges which could reflect quartz precipitated on the inclusion walls after entrapment (Figure 10C - D; Frezzotti, 2001).

2.4.2 Mineralogy of SMI

Analyses of the SMI by LA-ICP-MS, when combined with SEM data for homogenized and unhomogenized inclusions and petrographic observations, can clarify if the mineral phases contained in the SMI are true daughter phases (Figure 8K – L), accidentally trapped solids (Figure 8H), or formed via the down-temperature re-equilibration of enclosed silicate melt with the host quartz (Halter et al., 2002a; Zajacz and Halter, 2007). In this study, SMI commonly contain secondary mineral phases (e.g., ankerite, calcite, siderite, magnetite, pyrite/pyrrhotite in type III inclusions; Figure 10Q - S) that are inconsistent with expected liquidus phases in a felsic magmatic system, and/or primary phases with unusually high or variable mineral volumetric proportions (e.g., K-feldspar, calcic plagioclase, muscovite, biotite, zircon, apatite, ilmenite in types I/II/III inclusions; Figure 10G - J) not in appropriate phase proportions expected for crystallization magma aliquots. For example, SMI containing accidentally trapped K-feldspar and/or muscovite result in very high K contents in the quantified LA-ICP-MS analyses. For this reason, analyses of many SMI were eliminated from the final dataset. Likewise, LA-ICP-MS signals yielding unusually high Ca, Mg, and/or Fe were rejected as they were shown to contain accidentally-trapped plagioclase or oxides, or alteration carbonates (type III).

The variability in melt:mineral proportions due to accidentally trapped phases also causes difficulties in homogenization experiments. Melt inclusions containing large accidentally trapped mineral phases do not homogenize completely to a liquid at the same temperature as SMI with little to no accidentally trapped minerals (Student and Bodnar, 2004) and resulted in many (~90%) of the SEM analyses being rejected. This is generally

consistent with the results of other studies that homogenized felsic SMI to study their compositions (Student and Bodnar, 2004).

Examination of LA-ICP-MS transient signals allow the mineralogy of SMI to be clarified, at least partly, after analysis. For example, SMI from the Bousquet rhyolites usually contain K-feldspar, muscovite and plagioclase as major crystallized phases (Figure 13A – B). This can be seen in decoupled signal intensities for ^{39}K and ^{23}Na/ ^{44}Ca peaks in the inclusions (Figure 13B). Apatite, zircon, biotite and ilmenite (Table 5) are also recognizable in spectra from specific combinations of elements whose isotope intensities vary proportionally with one another. For example, apatite can be recognized from coincident Ca, P, U, Th, Sr and Mn signals, with or without a coentrapped melt proportion (Figure 13C – D). In type III (hourglass-related) inclusions, poly-minerallic assemblages containing muscovite with carbonate and allanite are distinguished in the LA-ICP-MS signals and differentiate these from type I/II inclusions (Figure 13E – F).

Many SMI with accidentally trapped mineral grains show distinct parts of the LA-ICP-MS signal that are melt-related at the start and/or end of inclusion signal (e.g., elevated ^{93}Nb and ^{39}K at the start of the signal in Figure 13F). Again, such signals had to be rejected from the final data set as it was clear that accidental entrapment of solids had occurred. Some type I/II inclusions also contain accidentally trapped metal-rich phases (sulfides?) that can be differentiated from sulfides present in type III inclusions based on composition. The occasional Cu-As-Ag-Bi-rich phases in type I/II SMI may have been saturated primary phases (Figure 13H) whereas other sulfides (e.g., pyrite) that occur in type III inclusions are likely post-solidus and formed during alteration/mineralization of the volcanics.

Type I/II SMI are distinguished from matrix/hourglass and mineral inclusions because they have characteristically consistent mineralogy after crystallization (see Figure 8K – L for an example; Severs et al., 2009). Preliminary identification of viable SMI in quartz phenocrysts is done by simply noting the optical properties of the solid phases in the SMI and comparing their proportions to each inclusion in the assemblage. For example, many SMI of unit 2.0 contain a greenish semi-opaque phase, a translucent phase, a yellowish high relief phase, and a small dark phase (Figure 8K – L) that occur in equal proportions from inclusion to inclusion. In addition to melt, hourglass, and mineral inclusions, Bousquet quartz phenocrysts have SMI co-entrapped with apatite, zircon, allanite, and monazite (Figures 8M – S and 11N).

The mineral assemblages of SMI, hourglass inclusions, and matrix rock were distinguished by systematically comparing their SEM-BSE data (Figures 10, 11, and 12B & F). The SMI, hourglass, and matrix assemblages share common minerals like biotite, K-feldspar, plagioclase, muscovite, ilmenite, and zircon (Figures 10E – J, O – T, and 11J, M - O; Table 5). However, the composition of muscovite in SMI is very low in Mg and Fe as compared to muscovite in the matrix and hourglass inclusions, meaning they are of different origins. There may also be a rim of post-entrapment authigenic quartz crystallization on the inclusion walls, which is evidenced by the textural difference seen in CL (i.e., halos around SMI; Figure 10C and D; Götze et al., 2001; Danyushevsky et al., 2002; Pettke et al., 2004). However, the LA-ICP-MS methods used in the present study accounted for the crystallization of host mineral on the inclusion walls by ablating and

analyzing the entire SMI and host mineral rim, and by using internal standardization for the quantification of SMI (Pettke et al., 2004).

The most abundant minerals in all types of inclusions are muscovite, plagioclase (An = 10 – 30%), and K-feldspar (orthoclase) which gives the inclusions bulk compositions that resemble a feldspar with elevated counts of Al_2O_3, SiO_2, K_2O, Na_2O, and CaO (Figure 13; Appendix 2). The assemblages are very similar which is not surprising because the matrix crystallized from the same melt preserved in SMI (Schiano, 2003). Schiano (2003) noted that melt inclusions sample small volumes of the parental liquids at intermediate steps in the evolution of the magma. Melt inclusion compositions are simply representations of discrete points on the liquid line of descent for the host rock (Fedele et al., 2003). This shows that SMI, in general, do not have very different minerals than the matrix (Figure 10G – J versus Q – T); their mineral assemblages are very similar even with the matrix having some modification by metamorphism (Veksler et al., 1998).

The SEM-EDS analyses of homogenized SMI revealed that they contain Cl (Table 9). This is a distinguishing characteristic of a melt because Cl does not diffuse out of SMI and it only degasses out of a melt at shallow pressure, well after H_2O and CO_2 (Spilliaert et al., 2006a; Le Voyer et al., 2014; Manzini et al., 2017). Even though allanite contains Cl and was a saturated phase at the time of melt entrapment (Figure 8S), the homogenized SMI do not show high P and REE so the Cl would not be from an accidentally trapped apatite.

2.4.3 Compositional classification of SMI

Figure 21 shows the SMI compositional data in conventional chemical discrimination diagrams that allow IUGS classification of the melt composition and tectonic discrimination (Harris et al., 1986; Le Bas et al., 1986; Pearce et al., 1984; Pearce, 1996; Ross and Bédard, 2009). Based on SEM-EDS data from homogenized SMI, the unit 2.0 and 5.3 magmas are classified as rhyolitic (Figure 21A, circles) consistent with the IUGC classification of these rocks noted in previous literature (Mercier-Langevin et al., 2007b, c, 2009; Wright-Holfeld et al., 2010; Galley and Lafrance, 2014; Yergeau et al., 2015) and the whole rock compositions (Figure 21A, squares). In Figure 21A, SMI show higher Na_2O + K_2O contents than the bulk rock analyses. Figure 21B - F utilize large ion lithophile element (LILE) and high field strength element (HFSE) abundances to provide a tectonic discrimination of the SMI compositions. Bulk rock data are also shown in the diagrams, for comparison. There are less data points for Figure 21A compared to the other frames because there was less data collected for SEM-EDS of homogenized SMI than for LA-ICP-MS of non-homogenized SMI.

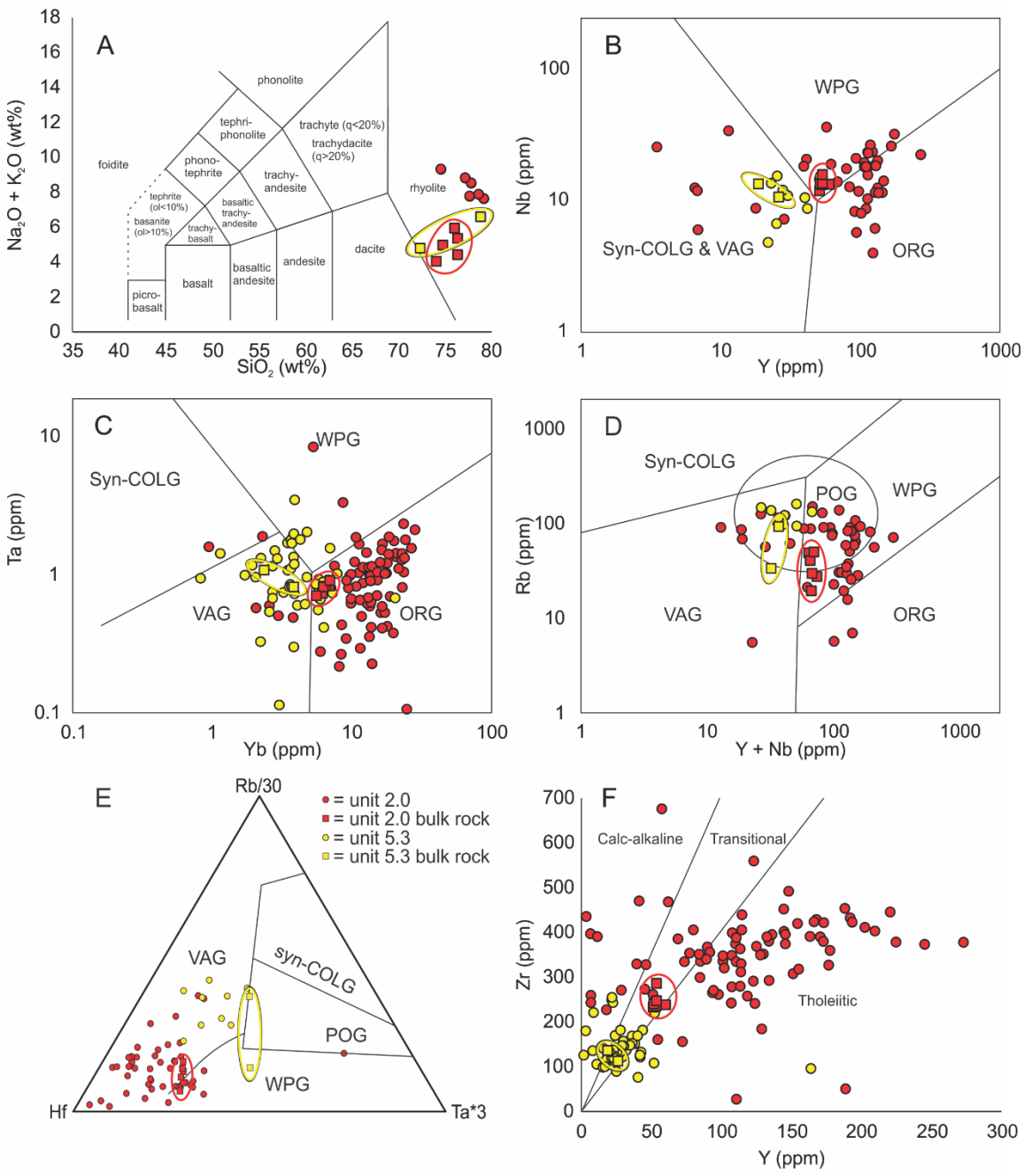
A
phonolite
tephri-phonolite
trachyte (q<20%)
trachydacite (q>20%)
foidite
phono-tephrite
trachy-andesite
rhyolite
tephrite (ol<10%)
basanite (ol>10%)
basaltic trachy-andesite
trachy-basalt
dacite
basaltic andesite
andesite
basalt
picro-basalt
Na2O + K2O (wt%)
SiO2 (wt%)
B
WPG
Syn-COLG & VAG
ORG
Nb (ppm)
Y (ppm)
C
WPG
Syn-COLG
VAG
ORG
Ta (ppm)
Yb (ppm)
D
Syn-COLG
POG
WPG
VAG
ORG
Rb (ppm)
Y + Nb (ppm)
E
Rb/30
= unit 2.0
= unit 2.0 bulk rock
= unit 5.3
= unit 5.3 bulk rock
VAG
syn-COLG
POG
WPG
Hf
Ta*3
F
Calc-alkaline
Transitional
Tholeiitic
Zr (ppm)
Y (ppm)

Figure 21 (previous page): Rock type and tectonic affinity discrimination diagrams showing compositional classifications of SMI and bulk rock analyses. Bulk rock data are circled and show considerably less scatter in composition than SMI compositions. (**A)** Total alkalis-silica rock type classification diagram from Le Bas et al. (1986); unit 2.0 SMI and bulk rock compositions plot in the rhyolite field; SMI data is from SEM-EDS analyses of homogenized SMI. (**B)** Nb vs. Y diagram from Pearce et al. (1984); the majority of unit 2.0 SMI plot in the within-plate granitoid (WPG) and ocean ridge granitoid (ORG) fields with some scatter into the syn-collisional granitoid (Syn-COLG) and volcanic arc granitoid (VAG) fields, whereas unit 5.3 SMI plot more strictly within the Syn-COLG and VAG fields. (**C)** Ta vs. Yb diagram from Pearce et al. (1984); similar to (B), the majority of unit 2.0 SMI plot in the ORG field with some scatter, whereas unit 5.3 SMI also show considerable scatter but plot dominantly in the VAG field. (**D)** Rb vs. (Y + Nb) diagram from Pearce (1996); similar to (B) and (C), the majority of unit 2.0 SMI plot in WPG and post-orogenic granitoid (POG) fields, whereas unit 5.3 SMI plot in the VAG field with some scatter into the POG field. **(E)** Rb/30-Hf-Ta x 3 ternary diagram from Harris et al. (1986); in this diagram, both units 2.0 and 5.3 SMI plot largely in the VAG field, with unit 5.3 SMI also in the WPG field. (**F)** Zr vs Y diagram from Barrett and MacLean (1993); unit 2.0 SMI plot mainly in the in the tholeiitic field with a very wide compositional range, but also scatter into the calc-alkaline and transitional fields, whereas unit 5.3 SMI are concentrated mainly in the in the transitional field.

Two major points are noted in these discrimination diagrams: (i) the spread in SMI compositions is much larger than that of the bulk rock data; and (ii) the SMI compositions of both units indicate a transition from an anorogenic to an orogenic tectonic setting from unit 2.0 (lower Bousquet Formation) to unit 5.3 (upper Bousquet Formation). To the first point, there is a tendency for SMI from one unit to record different compositions; whereas bulk rock analyses will show limited compositional range (De Vivo and Bodnar, 2003; Badanina et al., 2004). Scatter is inevitable with SMI data because melt inclusions are trapped in phenocrysts at various points in the evolution of a magma; therefore, variability is expected in the composition of the trapped melt even in a single unit if the host phenocryst grew over a long period (Badanina et al., 2004). Unit 2.0 bulk rock data cluster in single fields in each discrimination plot (Figure 21B – D), but the SMI data are clearly concentrated in both the within plate granite (WPG) and ocean ridge granites (ORG) fields depending on which trace elements are plotted (Figure 21B – D). Unit 5.3 bulk rock data also cluster in a single field [volcanic arc granites (VAG); Figure 21B - D] whereas the majority of SMI compositions are in the VAG field (Figure 21B – E) with some scatter into the ORG and WPG fields (Figure 21C). Some of the scatter seen in the diagrams must reflect small, accidentally trapped mineral grains (Nielsen et al., 1997; Créon et al., 2018). However, the main reason for the compositional spread in SMI from each unit is suggested to be primary differentiation processes during SMI entrapment.

The second major point noted in Figure 21 is the transition from an anorogenic to an orogenic tectonic setting. This evolution is consistent with that of a back-arc basin setting where volcanism is first caused by crustal extension and mantle diapirism below a thickened arc crust and later by subduction processes and differentiation in midcrustal

magma chambers (Mercier-Langevin et al., 2007c; Galley and Lafrance, 2014; Yergeau, 2015). Subduction-related magmas contaminated by continental crust are characteristic of the upper Bousquet Formation based on bulk rock geochemical studies at the LaRonde Penna Mine according to Mercier-Langevin et al. (2007c). This implies a mature arc setting. In particular, unit 5.3 is the most evolved (i.e., most felsic) and most strictly VAG-related (calc-alkaline) unit of the camp. It forms part of the 20 North lens hanging wall (the largest ore lens in the DBL camp) and part of the 20 South lens footwall at the LaRonde Penna mine, and also hosts part of (and overlies) the Bousquet 2 deposit (Mercier-Langevin et al., 2007b). Furthermore, unit 5.3 is also part of the hanging wall that contains the small VMS ore lenses at the Westwood Mine (Mercier-Langevin et al., 2009; Yergeau et al., 2015).

The setting of magma generation transitioned from a tholeiitic spreading ridge environment to a collisional subduction environment over time (Galley and Lafrance, 2007, 2014; McNicoll et al., 2014; Mercier-Langevin et al., 2007c, 2009, 2017). The bulk rock analyses for unit 2.0 cluster in the transitional, ORG, and WPG fields, but the SMI data are much more spread out in the tholeiitic, transitional, calc-alkaline, ORG, WPG, and VAG fields (Figure 21B - F). Together, the unit 2.0 and 5.3 SMI data show evidence for ORG and VAG origins, respectively. Whereas the transition from dominantly anorogenic to orogenic affinity (i.e., lower member to upper member transition of the Bousquet Formation; Mercier-Langevin et al., 2007c) is supported by these data, SMI compositions, in particular unit 2.0, spread between the compositional fields (Figure 21B – D, and F), consistent with sampling of liquids in phenocrysts at different times, transitioning from extensional to convergent tectonics (Davidson et al., 2005). This variation in the source

environment for magmas, as well as evidence of the variability due to processes such as assimilation and mixing as the magmas ascend through the lithosphere (Davidson et al., 2005), are not typically evident (or not as evident) in the spread of whole rock data from a single lithology. In some diagrams (Figure 21B-D, F), the SMI data are consistent with bulk rock analyses, differentiating the anorogenic nature of unit 2.0 from the orogenic nature of unit 5.3, but the extent of SMI compositional scatter is not reflected in the bulk rock data. The SMI provide a less ambiguous discrimination than the bulk rock data.

Unit 2.0 is relatively deep in the footwall and its tholeiitic nature, plus its $(La/Yb)_{CN}$ and Zr/Y ratios, makes it more akin to the Hébécourt Formation that underlies the Bousquet Formation which suggest a common source (Mercier-Langevin et al., 2007c). This unit may mark the start of the transition from the tholeiitic volcanism to the calc-alkalic magmatism in the upper member of the Bousquet Formation to which much of the ore is associated (Mercier-Langevin et al., 2007c). The spread in SMI data from ORG/WPG to VAG fields supports this transitional nature of unit 2.0 SMI (Figure 21B - F). It is unclear, however, if this mix of geochemical affinities is due to contamination by hydrous magmas and/or assimilation of Nb- and Ta-depleted rocks, or from subduction-related processes (Mercier-Langevin et al., 2007c).

Further discrimination of the SMI compositions and their host rocks involved the use of an SMI Ba-Rb-Sr granite discrimination diagram of El-Bouseily and El-Sokkary (1975; Figure 22). Barium is the most abundant of the three elements, relatively (Figure 22). Unit 5.3 SMI compositions fall into the “normal” granite field (Figure 22). The associated bulk compositions fall in the “normal” granite and anomalous granite fields (Figure 22). Unit 2.0 SMI compositions show a much wider range in classification with more than half of

the analyses in the “normal” granite field and the rest in the anomalous granite, granodiorite and quartz diorite, and diorite fields (Figure 22). Half of unit 2.0 bulk rock analyses fall in the anomalous granite field, while the rest are in the “normal” granite, and the granodiorite and quartz diorite fields (Figure 22). Thus, in general bulk rock classifications in this diagram coincide to SMI compositions. Those anomalously high Sr analyses leading to the spread to dioritic classifications reflects the removal of plagioclase during magma evolution (El-Bouseily and El-Sokkary, 1975). Furthermore, the diagram shows that the melts (and rhyolitic rocks) are not highly evolved as they do not plot near the Rb apex of the ternary (i.e., not strongly differentiated).

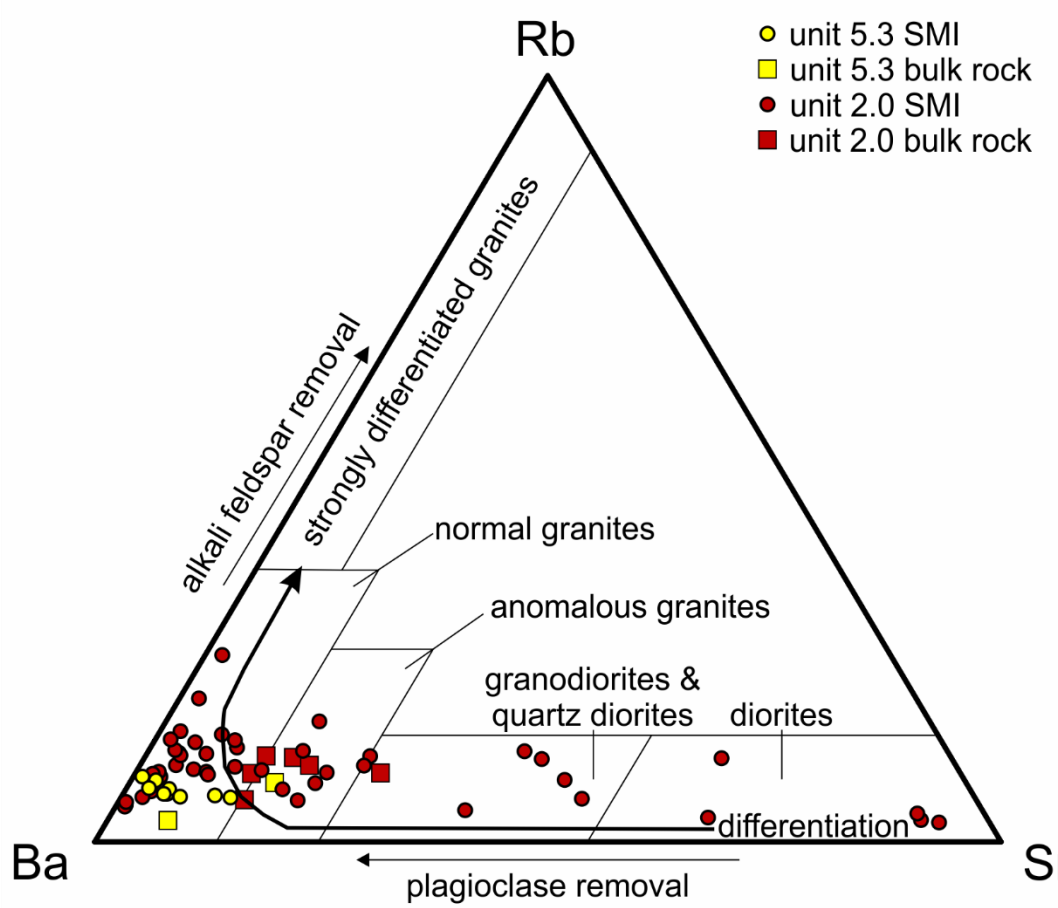

Figure 22: Rubidium-strontium-barium ternary granitoid classification diagram showing units 2.0 and 5.3 SMI and bulk rock compositions. (A) All unit 5.3 SMI analyses are in the normal granite field (n = 9), and the bulk rock analyses are split between the normal granite field (n = 1) and the anomalous granite field (n = 1). More than half of unit 2.0 SMI are in the normal granite field (n = 27), while the rest are in the anomalous granite field (n = 8), the granodiorite and quartz diorite field (n = 5), and the diorite field (n = 5). Half of unit 2.0 bulk rock analyses are in the anomalous granite field (n = 3), while the rest are in the normal granite field (n = 2) and the granodiorite and quartz diorite field (n = 1; modified from El-Bouseily and El-Sokkary, 1975).

The felsic rocks of units 2.0 and 5.3 are Ba-rich and Sr-depleted (Figure 22; El-Bouseily and El-Sokkary, 1975). This is consistent with patterns seen in rocks affected by the fractionation of plagioclase because Sr is incorporated into plagioclase (Martin, 1999; Richards and Kerrich, 2007; Moyen, 2009). There has been relatively much less crystallization of K-feldspar compared to plagioclase (An = 10 – 30%) since Ba is still high and Rb relatively low in the melt (Guo and Green, 1989). When the melt was being trapped in quartz, clearly feldspar fractionation influenced element concentrations locally.

Figure 23A - B show differentiation of post-2.5 Ga TTG and normal volcanic arc rocks (formed by partial melting of the asthenospheric wedge above the subducting slab) from Archean TTG suites and younger adakitic rocks (generated in arc environments by partial melting of the subducting oceanic basaltic crust; Martin, 1999; Richards and Kerrich, 2007). Silicate melt inclusions from units 2.0 and 5.3 are distinct in terms of their relative Sr-Y-La-Yb compositions (Figure 23; Martin, 1999; Richards and Kerrich, 2007; Moyen, 2009). Unit 5.3 SMI have higher Sr/Y and La/Yb ratios than unit 2.0 SMI and show some trending toward the adakitic field, though they still fall *entirely* within the "normal arc" field (Figure 23A, B). The much higher Y, and lower Sr/Y of unit 2.0 SMI suggests that those melts experienced much more plagioclase fractionation than the unit 5.3 magma (Figure 23A; Defant and Drummond, 1990; Defant and Drummond, 1993; Castillo et al., 1999; Richards and Kerrich, 2007). The much higher Yb and lower $(La/Yb)_{CN}$ ratio of unit 2.0 SMI reflects a lack of garnet in the source region for the parental magma of unit 2.0. In convergent margins, the mantle has an eclogitic garnet-bearing composition due to the subduction of Al-rich sediments that undergo dehydration and partial melting, and release Al-rich fluids at high pressure promoting metamorphic reactions that produce garnet

(Dasgupta et al., 2005; Hermann et al., 2006; Kerrick and Connolly, 1998; Molina and Poli, 2000; Poli et al., 2009; Malaspina et al., 2010; Dragovic et al., 2015).

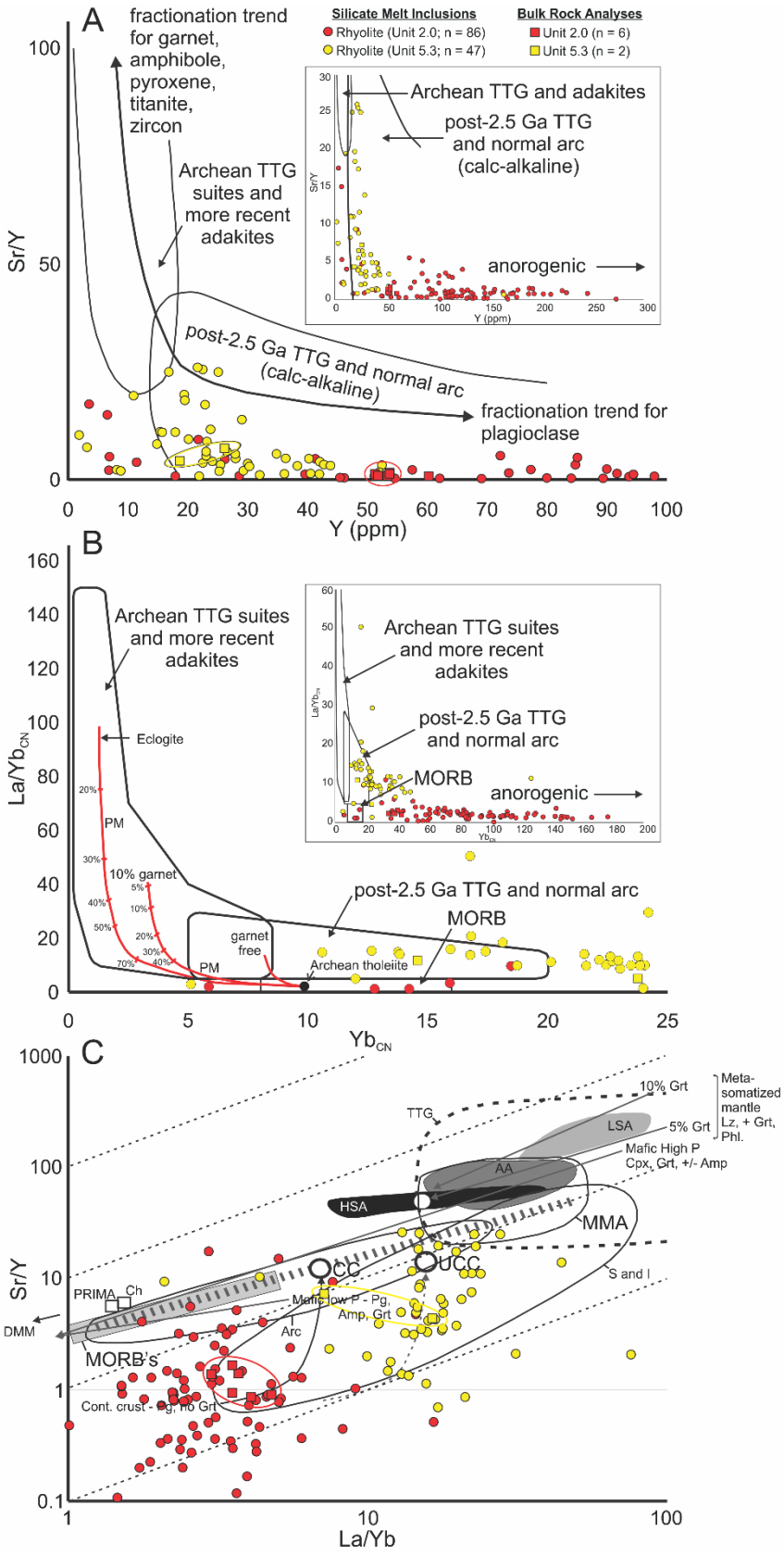
A
fractionation trend for garnet, amphibole, pyroxene, titanite, zircon
Archean TTG suites and more recent adakites
post-2.5 Ga TTG and normal arc (calc-alkaline)
fractionation trend for plagioclase
Sr/Y
Y (ppm)
Silicate Melt Inclusions
Rhyolite (Unit 2.0; n = 86)
Rhyolite (Unit 5.3; n = 47)
Bulk Rock Analyses
Unit 2.0 (n = 6)
Unit 5.3 (n = 2)
Archean TTG and adakites
post-2.5 Ga TTG and normal arc (calc-alkaline)
anorogenic
B
Archean TTG suites and more recent adakites
Eclogite
PM
10% garnet
garnet free
post-2.5 Ga TTG and normal arc
MORB
Archean tholeiite
La/Yb_CN
Yb_CN
anorogenic
C
TTG
LSA
AA
HSA
MMA
OCC
UCC
S and I
10% Grt
5% Grt
Meta-somatized mantle Lz, + Grt, Phl.
Mafic High P Cpx, Grt, +/- Amp
PRIMA
Ch
DMM
MORB's
Arc
Cont. crust - Pg, no Grt
Sr/Y
La/Yb

Figure 23 (previous page): Bousquet formation SMI and bulk rock source magma type discrimination diagrams based on Sr-Y-La-Yb systematics. (A) Sr/Y vs Y discrimination diagram (modified from Richards and Kerrich, 2007) of unit 2.0 and 5.3 SMI and bulk host rocks to SMI-bearing quartz phenocrysts. Roughly 90% of all analyses are in the "normal arc" field. The SMI from the Bousquet formation fall in the field of normal arc compositions, with unit 5.3 melt showing some scatter towards the adakite field whereas unit 2.0 melts scatter to much higher Y and lower Sr/Y ratios consistent with anorogenic settings (ocean ridge granitoids, tholeiites). Bulk rock analyses show a much narrower compositional range but generally fall within the same areas of the diagram. (**B)** Chondrite-normalised $(La/Yb)_{CN}$ vs. Yb_{CN} diagram (modified from Martin, 1999) showing unit 2.0 and 5.3 SMI. Chondritic values from Palme and Jones (2004). Continuous curves represent partial melting of an Archaean tholeiitic source, leaving residues of the following types: garnet free amphibolite, 10% garnet-bearing amphibolite and eclogite. These curves of equilibrium partial melting (PM) were calculated using the equations of Shaw (1970; modified from de Souza et al., 2001). Normal (non-adakitic) volcanic arc and trondjemite-tonalite-granite (TTG) compositional fields are from Hansen et al. (2002), and the mid-ocean ridge basalt (MORB) field is from Van Staal et al. (2009). Melt inclusions in the Bousquet volcanics fall well outside of the compositional field for Archean TTG, and within the field for "normal arc" and extend to much higher Yb_{CN}. (**C)** Sr/Y vs. La/Yb diagram showing discriminatory fields for various melt compositions formed through various source melting scenarios and through mantle/crust interactions (modified after Moyen, 2009). Various melting curves and resulting compositional fields for produced melts are shown: (i) Mafic mantle source, low P (10 kbar) and a garnet-plagioclase-amphibolite residuum; this generates melts below the mantle source array;(ii) Mafic mantle source, high P (20 kbar) melting of a similar source, generating high silicate adakite-like melts; (iii) Metasomatized mantle source (garnet-lherzolite, with 5 or 10% garnet), generating low silica adakites; (iv) Continental crust source (CC-solid curved line with arrow and UCC-dashed curved line with arrow), with a plagioclase-rich residuum. Melt inclusions from units 2.0 and 5.3 are distinct from one another in this diagram, both falling well outside of the field for TTG and most consistent with melts generated by volcanic arc magmas and normal S and I type granites. Compositional fields shown are: AA = Archean adakites, Arc = volcanic arc magmas, CC = continental crust, Ch = chondrite, DMM = depleted mantle, HSA = high silica adakites, LSA = low silica adakites, MMA = metasomatized mantle, MORB = mid ocean ridge basalt, OIB = ocean island basalt, PRIMA = primitive mantle, S and I = normal S and I type granites, TTG = trondjemite-tonalite-granite, UCC = upper continental crust. Mineral and rock type abbreviations: Amp=amphibole; Pg=plagioclase; Grt=garnet; Cpx=clinopyroxene; Lz=lherzholite; Phl=phlogopite.

The lower Y and larger spread in Sr/Y in unit 5.3 SMI compositions (at the border of the adakitic field), suggests that this melt composition was either more influenced by fractionation of other minerals (amphibole, pyroxene, titanite, zircon, garnet) or experienced much less plagioclase fractionation (Moyen, 2009). Generally, this also suggests that the unit 2.0 magma had lower initial water content than unit 5.3 magma (Nekvasil, 1992; Danyushevsky, 2001). As in other discrimination diagrams already discussed, the SMI from both units show a much larger spread in Sr/Y and La/Yb ratios, and Y, Yb abundances than their respective bulk rocks indicating that the SMI record a more extensive magma differentiation history (i.e., prior to eruption/emplacement). Importantly, both the SMI and bulk rocks do not have compositions consistent with Archean TTG magmas when plotted on these diagrams (Moyen, 2009). The presence of muscovite in SMI (Figure 10H & J) also supports the non-TTG classification of the magmas. Unit 5.3 SMI classify in the "normal arc" or post-2.5 Ga TTG field, and the majority of unit 2.0 SMI have compositions consistent with rhyolites in anorogenic settings (rifting and/or hot-spot related; Figure 21C and F; Green and Falloon, 2015).

Figure 23C compares both the Sr/Y and La/Yb ratios which clearly shows the melts fall in the fields of composition of magmas produced by extensive melting of crust (contaminated), and have experienced extensive plagioclase fractionation, and are not recognizable as having adakitic or TTG compositional affinity any longer. This is important because the related (coeval) intrusive system that is the same age (MIC) is considered a TTG complex based on its whole rock geochemistry and petrographic features (Galley and Lafrance, 2014).

2.4.4 Magmatic evolution of the Bousquet Formation rhyolites

In contrast to bulk rock analysis, trace element concentrations in SMI can give reliable information about the melt composition at the time of entrapment and reveal information about its evolution through primary magmatic processes (e.g., differentiation, mixing, saturation of magmatic volatiles; Webster et al., 1995; Chabiron et al., 2001, 2003; Halter et al., 2002a; Heinrich et al., 2003; Gray et al., 2011). Additionally, in volcanic rocks, whereas whole rock compositions may provide information only on the bulk liquid composition at the time of eruption/emplacement, the pre- to syn-eruptive history of fractionation can be preserved in SMI within phenocryst phases in a single rock unit (Roedder, 1992; Frezzotti, 2001).

Normative abundance diagrams show LA-ICP-MS data for units 2.0 (Figures 24A and 25A) and 5.3 (Figures 24B and 25B) SMI compared to their respective bulk rock values, and SMI from two barren arc granites (i.e., Rito del Medio and Cañada Pinabete plutons; Audétat and Pettke, 2003). Data are normalized to upper continental crust (Figure 24; McDonough and Sun, 1995) and primitive mantle (Figure 25; McDonough and Sun, 1995). The normative abundance diagrams illustrate three important points. First, they show that when bulk rock analyses and SMI compositions are compared, while the overall bulk rock abundance patterns mimic the SMI compositions (similar overall slope, and relative enrichments and depletions), there are notable differences: (i) Eu and Sr anomalies are more pronounced in the SMI than in the bulk rock analyses (Figures 24 and 25); and (ii) there is a larger range (by about 1 order of magnitude) in overall concentrations shown by the trace element data for the SMI compared to the bulk rock. For example, the SMI of unit

2.0 have Na_2O and Cs values with ranges of two orders of magnitude while their bulk rock values have a range of one order of magnitude or less (Figures 16 and 17). Overall, there are large ranges in Na_2O, K_2O, Cs, Zr, Hf, Y, Yb, and various ore and accessory metals in the SMI (Figures 16 and 17). Large ranges in melt composition are attributed to the fractionation of a relatively simple assemblage of plagioclase, K-feldspar, quartz, and apatite. The bulk rocks may not preserve evidence of such extensive fractionation as recorded in SMI (Zajacz and Halter, 2007) because they represent melt compositions only at the time of eruption and after modification. However, the bulk rocks and SMI compositions have similar relative enrichments and depletions: (i) unit 2.0 for Sr, Eu, U, and Th (likely partitioned into apatite; Figure 24A) and LILE (Rb and Ba likely partitioned into K-feldspar; Figure 25A), and unit 5.3 for Cs, Sr, and Y (Figure 24B); and Zr, Hf, U, and Th (Figure 25B).

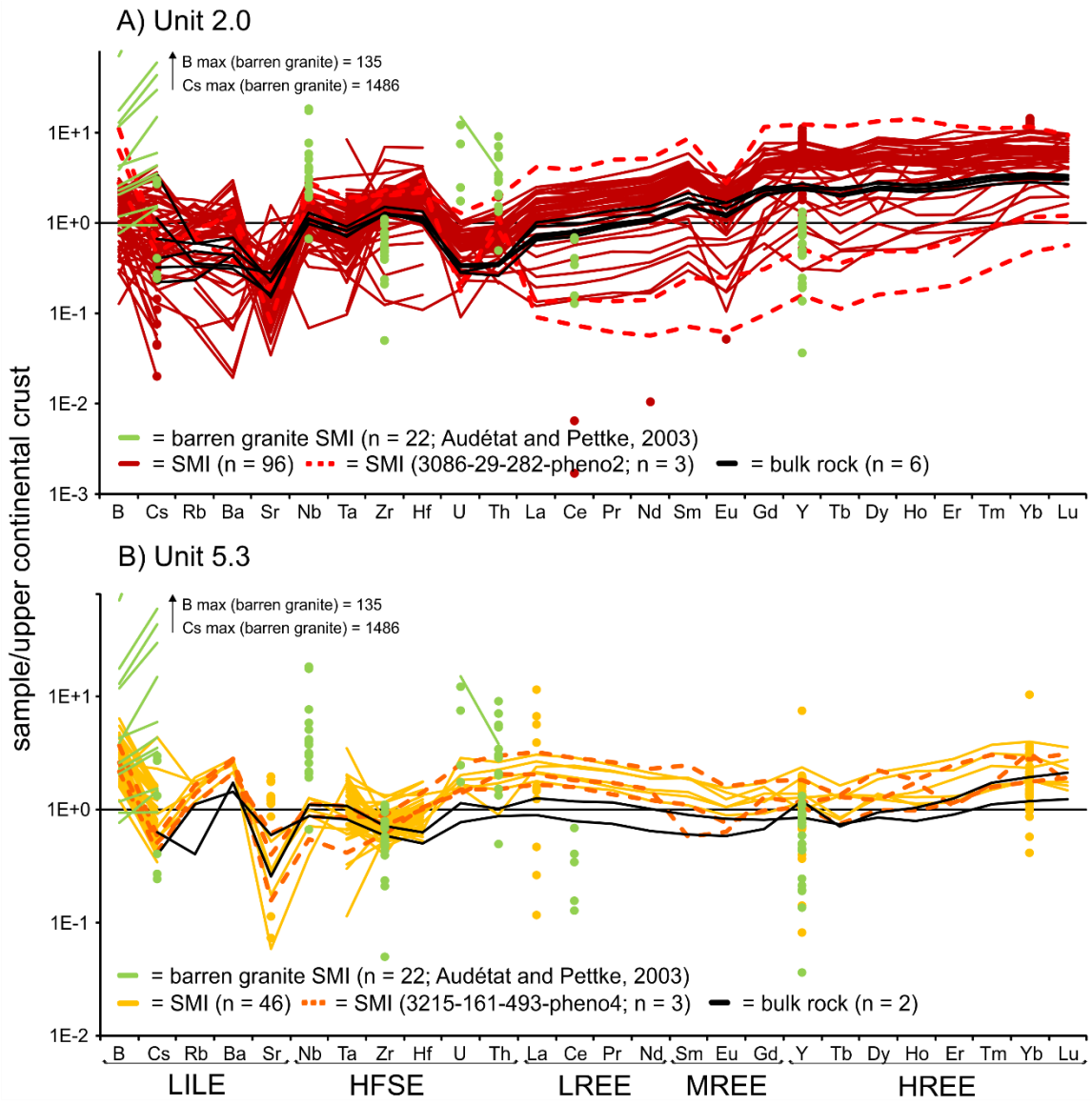
A) Unit 2.0
B max (barren granite) = 135
Cs max (barren granite) = 1486
1E+1
1E+0
1E-1
1E-2
1E-3
= barren granite SMI (n = 22; Audétat and Pettke, 2003)
= SMI (n = 96)
= SMI (3086-29-282-pheno2; n = 3)
= bulk rock (n = 6)
B Cs Rb Ba Sr Nb Ta Zr Hf U Th La Ce Pr Nd Sm Eu Gd Y Tb Dy Ho Er Tm Yb Lu
B) Unit 5.3
B max (barren granite) = 135
Cs max (barren granite) = 1486
sample/upper continental crust
1E+1
1E+0
1E-1
1E-2
= barren granite SMI (n = 22; Audétat and Pettke, 2003)
= SMI (n = 46)
= SMI (3215-161-493-pheno4; n = 3)
= bulk rock (n = 2)
B Cs Rb Ba Sr Nb Ta Zr Hf U Th La Ce Pr Nd Sm Eu Gd Y Tb Dy Ho Er Tm Yb Lu
LILE
HFSE
LREE
MREE
HREE

Figure 24 (previous page): Normative abundance diagrams (relative to upper continental crust) of SMI and bulk rock analyses for units 2.0 and 5.3. Normative abundance diagram summarizing LA-ICP-MS analyses of quartz-hosted SMI and host bulk rock data, as well as SMI data from two barren arc granites (Rito del Medio and Cañada Pinabete plutons, New Mexico, USA; Audétat and Pettke, 2003). Normalization values for upper continental crust from McDonough and Sun (1995). (**A)** Data from unit 2.0. The majority of SMI analyses are higher in concentration in most trace elements compared to the bulk rock values, except for Cs, Sr, Nb, Ta, U and Eu. The SMI values for B, Cs, Nb, U and Th are notably lower than the barren granites. Note the large ranges (up to two orders of magnitude) for the LILE, HFSE and REE in the SMI but general similarity in the abundance patterns between bulk rock and SMU values. Dashed lines (bright red) represent SMI from one phenocryst. (**B)** Data from unit 5.3. The majority of SMI values are higher in concentration in most trace elements compared to the bulk rock values, except for Sr and Nb. The SMI values for B, Cs, Nb, U and Th are lower than the barren granites. Note the large ranges (up to two orders of magnitude) for Sr, La, Y, and Yb. Dashed lines (orange) represent SMI from one phenocryst.

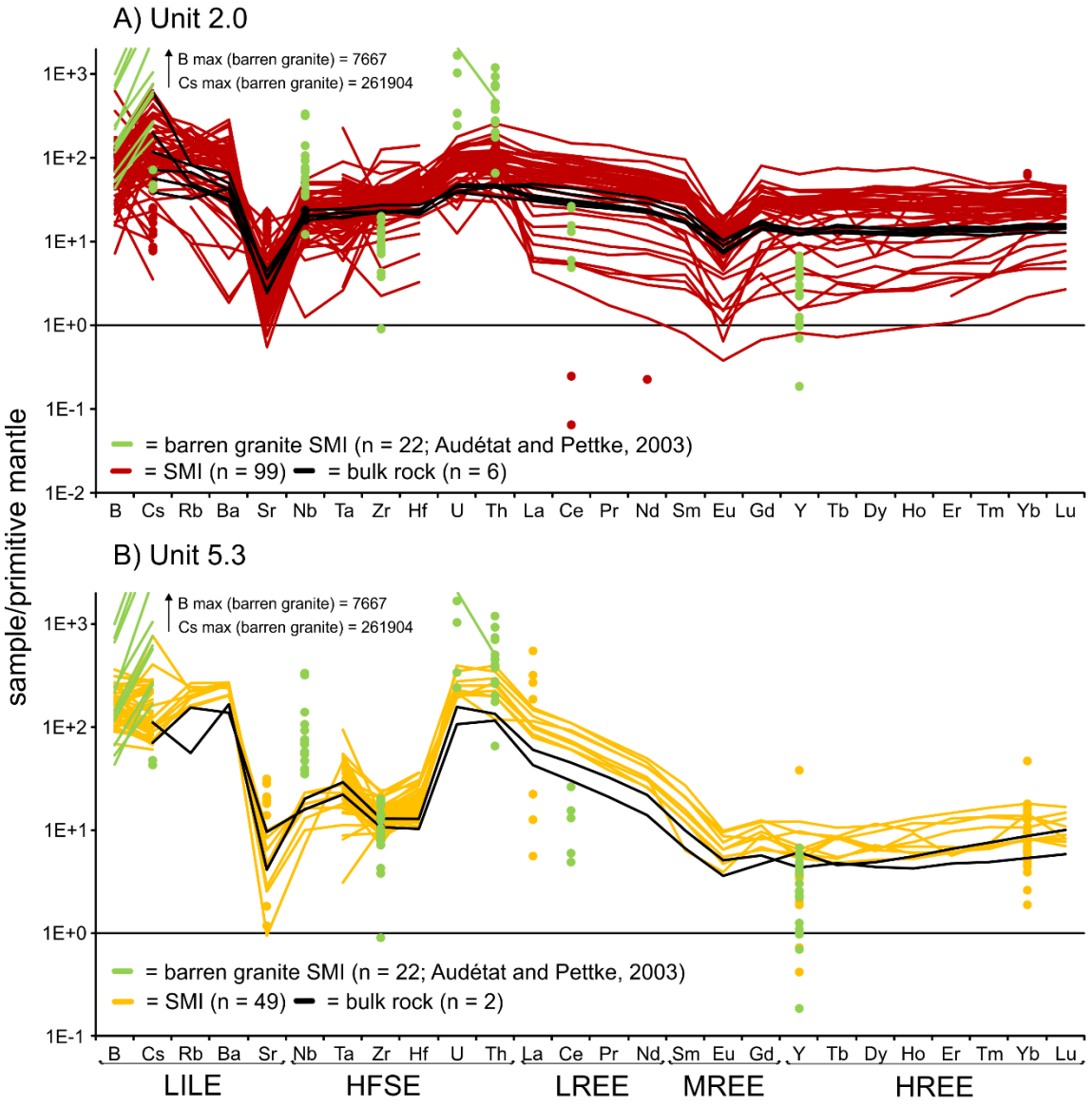
A) Unit 2.0
B max (barren granite) = 7667
Cs max (barren granite) = 261904
1E+3
1E+2
1E+1
1E+0
1E-1
1E-2
= barren granite SMI (n = 22; Audétat and Pettke, 2003)
= SMI (n = 99)
= bulk rock (n = 6)
B Cs Rb Ba Sr Nb Ta Zr Hf U Th La Ce Pr Nd Sm Eu Gd Y Tb Dy Ho Er Tm Yb Lu
B) Unit 5.3
sample/primitive mantle
B max (barren granite) = 7667
Cs max (barren granite) = 261904
1E+3
1E+2
1E+1
1E+0
1E-1
= barren granite SMI (n = 22; Audétat and Pettke, 2003)
= SMI (n = 49)
= bulk rock (n = 2)
B Cs Rb Ba Sr Nb Ta Zr Hf U Th La Ce Pr Nd Sm Eu Gd Y Tb Dy Ho Er Tm Yb Lu
LILE
HFSE
LREE
MREE
HREE

Figure 25 (previous page): Normative abundance diagrams (relative to primitive mantle) of SMI and bulk rock analyses for units 2.0 and 5.3. Normative abundance diagram summarizing LA-ICP-MS analyses of quartz-hosted SMI and host bulk rock data, as well as SMI from two barren arc granites (Rito del Medio and Cañada Pinabete plutons, New Mexico, USA; Audétat and Pettke, 2003). Normalization values for primitive mantle from McDonough and Sun (1995). **(A)** Data from unit 2.0. The majority of SMI analyses are higher in concentration in most trace elements compared to the bulk rock values, except for Cs. The SMI analyses for B, Cs, Nb, U and Th are lower, whereas the analyses for Zr, Ce, and Y are higher, than the barren granites. Note the large ranges (up to two orders of magnitude) for B, Cs, and REE. (**B)** Data from unit 5.3. The majority of SMI analyses are higher in concentration in trace elements compared to the bulk rock values. The SMI analyses for B, Cs, Nb, U and Th are lower, whereas Zr, Ce, and Y are higher, than the barren granites. Note the large ranges (up to two orders of magnitude) for Sr, La, Y, and Yb.

A second important observation is that the normative abundance diagrams show different trace element chemistry for unit 2.0 and unit 5.3 SMI: (i) Unit 2.0 SMI data show depletions in Rb and Ba (unit 5.3 SMI data do not) attributed to more K-feldspar and plagioclase ($An_{10-30\%}$) crystallization, respectively, from the unit 2.0 magma (Figures 24 and 25); (ii) the Eu anomaly is much more pronounced in unit 2.0 SMI than in unit 5.3 SMI; (iii) U and Th show depletions in unit 2.0 SMI (Figure 24A) relative to unit 5.3 SMI (Figure 24B), possibly linked to more apatite fractionation from the unit 2.0 magma prior to entrapment; (iv) Nb-Ta-Zr-Hf are distinctly depleted in unit 5.3 SMI (Figure 25B). Overall, the two units have very different geochemical signatures, suggesting different parental magmas for, or conditions of, melting. All of these features in the SMI are absent in the bulk rock data.

A third important observation involves the comparison of the Bousquet SMI compositions to SMI in other unmineralized felsic igneous systems (younger "barren" arc granitoids, the only data from a barren environment reported in the literature; Audétat and Pettke, 2003; Figures 24 and 25). This comparison shows that strongly incompatible elements such as B, Cs, Nb, Th, and U can reach much higher concentrations (up to an order of magnitude or more) in other unmineralized felsic igneous systems. This suggests that the Bousquet melts are much less evolved and fractionated (Thomas et al., 2003). Importantly, even though barren granitic melts reported by Audétat and Pettke (2003) are quite evolved, they did not saturate in incompatible element-rich mineral phases (tourmaline, Cs micas, columbite, uraninite; London, 1986; Ertl et al., 1997; Adam and Green, 2006), except locally in the most evolved pegmatitic segregations (e.g., Cañada

Pinabete pluton, Cs values up to 5400 ppm), but they did saturate common rock-forming minerals (K-feldspar, quartz, plagioclase, biotite, and muscovite). Thus, whereas th e mineralogy (and therefore, major element composition) can be very similar between two different felsic igneous systems, the SMI data illustrate that the relative extent of fractionation can be quite different.

Audetat and Pettke (2003) evaluated the relationship between the Cs content of a melt phase and the degree of fractionation in a felsic magma. As Cs is very incompatible in all common-rock forming minerals, and does not partition preferentially into exsolving volatiles, measuring its concentration in SMI can be used as a semi-quantitative proxy for fractionation (Audétat and Pettke, 2003; see their Figure 7). Using this model and assuming a similar felsic starting composition, the Bousquet rhyolitic SMI have Cs ranges of 0.1 – 15.8 ppm (average = 3.2 ppm; unit 2.0) and 1.3 – 16.2 ppm (average = 3.5 ppm; unit 5.3), indicating that they had a similar maximum extent of differentiation at the time of SMI entrapment, after 0 - 96% (average = 70%; unit 2.0) and 0 - 97% (average = 75%; unit 5.3) crystallization of parental magmas. In comparison, the barren granite at Cañada Pinabete (Audetat and Pettke, 2003) contains SMI in quartz phenocrysts with Cs concentration range from 1.5 to 5500 ppm (average = 1068 ppm), resulting from 50 – 99% (average = 99%) crystallization (Audétat and Pettke, 2003).

Despite not reaching such extreme levels of differentiation as younger, barren arc granitoids, the SMI in units 2.0 and 5.3 do record an extensive history of fractionation prior to eruption, as their host quartz phenocrysts were growing at depth. A long history of fractionation recorded in the SMI is typical of host phenocrysts in felsic-intermediate

composition magmas that grow over a long residence time in staging chambers (e.g., Roedder, 1992; Frezzotti, 2001; Danyushevsky et al., 2002). This record of fractionation is clearly shown in the normative abundance patterns of SMI from both Bousquet units (Figures 24 and 25). As indicated earlier, the SMI show a large range in trace element concentrations but having similar overall patterns. The range in fractionation can even be seen in *single* phenocrysts of unit 2.0 that have SMI with up to two orders of magnitude of variation in REE (Figure 24A: Appendix 2A). A few patterns that deviate significantly away from the normal fractionation trends are likely due to the inclusion of minor accidentally trapped mineral phases that were not resolved/rejected during data reduction. Variations in element concentration, when the entire data set is considered, are likely the result of (i) accidentally trapped liquidus mineral phases, and (ii) compositional diversity in the melt induced by normal fractionation processes and melt evolution (Richter, 1986; Student and Bodnar, 2004; Zajacz and Halter, 2007; Gray et al., 2011).

Most SMI have incompatible element patterns that are higher in abundance than the bulk rock because the Bousquet rhyolites contain significant K-feldspar, plagioclase, and quartz. Fractionation of these minerals that are poor in incompatibles dilute the melt, resulting in flows/sills that are liquid + crystals. The melts that are trapped in quartz became rich in incompatibles but are depleted in Eu + Sr (plagioclase), Rb + Ba (K-feldspar), U + Th (apatite), and Zr + Hf (zircon) compared to the bulk rocks. Mixtures of crystals and liquid contain less incompatible elements than the trapped liquid-only aliquot in SMI. Thus the bulk rocks are not representative of bulk liquid compositions and must represent samples from units that contain significant accumulations of feldspar and quartz crystals (Gray et al., 2011). It should also be noted that some of the elements, like the LILE, may

be lower in the bulk rock due to alteration which may modify the LILE whereas SMI preserve the original range in LILE values.

Based on the arguments above, if the potential for a magma to supply ore metals is related in part to its degree of differentiation, which causes incompatible ore metal concentrations to increase, the Bousquet volcanics are clearly not anomalous in this respect based on primary SMI data, questioning whether they are, in fact, the causative volcanic units contributing ore metals to mineral deposits in the region.

It should be noted that the wide range in trace element enrichments and depletions in the Bousquet SMI (relative to the bulk rock analyses) are not due to boundary layer effects (i.e., variable diffusivities of trace elements relative to inclusion entrapment duration; Harrison and Watson, 1984; Bacon, 1989; Lu et al., 1995). Using the approach of Baker (2008), ratios of trace elements with contrasting diffusivities (e.g., Cs/Zr) do not vary as a function of melt inclusion size (Table 11).

Table 11: Boundary layer effect as function of Cs/Zr ratio and size of SMI

Sample	Unit	Size in diameter (μm)	Zr (ppm)	Cs (ppm)	Cs/Zr	Sample	Unit	Size in diameter (μm)	Zr (ppm)	Cs (ppm)	Cs/Zr
3086-29-278-pheno2-melt1	2	15	406	1.8	0.004	R17678-16-U4.3-pheno2-melt2	4.3	28	10	3.0	0.295
3086-29-278-pheno2-melt2	2	15	351	1.6	0.005	3086-29-188.5-pheno4-melt2	2	30	469	4.1	0.009
3086-29-278-pheno4-melt3	2	15	243	1.9	0.008	3086-29-218-pheno4-melt1	2	30	242	3.0	0.013
3215-166-131.8-pheno1-melt2	2	15	271	5.2	0.019	3086-29-218-pheno4-melt2	2	30	278	2.1	0.008
3086-29-188.5-pheno7-melt2	2	16	241	<1.8	N/A	3086-29-282-pheno1-melt1	2	30	352	1.5	0.004
3086-29-278-pheno4-melt2	2	17	429	<1.1	N/A	3086-29-282-pheno3-melt1	2	30	26.5	1.0	0.037
3086-29-282-pheno2-melt1	2	18	378	1.7	0.005	3086-29-282-pheno3-melt2	2	30	291	1.9	0.007
3215-161-493-pheno4-melt3	5.3	18	116	2.2	0.019	3215-161-493-pheno3-melt2	5.3	30	130	3.4	0.026
3215-166-79.3-pheno6-melt3	2	18	492	11	0.022	R17678-16-U4.3-pheno3-melt1	4.3	33	3.8	1.8	0.483
R17678-16-U4.3-pheno5-melt1	4.3	19	10.0	<0.4	N/A	3086-29-218-pheno1-melt2	2	35	293	2.4	0.008
3086-29-177-pheno2-melt1	2	20	1189	11	0.009	3215-166-131.8-pheno2-melt2	2	35	105	1.5	0.014
3086-29-177-pheno2-melt2	2	20	677	7.2	0.011	3215-166-131.8-pheno5-melt1	2	35	160	7.2	0.045
3086-29-218-pheno2-melt1	2	20	356	2.0	0.006	3086-29-218-pheno1-melt4	2	40	265	2.4	0.009
3086-29-282-pheno1-melt2	2	20	249	<0.3	N/A	3215-166-79.3-pheno6-melt1	2	40	329	7.0	0.021
3215-161-493-pheno1-melt2	5.3	20	125	2.6	0.021	3086-29-177-pheno4-melt1	2	43	440	1.3	0.003
3215-166-131.8-pheno2-melt1	2	20	350	3.8	0.011	3086-29-188.5-pheno6-melt1	2	44	397	3.7	0.009
3215-166-131.8-pheno6-melt1	2	20	324	6.5	0.020	3086-29-177-pheno3-melt2	2	45	3.68	0.8	0.213
3215-166-79.3-pheno1-melt4	2	20	395	8.6	0.022	3086-29-282-pheno1-melt4	2	50	184	0.5	0.003
3086-29-218-pheno1-melt3	2	23	1.5	2.0	1.324	3086-29-282-pheno4-melt2	2	50	258	1.9	0.007
3215-161-493-pheno3-melt3	5.3	23	181	2.1	0.012	3215-161-493-pheno2-melt1	5.3	50	255	8.5	0.033
3086-29-177-pheno2-melt3	2	25	261	2.6	0.010	3215-166-131.8-pheno3-melt1	2	50	320	3.1	0.010
3086-29-188.5-pheno1-melt2	2	25	85	3.5	0.041	3086-29-282-pheno2-melt2	2	55	436	2.4	0.005
3086-29-188.5-pheno1-melt3	2	25	259	3.7	0.014	3215-161-493-pheno2-melt3	5.3	55	108	16	0.150
3086-29-218-pheno1-melt1	2	25	261	2.0	0.008	3086-29-177-pheno3-melt3	2	60	470	0.7	0.001
3086-29-278-pheno1-melt2	2	25	381	1.3	0.003	3215-166-131.8-pheno3-melt3	2	60	227	4.3	0.019
3215-161-493-pheno1-melt1	5.3	25	146	2.1	0.014	3215-166-131.8-pheno7-melt1	2	60	5.88	11	1.808
3215-161-493-pheno4-melt1	5.3	25	169	1.9	0.011	3215-166-79.3-pheno2-melt3	2	60	1736	48	0.028
3215-161-493-pheno4-melt2	5.3	25	137	1.6	0.011	3215-166-79.3-pheno4-melt2	2	60	388	9.1	0.023
3215-166-131.8-pheno1-melt1	2	25	97.2	3.0	0.031	3086-29-282-pheno2-melt3	2	70	391	2.3	0.006
3215-166-131.8-pheno2-melt3	2	25	253	18	0.070	3086-29-282-pheno4-melt1	2	70	279	0.9	0.003
3215-166-79.3-pheno1-melt3	2	25	453	6.4	0.014	3086-29-282-pheno4-melt4	2	80	327	2.8	0.009
3215-166-79.3-pheno4-melt3	2	25	363	5.1	0.014	3215-166-131.8-pheno4-melt1	2	80	386	2.2	0.006
3086-29-278-pheno3-melt1	2	27	270	0.7	0.003	3215-166-79.3-pheno5-melt2	2	80	232	3.6	0.016
3086-29-188.5-pheno4-melt1	2	28	330	3.7	0.011	3215-166-79.3-pheno3-melt2	2	110	406	13	0.032

The SMI of the Bousquet rhyolites recorded fractionation as shown by the large range of at least an order of magnitude in the box-whisker plots, and the scatter plots that show trends indicating fractionation (Figures 16, 17, and 26). There are five key mineralogical trends of fractionation in this study:

(i) Plagioclase fractionation is evident in the trends of decreasing Sr (Figure 26A) and Na_2O (Figure 26B) and increasing K_2O (Figure 26C). Strontium and CaO have a positive correlation, but mineral fractionation is from right to left on the graph (Figure 26D) because Sr and Ca strongly partition into plagioclase (Bacon and Druitt, 1988). Although not plotted, the SMI analyses have negative correlations of Al_2O_3, Na_2O and CaO with K_2O, FeO, and MgO, reflecting the crystallization of large amounts of plagioclase during melt entrapment. Petrographic observations also support the saturation of plagioclase while melt was being trapped (Figure 10G – I).

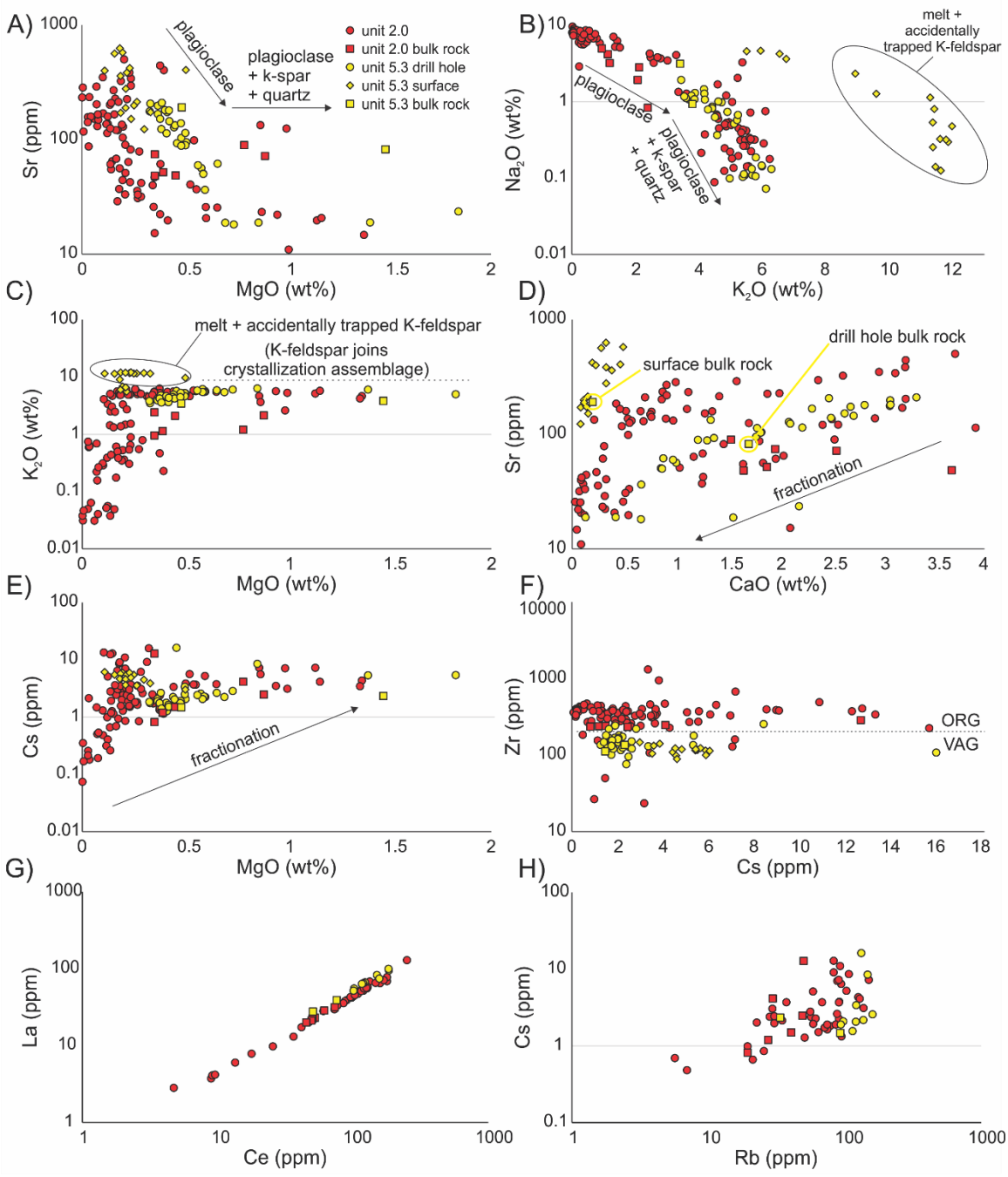
A)
Sr (ppm)
MgO (wt%)
plagioclase
plagioclase
+ k-spar
+ quartz
unit 2.0
unit 2.0 bulk rock
unit 5.3 drill hole
unit 5.3 surface
unit 5.3 bulk rock
B)
Na2O (wt%)
K2O (wt%)
plagioclase
plagioclase
+ k-spar
+ quartz
melt +
accidentally
trapped K-feldspar
C)
K2O (wt%)
MgO (wt%)
melt + accidentally trapped K-feldspar
(K-feldspar joins
crystallization assemblage)
D)
Sr (ppm)
CaO (wt%)
surface bulk rock
drill hole bulk rock
fractionation
E)
Cs (ppm)
MgO (wt%)
fractionation
F)
Zr (ppm)
Cs (ppm)
ORG
VAG
G)
La (ppm)
Ce (ppm)
H)
Cs (ppm)
Rb (ppm)

Figure 26 (previous page): Correlation graphs of units 2.0 and 5.3 SMI and bulk rock data. Chemistry of the SMI measured by LA-ICP-MS analysis. Unit 5.3 SMI showed distinct trends for the drill hole sample versus the surface sample. Unit 2.0 SMI showed uniform trends when all samples (n = 8) were grouped together. Bulk rock data include unit 5.3 drill hole (n = 1), unit 5.3 surface (n = 1), and unit 2.0 (n = 6). **(A)** Sr (ppm) vs MgO (wt%): Analyses of unit 5.3 drill hole SMI (n = 32) show a strong negative correlation, with its bulk rock not following along trend. Analyses of unit 2.0 SMI (n = 81) show a weak inverse correlation, with its bulk rock roughly following along trend. Correlations illustrate plagioclase, followed by plagioclase + K-spar + quartz fractionation. **(B)** Na_2O (wt%) vs K_2O (wt%): Analyses of unit 5.3 drill hole SMI (n = 33) and surface (n = 16) show negative correlations, with the drill hole bulk rock following along trend but the surface bulk rock does not follow the trend. Higher K_2O values for the surface sample analyses illustrate the accidental trapping of K-feldspar (circled). Analyse of unit 2.0 SMI (n = 99) show a negative correlation, with its bulk rock following along trend. At the pivot point, plagioclase fractionation changes to plagioclase + K-spar + quartz fractionation. Note that SMI with very high Na_2O contents (>8%) may contain accidentally trapped albitic plagioclase. **(C)** K_2O (wt%) vs MgO (wt%): Analyses of unit 5.3 drill hole SMI (n = 33) show a flat trend which is due to the fractionation of K-feldspar. Analyses of unit 2.0 SMI (n = 94) show a positive correlation, with its bulk rock following along trend. A group of surface sample analyses illustrate melt with accidentally trapped K-feldspar (circled). **(D)** Sr (ppm) vs CaO (wt%): Analyses of unit 5.3 drill hole and surface SMI show strong positive correlations, with both their bulk rocks following along trend. Analyses of unit 2.0 SMI (n = 88) show a weak positive correlation, with its bulk rock following along trend. Fractionation goes from right to left (arrow). **(E)** Cs (ppm) vs MgO (wt%): Analyses of unit 5.3 drill hole SMI (n = 33) show a slight positive correlation. Analyses of unit 2.0 SMI (n = 90) show a positive correlation, with its bulk rock following along trend. There are accidentally trapped K-feldspar in the surface samples which lowers the MgO and raises the Cs concentrations. **(F)** Zr (ppm) vs Cs(ppm): Analyses of unit 2.0 SMI (n = 90) show higher Zr values than unit 5.3 SMI (n = 49). There is no correlation for either group. **(G)** La (ppm) vs Ce (ppm): SMI of both units show strong positive correlations. **(H)** Cs (ppm) vs Rb (ppm): SMI of both units show positive correlations.

(ii) Potassium feldspar growth and accidental entrapment: In the graphs of Figure 26, the trends reflect mineral fractionation while the separate groups of SMI (from the same unit) reflect variations in accidentally trapped mineral phases. There is a point during fractionation in which K_2O and other elements (Cs, Sr) level out and no longer increase or decrease (Figure 26A, C, and E), corresponding to the point at which K-feldspar joins the crystallizing assemblage. Petrographic observations show that K-feldspar removal was ongoing while SMI were being trapped in quartz (Figures 10H & J, and 11N & O). Unit 5.3 surface sample analyses have higher K_2O but lower MgO concentrations than drill hole sample analyses (Figure 26C) due to contamination of accidentally trapped K-feldspar, raising the relative concentration of K_2O and lowering the relative concentration of MgO in the melt (Goodrich et al., 2013). Regardless of contamination, the surface sample analyses still follow the same fractionation trends as the drill hole analyses (Figure 26A - C). The unit 5.3 surface sample SMI also show a decrease in Sr and CaO as fractionation progressed but it has been shifted relative to the drill hole sample SMI (Figure 26D). This is consistent with the dilution of the trapped melt with a Ca-poor mineral like K-feldspar (Goodrich et al., 2013). It is important to note that the bulk composition mimics the SMI composition of unit 5.3, so K-feldspar is impacting both the SMI and the bulk rock (Figure 26D). There is a curvilinear trend in the Cs versus MgO plot with higher levels of Cs indicating a more evolved/fractionated melt (Figure 26E; Bea et al., 1994). The surface sample and many unit 2.0 SMI analyses sit higher on the Cs axis due to accidentally trapped micas, like biotite (Figure 26E; Bea et al., 1994; Adam and Green, 2006).

(iii) There are pivots in the patterns in Figure 26 indicating changes in mineralogy. Strontium is partitioning into plagioclase until it hits a pivot point and starts to crystallize

plagioclase + K-feldspar + quartz (Figure 26A). Halfway through the fractionation trend in Figure 26B, the same assemblage (plag + K-spar +qtz) begins to crystallize as plagioclase removal decreases while quartz and K-feldspar removal increases.

(iv) The history of mineral growth and lack of crystallized mafic phases is shown in the tight minor and trace element correlations of both units. For example, Sr in both units shows inverse correlations with majors (e.g., MgO; Figure 26A), which is consistent with Sr being pulled out by plagioclase (Bacon and Druitt, 1988; Bea et al., 1994). Plagioclase crystallization and removal ceases when Sr stops decreasing and levels off; while elements, like MgO, begin to increase (Figure 26A). The continuous increase of MgO indicates that not many mafic minerals crystallized while plagioclase was being removed. Over the entrapment history of the melts, it does not appear that many mafic minerals were crystallizing because the more evolved SMI (i.e., deepest Eu anomalies, and richest in Rb and Cs) have high concentrations of K_2O, FeO, and MgO (Appendix 2A and B). FeO and MgO are not decreasing as the melt evolves because so much plagioclase is growing that even if FeO and MgO are coming out of the melt, they are not being removed at a rate faster than the plagioclase is growing.

(v) Accessory phases crystallized, impacting the rare earth and incompatible trace elements of the SMI. There is no correlation between Zr and Cs (Figure 26F) which means they are not strictly behaving incompatibly even though they are typically two very incompatible elements (Mittlefehldt, 1999; Burnham, 2018). The upper limit in Cs is similar for both units (i.e., 16 ppm) which means that they both reached the same point of fractionation (Figure 26F). Zircon and rutile strongly partition Zr and must have been saturated during the entire evolution of the melt because the Zr values stay constant and

never drop (Figure 26F; Foley et al., 2000). The Zr contents of the two units are very different which is consistent with the VAG versus ORG argument (Figure 26F; Hemayat, 2016). The ORG (i.e., unit 2.0) melts are higher in Zr than the VAG (i.e., unit 5.3) melts (Figure 26F). Unit 5.3 has low Zr and Hf contents with a low average Zr/Hf ratio (25.7 ± 5.4) compared to unit 2.0 (29 ± 5.2), it does not have a strong negative Eu anomaly (Figure 24B), and it has a high LREE/HREE ratio (3.3 ± 2.7) compared to unit 2.0 (0.9 ± 0.8). All these features indicate a more evolved and mineralized magma that occurs particularly in mature arcs (Hemayat, 2016).

There are near perfect fractionation trends in the SMI data as shown by incompatible elements, like La and Ce (Figure 26G). Rare earth elements are very good monitors of fractionation and are, therefore, very good at showing the extent of fractionation across the data set. Elements like Cs and Rb do not have a perfect trend (Figure 26H), likely due to fluid exsolution. Fluid exsolution does not impact the REE, owing to their much lower solubility in magmatic fluids. The normal fractionation of incompatible trace elements in melt, however, can be influenced by the crystallization of accessory minerals (Schwindinger et al., 2020). For example, U and Th preferentially partition into allanite and zircon, while La and Ce partition into apatite and zircon (Figure 26G; Gray et al., 2011). Accessory mineral inclusions in Bousquet quartz phenocrysts indicate that zircon, apatite and allanite were saturated phases at the time of melt entrapment (Figure 8M – S). This can be seen in the SMI chemistry from variations in the enrichment and depletion of REE and U (Figure 24). For example, unit 2.0 SMI have depleted U values which could be partially due to the presence of zircon grains (Figure 24A; Bea et al., 1994). In addition to

zircon, variations in REE content can be due in part by the presence of apatite which is a main carrier of REE, reducing their concentration in coexisting melt (Frondel and Marvin, 1959; Banfield and Eggleton, 1989; Morteani and Preinfalk, 1996; Taunton et al., 1998; Pan and Stauffer, 2000). Both units contain allanite (Figure 8S) and unit 5.3 contains monazite (Figure 11N); these accessory minerals are the main hosts and repository for LREE, thus increasing the concentration of HREE in the magma (Gromet and Silver, 1983; Bea, 1996; Gieré and Sorensen, 2004). This phenomenon only had a noticeable effect on the REE patterns of unit 2.0, which dip toward the LREE relative to the HREE when normalized to upper continental crust (Figure 24A).

Interestingly, in both units, the SMI with the highest REE values (i.e., most fractionated) have amongst the highest U values (Figure 24). This suggests that U is tracking with the normal progression of fractionation. If zircons were forming consistently throughout the evolution of the magma, the most fractionated melts would display the biggest U anomalies. This is not the case for units 2.0 and 5.3; therefore, another mineral may be partitioning U, unless the zircons were transiently soluble during the evolution of the magma. Zircon fractionation did not increase throughout the evolution of the magma as can be seen by the lack of correlation with Zr and Cs (Figure 26F). Cesium changes due to fractionation and Zr should change as well, but there is no correlation. This must mean that zircon is crystallizing continuously as the melt fractionates.

Inclusions of apatite are trapped coevally with melt (Figure 8M – R) and give a snapshot of the chemistry of apatite in equilibrium with those melts at the time of entrapment. Sometimes the apatite grains are trapped inside the SMI (Figures 8M and 13I). The apatites

are recording chemistries that are very different from one another. The apatites, by proxy, are recording differences in melt chemistry just like the SMI which allows for classification of magma type (Figure 27; Belousova et al., 2002). The apatites are showing evidence of Eu removal which means there was fractionation of plagioclase in the magma (Figure 27D). This is a reassertion that plagioclase removal affects the chemistries of the apatites. In the Sr/Y vs Y diagram, it shows that there is much more plagioclase removal in the unit 2.0 magma which is backed up by the larger Eu anomaly as compared to unit 5.3 (Figures 23 and 27D).

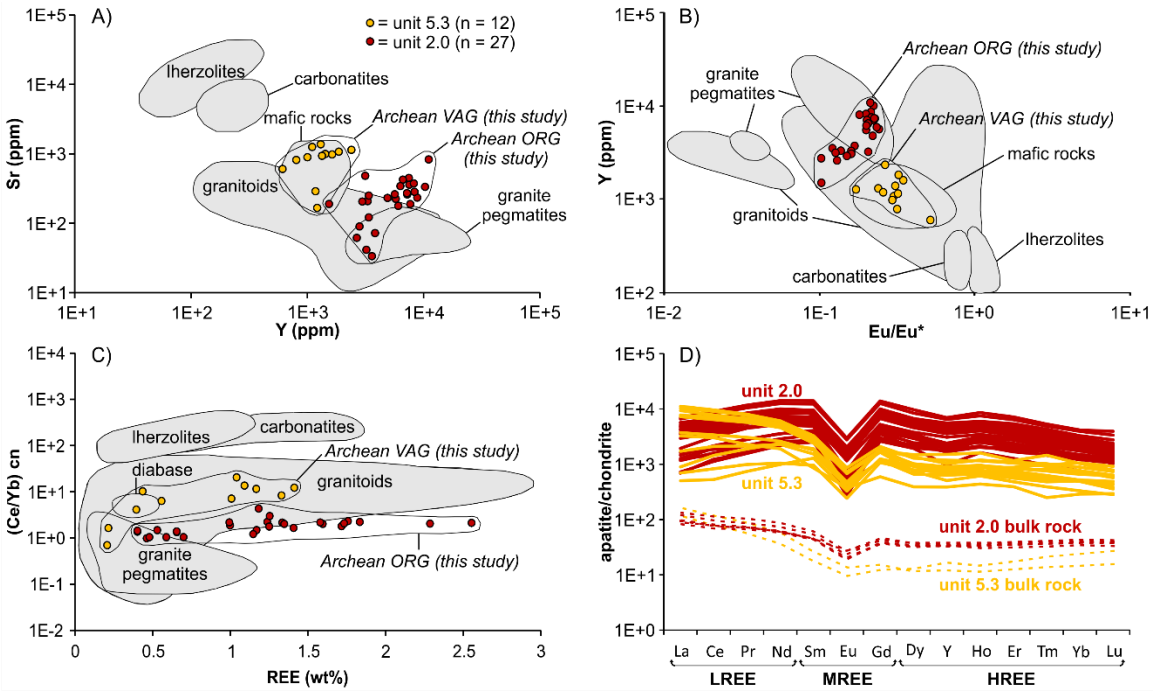

Figure 27: Discrimination diagrams and normative abundance patterns for SMI-coeval, quartz phenocryst-hosted apatite. Compositional fields for apatite from different igneous rock types (grey fields) are from Belousova et al. (2002). New fields delineated for Archean VAG and ORG are from this study. **(A)** Sr vs Y; unit 5.3 apatites plot in the mafic rocks field whereas most unit 2.0 apatites fall in the granitoid and granite pegmatite fields **(B)** Y vs Eu/Eu*; unit 5.3 apatites plot in the mafic rocks field whereas unit 2.0 apatites plot in the granitoid and granite pegmatite fields, consistent with (A). **(C)** $(Ce/Yb)_{chondrite\text{-}normalized}$ vs REE (total); both units 5.3 and 2.0 apatites follow the granitoid and granite pegmatite fields; **(D)** Chondrite-normalized REE data. data; note the more pronounced Eu anomaly, higher MREE and HREE, and lower LREE composition of unit 2.0 apatites compared to unit 5.3. For comparison, =bulk rock data are also (red dashed lines = unit 2.0; yellow dashed lines = unit 5.3).

The apatite data, by itself, gives great insight into the bulk compositional differences between the magmas of each unit (Figure 27). The apatite shows something that is not apparent in the bulk rock chemistry. It mimics the melt chemistry very closely, specifically with the deeper Eu and much shallower LREE pattern and much lower MREE and HREE for the unit 2.0 apatite. This confirms that apatite REE chemistry is a good proxy for melt chemistry and they are likely in equilibrium with the melt in the melt inclusions. For example, unit 2.0 apatites share the same range in composition as granites whereas unit 5.3 apatites fall in more mafic range (Figure 27A – B). These differences in apatite chemistry imply that the stage of liquid evolution that crystallized apatites of one unit is very different than the other unit and there is a possible influence of more basic magmas. However, there are similarities in the apatite chemistry of both units, like their shared Eu anomalies (Figure 27D). These apatites were likely growing in the presence of a magma that had plagioclase removed from it. Most of the REE values of both units are in the granitoid field and indicate that the apatites equilibrated with a typical granitic liquid (Figure 27C).

The LA-ICP-MS data of quartz-hosted apatite grains from units 2.0 (n= 27) and 5.3 (n = 12) are summarized in discrimination diagrams and normative abundance plots (Figure 27; Table 8) along with bulk rock data for both units for comparison. Proposed discrimination fields for apatite compositions crystallized from different rock compositions were from Belousova et al. (2002). Based on concentrations of Sr and Y, unit 5.3 apatites fall in the “mafic” field and most unit 2.0 apatites fall in the granitoid/ granite pegmatite fields (Figure 27A). A similar result is seen based on the parameters Y vs Eu/Eu* showing unit 5.3 apatites plot in the “mafic” field and unit 2.0 apatites in the granitoid/ granite

pegmatite fields (Figure 27B). Concentrations of (Ce/Yb)cn vs REE showed that unit 5.3 apatites were in the granitoid, diabase, and granite pegmatite fields, and most unit 2.0 apatites were in the granitoid and granite pegmatite fields (Figure 27C).

The apatite and SMI data demonstrate that the bulk rock compositions are quite different than the SMI compositions (Figures 24, 25, and 27). There are two major themes that comparison of apatite, SMI, and bulk rock data show: (i) The data show that the SMI and apatites are recording a much broader history of melt evolution than bulk rocks at depth; and (ii) In the next section, metals in SMI are defined in terms of concentration relative to the bulk rock metals which have been metamorphosed and modified; the metal concentrations in the bulk rocks are not representative of the original metal tenor of the magmatic system. The liquid line of decent of magmatic systems is defined by primary melt inclusions that formed at different stages of evolution of the melts (Schiano, 2003).

2.4.5 Relationships between metals and magmatic evolution

The data in the present study provide the first constraints on metal concentrations in a pre-emplacement/eruptive magmatic system in the Archean. Normative abundance diagrams (Figures 28 and 29) and box-whisker plots (Figures 30 and 31) illustrate the differences between bulk rock metal concentrations and SMI metal concentrations. There are few published studies of SMI metal concentrations in barren granitic rocks.

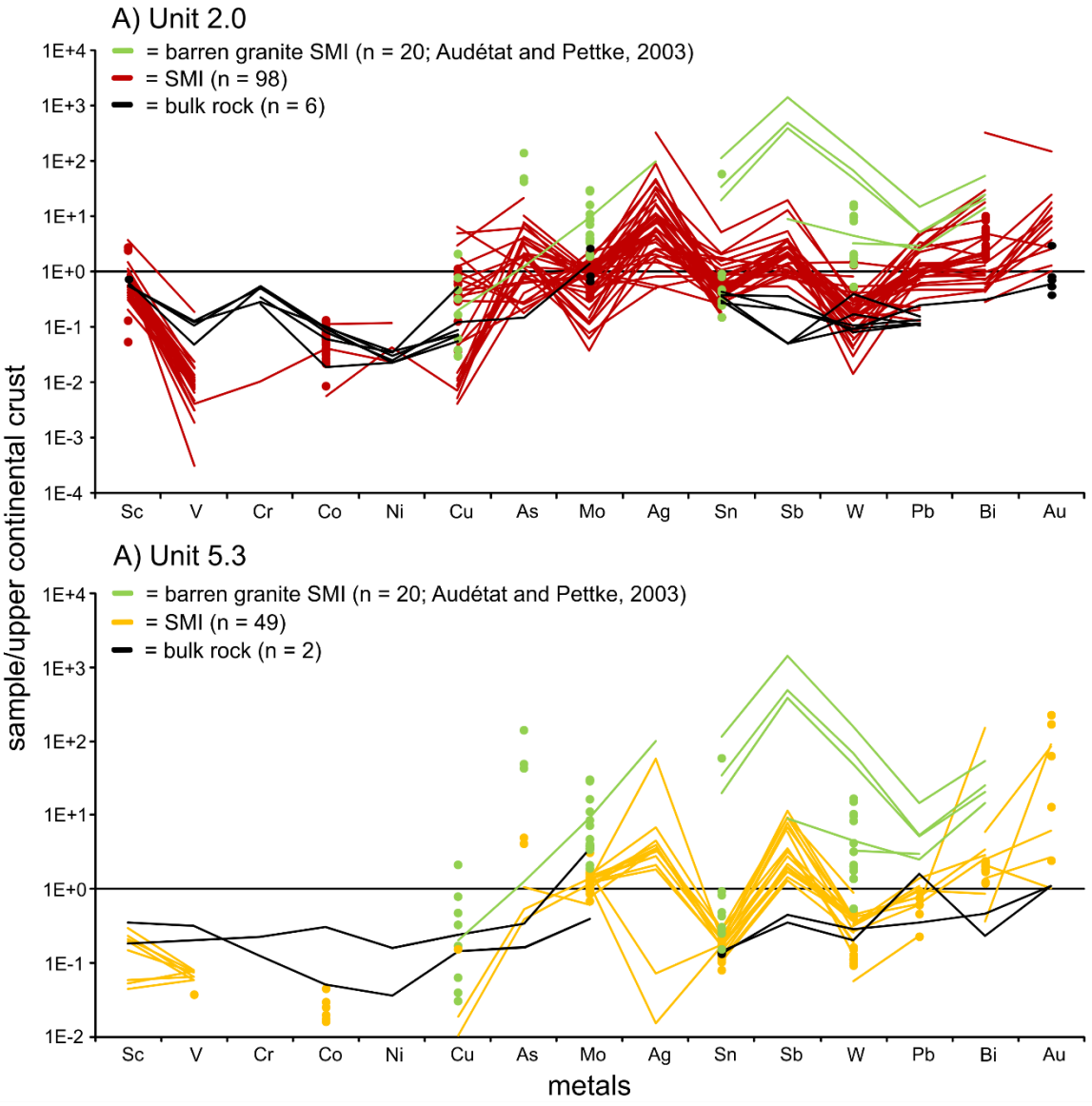
A) Unit 2.0
= barren granite SMI (n = 20; Audétat and Pettke, 2003)
= SMI (n = 98)
= bulk rock (n = 6)
1E+4
1E+3
1E+2
1E+1
1E+0
1E-1
1E-2
1E-3
1E-4
Sc V Cr Co Ni Cu As Mo Ag Sn Sb W Pb Bi Au
A) Unit 5.3
= barren granite SMI (n = 20; Audétat and Pettke, 2003)
= SMI (n = 49)
= bulk rock (n = 2)
1E+4
1E+3
1E+2
1E+1
1E+0
1E-1
1E-2
Sc V Cr Co Ni Cu As Mo Ag Sn Sb W Pb Bi Au
sample/upper continental crust
metals

Figure 28 (previous page): Normative abundance diagrams (relative to continental crust) of SMI and bulk rock analyses for units 2.0 and 5.3 metals. Normative abundance diagrams summarizing LA-ICP-MS analyses of quartz-hosted SMI and host bulk rock data, as well as SMI from two barren arc granites (Rito del Medio and Cañada Pinabete plutons, New Mexico, USA; Audétat and Pettke, 2003). Normalization values for continental crust from McDonough and Sun (1995). **(A)** Data from unit 2.0. The majority of SMI analyses (except V, Cr, and Mo) are higher in concentration compared to the bulk rock values (e.g., As, Sn, Sb, Pb, Bi, and Au). The majority of SMI analyses are lower in concentration compared to the barren arc granites (e.g., As, Mo, Ag, Sb, W, Pb, and Bi). Note the large ranges (up to four orders of magnitude) for Sc, V, Cu, As, Mo, Ag, W, Bi and Au. **(B)** Data from unit 5.3. The majority of SMI analyses (except Sc, V, Co, and Cu) are higher in concentration compared to the bulk rock values (e.g., As, Sn, Sb, W, Bi, and Au). The majority of SMI analyses are lower in concentration compared to the barren arc granites (e.g., Cu, As, Mo, Sn, Sb, W, Pb, and Bi). Note the large ranges (up to three orders of magnitude) for Ag, Bi, and Au.

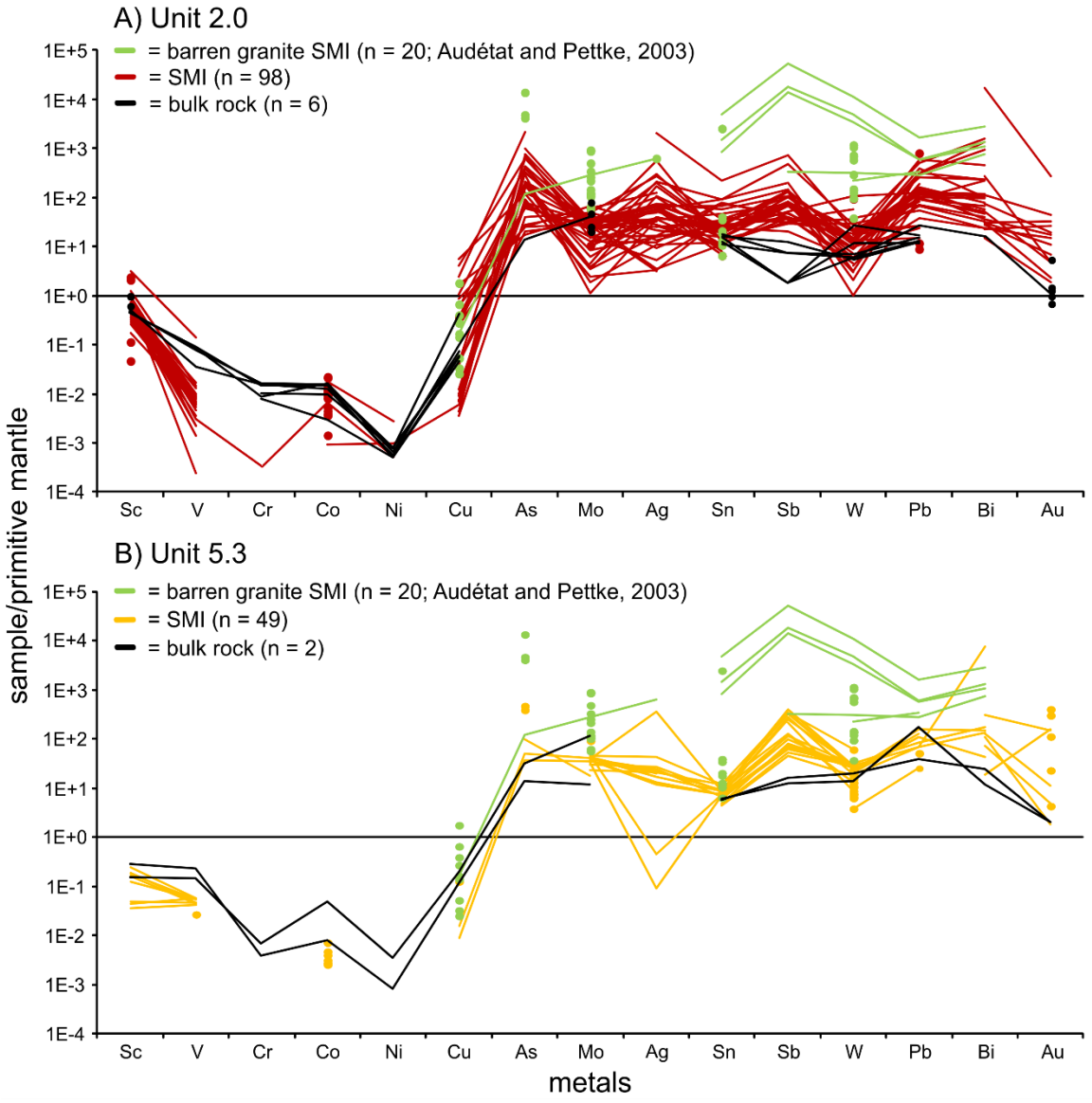
A) Unit 2.0
= barren granite SMI (n = 20; Audétat and Pettke, 2003)
= SMI (n = 98)
= bulk rock (n = 6)
1E+5
1E+4
1E+3
1E+2
1E+1
1E+0
1E-1
1E-2
1E-3
1E-4
Sc V Cr Co Ni Cu As Mo Ag Sn Sb W Pb Bi Au
B) Unit 5.3
= barren granite SMI (n = 20; Audétat and Pettke, 2003)
= SMI (n = 49)
= bulk rock (n = 2)
sample/primitive mantle
metals

Figure 29 (previous page): Normative abundance diagrams of units 2.0 and 5.3 metals normalized to primitive mantle. Normative abundance diagrams summarizing LA-ICP-MS analyses of quartz-hosted SMI and host bulk rock data, as well as SMI from two barren arc granites (Rito del Medio and Cañada Pinabete plutons, New Mexico, USA; Audétat and Pettke, 2003). Normalization values for primitive mantle from McDonough and Sun (1995). **(A)** Data from unit 2.0. The majority of SMI analyses (except V, Cr, and Mo) are higher in concentration compared to the bulk rock values (e.g., As, Sn, Sb, Pb, Bi, and Au). The majority of SMI analyses are lower in concentration compared to the barren arc granites (e.g., As, Mo, Ag, Sb, W, Pb, and Bi). Note the large ranges (up to four orders of magnitude) for Sc, V, Cu, As, Mo, Ag, W, Bi and Au. **(B)** Data from unit 5.3. The majority of SMI analyses (except Sc, V, Co, and Cu) are higher in concentration compared to the bulk rock values (e.g., As, Sn, Sb, W, Bi, and Au). The majority of SMI analyses are lower in concentration compared to the barren arc granites (e.g., Cu, As, Mo, Sn, Sb, W, Pb, and Bi). Note the large ranges (up to three orders of magnitude) for Ag, Bi, and Au.

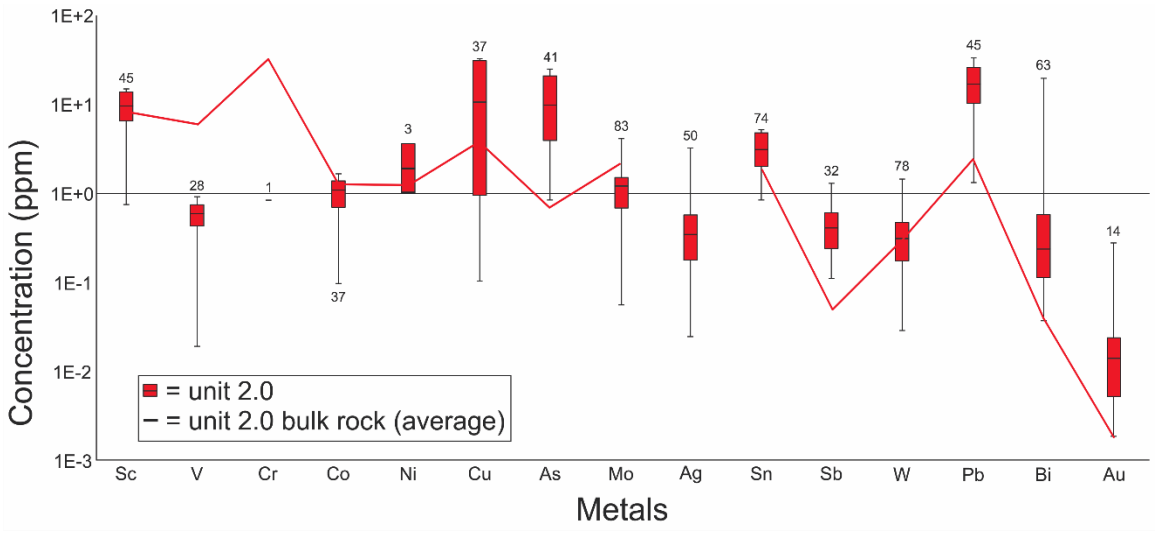

Figure 30: Box and whisker plot of metals from units 2.0 SMI. Shown are the 1st and 3rd quartile ranges, averages, and error bars of metals. Metal concentrations were collected by LA-ICP-MS. Numbers near each box and whisker represent the number of SMI with analyses above detection limit. Bulk rock data are averages from collected samples and overlay the box and whiskers for comparison.

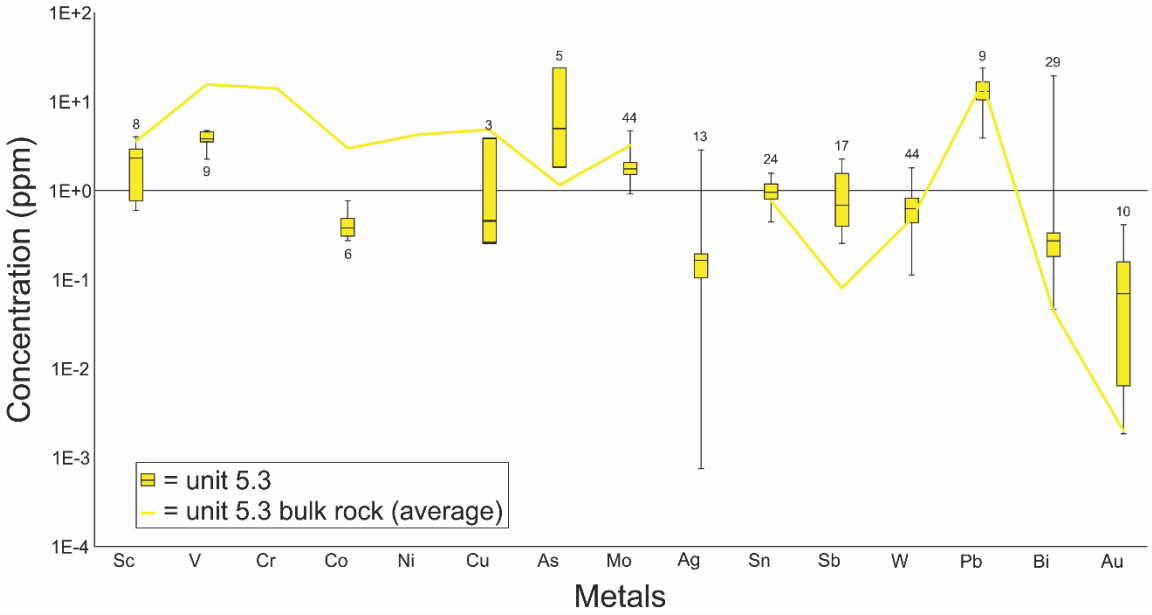

Figure 31: Box and whisker plot of metals from units 5.3 SMI. Shown are the 1st and 3rd quartile ranges, averages, and error bars of metals. Metal concentrations were collected by LA-ICP-MS. Numbers near each box and whisker represent the number of SMI with analyses above detection limit. Bulk rock data are averages from collected samples and overlay the box and whiskers for comparison.

For both Bousquet units, As-Sb-Sn-Pb-Bi-Cu-Au are significantly higher than the bulk rock analyses, suggesting that the SMI preserve the original metal concentrations in the melt with concentrations varying as a result of fractionation like other incompatible elements (Roedder, 1984; Sobolev, 1996; Frezzotti, 2001; Lowenstern, 2003). However, the metal chemistry of the bulk rocks can be modified during the evolution of the system in several ways giving the appearance that the SMI have more fractionated compositions: (i) the bulk rocks can be hydrothermally altered and metals stripped out (Mathieu, 2018); (ii) metals can be *removed* by alteration (der Straaten et al., 2011); (iii) volatiles can saturate and extract metals after melt entrapment (Holloway, 1976; Webster, 1997); and (iv) the bulk rock represents melt diluted with crystals, causing the bulk rock metals to be lower than the true liquid composition found in SMI (Kent, 2008). It is likely that a combination of these processes/scenarios apply in this case, but the evidence suggests that volatile exsolution, fractionation, and crystal dilution explain the SMI-bulk rock differences.

The anomalous ore and accessory metals that are higher in the SMI comprise an association of chalcophile elements commonly associated with magmatic volatile contributions to hydrothermal fluids in porphyry-epithermal type settings (e.g., Au-Ag-As-Sb ± Bi-Hg-Te; Halbach et al., 2003; Glasby et al., 2004; Halter et al., 2005; Audétat et al., 2008; Glasby et al., 2008; Rusk et al., 2008b; Mercier-Langevin et al., 2011a). These metals are also present in the LaRonde Penna deposit within accessory mineral assemblages in the ores (e.g., As = arsenopyrite, Sb = tetrahedrite, Sn = stannite, Bi & Au = Bi-Au tellurides, and Pb & Ag = Pb-Ag sulphosalts; Mercier-Langevin et al., 2007a). Thus, on the basis of

metal associations alone, the metals within the Bousquet rhyolites could have degassed or been leached from glassy matrix in the bulk rocks in the shallow crust. For example, this could have happened at depth through the decomposition of magmatic sulphides during degassing of the magmas. This process releases S, Cu, Au, and other chalcophile elements such as Ag, Sb, Pb and Bi (Keith et al., 1997; Halter et al., 2002b; Halter et al., 2005; Stavast et al., 2006; Audétat et al., 2008).

Whereas the bulk volcanic rocks are at or below continental crust metal values, the SMI compositions are commonly well above normal continental crust levels (Figure 28). Some of the metals like As, Ag, Sb, Bi, and Au have concentrations in the SMI that are one to two orders of magnitude higher than normal continental crust (Figure 28). This illustrates that these melts are highly anomalous in terms of their metal contents. Aside from Sn which shows a weak inverse correlation with Sr, there are no significant correlations between metals in the SMI (Figure 32) and elements like B and Cs that are strongly incompatible and increase with progressive fractionation.

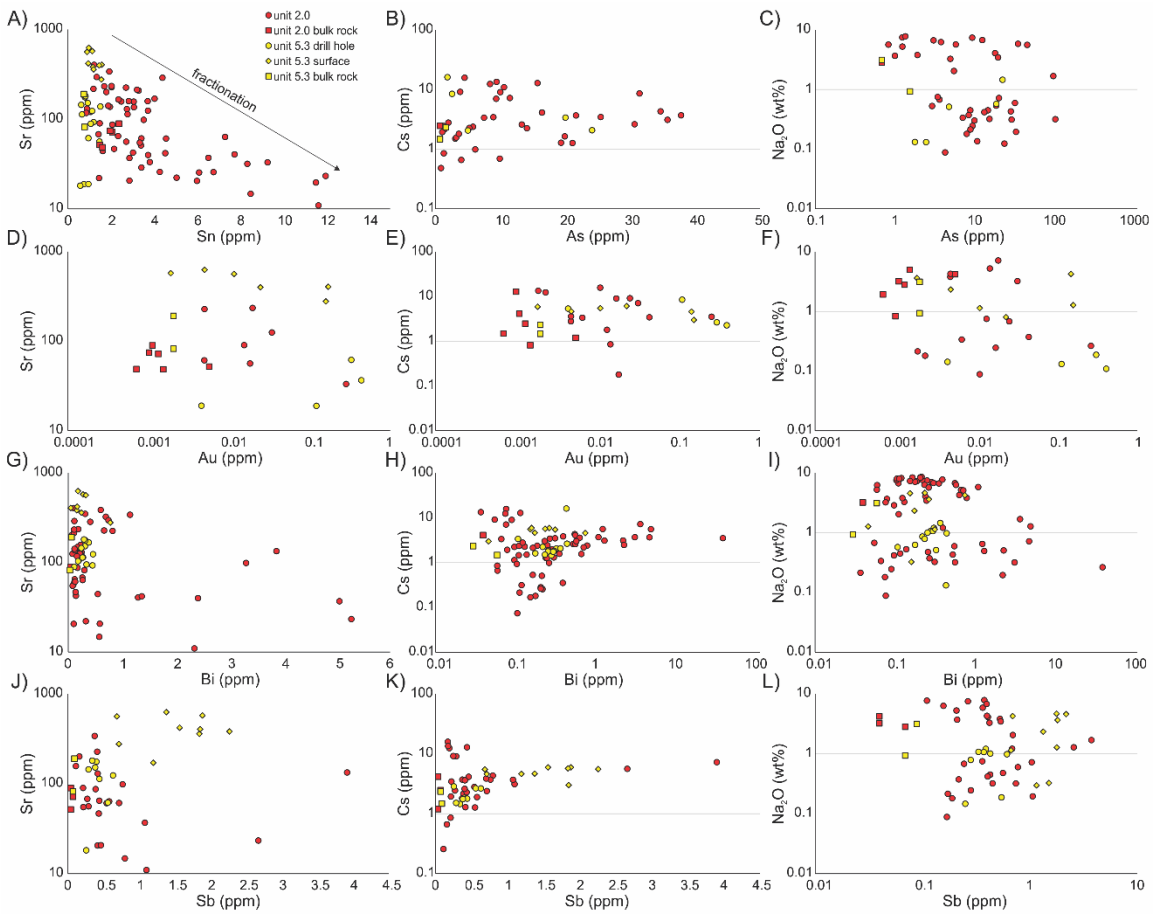

Figure 32: Correlation graphs of metal concentrations for units 2.0 and 5.3 SMI. Unit 2.0 data are red, and unit 5.3 data are yellow, with circles and diamonds for SMI and squares for bulk rock. **(A, H, K)** The only graphs that show correlations of metals with trace elements (Sr vs Sn = negative; Cs vs Bi and Cs vs Sb = curvilinear positive). **(B-G, I, J, and L)** Various metal plots that show no correlation with Sr, Cs, and Na_2O which are key elements that indicate fractionation.

As well, both magnetite and ilmenite are indicator minerals for oxidizing and reducing environments, respectively, and are present in units 2.0 and 5.3 as daughter and accidentally trapped (saturated) phases (Figures 10 and 11; Hart et al., 2004; Ishihara, 2007; Maulana et al., 2013). Oxidized magnetite-series granitoids concentrate metals such as Mo, Cu, Zn, Pb, Ag, and Au; whereas, reduced ilmenite-series magmas have lower abundances of these but tend to have higher concentrations of Sn and W (Ishihara, 2007). The SMI analyses show that the metals associated with reducing magmas (Sn and W) are present but at lower abundances compared to the others (Figures 28 and 29). The metal concentrations of the magmas at depth are initially established by a parental liquid composition and change as the magmas differentiated in the crust before eruption/emplacement. However, B and Cs do not show any correlations with metals in the SMI (Figure 32). This contradicts the idea that fractionation controlled (increases) the chalcophile metal content of the Bousquet magmas. For example, even though there was extensive fractionation of plagioclase, the metal content did not increase during plagioclase removal. If the melts were trapped along a typical differentiation path, then there would have been correlations between the metals and the incompatible element parameters like Cs (Audétat et al., 2000). Therefore, the record of fractionation control on metal endowment has been obtained (i.e., by degassing or sulphide saturation). The high concentrations of metals are likely tracked to the magmatic source region (Yang and Scott, 1996, 2002, 2005, 2006; Beaudoin et al., 2007; Marques et al., 2009, 2011, 2020).

However, the SMI from unit 2.0 have many ore and accessory metals (i.e., As, Mo, Ag, Sb, W, Pb, and Bi) lower in concentration than younger barren arc granites (Rito del Medio

and Cañada Pinabete plutons, New Mexico, USA; Audétat and Pettke, 2003; Figure 28A). Another comparison was made with SMI from the Timbarra composite granitic pluton, Australia (Mustard et al., 2006). All plutons have significantly higher concentrations of some metals (Sb, As, W, Mo, Pb, Bi, Sn) than the Bousquet rhyolite melts but comparable Au, Cu, and Ag. Overall, the more modern barren granites are more concentrated in metals than the SMI from Bousquet rhyolites (Figures 28 and 29), but this could be related to the higher degree of fractionation of these examples. Despite showing relatively low degrees of fractionation, the Bousquet rhyolites illustrate that having a fractionated liquid is not necessarily the sole prerequisite for metal-enriched magmas. In general, metal tenor depends on more factors than just fractionation (e.g., composition of the source region, f_{O2}; Blevin and Chappell, 1992). Elevated Au and Ag (and other accessory metals like Mo, Pb, Sb, Sn, As) well above normal upper crustal concentrations could reflect an oxidized source magma for the Bousquet formation rocks (Figure 28; Hedenquist and Lowenstern, 1994; Sillitoe et al., 1996).

2.4.6 Volatiles in SMI

Characterization of the SMI should include determination of volatile content, homogenization characteristics and assessment of fluid-melt entrapment (Cannatelli et al., 2016), as these parameters may shed light on processes that have impacted metal enrichment and loss from magmas. Previous research on volatiles associated with mantle xenoliths show that there is a significant CO_2-rich component in the lithospheric mantle in alkaline arc systems (e.g., Berkesi et al., 2012). CO_2 saturation in arc environments is driven by carbonate rocks that are subducted and melted, producing CO_2-rich fluids that

metasomatize and enrich the mantle (Yaxley et al., 2019). CO_2 is also prevalent in melts produced in alkaline arc environments due to the low degrees of partial melting of the metasomatized mantle responsible for alkaline magmatism (Yaxley et al., 2019). However, aside from lower-crustal/upper-mantle xenoliths (e.g., Hansteen et al, 1991; Schiano & Clocchiatti, 1994; Schiano et al, 1992; Chupin & Tomilenko, 1995; Szabo et al, 1996) and komatiites (e.g., Anderson, 1995; Shimizu et al., 2009; Kamenetsky et al., 2010), the few studies of SMI in Archean environments have yet to demonstrate CO_2 in SMI.

Preliminary microthermometric analysis of a unit 4.3 SMI gave a first melting T of 692°C (Figure 18) which is somewhat higher than the solidus T expected for a felsic melt high in H_2O content and trapped at high P (500 – 600°C; Lutgens and Tarbuck, 2000). However, laser Raman microspectroscopy yielded spectra with negligible water band peaks (3500 – 3650 cm^{-1}) for homogenized glass in the SMI of units 2.0 and 5.3 (Figure 19A). The H_2O content was not quantified but based on the size of the H_2O peak corresponding to 0.95 wt% H_2O (Figure 19A) that are typical of hydrous SMI (Zajacz et al., 2005), the Bousquet SMI have <<1 wt% H_2O (Figure 19A). Petrographic and Raman spectroscopy observation (Figure 19B and C) show that silicate melt and immiscible CO_2 liquid were trapped at depth in a magma chamber or as the quartz phenocrysts ascended through the crust. Unhomogenized SMI show the immiscible CO_2 phase clearly (Figure 18) and therefore it is not an artifact of heating the inclusions.

Clearly, the Bousquet rhyolites were CO_2 saturated prior to eruption/emplacement and the evidence for immiscible entrapment of CO_2 in unambiguous (Figure 19). Commonly, the CO_2 saturation point and a decreased CO_2/H_2O ratio are reached by progressive

decompression and CO_2 exsolution while the magma rises to the surface (Lowenstern, 2001; Wallace, 2003). The rise to a shallower crustal environment reduces the pressure and CO_2 is lost due to first boiling (Moss et al., 1997). Carbon dioxide solubility drops dramatically because it is more a function of pressure than temperature. Deep mid crust magmas (10-15 km) under high pressure are commonly vapour saturated and CO_2 is an appreciable part of this exsolved vapour (Lowenstern, 2001). The temperature at which CO_2 is soluble is dependent on the speciation of CO_2 (Lowenstern, 2001). Carbon dioxide dissolves in rhyolites in a molecular form (retrograde temperature solubility), but typically dissolves as carbonate group minerals in basalts (prograde; Lowenstern, 2001).

However, the CO_2/H_2O ratio is very high in the Bousquet rhyolitic melts so the normal saturation and exsolution processes described above cannot be the only explanation. The amount of CO_2 observed in the inclusions is way beyond the amount soluble in a felsic melt even at high P (from Lowenstern, 1994: 960 ppm CO_2 at 4.3 kbar or 16 km) and so the melts did not exsolve that CO_2 after entrapment. If excess CO_2 was added to the system from an external source during its evolution, the Bousquet melts would have become CO_2-saturated forcing H_2O to exsolve (Frezzotti, 2001; Lowenstern, 2001). If the CO_2-bearing fluid was in constant contact with the melt, H_2O would continue to degas, and the resulting SMI would be H_2O-poor with immiscible CO_2 (Bodnar and Sterner, 1987; Joyce and Holloway, 1993; Lowenstern, 2001). It is difficult to determine where the CO_2 originated. One option is that during melt generation, storage, fractionation and ascent, a CO_2-bearing fluid was released from assimilated sedimentary rocks (Ganino et al., 2008; Blythe et al., 2015). This is consistent with trace element chemistries and mixed geochemical affinities (Figure 21B – F) of the Bousquet melts that could be due to the assimilation of Nb- and

Ta-depleted rocks. However, the only two relevant sedimentary rocks in the study area belong to the <2686 Ma Cadillac Group (Davis, 2002) and the <2676 Ma Timiskaming Group (Davis, 2002), these are younger than the volcanics and could not have been assimilated during emplacement/eruption.

There is evidence that CO_2-saturated magmas within the middle to upper crust cannot ascend through the crust without freezing (Frezzotti, 2001; Lowenstern, 2001). In general, adding CO_2 to a magma should cause it to crystallize as H_2O is distilled out, forcing the magma to cross its solidus and crystallize (Lowenstern, 2001). Importantly, this specific process of H_2O degassing only happens when CO_2 is added at a later stage in the evolution of the magma. Water will not degas before CO_2 under normal equilibrium (open or closed system) degassing of initially dissolved (primary) H_2O (Lowenstern, 2001). For example, if a rhyolitic magma follows a normal trend of equilibrium degassing, it will lose CO_2 first as pressure decreases and second as solids form (first and second "boiling," respectively). As quartz phenocrysts grow, they incorporate samples of melt ± saturated K-feldspar or other crystallized phases, and small droplets of immiscible CO_2. However, at this stage water has not been lost from the magma. With progressive decrease in P and/or combined crystallization, the droplets change from CO_2- to H_2O-rich (Yardley and Bodnar, 2014). A model degassing curve shows this change in dissolved volatile content as a magmatic system decompresses (rises through the crust) and crystallizes (Thomas et al., 2010).

Ultramafic arc magmas, however, are H_2O-poor with 0.54 – 4.25 wt.% dissolved H_2O as compared to 1.9 – 6.3 wt.% H_2O in typical primitive arc magmas at high pressures deep below the surface (Lowenstern, 2001; Créon et al., 2017). Ultimately, there was likely high

concentrations of CO_2 at the entrapment pressures of the Bousquet SMI to make free bubbles of CO_2 in the melt. However, the Bousquet rocks studied are rhyolites which have a lower CO_2 solubility than mafic liquids but could still have 1000s ppm of CO_2 because typical arc magmas, which are a combination of mafic and felsic liquids, have up to 2500 ppm CO_2 (Créon et al., 2017). Carbon dioxide saturation as seen in the homogenized SMI (i.e., free CO_2 bubbles) of the Bousquet volcanics indicates that degassing was in progress which made water contents drop down into the sub-weight percent range (Figure 19)

It is possible that metals could have been lost early in the evolution of the Bousquet magmas when melt interacted with a CO_2-rich lithology, like a basaltic melt (e.g., unit 5.4 basaltic andesite; Lowenstern, 2001). This type of interaction can disrupt normal fractionation and cause metal-rich fluids to leave the magmatic system (Lowenstern, 2001). Carbon dioxide may carry metals as well, but it is more likely that an exsolved saline aqueous fluid will be a more potent carrier (Lowenstern, 2001; Audétat et al., 2000, 2008). The metal contents of units 2.0 and 5.3 SMI are highly variable which could be the result of magma interaction with an external CO_2-bearing fluid, forcing the metals to leave along the whole fractionation path. This is also consistent with the lack of correlations observed between ore metals and strongly incompatible elements since periodic metal loss would destroy the normal (expected) differentiation relationships between elements like Cs and ore metals seen in fluid undersaturated melt systems (e.g., Audétat and Pettke, 2003; Figure 32).

It should be noted that while the SMI contain primary hydrous minerals (i.e., biotite, muscovite) the modal abundance and likely water content of these minerals are consistent with the SMI being H_2O-bearing but not necessarily H_2O-rich based on mass balance.

2.4.7 Pressure-temperature constraints on SMI entrapment

The concentrations of Ti in magmatic quartz saturated in rutile ($a_{TiO2} = 1$) provides the only numerical constraint on the P-T conditions (Thomas et al., 2010) of phenocryst growth and, therefore, SMI entrapment. Titanium-in-quartz concentrations were resolved from LA-ICP-MS analyses of the quartz host surrounding SMI as well as in magmatic quartz domains adjacent to SMI. Small, evenly distributed rutile needles (Figure 8C, E, and F) are abundant and were formed after the quartz crystallized during cooling-induced titanium exsolution (Adachi et al., 2010) or decompression (Zhang et al., 2003; Kawasaki and Motoyoshi, 2007; Adachi et al., 2010). It is unlikely that there were tiny rutile needles throughout the magma chamber that were then trapped in quartz because of the infrequent occurrence of primary rutile in felsic igneous rocks (Hayden and Watson, 2007). The initial amount of dissolved Ti in quartz before rutile exsolution can be reconstructed using a large beam diameter in-situ analytical method such as LA-ICP-MS or EMP (e.g., Adachi et al., 2010). Each spot analysis incorporates quartz and rutile needles.

Initially, it was observed that analyses of darker (CL) and/or fractured areas in the phenocrysts yielded low Ti concentrations probably reflecting quartz formed or modified during post-magmatic events (cf. Spear and Wark, 2009). In contrast, analyses of quartz from the brighter blue (CL) regions of phenocrysts gave higher and very consistent Ti

values considered to be magmatic concentrations (Spear and Wark, 2009). Hot CL and SEM-CL analyses of units 2.0 and 5.3 quartz phenocrysts showed that the targeted SMI (and host quartz for Ti determination) resided in these brighter magmatic domains. The range in Ti values for phenocrysts in both units is very small (Table 10).

The P-T conditions for quartz in units 2.0 and 5.3 were constrained by finding the intersection of the Ti-in-quartz T trajectories through P-T space with P constraints for the early crystallization of MIC Phases B and C which were established through Ti-in-zircon thermometry and Ti-in-quartz thermometry (Figure 33; Neyedley et al., 2021). The P-unconstrained Ti-in-quartz trajectories pass through the P-T window for early crystallizing phases (zircon, quartz) in the MIC phases B and C. The minimum and maximum P from those early MIC phases brackets the P-T window for the Bousquet quartz phenocrysts between ~6.5 – 13.5 kbar and ~650 - 850°C. Unit 2.0 phenocrysts yield a crystallization T range of 653 ± 33˚C (at 6.5 kbar) to 809 ± 39˚C (at 13.5 kbar), and unit 5.3 phenocrysts yield a crystallization T range of 686 ± 26˚C (at 6.5 kbar) to 848 ± 30˚C (at 13.5 kbar; Figure 33; Table 10). Textural and compositional observations (fine exsolution and narrow Ti concentration ranges) indicate that equilibrium was well established between rutile and quartz.

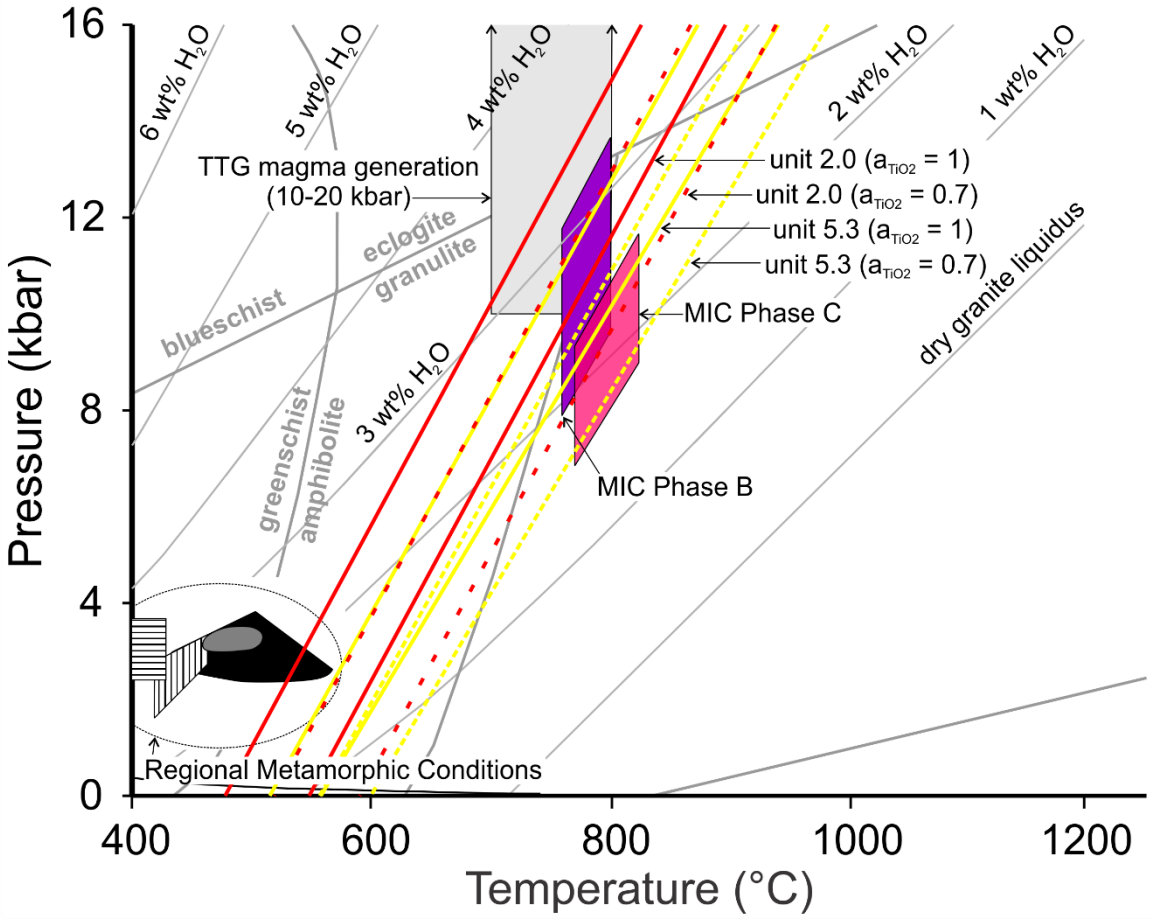

Figure 33: Pressure-temperature trapping conditions of Bousquet Formation SMI. Temperature trajectories (diagonal fields) calculated from Ti concentrations in quartz phenocrysts from unit 5.3 (n = 83), and unit 2.0 (n = 182), with a_{TiO2} of 1 (rutile saturated = solid lines) and 0.7 (ilmenite saturated = dashed lines). Pressure-temperature conditions for the MIC phases B and C are from Neyedley et al., 2021. Water-saturated granite liquidi at various dissolved H_2O concentrations are from Holtz and Johannes (1991). Maximum metamorphic conditions for the Bousquet Formation are from Tourigny et al. (1989, 1993), Marquis et al. (1990a), Mercier-Langevin (2005), and Yergeau et al. (2015). The P-T range of TTG magma generation is from Condie (2005), Clemens et al. (2006), Getsinger et al. (2009), and Hoffman et al. (2014).

In agreement with the MIC Phase B and C constraints on the P of phenocryst growth, the suggested TTG affinity of the volcanic source magma (Galley and Lafrance, 2014) requires a source depth of greater than ~10 kbar (Figure 33; Condie, 2005, Clemens et al., 2006, Getsinger et al., 2009, and Hoffman et al., 2014). Unit 2.0 and 5.3 phenocrysts grew at conditions that overlap with both the lower P range for TTG generation and Phase B/C zircon and quartz crystallization conditions. This is evidence that the Bousquet volcanics were linked to the MIC magma evolution, storage, and fractionation at depth.

The maximum metamorphic grade of the Bousquet Formation rhyolites is upper greenschist to lower amphibolite facies (Figure 33; Mercier-Langevin et al., 2007b). The black field in Figure 33 straddling the greenschist/amphibolite transition (Yergeau et al., 2015) yields a maximum pressure of 4 kbar and T of ~550°C for peak metamorphism (Tourigny et al., 1993; Marquis et al., 1990a). These conditions are at substantially lower P-T than the estimates of crystallization conditions of the quartz phenocrysts. If the P-T fields estimated for units 2.0 and 5.3 phenocrysts are extrapolated down to a lower P, only a small portion of the field for unit 2.0 intersects the upper end of the metamorphic field and most of the T window for both units 2.0 and 5.3 exceed the maximum metamorphic T of 550°C (Yergeau et al., 2015). However, this scenario is impossible since the phenocrysts contain SMI and entrapment T of a “normal” granitic liquid at such low T would be very unlikely.

The entrapment temperatures for both units at the lower P constraint are low for rhyolitic magmas but possible if saturated in volatiles in a high-pressure environment (Foley and Pintér, 2018). The liquidus and solidus of a rhyolite is lowered substantially at high

dissolved H_2O and CO_2 (Wallace and Green, 1988; Foley and Pintér, 2018). The H_2O-saturated liquidi (Figure 33) from Holtz and Johannes (1991) demonstrate that as the concentration of H_2O in the magma increases, the liquidus temperature decreases (Figure 33). For example, the 3 wt% H_2O liquidus shows the upper P-T limit that solids would exist in a magma with 3 wt% H_2O. It is important to note that, at the P-T conditions for SMI entrapment, the magma should contain ~3 wt% H_2O. As there is much less than 1 wt% H_2O in the SMI (Figure 19) this suggests that the magma had already degassed H_2O by the time of entrapment (i.e., by CO_2 incorporation causing H_2O exsolution; Lowenstern, 2001).

It is important to note that the Bousquet did not completely crystallize in situ. Instead, the volcanics were emplaced as very viscous partially crystallized magmas in which SMI had already been trapped at high pressures. The liquid CO_2 phase in the SMI is thought to be the result of volatiles mingling with the partially crystallized magma in a very high-pressure environment. The phenocryst, therefore, rose from a substantial depth in the crust.

In general, the results presented suggest that at considerable depth (i.e., a mid-crustal magma chamber) the Bousquet magmas had already lost several wt% H_2O and gained immiscible CO_2. This has very important implications not only for VMS systems but also for Archean Au deposits whose ore fluids contained high CO_2 contents derived from the degassing of wall rocks during metamorphism or interaction with TTG magmas (Lowenstern, 2001; Spilliaert et al., 2006b; Blundy et al., 2010; Hinsberg et al., 2016). Early volatile loss may reduce the fertility of VMS ore-related magmas while the Au content of the magmas may be sequestered into CO_2 that goes on to supply Au to Archean

gold deposits - but this investigation is beyond the scope of this paper. However, it is possible that this information provides a new direction of research as to the source of the fluids that produce Au deposits such as those in the DBL camp. Gold-enrichments in the DBL camp could be associated with fluids rich in Au (but no other metals) and CO_2 sourced from sedimentary wall rocks at depth that degassed deep in the crust during interaction with Bousquet-type magmas (Ganino et al., 2014).

2.4.8 Comparison of metal ratios in SMI and regional ore deposits

Previous studies of melt inclusions in magmatic-hydrothermal ore forming systems have shown that inclusion metal ratios overlap with ore metal ratios, indicating that magmatic liquids exert a direct control on ore tenor and metal ratios (e.g., Cu/Au) may be conservative (Halter et al., 2002). Ratios of Au/As, Sb/Bi, Cu/Au, and Cu/As in mineralized systems within the DBL district (Dubé et al., 2004; Geological Survey of Canada, unpublished) were compared to data from SMI (Appendix 2A and B) in the Bousquet Formation (Figure 34). While only one SMI has all these metals above detection limit for unit 5.3, unit 2.0 has several SMI analyses which show overlap in metal ratios (i.e., Au/As vs Sb/Bi, and Cu/Au vs Cu/As) with the LaRonde Penna ore bodies (i.e., Zn-rich 20N lens, Zn-rich 20S lens, and Au-rich 20N lens; Figure 34). Maximum and minimum metal ratios are included for SMI analyses that had metals below detection limit (Figure 34). The unit 2.0 rhyolite does not host the LaRonde Penna ore (vs. the unit 5.3 which hosts the majority of the 20N lens hanging wall zone) but is the earliest Bousquet Formation unit and is a sills complex emplaced in the stratigraphically lower Hébécourt Formation. Metal ratios in other deposits do not overlap with those of unit 2.0 SMI. Both

the SMI and LaRonde Penna ore bodies are characterized by low Au/As and Cu/As ratios, compared to the Mouska, Doyon and Westwood deposits. For example, Au/As ratios for unit 2.0 SMI analyses have an average of 0.004 and Doyon ore bodies have an average of 0.644, which is roughly a difference of 200x. The exact mechanism of metal transfer to the LaRonde Penna hydrothermal system is not known (e.g., metals lost through volatile exsolution, or passive leaching from volcanics) but this comparison suggests that metal tenors in the LaRonde Penna ores were controlled (at least locally) by the associated magmatic metal chemistry. There is a lack of correlation between very strongly incompatible elements (e.g., Cs) and ore metals (in SMI) which is consistent with disturbance of the original metal contents of SMI by immiscible or exsolving fluid phases. However, the overlap between metal ratios (i.e., Cu/Au, Cu/As, Au/As, Sb/Bi) of the SMI and the LaRonde Penna deposit ore bodies suggests that even in the presence of saturated volatiles, ore metal ratios are conservative. The overlap in metal ratios is an indication that the volcanic rocks have had some direct influence, either through active degassing or passive leaching, on the ore metal content of the LaRonde Penna VMS system.

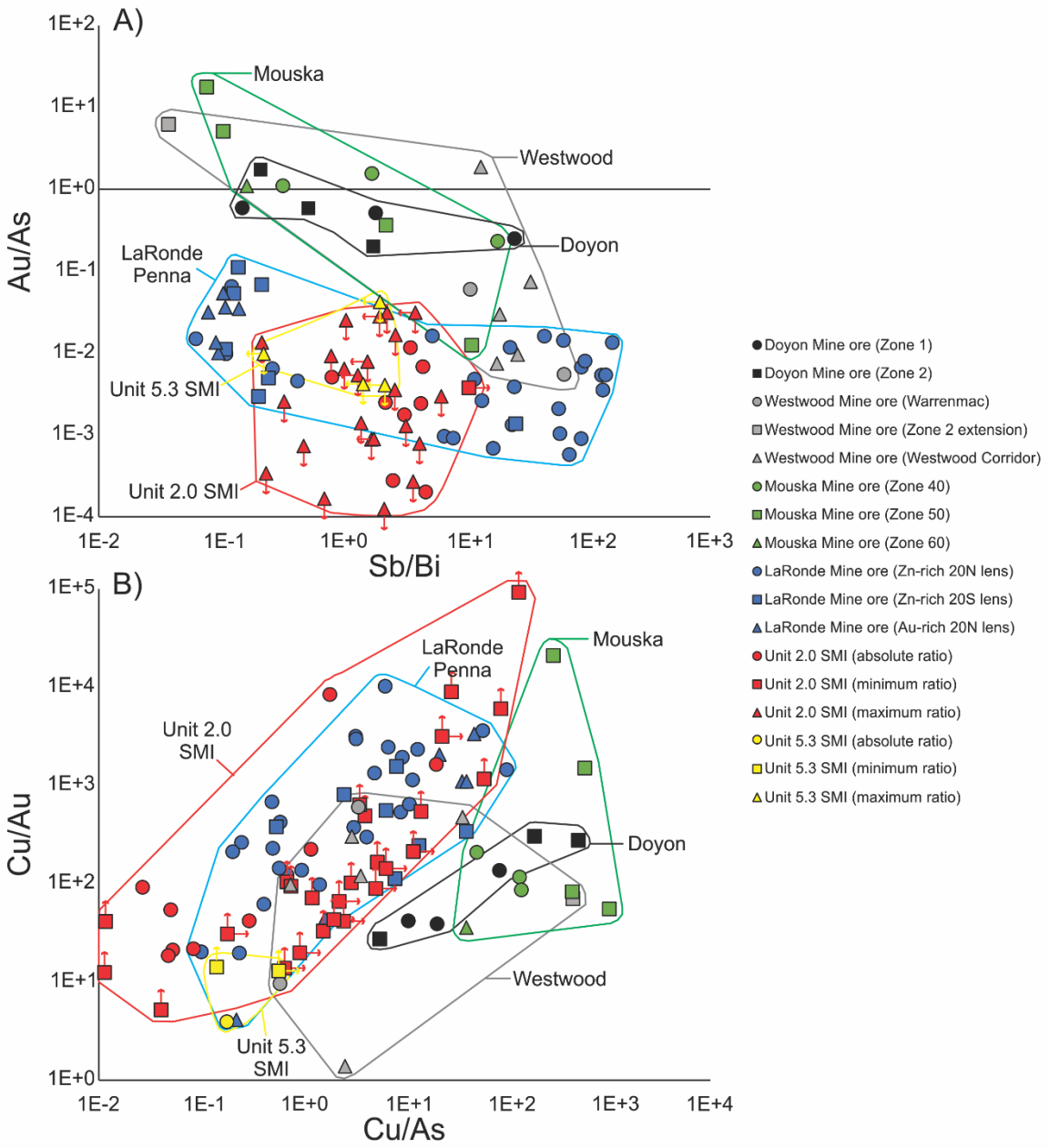

Figure 34: Ore metals compared to SMI metals of the Bousquet Formation. Metal ratios of Au/As vs Sb/Bi, and Cu/Au vs Cu/As in mineralized systems (i.e., Doyon Mine, Westwood Mine, Mouska Mine, and LaRonde Penna Mine) within the DBL district and SMI of the Bousquet Formation. Notes: Data for Doyon deposit, Westwood deposit, and Mouska deposit ores from the Geological Survey of Canada, unpublished. Data for LaRonde ore from Dubé et al., 2004.

2.4.9 Mass balance considerations

Figure 35 shows the absolute best-case scenario in terms of the volume of magma (in km^3) would have been required to source Au in the LaRonde Penna deposit, at various concentrations of Au in the magma (based on SMI measurements by LA-ICP-MS). By "best-case" scenario, this means that all the Au in the magma gets extracted and deposited. Therefore, this approximation relates to the minimum magma volume required. The SMI of unit 5.3 have a median of 0.069 ppm Au (1^{st} quartile = 0.006 ppm, 3^{rd} quartile = 0.159 ppm, n = 10) while unit 2.0 SMI have a median of 0.014 ppm Au (1^{st} quartile = 0.005 ppm, 3^{rd} quartile = 0.024 ppm, n = 14); at these Au concentrations, a minimum range of 0.5 – 15 km^3 and 4 – 19 km^3 of magma volume would be required, respectively, to produce the total amount of Au in the LaRonde Penna VMS deposits (Figure 35). Note that this is a very small amount of magma compared to the volume of magma estimated for other low-grade Au deposits (e.g., Cu porphyry deposit >1000 km^3; Chelle-Michou et al., 2017).

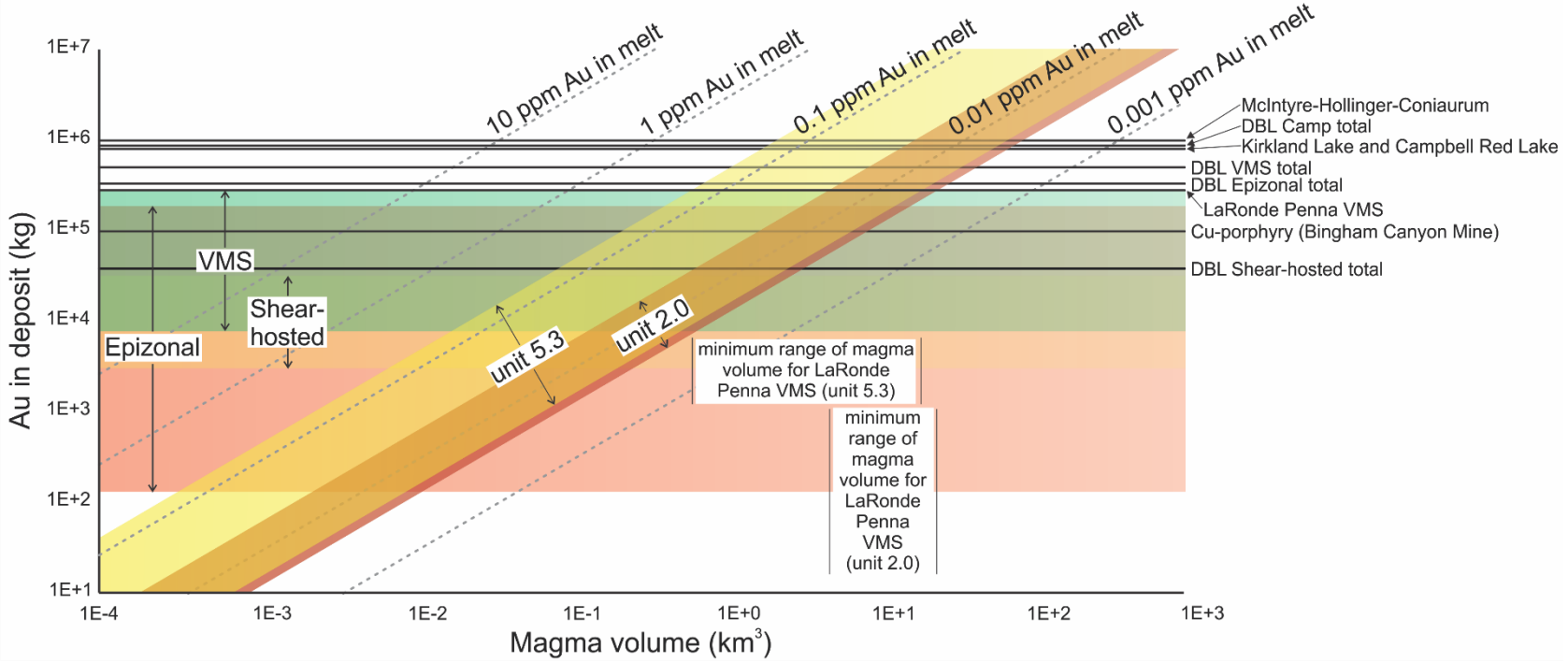

Figure 35: Amount of magma for Au tonnage. The amount of magma (in km^3) needed to supply various deposits with their Au tonnage (in kg) based on variable concentrations of Au (in ppm). Included are ranges for Au tonnage in deposit types (i.e., epizonal, VMS, and shear-hosted) of the DBL camp, as well as total Au tonnage for the DBL camp. For comparison, total Au tonnage for other world-class camps (i.e., McIntyre-Hollinger-Coniaurum, Kirkland Lake, and Campbell Red Lake), and for the Bingham Canyon Mine Cu-porphyry are presented. The ranges for minimum magma volume required to produce the LaRonde Penna VMS deposits are based on the Au concentrations of unit 2.0 and unit 5.3 melts. Unit 2.0 has a median Au concentration of 0.014 ppm, a 1st quartile of 0.005 ppm, and a 3rd quartile of 0.024 ppm. Unit 5.3 has a median Au concentration of 0.0695 ppm, a 1st quartile of 0.0064 ppm, and a 3rd quartile of 0.159 ppm. Notes: Data for DBL camp from Mercier-Langevin et al., 2017. Data for Bingham Canyon Mine from MDO Data Online, 2020. Data for McIntyre-Hollinger-Coniaurum, Kirkland Lake, and Campbell Red Lake from Mercier-Langevin et al., 2007a.

The calculations, as stated, assume that all Au in the magma is transferred to the deposit and that the magma represents the initial composition available for metal transfer. There are several reasons why this is not possible: (i) Not all the Au will be sequestered and transferred in a volatile phase by degassing. The efficiency of fluids leaving the magma and carrying gold is partly controlled by the partition coefficient ($K_D^{fluid/melt}$) which is a function of fluid and magma composition, and many other variables (Zajacz et al., 2012). The range in $K_D^{fluid/melt}$ for Au is ~10 - 100, respectively (Simon et al., 2005; Zajacz et al., 2012; Chiaradia and Caricchi, 2017). This means that under some conditions, most but not all the Au in the magma will go into the fluid phase. (ii) Not all the Au will be precipitated (i.e., as sulphides) from the fluid. For porphyry systems, Chiaradia (2020) showed quantitively that Au-rich deposits are the result of better efficiency of Au precipitation than Cu-rich porphyries but so far this type of modelling has not been done on a VMS system. In a VMS system, not all the Au that is carried by fluid will be precipitated efficiently because not all Au leaves the solution. Some Au remains tied up with ligands and gets dispersed in areas that do not form economic deposits. (iii) Not all the magma interacts with the volatiles, and only part of the magma volume may degas near structures in such a way that volatiles bearing Au can be transferred to the hydrothermal system (i.e., focusing of fluids; Sparks, 2003; Huber et al., 2012; Chelle-Michou et al., 2017). All three of these factors play into the efficiency of Au transfer - if the transfer from magma to fluid, and from fluid to deposit is less efficient, more magma (with the Au concentrations measured) will be needed to provide the same amount of Au to the deposit.

It is also important to note that in the case of the Bousquet melts, there is evidence of volatile loss (low H_2O) and the presence of abundant CO_2 (as a saturated phase introduced

before the time of entrapment), so it is likely that the SMI Au (and other metal) concentrations are minimum concentrations available to ore-forming processes. Thus, assuming transfer of all Au without the inefficiencies, even less magma than stated above would have been needed to source the Au in the LaRonde Penna VMS deposits.

Degassing of a magma is an "active" process to supply metals to a VMS system. "Passively" the metals are brought into the hydrothermal system by the convection of seawater through volcanic and sedimentary rocks. The metals, leached from glass (and fine-grained matrix crystals), in the subsurface volcanics sample metals from interstitial (quenched) melt. However, like magma degassing, this is not necessarily an efficient process because seawater would not circulate through the entire Bousquet Formation because the process of leaching/extraction by heated seawater is more localized to the vent locations (Scott and Binns, 1995). This is another example of the inefficiency of metal extraction from magmas or magmatic rocks. Thus, by either scenario (passive or active) the amount of Au and magma volumes shown in Figure 35 are minimum values.

Both units 2.0 and 5.3 were saturated in CO_2 which means that the higher concentrations of Au in unit 5.3 SMI are truly due to a difference in bulk composition of the melts. The upper member of the Bousquet Formation was clearly more enriched in Au even after CO_2 interaction and H_2O loss. Using Au concentrations from SMI in the upper member, and a conservative estimate of the volume of the upper member of the Bousquet Formation (approximately ~7.5 km^3;15 x 0.5 x 1km; Figure 3), approximately 0.5 – 15 km^3 of unit 5.3 melt [minimum of 0.069 ppm Au (1^{st} quartile = 0.006 ppm, 3^{rd} quartile = 0.159 ppm, n = 10)] would be needed to supply Au to the LaRonde Penna VMS deposits (Figure 35). It is important to reiterate that the melt may have already lost Au to a volatile phase (SMI are

saturated in carbonic fluid and have lost H_2O; see Section 2.4.6); therefore, the values measured in the SMI are minimums and, counteracting inefficiencies, the volumes of magma required may in fact be maximums rather than minimums.

Overall, there are two phenomena working in tandem to consider for the study area when calculating the amount of Au-bearing magma required to source Au in this district, if a magmatic source for Au is to be entertained (via degassing of magmatic volatiles): (i) parts of the magmatic system have degassed, and were saturated with externally-derived volatiles *at depth*, so the measured metal concentrations in the melts used in the calculations are likely minimum values; and (ii) there is an efficiency of Au transfer problem which means that not all the Au in the magma will be transferred to the volatile phase. It is a complex process to quantitatively evaluate these factors in the calculations of magma volume and it is beyond the scope of this paper. For these reasons, the amount of magma shown in Figure 35 that would be needed to supply Au to the deposits in the district are minimums.

2.5 Conclusion

A comprehensive study of silicate melt inclusions from the lower and upper Bousquet Formation, Blake River Group, Doyon-Bousquet-LaRonde mining district was undertaken to characterize the chemistry and volatile content of magmas in an Archean ore district, and to examine possible links between the original magmatic metal endowment and exceptionally Au-rich VMS deposits in the DBL camp. The key results of this study and implications are summarized below:

(i) Only two volcanic lithologies within the Bousquet Formation contain suitable SMI appropriate for detailed study: SMI within magmatic quartz phenocrysts of units 2.0 [quartz feldspar porphyry (QFP) rhyolite sills] and 5.3 (QFP rhyolite flows). Despite recrystallization, primary SMI are preserved in phenocrysts and have bulk compositions consistent chemically and mineralogically with trapped silicate liquids. Careful evaluation of each melt inclusion assemblage, based on petrographic and compositional criteria, is required to differentiate true SMI from hourglass-type inclusions and to evaluate contamination by accidental entrapment of saturated phases, or modification by post-entrapment modification. A combination of cathodoluminescence imaging, inclusion and host petrography (SEM, optical, Raman) and scrutiny of LA-ICP-MS data after analyses of single inclusions is required to do this robustly. Trace element dissemination based on LA-ICP-MS data show that unit 2.0 SMI are of ORG or WPG (anorogenic) tectonic settings whereas unit 5.3 SMI are consistent with a syn-COLG or VAG classification. However, no SMI have trace element (Sr-Y-La-Yb) characteristics consistent with Archean TTG, suggesting considerable compositional modification (e.g., by extensive plagioclase fractionation, and crustal contamination) prior to entrapment.

(ii) Even though the bulk compositions of the SMI and bulk rocks are similar and have similar tectonic affinity classifications, the range in major and trace elements, including ore metals, is much wider in the SMI. This reflects a combination of many processes: differentiation (prior to entrapment and eruption), crystal accumulation (diluting incompatible melt constituents in the rhyolites), possibly degassing/interaction with carbonic volatiles at depth, and post-solidus

alteration/metamorphism. Metal concentrations in bulk rocks assayed in this geological environment are *not* representative of the composition of the initial magmatic liquids.

(iii) Comparative analysis of apatite, SMI, and bulk rock data shows that at depth, prior to eruption-emplacement, the SMI and coeval apatite document the crystallization of significant amounts of plagioclase, K-feldspar, and apatite. SMI record significant differentiation of the rhyolite (at least 70 – 75% crystallization) over its entrapment history indicating a lengthy phenocryst residence at depth in a staging chamber or deeper source region. Based on preliminarly constraints from SMI homogenization experiments combined with Ti-in-quartz thermometry, SMI were trapped in quartz phenocrysts at P = 10 - 13.5 kbar, consistent with the predicted range of early paragenesis for the magmas of the Mooshla Intrustive Complex. Homogenized SMI show that co-entrapment of an immiscible carbonic fluid (CO_2-dominant) took place, suggesting that the melt was saturated in CO_2 at the time of entrapment in the phenocrysts. The presence of CO_2 in SMI of the Bousquet rhyolites, due to their advanced age, suggests that any SMI trapped in a magmatic system may potentially have CO_2 as a saturated phase. The Bousquet magmatic system continuously received CO_2-bearing fluids from an outside source, became CO_2 saturated, and underwent constant fractionation iterations with degassing causing early removal of metal-bearing H_2O fluids. Mingling of silicate melt with immiscible CO_2 (e.g., derived from wall rocks) may have stripped some ore metals out of the magma before entrapment in SMI.

(iv) The SMI of unit 5.3 have a range of 6 ppb Au (1st quartile) to 159 ppb Au (3rd quartile; n = 10) while unit 2.0 SMI have a range of 5 ppb Au (1st quartile) to 24 ppb Au (3rd quartile; n = 14); at these Au concentrations, a *minimum* of 0.5 – 15 km^3 and 4 – 19 km^3 of rhyolitic magma would be required, respectively, to source the Au in the LaRonde Penna VMS deposits through leaching or devolatilization. A conservative estimate of the volume of the Upper Member of the Bousquet Formation is approximately ~7.5 km^3. Therefore, it is not unwarranted that with a correction for efficiency, the rhyolitic units of the Bousquet Formation supplied magmatic Au to the VMS deposits. However, it is important to note that while these metal concentrations are well above upper crustal concentrations, the Bousquet Formation rhyolitic melts were not unusually evolved or enriched in ore metals when compared to younger, felsic magmas in arc and transitional ore-forming settings.

(v) The presence of co-entrapped carbonic liquid, and very low water content, in the SMI from both Units 5.3 and 2.0 may suggest that ore metal contents in the SMI are minimum values. A lack of correlation between very strongly incompatible elements (e.g., Cs) and ore metals (in SMI) is consistent with disturbance of the original metal contents of SMI by immiscible or exsolving fluid phases. On the other hand, selected metal ratios for elements consistently enriched in the SMI (Cu/Au, Cu/As, Au/As, Sb/Bi) overlap between the SMI and the LaRonde Penna deposit ore bodies and this is unlikely to be a coincidence, suggesting that even in the presence of saturated volatiles, these ore metal ratios are conservative. Both the SMI and ore bodies are characterized by low Au/As and Cu/As ratios, compared to the Mouska, Doyon and Westwood deposits. The overlap in metal ratios between the LaRonde Penna ore and

SMI is an indication that the volcanic rocks have had some direct influence, either through active degassing or passive leaching, on the ore metal content of the LaRonde Penna VMS system.

2.6 References

Abersteiner, A., Kamenetsky, V.S., Goemann, K., Giuliani, A., Howarth, G.H., Castillo Oliver, M., Thompson, J., Kamenetsky, M., and Cherry, A. (2019). Composition and emplacement of the Benfontein kimberlite sill complex (Kimberley, South Africa): Textural, petrographic and melt inclusion constraints. *Lithos, 324-325,* p. 297-314.

Adachi, T., Hokada, T., Osanai, Y., Toyoshima, T., Baba, S., and Nakano, N. (2010). Titanium behavior in quartz during retrograde hydration: Occurrence of rutile exsolution and implications for metamorphic processes in the Sør Rondane Mountains, East Antarctica. Polar Science, 3, p. 222-234.

Adam, J. and Green, T. (2006). Trace element partitioning between mica- and amphibole-bearing garnet lherzolite and hydrous basanitic melt: 1. Experimental results and the investigation of controls on partitioning behavior. *Contributions to Mineralogy and Petrology, 152,* p. 1-17.

Allen, R. L., Weihed, P., and Svesen, S-A (1996). Setting of Zn-Cu-Au-Ag massive sulfide deposits in the evolution and facies architecture of a 1.9 Ga marine volcanic arc, Skellefte district, Sweden: Economic Geology, v. 91, p. 1022-1053.

Alt, J. C. (1995). Sulfur isotopic profile through the oceanic crust - sulfur mobility and seawater-crustal sulfur exchange during hydrothermal alteration. *Geology, 23,* p. 585-588.

Andersen, T., and Neumann, E.R., (2001). Fluid inclusions in mantle xenoliths. Lithos 55, p. 299–318.

Anderson, A.T. (1991). Hourglass inclusions: Theory and application to the Bishop Rhyolitic Tuff. *American Mineralogist, 76,* p. 530-547.

Anderson, A.T. (1995). CO2 and the eruptibility of picrite and komatiite. *Lithos, 34(1-3),* p. 19-25.

Anderson, A.T., Davis, A.M., and Fangqiong, L. (2000). Evolution of Bishop Tuff Rhyolitic Magma Based on Melt and Magnetite Inclusions and Zoned Phenocrysts. *Journal of Petrology, 41(3),* p. 449-473.

Arribas, A., Jr., (1995). Characteristics of high-sulfidation epithermal deposits, and their relation to magmatic fluid. *Mineralogical Association of Canada Short Course Series, v. 23,* p. 419–454.

Audétat, A., Gunther, D. and Heinrich, C.A. (2000). Magmatic-hydrothermal evolution in a fractionating granite: A microchemical study of the Sn-W-F-mineralized Mole Granite (Australia). *Geochimica Et Cosmochimica Acta, 64,* p. 3373-3393.

Audétat, A., and Pettke, T. (2003). The magmatic-hydrothermal evolution of two barren granites: A melt and fluid inclusion study of the Rito del Medio and Cañada Pinabete plutons in northern New Mexico (USA). *Geochimica et Cosmochimica Acta, 67,* p. 97-121.

Audétat, A. and Pettke, T. (2006). Evolution of a porphyry-Cu mineralized magma system at Santa Rita, New Mexico (USA). *Journal of Petrology, 47,* p. 2021-2046.

Audétat, A., Pettke, T., Heinrich, C.A., and Bodnar, R.J. (2008). Special Paper: The Composition of Magmatic-Hydrothermal Fluids in Barren and Mineralized Intrusions. Economic Geology, 103, p. 877-908.

Ayer, J., Amelin, Y., Corfu, F., Kamo, S., Ketchum, J., Kwok, K., and Trowell, N. (2002). Evolution of the southern Abitibi greenstone belt based on U-Pb geochronology: Autochtonous volcanic construction followed by plutonism, regional deformation and sedimentation. *Precambrian Research, v. 115,* p. 63−95.

Bacon, C.R. (1989). Crystallization of accessory phases in magmas by local saturation adjacent to phenocrysts. *Geochimica et Cosmochimica Acta, 53,* p. 1055–1066.

Bacon, C.R. and Druitt, T.H. (1988). Compositional Evolution of the Zoned Calcalkaline Magma Chamber of Mount-Mazama, Crater Lake, Oregon. *Contributions to Mineralogy and Petrology 98(2),* p. 224-256.

Badanina, E.V., Veksler, I.V., Thomas, R., Syritso, L.F., and Trumbull, R.B. (2004). Magmatic evolution of Li–F, rare-metal granites: A case study of melt inclusions in the Khangilay complex, Eastern Transbaikalia (Russia). *Chemical Geology, 210,* p. 113-133.

Baker, D.A. (2008). The fidelity of melt inclusions as records of melt composition. *Contributions to Mineralogy and Petrology, 156,* p. 377–395.

Baker, E.T. (2009). Relationships between hydrothermal activity and axial magma chamber distribution, depth, and melt content. Geochemical and Geophysical Geosystems, 10, Q06009, 15 p. 1-15.

Ballhaus, C., Ryan, C.G., Mernagh, T.P., and Green, D.H. (1994). The partitioning of Fe, Ni, Cu, Pt, Au between sulfide, metal, and fluid phase: a pilot study. *Geochimica et Cosmochimica Acta, 58,* p. 811-826.

Banfield, J.F. and Eggleton, R.A. (1989). Apatite replacement and rare earth mobilization, fractionation and fixation during weathering. Clays and Clay Minerals,
37, p. 113–127.

Barbarin, B. (1990). Granitoids: Main petrogenetic classifications in relation to origin and tectonic setting. *Geological Journal, 25,* p. 227-238.

Barrett, T.J., and MacLean, W.H. (1993). Lithogeochemical technique using immobile elements. *Journal of Geochemical Exploration, 48(2)*, p. 109-133.

Barrett, T.J., MacLean, W.H., and Tennant, S.C. (2001). Volcanic sequence and alteration at the Parys Mountain volcanic hosted massive sulfide deposit, Wales, United Kingdom: Applications of immobile element lithogeochemistry; Economic Geology, v. 96, p. 1279-1306.

Barrie, C.T., Ludden, J.N., and Green, T.H. (1993). Geochemistry of volcanic rocks associated with Cu-Zn and Ni-Cu deposits in the Abitibi Subprovince. *Economic Geology, v. 88*, p. 1341–1358.

Barrie, C.T., Cathles, L.M., Erendi, A., Schwaiger, H., and Murray, C. (1999). Heat and fluid flow in volcanic-associated massive sulfide-forming hydrothermal systems. Reviews in Economic Geology, 8, p. 201-219.

Barrie, C.T., and Hannington, M.D. (1999). Introduction: Classification of volcanic-associated massive sulfide deposits based on host-rock composition. *Reviews in Economic Geology, 8*, p.2-10.

Bea, F. (1996). Residence of REE, Y, Th and U in granites and crustal protoliths; implications for the chemistry of crustal melts. Journal of Petrology, 37, p. 521-552.

Bea, F., Pereira, M.D. and Stroh, A. (1994). Mineral/leucosome trace-element partitioning in a peraluminous migmatite (a laser ablation-ICP-MS study). *Chemical Geology 117*, p. 291-312.

Beane, R. (1994). A graphic view of hydrothermal mineral stabilities, in Lentz, D.R., ed., Alteration and alteration processes associated with ore-forming systems: Geological Association of Canada, Short Course Notes, v. 11, p. 1–30.

Beaudoin, Y., Scott, S.D., Gorton, M.P., Zajacz, Z., and Halter, W. (2007). Pb and other ore metals in modern seafloor tectonic environments: evidence from melt inclusions. *Marine Geology, 242*, p. 271-289.

Beaudoin, G., Mercier-Langevin, P., Dubé, B., and Taylor, B.E. (2014). Low-temperature alteration at the world-class LaRonde Penna Archean Au-rich volcanogenic massive sulfide deposit, Abitibi Subprovince, Quebec, Canada: Evidence from whole-rock oxygen isotopes. Economic Geology, 109, p. 167-182.

Belkabir, A., and Hubert, C. (1995). Geology and structure of a sulfide-rich gold deposit: an example from the Mouska gold mine, Bousquet district, Canada. Economic Geology, 90, p. 1064-1079.

Belkabir, A., Hubert, C., and Hoy, L. (2004). Gold emplacement and hydrothermal alteration in metabasic rocks at the Mouska mine, Bousquet district, Abitibi, Quebec, Canada: *The Canadian Mineralogist, v. 42,* p. 1079-1096.

Belkin, H.E., De Vivo, B., Török, K., and Webster, J.D. (1998). Pre-eruptive volatile content, melt-inclusion chemistry, and microthermometry of interplinian Vesuvius lavas (pre-A.D. 1631). *Journal of Volcanology and Geothermal Research, 82(1-4),* p. 79-95.

Belousova E., Griffin W. L., O'Reilly S. Y., and Fisher N. (2002). Apatite as an indicator mineral for mineral exploration: Trace-element compositions and their relationship to host rock type. Journal of Geochemical Exploration, 76(1), p. 45-69.

Bergman Weihed J, Bergstrom U, Billstrom K, and Weihed P (1996). Geology, tectonic setting, and origin of the Paleoproterozoic Boliden Au–Cu–As deposit, Skellefte district, Northern Sweden. Economic Geology, 91, p.1073–1097.

Berkesi, M., Guzmics, T., Szabó, C., Dubessy, J., Bodnar, R.J., Hidas, K., and Ratter, K. (2012). The role of CO_2-rich fluids in trace element transport and metasomatism in the lithospheric mantle beneath the Central Pannonian Basin, Hungary, based on fluid inclusions in mantle xenoliths. Earth and Planetary Science Letters, 331–332 (15), p. 8 - 20.

Berry, A., Danyushevsky, L., O'Neill, St.C.H., Newville, M., and Sutton, S.R. (2008). Oxidation state of iron in komatiitic melt inclusions indicates hot Archaean mantle. *Nature, 455,* p. 960–963.

Binns, R.A., and Scott, S.D. (1993). Actively forming polymetallic sulfide deposits associated with felsic volcanic rocks in the eastern Manus back-arc basin, Papua New Guinea. Economic Geology, 88, p. 2226-2236.

Blevin, P.L., and Chappell, B.W. (1992). The role of magma sources, oxidation states and fractionation in determining the granite metallogeny of eastern Australia. Earth and Environmental Science Transactions of the Royal Society of Edinburgh, 83(1-2), 305-316.

Blundy, J., Cashman, K.V., Rust, A., and Witham, F. (2010). A case for CO2-rich arc magmas. *Earth and Planetary Science Letters, 290,* 289–301.

Blythe, L.S., Deegan, F.M., Freda, C., Jolis, E.M., Masotta, M. Misiti, V., Taddeucci, J., and Troll, V.R. (2015). CO_2 bubble generation and migration during magma–carbonate Interaction. *Contributions to Mineral Petrolpgy, 169:*42.

Bodnar, R.J., and Sterner, S.M. (1987). Synthetic fluid inclusions. *In:* Ulmer, G.C., Barnes, H.L. (eds.) Hydrothermal experimental techniques. *Wiley Interscience, New York,* p. 423 – 457.

Bodnar, R.J., and Student, J.J. (2006). Chapter 1: Melt inclusions in plutonic rocks: Petrography and microthermometry. In Melt inclusions in plutonic rocks. Edited by J.D. Webster. Mineralogical Association of Canada Short Course Series, 36.

Boily-Auclair, É., Mercier-Langevin, P., Ross, P.-S., and Pitre, D. (2020). Stratigraphic setting of the LZ5 and Ellison mineralized zones, LaRonde Zone 5 project, Doyon-Bousquet-LaRonde mining camp, Abitibi, Quebec; in Targeted Geoscience Initiative 5: Contributions to the Understanding of Canadian Gold Systems, (ed.) P. Mercier-Langevin, C.J.M. Lawley, and S. Castonguay; *Geological Survey of Canada, Open File 8712*, p. 57–73.

Bonnet, A.-L., and Corriveau, L. (2007). Alteration vectors to metamorphosed hydrothermal systems in gneissic terranes, in Goodfellow, W.D., ed., Mineral deposits of Canada—A synthesis of major deposit-types, district metallogeny, the evolution of geological provinces, and exploration methods: Geological Association of Canada, Mineral Deposits Division, Special Publication No. 5, p. 1035–1049.

Brauhart, C.W., Groves, D.I., and Morant, P. (1998). Regional alteration systems associated with volcanogenic massive sulfide mineralization at Panorama, Pilbara, Western Australia. Economic Geology, 93, p. 292-302.

Burnham, A.D. (2018). Zircon. In Reference Module in Earth Systems and Environmental Sciences.

Burnham, W.C. (1997). Magmas and hydrothermal fluids, in Barnes, H.L. ed., Geochemistry of hydrothermal ore deposits, 3rd ed.: New York, John Wiley and Sons, p. 63–123.

Buthelezi, M., Ashwal, L.D., and Horváth, P. (2017). Application of titanium-in-quartz geothermometry to magmatic quartz in evolved rocks from the Bushveld Complex, South Africa. *South African Journal of Geology, 120(2)*, p. 241–250.

Butterfield, D.A., Massoth, G.J., McDuff, R.E., Lupton, J.E., and Lilley, M.D. (1990). Geochemistry of hydrothermal fluids from axial seamount hydrothermal emissions study vent field, Juan de Fuca Ridge: subseafloor boiling and subsequent fluid-rock interaction. *Journal of Geophysical Research: Solid Earth, 95,* p.12895–12921.

Çağatay, M.N., and Boyle, D.R. (1977). Geochemical prospecting for volcanogenic sulfide deposits, eastern Black Sea region, Turkey: *Journal Geochemical Exploration, v.8*, p. 49-71.

Çağatay, M.N. (1993). Hydrothermal alteration associated with volcanogenic massive sulfide deposits: Examples from Turkey. *Economic Geology, 88*, p. 606-621.

Campbell, I.H., Franklin, J.M., Gorton, M.P., Hart, T.R., and Scott, S.D. (1981). The role of synvolcanic sills in the generation of massive sulfide deposits. Economic Geology, 76, p. 2248-2253.

Cannatelli, C., Doherty, A.L., Esposito, R., Lima, A., and De Vivo, B. (2016). Understanding a volcano through a droplet: A melt inclusion approach. Journal of Geochemical Exploration, 171, p. 4-19.

Carvalho, D., Barriga, F.J.A.S., and Munha, J. (1999). Bimodal-siliciclastic systems - The case of the Iberian Pyrite Belt, in Barrie, C.T., and Hannington, M.D., eds., Volcanic-Associated Massive Sulfide Deposits: Processes and Examples in Modern and Ancient Settings: Reviews in Economic Geology, v. 8, p. 375-402.

Castillo, P.R., Janney, P.E., and Solidum, R.U. (1999). Petrology and geochemistry of Camiguin Island, southern Philippines: Insights to the source of adakites and other lavas in a complex arc setting. *Contributions to Mineralogy and Petrology, v. 134,* p. 33–51.

Cathles, L.M. (1981). Fluid flow and genesis of hydrothermal ore deposits. Economic Geology 75th Anniversary Volume, p. 442-457.

Cathles, L.M., Erendi, A.H., and Barrie, T. (1997). How long can a hydrothermal system be sustained by a single intrusive event: *Economic Geology, 92,* p. 766-771.

Cervantes, P. Kamenetsky, V. and Wallace, P. (2002). Melt Inclusion Volatile Contents, Pressures of Crystallization for Hawaiian Picrites, and the Problem of Shrinkage Bubbles. American Geophysical Union, Fall Meeting 2002, abstract id. V22A-1217.

Chabiron, A., Alyoshin, A.P., Cuney, M., Deloule, E., Golubev, V.N., Velitchkin, V.I., and Poty, B. (2001). Geochemistry of the rhyolitic magmas from the Streltsovka caldera (Transbaikalia, Russia): A melt inclusion study. Chemical Geology, v. 175, p. 273–290.

Chabiron, A., Cuney. M., and Poty, B. (2003). Possible uranium sources for the largest uranium district associated with volcanism: The Streltsovka caldera (Transbaikalia, Russia). Mineralium Deposita, v. 38, p. 127–140.

Chelle-Michou, C., Rottier, B., Caricchi, L., & Simpson, G. (2017). Tempo of magma degassing and the genesis of porphyry copper deposits. *Scientific reports, 7,* 40566.

Chiaradia, M., Tripodi, D., Fontboté, L., and Reza, B. (2008). Geologic setting, mineralogy, and geochemistry of the Early Tertiary Au-rich volcanic-hosted massive sulfide deposit of La Plata, Western Cordillera, Ecuador. *Economic Geology, 103,* p.161–183.

Chiaradia, M. and Caricchi, L (2017). Stochastic modelling of deep magmatic controls on porphyry copper deposit endowment. *Science Repository, 7,* 44523.

Chiaradia, M (2020). Gold endowments of porphyry deposits controlled by precipitation efficiency. *Nature Communications.*

Chown, E.H., Daigneault, R., Mueller, W., and Mortensen, J.K. (1992). Tectonic evolution of the northern volcanic zone, Abitibi belt, Quebec. Canadian Journal of Earth Sciences, 29, p. 2211-2225.

Chukanov N.V., and Vigasina M.F. (2020). Raman Spectra of Minerals. In: Vibrational (Infrared and Raman) Spectra of Minerals and Related Compounds. Springer Mineralogy. Springer, Cham.

Chupin, V.P and Tomilenko, A.A. (1995). Melt and fluid inclusions in high-pressure minerals (kyanite, garnet, quartz): features of study and interpretation. *Bol. Soc. Esp. Mineral, 18,* p. 39-40.

Chupin, V.P., Vetrin, V.R., Rodionov, N.V., Matukov, D.I., Berezhnaya, N.G., and Sergeev, S.A. (2006). Composition of Melt Inclusions and Age of Zircons from Plagiogneisses of the Archean Complex in the Kola Superdeep Borehole, Baltic Shield, *Doklady Earth Sciences, Vol. 406(1),* p. 153–157.

Christenson, B.W. (2000). Geochemistry of fluids associated with the 1995–1996 eruption of Mt. Ruapehu, New Zealand: Signatures and processes in the magmatic-hydrothermal system. *Journal of Volcanology and Geothermal Research, v. 97,* p. 1–30.

Clemens, J.D., Yearron, L.M., and Stevens, G. (2006). Barberton (South Africa) TTG magmas: geochemical and experimental constraints on source-rock petrology, pressure of formation and tectonic setting. *Precambrian research, v. 151,* p. 53-78.

Colley, H., and Rice, C.M. (1975). A Kuroko-type ore deposit in Fiji. *Economic Geology, 70,* p. 1373–1386.

Condie, K.C. (2005). TTGs and adakites: are they both slab melts? *Lithos, v. 80,* p. 33-44.

Créon, L., Rouchon, V., Youssef, S., Rosenberg, E., Delpech, G., Szabó, C., Remusat, L., Mostefaoui, S., Asimow, P.D., Antoshechkina, P.M., Ghiorso, M.S., Boller, E., Guyot, F. (2017). Highly CO_2-supersaturated melts in the Pannonian lithospheric mantle – A transient carbon reservoir? *Lithos, 286-287,* p. 519 – 533.

Créon, L., Levresse, G., Remusat, L., Bureau, H., and Carrasco-Núñez, G. (2018). New method for initial composition determination of crystallized silicate melt inclusions. *Chemical Geology, 483,* p. 162-173.

Danyushevsky, L.V. (2001). The effect of small amounts of H2O on crystallisation of mid ocean ridge and backarc basin magmas. *Journal of Volcanology and Geothermal Research, 110(3-4),* p. 265-280.

Danyushevsky, L.V., McNeill, A.W., and Sobolev, A.V. (2002). Experimental and Petrological studies of melt inclusions in phenocrysts from mantle-derived magmas: an overview of techniques, advantages and complications. *Chemical Geology, 183,* p. 5-24.

Dasgupta, R., Hirschmann, M.M., and Dellas, N. (2005). The effect of bulk composition on the solidus of carbonated eclogite from partial melting experiments at 3 GPa. *Contributions to Mineralogy and Petrology, 149,* p. 288–305.

Davidson, J.P., Hora, J.M., Garrison, J.M. and Dungan, M.A. (2005). Crustal forensics in arc magmas. *Journal of Volcanology and Geothermal Research, 140,* p. 157-170.

Davis, D.W. (2002). U-Pb geochronology of Archean metasedimentary rocks in the Pontiac and Abitibi subprovinces, Quebec, constraints on timing, provenance, and regional tectonics. *Precambrian Research, 115*, p. 97−117.

Debreil, J.-A., Ross, P.-S., and Mercier-Langevin, P. (2018). The Matagami District, Abitibi Greenstone Belt, Canada: Volcanic controls on Archean volcanogenic massive sulfide deposits associated with voluminous felsi volcanism. *Economic Geology, v. 113(4),* p. 891-910.

Defant, M.J., and Drummond, M.S. (1990). Derivation of some modern arc magmas by melting of young subducted lithosphere: *Nature, v. 347,* p. 662–665.

Defant, M.J., and Drummond, M.S. (1993). Mount St. Helens: Potential example of the partial melting of the subducted lithosphere in a volcanic arc: *Geology, v. 21,* p. 547–550.

De Ronde, C.E.J., (1995). Fluid chemistry and isotopic characteristics of seafloor hydrothermal systems and associated VMS deposits—Potential for magmatic contributions, in Thompson, J.F.H., ed., Magmas, fluids and ore deposits: Ottawa, Ontario, *Mineralogical Association of Canada Short Course Series, v. 23,* p. 479–510.

De Ronde, C.E.J., Hannington, M.D., Stoffers, P., Wright, I.C., Ditchburn, R.G., Reyes, A.G., Baker, E.T., Massoth, G.J., Lupton, J.E., Walker, S.L., Greene, R.R., Soong, C.W.R., Ishibashi, J., Lebon, G.T., Bray, C.J., and Resing, J.A. (2005). Evolution of a submarine magmatic-hydrothermal system: Brothers Volcano, Southern Kermadec Arc, New Zealand. *Economic Geology, v.100,* p. 1097-1133.

De Souza, Z.S., Potrel, A., Lafon, J.-M., Althoff, F.J., Pimentel, M.M., Dall'Agnol, R., and De Oliveira, C.G. (2001). Nd, Pb and Sr isotopes in the Identidade Belt, an Archaean greenstone belt of the Rio Maria region (Caraja´s Province, Brazil): implications for the

Archaean geodynamic evolution of the Amazonian Craton. *Precambrian Research, 109,* p. 293-315.

De Vivo, B., and Bodnar, R.J. (2003). *Melt inclusions in volcanic systems: Methods, applications, and problems* (1st ed.). Elsevier, 274 p.

DeVore, G.W. (1969). Differential thermal contractions and compressibilities as a cause for mineral fracturing and annealing. *Rocky Mountain Geology, 8(1),* p. 21-36.

Dietrich, A., Lehmann, B., and Wallianos, A. (2000). Bulk Rock and Melt Inclusion Geochemistry of Bolivian Tin Porphyry Systems. *Economic Geology, 95,* p. 313-326.

Dimroth, E., Imreh, L., Goulet, N., and Rocheleau, M. (1983a). Evolution of the south-central part of the Archean Abitibi belt, Quebec. Part II: Tectonic evolution and geomechanical model: *Canadian Journal of Earth Sciences, v. 20,* p. 1355–1373.

Dimroth, E., Imreh, L., Goulet, N., and Rocheleau, M. (1983b). Evolution of the south-central part of the Archean Abitibi belt, Quebec. Part III: Plutonic and metamorphic evolution and geotectonic model: *Canadian Journal of Earth Sciences, v. 20,* p. 1374–1388.

Dixon J.E., Stolper E.M., and Holloway J.R. (1995). An experimental study of water and carbon dioxide solubilities in mid-ocean ridge basaltic liquids. Part I: calibration and solubility models. Journal of Petrology, 36,1607-1631.

Doyle, M.G., and Allen, R.L. (2003). Subsea-floor replacement in volcanichosted massive sulfide deposits: Ore Geology Reviews, v. 23, p. 183–222.

Doyle, M.G., and McPhie, J. (2000). Facies architecture of a silicic intrusiondominated volcanic centre at Highway-Reward, Queensland, Australia: Journal of Volcanology and Geothermal Research, v. 99, p. 79-96.

Dragovic, B., Baxter, E.F., and Caddick, M.J. (2015). Pulsed dehydration and garnet growth during subduction revealed by zoned garnet geochronology and thermodynamic modeling, Sifnos, Greece. *Earth and Planetary Science Letters, 413,* p. 111-122.

Dubé, B., Mercier-Langevin, P., Hannington, M.D., Davis, D.W., and Lafrance, B. (2004). Le gisement de sulfures massifs volcanogènes aurifères LaRonde, Abitibi, Quebec: Altération, minéralisations, et implications pour l'exploration. Ministère des Ressources naturelles, de la Faune et des Parcs, Quebec Report MB 2004-03, 112.

Dubé, B., Gosselin, P., Mercier-Langevin, P., Hannington, M.D., and Galley, A. (2007a). Gold-rich volcanogenic massive sulphide deposits, in Goodfellow, W.D., ed., Mineral Deposits of Canada: A Synthesis of Major Deposit-Types, District Metallogeny, the

Evolution of Geological Provinces, and Exploration Methods: Geological Association of Canada, Mineral Deposits Division, Special Publication No. 5, p. 75-94.

Dubé, B., Mercier-Langevin, P., Hannington, M.D., Lafrance, B., Gosselin, G., and Gosselin, P. (2007b). The LaRonde Penna world-class Au-rich volcanogenic massive sulfide deposit, Abitibi, Quebec: Mineralogy and geochemistry of alteration and implications for genesis and exploration.
Economic Geology, 102, p. 633−666.

Dubé, B., Mercier-Langevin, P., Kjarsgaard, I., Hannington, M., Bécu, V., Côté, J., Moorhead, J., Legault, M., and Bédard, N. (2014). The Bousquet 2-Dumagami world-class Archean Au-rich volcanogenic massive sulfide deposit, Abitibi, Quebec: Metamorphosed submarine advanced argillic alteration footprint and genesis. Economic Geology, 109, p. 121-166.

Dubé, B., and Mercier-Langevin, P. (2015). Targeted Geoscience Initiative 4: Contributions to the Understanding of Precambrian Lode Gold Deposits and Implications for Exploration; Geological Survey of Canada, Open File 7852, p. 1 - 293.

Dusel-Bacon, C., Wooden, J.L., and Hopkins, M.J. (2004). U-Pb zircon and geochemical evidence for bimodal mid-Paleozoic magmatism and syngenetic base-metal mineralization in the Yukon-Tanana Terrane, Alaska; Geological Society of America Bulletin, v. 116, p. 989-1015.

El-Bouseily, A.M., and El-Sokkary, A.A. (1975). The relation between Rb, Ba, and Sr in granitic rocks. *Chemical Geology, 16(3),* p. 207-219.

Ertl, A., Pertlik, F., and Bernhardt, H.-J. (1997). Investigations on Olenite with Excess Boron from the Koralpe, Styria, Austria. *Anzeiger Abt. I, 134,* p. 3-10.

Ewart, A. and Griffin, W.L. (1994). Application of Proton-Microprobe Data to Trace-Element Partitioning in Volcanic-Rocks. Chemical Geology 117(1-4): 251-284.

Fedele, L., Bodnar, R.J., DeVivo, B., and Tracy, R. (2003). Melt inclusion geochemistry and computer modeling of trachyte petrogenesis at Ponza, Italy. *Chemical Geology, 194,* p. 81 – 104.

Fenner, C.N. (1933). Pneumatolytic processes in the formation of minerals and ores, in Ore deposits of the Western States (Lindgren volume): New York, American Institute of Mining and Metallurgical Engineers, p. 58-106.

Fillion, M., Vallee, M., and Lavoie, C. (1977). Les gisements d'or de la SOQUEM Silverstack, Canton Bousquet, Quebec. *CIM Bulletin, 70,* p. 159−172.

Fleet, M.E., and Wu, T.W. (1995). Volatile transport of precious metals at 1000˚C: Speciation, fractionation, and effect of base-metal sulfide. *Geochimica Cosmochimica Acta, 59,* p. 487-495.

Foley, S.F., and Pintér, Z. (2018). Chapter 1: Primary melt compositions in the Earth's mantle. In Magmas under pressure: advances in high-pressure experiments on structure and properties of melts. Amsterdam, Netherlands: Elsevier.

Foley, S.F., Barth, M.G. and Jenner, G.A. (2000). Rutile/melt partition coefficients for trace elements and an assessment of the influence of rutile on the trace element characteristics of subduction zone magmas. Geochimica et Cosmochimica Acta 64(5): 933-938.

Franklin, J.M., Kasarda, J., and Poulsen, K.H. (1975). Petrology and chemistry of the alteration zone of the Mattabi massive sulfide deposit. *Economic Geology, 70,* p. 63–79.

Franklin, J.M., Lydon, J.W., and Sangster, D.F. (1981). Volcanic associated massive sulfide deposits. Economic Geology, 75th Anniversary Volume, p. 485-627.

Franklin, J.M., Gibson, H.L., Jonasson, I.R. and Galley, A.G. (2005). Volcanogenic Massive Sulphide Deposits: in Hedenquist, J.W., Thompson, J.F.H., Goldfarb, R.J., and Richards, J.P., eds., *Economic Geology, 100th Anniversary Volume, The Economic Geology Publishing Company,* p. 523-560.

Frelinger, S.N., Ledvina, M.D., Kyle, J.R., and Zhao, D. (2015). Scanning electron microscopy cathodoluminescence of quartz: Principles, techniques and applications in ore geology. *Ore Geology Reviews, 65,* p. 840-852.

Frezzotti, M-L. (2001). Silicate-melt inclusions in magmatic rocks: applications to petrology. *Lithos, 55,* p. 273-299.

Frondel, J.W. (1975). Lunar mineralogy, p. 323. New York: Wiley-Interscience.

Frondel, C. and Marvin, U.B. (1959). Cerianite, CeO2, from Pocos de Caldas, Brazil. *American Mineralogist, 44,* p. 882–884.

Gaal, G., (1977). Structural features of Precambrian stratabound sulfide-ore deposits in Finland: *Geologiska Föreningens I Stockholm Förhandlingar, v. 99,* p. 118-126.

Gaboury, D., and Pearson, V. (2008). Rhyolite geochemical signatures and association with volcanogenic massive sulfide deposits: Examples from the Abitibi Belt, Canada. *Economic Geology, v. 103,* p. 1531-1562.

Galley, A.G. (1993). Characteristics of semi-conformable alteration zones associated with volcanogenic massive sulphide districts. *Journal of Geochemical Exploration, v. 48*, p. 175–200.

Galley, A.G. (1996). Geochemical characteristics of subvolcanic intrusions associated with Precambrian massive sulfide deposits. *Geological Association of Canada Short Course Notes, 12,* p. 239-278.

Galley, A. G. (2003). Composite synvolcanic intrusions associated with Precambrian VMS-related hydrothermal systems. *Mineralium Deposita, 38,* p. 443–473.

Galley, A.G., and Pilote, P. (2002). Géologie et métallogénie de l'intrusion de Mooshla, district minier de Bousquet, Cadillac, Québec: *Ministère des Ressources naturelles du Québec, DV 2002-10,* p. 37.

Galley, A.G., Pilote, P., and Davis, D. (2003). Metallogeny of the subvolcanic Mooshla Intrusive Complex, Bousquet mining district, Quebec [abs.]. Timmins 2003 Field Conference, Ore deposits at Depth: *Challenges and Opportunities, Technical Sessions Abstract,* p. 17.

Galley, A.G., and Lafrance, B. (2007). Évolution et métallogénie du pluton de Mooshla: *Ministère des Ressources naturelles et de la Faune, ET 2007-02,* 31 p.

Galley, A.G., and Lafrance, B. (2014). Setting and evolution of the Archean synvolcanic Mooshla Intrusive Complex, Doyon-Bousquet-LaRonde mining camp, Abitibi greenstone belt: emplacement history, petrogenesis, and implications for Au metallogenesis. *Economic Geology, 109,* p. 205-229.

Galley, A. G., Hannington, M. D., and Jonasson, I. R. (2007). Volcanogenic massive sulphide deposits. Mineral Deposits of Canada: A Synthesis of Major Deposit-Types, District Metallogeny, the Evolution of Geological Provinces, and Exploration Methods. *Geological Association of Canada, Mineral Deposits Division, Special Publication No. 5,* p. 141-161.

Ganino, C., Arndt, N., Zhou, M.-F., Gaillard, F., and Chauvel, C. (2008). Interaction of magma with sedimentary wall rock and magnetite ore genesis in the Panzhihua mafic intrusion, SW China. *Mineralium Deposita, Spinger, 43,* p.677-694.

Ganino, C., Arndt, N., Chauvel, C., and Tornos, F. (2014). Metamorphic degassing of carbonates in the contact aureole of the Aguablanca Cu–Ni–PGE deposit, Spain. *Contributions to Mineralogy and Petrology, 168,* 1053.

Gaudreau, R. (1986). Intrusion syn-volcanique et minéralisations aurifères: Exemple du Intrusive complexe de Mooshla, Canton de Bousquet, Abitibi. *Unpublished M.Sc. thesis, Québec, Canada, Université Laval, 47.*

Getsinger, A., Rushmer, T., Jackson, M.D., and Baker, D. (2009). Generating High Mg-numbers and Chemical Diversity in Tonalite-Trondhjemite-Granodiorite (TTG) Magmas during Melting and Melt Segregation in the Continental Crust: *Journal of Petrology, v. 50,* p. 1935-1954.

Ghiorso, M.S. (1984). Activity/composition relations in the ternary feldspars. *Contributions to Mineralogy and Petrology, 87,* p. 282-296.

Gibson, H. (1999). Submarine volcanic processes, deposits, and environments favorable for the location of volcanic-associated massive sulfide deposits: *Reviews in Economic Geology, v. 8,* p. 13–52.

Gibson, H.L., Morton, R.L., and Hudak, G.J. (1999). Submarine volcanic processes, deposits, and environments favorable for the location of volcanicassociated massive sulfide deposits: *Reviews in Economic Geology, v. 8,* p. 13–51.

Gibson, H. L., and Galley, A. G. (2007). Volcanogenic massive sulphide deposits of the Archean, Noranda District, Quebec. In W. D. Goodfellow, Mineral deposits of Canada: A synthesis of major deposit-types, district metallogeny, the evolution of geological provinces, and exploration methods, special publication No. 5, Mineral Deposits Division, Geological Association of Canada, p. 533-552.

Gibson, H.L., Allen, R.L., Riverin, G., and Lane, T.E. (2007). The VMS model: Advances and application to exploration targeting. Ore Deposits and Exploration Technology, 49. *In* "Proceedings of Exploration 07: Fifth Decennial International Conference on Mineral Exploration" edited by B. Milkereit, 2007, p. 713-730.

Gieré, R., and Sorensen, S.S. (2004). Allanite and Other REE-Rich Epidote-Group Minerals. Reviews in Mineralogy and Geochemistry, 56, p. 431-493.

Giggenbach, W.F. (1996). Chemical composition of volcanic gases, in Tilling, R.I., and Scarpa, R., eds., Monitoring and mitigation of volcano hazards: Berlin, Springer-Verlag, p. 221–256.

Gilligan, L.B., and Marshall, B. (1987). Textural evidence for remobilization in metamorphic environment: *Ore Geology Reviews, v. 2,* p. 399-404.

Glasby, G.P., Yamanaka, T., Yamamoto, J., Sato, H., and Notsu, K., (2004). Kuroko and hydrocarbon deposits from northern Honshu, Japan: a possible common hydrothermal/magmatic origin? *Resource Geology 54,* p. 413–425.

Glasby, G.P., Iizasa, K., Hannington, M., Kubota, H., and Notsu, K. (2008). Mineralogy and composition of Kuroko deposits from northeastern Honshu and their possible modern

analogues from the Izu-Ogasawara (Bonin) Arc south of Japan: Implications for mode of formation. *Ore Geology Reviews, 34,* p. 547-560.

Goldstein, R.H. (2003). Petrographic analysis of fluid inclusions. *In* I. Samson, A. Anderson, and D. Marshall, eds. Fluid Inclusions: Analysis and Interpretation. *Mineralogical Association of Canada, Short Course 32,* 9-54.

Goodfellow, W.D., and Zierenberg, R.A. (1999). Genesis of massive sulfide deposits at sediment-covered spreading centers: *Reviews in Economic Geology, v. 8*, p. 297–324.

Goodrich, C.A., Treiman, A.H., Filiberto, J., Gross, J., and Jercinovic, M. (2013). K_2O rich trapped melt in olivine in the Nakhla meteorite: Implications for petrogenesis of nakhlites and evolution of the Martian mantle. *Meteoritics & Planetary Science, 48,* p. 2371-2405.

Gosselin, G., (1998). Veines de quartz aurifères précoces à la zone ouest de la mine Doyon, Canton de Bousquet, Preissac, Abitibi. *Unpublished M.Sc. thesis, Chicoutimi, Canada, Université du Québec à Chicoutimi, 128*.

Götze, J. (2012). Application of cathodoluminescence microscopy and spectroscopy in geosciences. Microscopy and Microanalysis, 18, p. 1270-1284.

Götze, J., Plötze, M., and Habermann, D. (2001). Origin, spectral characteristics and practical applications of the cathodoluminescence (CL) of quartz - a review. Contributions to Mineralogy and Petrology, 71, p. 225-250.

Gray, T.R., Hanley, J.J., Dostal, J., and Guillong, M. (2011). Magmatic enrichment of uranium, thorium, and rare earth elements in late Paleozoic rhyolites of southern New Brunswick, Canada: Evidence from silicate melt inclusions. Economic Geology, 106, p. 127-143.

Green, D.H., and Falloon, T.J. (2015). Mantle-derived magmas: intraplate, hot-spots and mid-ocean ridges. *Science Bulletin, 60,* p. 1873-1900.

Gromet, L.P., and Silver, L.T. (1983). Rare earth element distributions among minerals in a grandiorite and their petrogenetic implications. *Geochimica Cosmochimica acta, 47*, p. 925-939.

Guha, J., Gauthier, A., Vallée, M., Descareaux, J., and Lange-Brard, F. (1983). Gold mineralization patterns at the Doyon mine (Silverstack), Bousquet, Quebec: *Canadian Institute of Mining and Metallurgy Special Volume 24*, p. 50−57.

Guillong, M. M., Maier, D.L., Allan, M.M., Heinrich, C.A., and Yardley, B.W.D. (2008). Appendix A6: SILLS: a MATLAB based program for the reduction of laser ablation ICP-MS data of homogeneous materials and inclusions. In Laser Ablation ICP-MS in the Earth

Sciences: Current Practices and Outstanding Issues. Edited by P. Sylvester. Mineralogical Association of Canada Short Course Series, 40.

Gunning, H.C. (1941). Region de Bousquet-Joannes, Quebec. Geological Survey of Canada Memoir 206, 80.

Guo, J., and Green, T.H. (1989). Barium partitioning between alkali feldspar and silicate liquid at high temperature and pressure. *Contributions to Mineralogy and Petrology, 102,* p. 328-335.

Gurenko, A.A., Hansteen, T.H., and Schmincke, H.-U. (1996). Evolution of parental magmas of Miocene shield basalts of Gran Canaria (Canary Islands): constraints from crystal, melt and fluid inclusions in minerals. *Contrib. Mineral. Petrol. 124,* 422–435.

Halbach, P.E., Fouquet, Y., and Herzig, P. (2003). Mineralization and compositional patterns in deep-sea hydrothermal systems. In: Halbach, P.E., Tunnicliffe, V., Hein, J.R. (Eds.), Energy and Mass Transfer in Marine Hydrothermal Systems. *Dahlem University Press, Berlin,* p. 85–122.

Halter, W.E., Pettke, T., Heinrich, C.A., and Rothern-Rutishauser, B. (2002a). Major to trace element analysis of melt inclusions by laser-ablation ICP-MS: method of quantification. *Chemical Geology, 183,* p. 63-86.

Halter, W.E., Pettke, T., and Heinrich, C.A. (2002b). The origin of Cu/Au-ratios in porphyry-type ore deposits: *Science, 296,* p. 1844–1846.

Halter, W.E., Pettke, T., and Heinrich, C.A. (2004). Laser-ablation ICP-MS analysis of silicate and sulfide melt inclusions in an andesitic complec I: analytical approach and data evaluation. *Contributions to Mineralogy and Petrology, v. 147,* p. 385-396.

Halter, W.E., Heinrich, C.A., and Pettke, T., (2005). Magma evolution and the formation of porphyry Cu-Au ore fluids: Evidence from silicate and sulfide melt inclusions. *Mineralium Deposita, 39,* p. 845–863.

Hamlyn, P., Keays, R.R., Cameron, W.E., Crawford, A.J., and Waldron, H.M. (1985). Precious metals in magnesian low-Ti lavas: Implications for metallogenesis and sulfur saturation in primary magmas: *Geochimica et Cosmochimica Acta, v. 49,* p. 1797–1811.

Hanley, J.J., Mungall, J.E., Pettke, T., Spooner, E.T.C., and Bray, C.J. (2008). Fluid and Halide Melt Inclusions of Magmatic Origin in the Ultramafic and Lower Banded Series, Stillwater Complex, Montana, USA. *Journal of Petrology, 49(6),* p. 1133-1160.

Hannington, M.D., Peter, J.M., and Scott, S.D. (1986). Gold in Sea-Floor Polymetallic Sulfide Deposits, *Economic Geology, 81,* p. 1867-1883.

Hannington, M.D., Jonasson, I.R., Herzig, P.M., and Petersen, S. (1995). Physical and chemical processes of seafloor mineralization at mid-ocean ridges, in Seafloor Hydrothermal Systems: Physical, Chemical, Biological and Geological Interactions, (eds.) S.E. Humphris, R.A. Zierenberg, L.S. Mullineaux, and R.S. Thomson; *American Geophysical Union, Monograph 91,* p. 115-157.

Hannington, M.D., Poulsen, K.H., Thompson, J.F.H., and Sillitoe, R.H., (1999). Volcanogenic gold in the massive sulfide environment, in Barrie, C.T., and Hannington, M.D., eds., Volcanic-Associated Massive Sulfide Deposits: Processes and Examples in Modern and Ancient Settings: *Reviews in Economic Geology, Vol. 8,* p. 325-356.

Hannington, M.D., Santaguida, F., Kjarsgaard, I.M., and Cathles, L.M. (2003). Regional-scale hydrothermal alteration in the central Blake River Group, western Abitibi subprovince, Canada—Implications for VMS prospectivity. *Mineralium Deposita, v. 38,* p. 392–422.

Hannington, M.D., de Ronde, C.E.J., and Petersen, S., 2005, Sea floor tectonics and submarine hydrothermal systems, in Economic Geology One Hundredth Anniversary Volume, 1905-2005, (eds.) J.W. Hedenquist, J.F.H., Thompson, R.J., Goldfarb, and J.P., Richards; Society of Economic Geologists, p. 111-142.

Hansen, J., Skjerlie, K.P., Pedersen, R.B., and De La Rosa, J. (2002). Crustal melting in the lower parts of island arcs: an example from the Bremanger Granitoid Complex, west Norwegian Caledonides; *Contributions to Mineralogy and Petrology, v. 143,* p. 316-335.

Hansteen, T.H., Andersen, T., Neumann, E.R., and Jelsma, H. (1991): Fluid and silicate glass inclusions in ultramafic and mafic xenoliths from Hierro, Canary Islands: implications for mantle metasomatism. *Contrib. Mineral. Petrol., 107,* p. 242-254.

Harris, N.B.W., Pearce, J.A., and Tindle, A.G. (1986). Geochemical characteristics of collision-zone magmatism. In: Coward, M.P., Ries, A.C. (Eds.), Collision Tectonics. *Geological Society Special Publications, London,* pp. 67–81.

Hart, C.J.R., Mair, J.L., Goldfarb, R.J., and Groves, D.I. (2004). Source and redox controls on metallogenic variations in intrusion-related ore systems, Tombstone-Tungsten Belt, Yukon Territory, Canada. *Transactions of the Royal Society of Edinburgh GSA Special Paper 389 95,* p. 339-356

Hayden, L.A., and Watson, E.B. (2007). Rutile saturation in hydrous siliceous melts and its bearing on Ti-thermometry of quartz and zircon. Earth and Planetary Science Letters, 258, p. 561-568.

Hedenquist, J.W., and Lowenstern, J.B. (1994). The role of magmas in the formation of hydrothermal ore deposits. Nature, 370, p. 519-527.

Heinrich, C.A., Pettke, T., Halter, W.E., Aigner-Torres, M., Audétat, A., Günther, D., Hattendorf, B., Bleiner, D., Guillong, M., and Horn, I. (2003). Quantitative multi-element analysis of minerals, fluid and melt inclusions by laser-ablation inductively-coupled-plasma mass spectrometry. Geochimica et Cosmochimica Acta, v. 67, p. 3473–3497.

Jamali, Hemayat. (2016). The behavior of rare-earth elements, zirconium and hafnium during magma evolution and their application in determining mineralized magmatic suites in subduction zones: Constraints from the Cenozoic belts of Iran. *Ore Geology Reviews. 81*.

Hemley, J.J., and Jones, W.R. (1964). Chemical aspects of hydrothermal alteration with emphasis on hydrogen metasomatism: Economic Geology, v. 59, p. 538–569.

Hermann, J., Spandler, C., Hack, A., and Korsakov, A.V. (2006). Aqueous fluids and hydrous melts in high-pressure and ultra-high pressure rocks: implications for element transfer in subduction zones. *Lithos, 92,* p. 399–417.

Herrington, R.J., Zaykov, V.V., Maslennikov, V.V., Brown, D., and Puchkov, V.N. (2005b). Mineral deposits of the Urals and links to geodynamic evolution. In: Hedenquist JW, Thompson JFH, Goldfarb RJ, Richards JR (eds) *Economic geology one hundredth anniversary volume 1905-2005,* p. 1069–1095.

Harrison, T.M., and Watson, E.B., (1984). The behavior of apatite during crustal anatexis: Equilibrium and kinetic considerations: *Geochimica et Cosmochimica Acta, 48,* p. 1467–1477.

Herzig, P. M., Hannington, M. D. and Arribas, A. (1998). Sulfur isotopic composition of hydrothermal precipitates from the Lau back-arc: Implications for magmatic contributions to seafloor hydrothermal systems. *Mineralium Deposita, 33,* p. 226-237.

Hoffman, J.E., Nagel, T.J., Münker, C., Naeraa, T., and Rosing, M.T. (2014). Constraining the process of Eoarchean TTG formation in the Itsaq Gneiss Complex, southern West Greenland. *Earth and Planetary Science Letters, v. 388,* p. 374-386.

Hogan, J. P. (1993). Monomineralic glomerocrysts: textural evidence for mineral resorption during crystallization of igneous rocks. *Journal of Geology101,* p. 531–540.

Holloway, J.R. (1976). Fluids in the evolution of granitic magmas: Consequences of finite CO2 solubility. *GSA Bulletin, 87(10),* p. 1513–1518.

Holloway, J.R. (1981) Volatile Interactions in Magmas. In: Newton, R.C., Navrotsky, A., and Wood, B.J. (eds) Thermodynamics of Minerals and Melts. Advances in Physical Geochemistry, vol 1. Springer, New York, NY.

Holtz, F., and Johannes, W. (1991). Genesis of Peraluminous Granites I. Experimental Investigation of Melt Compositions at 3 and 5 kb and Various H+O Activities. *Journal of Petrology, 32(5),* p. 935-958.

Hoskin, P.W.O., Kinny, P.D., Wyborn, D., and Chappell, B.W. (2000). Identifying Accessory Mineral Saturation during Differentiation in Granitoid Magmas: An Integrated Approach. *Journal of Petrology, 41(9),* p. 1365-1396.

Huber C., Bachmann O., Vigneresse J.-L., Dufek J. and Parmigiani A. (2012). A physical model for metal extraction and transport in shallow magmatic systems. *Geochemistry Geophysics Geosystems, 13,* Q08003.

Hubert, C., Trudel, P., and Gélinas, L., 1984, Archean wrench-fault tectonics and structural evolution of the Blake River Group, Abitibi belt, Quebec: *Canadian Journal of Earth Sciences,v. 21,* p. 1024–1032.

Huston, D.L. (2000). Gold in volcanic-hosted massive sulfide deposits; distribution, genesis, and exploration, in Hagemann, S.G. ed., Gold in 2000: Reviews in Economic Geology, v. 13, p. 401-426.

Huston, D.L., and Large, R.R. (1989). A chemical model for the concentration of gold in volcanogenic massive sulphide deposits. *Ore Geology Review, 4,* p.171–200.

Huston, D.L., Relvas, J., Gemmell, J.B., and Drieberg, S. (2011). The role of granites in volcanic-hosted massive sulfide ore-forming systems: What is their contribution to the ores? Mineralium Deposita, 46, p. 473-507.

Hutchinson, R.W. (1973). Volcanogenic sulfide deposits and their metallogenic significance: Economic Geology, v. 68, p. 1223–1246.

Hutchinson, R.W. (1980). Massive base metal sulphide deposits as guides to tectonic evolution, in Strangway, D.W., ed., *Geological Association of Canada Special Paper 20,* p. 659–684.

Ikramuddin, M., Lipschutz, M.E., and Van Schmus, W.R. (1975). Effect of thermal metamorphic conditions on mineralogy and trace element retention in the Allende meteorite. *Nature, v. 253,* p. 703-705.

Ioannou, S.E., Spooner, E.T.C., and Barrie, C.T. (2007). Fluid temperature and salinity characteristics of the Matagami volcanogenic massive sulfide district, Quebec. Economic Geology, 102, p. 691-715.

Ishihara, S. (2007). Origin of the Cenozoic–Mesozoic magnetite-series and ilmenite-series granitoids in East Asia. Gondwana Research, 11, p. 247-260.

Jamieson, J.W., Wing, B.A., Farquhar, J., and Hannington, M.D. (2012). Neoarchaean seawater sulphate concentrations from sulphur isotopes in massive sulphide ore. *Nature Geoscience, 6,* p. 61-64.

Javoy, M., and Pineau, F. (1991). The volatiles record of a "popping' rock from the Mid-Atlantic Ridge at 14°N: chemical and isotopic composition of gas trapped in the vesicles. Earth and Planetary Science Letters, 107, p. 598-611.

Joyce, D.B., and Holloway, J.R. (1993). An experimental determination of the thermodynamic properties of H2O-CO2-NaCl fluids at high pressures and temperatures. *Geochimica Cosmochimica Acta, 75,* p. 733 – 746.

Kamenetsky, V.S., Crawford, A.J., Eggins, S., and Muhe, R. (1997). Phenocryst and melt inclusion chemistry of near-axis seamounts, Valu Fa Ridge, Lau Basin: insight into mantle wedge melting and addition of subduction components. *Earth Planet. Sci. Lett. 151*, 205–223.

Kamenetsky, V.S., Wolfe, R.C., Eggins, S.M., Mernagh, T.P. and Bastrakov, E. (1999). Volatile exsolution at the Dinkidi Cu-Au porphyry deposit, Philippines: A melt-inclusion record of the initial ore-forming process. *Geology, 27,* p. 691-694.

Kamenetsky, V.S., Gurenko, A.A., and Kerr, A.C. (2010). Composition and temperature of komatiite melts from Gorgona Island, Colombia, constrained from olivine-hosted melt inclusions, *Geology, 38(11),* p. 1003-1006.

Kawasaki, T., and Motoyoshi, Y. (2007). In: Cooper, A., Raymond, C. (Eds.), Antarctica: A Keystone in a Changing World. US Geological Survey Open-File Report 2007-1047. Solubility of TiO2 in garnet and orthopyroxene: Ti thermometer for ultra-high temperature granulites. doi:10.3133/of2007-1047.srp038 Short Research Paper 038.

Keith, J.D., Whitney, J.A., Hattori, K., Ballantyne, G.H., Christiansen, E.H.,
Barr, D.L., Cannan, T.M., and Hook, C.J. (1997). The role of magmatic sulfides and mafic alkaline magmas in the Bingham and Tintic mining districts, Utah. Journal of Petrology, 38, p. 1679–1690.

Keith, J.D., Pulsipher, T., Maughan, D.T., Waite, K.A., Christiansen, E.H., and Tingey, D.G. (1999). New developments in the geological understanding of magmatic processes that generate porphyry and associated ore deposits. In: New developments in the geological understanding of some major ore types and environments, with implications for exploration. Prospectors and Developers Association of Canada Short Course Proceedings, p. 47–63.

Kent, Adam. (2008). Melt Inclusions in Basaltic and Related Volcanic Rocks. *Reviews in Mineralogy & Geochemistry, 69,* p. 273-331.

Kerr, D.J., and Mason, R. (1990). A re-appraisal of the geology and ore deposits of the Horne mine complex at Rouyn-Noranda, Quebec: *Canadian Institute of Mining and Metallurgy Special Volume 43,* p. 153−165.

Kerrick, D.M., and Connolly, J.A.D. (1998). Subduction of ophicarbonates and recycling of CO_2 and H_2O. *Geology, 26,* p. 375–378.

Lafrance, B., Moorhead, J., and Davis, D.W. (2003a). Cadre géologique du camp minier de Doyon-Bousquet-LaRonde: Ministere des Ressources naturelles, de la Faune et des Parcs. Quebec Reports ET 2002-07, 45.

Lafrance, B., Mercier-Langevin, P., Dubé, B., Galley, A.G., Hannington, M.D., Davis, D.W., Moorhead, J., Pilote, P., and Mueller, W.U. (2003b). Carte synthèse de la Formation de Bousquet : partie est : *Ministère des Ressources naturelles, de la Faune et des Parcs du Québec, DV 2003-08,* scale 1:20 000.

Lafrance, B., Mercier-Langevin, P., Dubé, B., Galley, A.G., Hannington, M.D., Davis, D.W., Moorhead, J., Pilote, P., and Mueller, W.U. (2003c). Carte synthèse de la Formation de Bousquet: partie ouest: *Ministère des Ressources naturelles, de la Faune et des Parcs du Québec, DV 2003-08,* scale 1:20 000.

Lafrance, B., Davis, D.W., Goutier, J., Moorhead, J., Pilote, P., Mercier-Langevin, P., Dubé, B., and Galley, A. (2005). Nouvelles datations isotopiques dans la portion quebecoise du Groupe de Blake River et des unites adjacentes: Ministere des Ressources naturelles et de la Faune. Quebec Report RP 2005-01, 26.

Lamadrid, H.M., Lamb, W.M., Santosh, M., and Bodnar, R.J. (2014). Raman spectroscopic characterization of H_2O in CO_2-rich fluid inclusions in granulite facies metamorphic rocks. *Gondwana Research, 26,* p. 301-310.

Langshur, A. (1990). The geology, geochemistry and structure of the Mooshla intrusion, Bousquet mining centre, Quebec. Unpublished M.Sc. thesis, Ottawa, Canada, University of Ottawa, 172.

Large, R.R. (1992). Australian volcanic-hosted massive sulfide deposits: Features, styles and genetic models: *Economic Geology, v. 87,* p. 471–510.

Large, R.R., Allen, R.L., Blake, M.D., and Herrmann, W. (2001a). Hydrothermal alteration and volatile element halos for the Rosebery K Lens volcanic-hosted massive sulphide deposit, western Tasmania, *Economic Geology, 96,* p. 1055–1072.

Large, R.R., McPhie, J., Gemmell, J.B., Herrmann, W., and Davidson, G.J. (2001b). The spectrum of ore deposit types, volcanic environments, alteration halos, and related exploration vectors in submarine volcanic successions: Some examples from Australia: *Economic Geology, v. 96,* p. 1037-1054.

Larocque, A.C., Hodgson, C.J., and Lafleur, P.-J. (1993). Gold Distribution in the Mobrun Volcanic-Associated Massive Sulfide Deposit, Noranda, Quebec: A Preliminary Evaluation of the Role of Metamorphic Remobilization, *Economic Geology, 88*, p. 1443-1459.

Le Bas, M.J., Le Maitre, R.W., Streckeisen, A., and Zanettin, B. (1986). A chemical classification of volcanic rocks based on the total alkali-silica diagram. *Journal of petrology, 27(3),* p. 745-750.

Le Voyer, M., Asimow, P.D., Mosenfelder, J.L., Guan, Y., Wallace, P.J., Schiano, P., Stolper, E.M., and Eiler, J.M., (2014). Zonation of H_2O and F concentrations around melt inclusions in olivines. *Journal of Petrology, 55,* p. 1–23.

Lerchbaumer, L. and Audétat, A. (2013). The Metal Content of Silicate Melts and Aqueous Fluids in Subeconomically Mo Mineralized Granites: Implications for Porphyry Mo Genesis. *Economic Geology, 108,* p. 987-1013.

Lilley, M.D., Butterfield, D.A., Lupton, J.E., and Olson, E.J., 2003, Magmatic events can produce rapid changes in hydrothermal vent chemistry. *Nature, v. 422,* p. 878–881.

London, D. (1986). Formation of tourmaline-rich gem pockets in miarolitic pegmatite. *American Mineralogist, 71,* p. 396-405.

Lovering, J.F., and Wark, D.A. (1974). Rare earth element fractionation in phases crystallising from lunar late-stage magmatic liquids (abstract). In: Lunar science-V, pp. 445-446. Houston: The Lunar Science Institute.

Lowenstern, J.B. (1994). Dissolved volatile concentrations in an ore-forming magma. *Geology, 22,* p. 893-896.

Lowenstern, J. B. (2001). Carbon dioxide in magmas and implications for hydrothermal systems. *Mineralium Deposita, 36,* p. 490-502.

Lowenstern, J.B. (2003). Melt inclusions come of age: volatiles, volcanoes, and sorby's legacy. B. de Vivo, R.J. Bodnar (Eds.), Developments in Volcanology. Melt inclusions in Volcanic Systems: Methods, Applications and Problems (2003), pp. 1-21.

Lu, F., Anderson, A.T., and Davis, A.M. (1995). Diffusional gradients at the crystal/melt interface and their effect on the composition of melt inclusions. *Journal of Geology, 103,* p. 591–597.

Lutgens, F.K., and Tarbuck, E.J. (2000). Essentials of Geology, 7th Ed., Prentice Hall.

Lydon, J.W. (1984). Ore deposit models: Volcanogenic massive sulphide deposits. Part 1: A descriptive model. *Geoscience Canada, 11,* p. 195–202.

Lydon, J.W. (1988). Ore deposit models: Volcanogenic massive sulphide deposits. Part 2: Genetic models: *Geoscience Canada, 15,* p. 43–65.

Lydon, J.W., (1996). Characterisitcs of volcanogenic massive sulphide deposits: Interpretation in terms of hydrothermal convection systems and magmatic-hydrothermal systems: *Instituto Technologico Geominero de Espaņa, Bolitin Geologico y Minero, v. 107*, p. 15−64.

Malaspina, N., Scambelluri, M., Poli, S., Van Roermund, H.L.M., and Langenhorst, F. (2010). The oxidation state of mantle wedge majoritic garnet websterites metasomatised by C-bearing subduction fluids. *Earth and Planetary Science Letters, 298,* p. 417-426.

Manley, C.R. (1996). Morphology and maturation of melt inclusions in quartz phenocrysts from the Badlands rhyolite flow, southwestern Idaho. American Mineralogist, 81, p. 158–168.

Manzini, M., Bouvier, A.-S., Barnes, J.D., Bonifacie, M., Rose-Koga, E.-F., Ulmer, P., Métrich, N., Bardoux, G., Williams, J., Layne, G.D., Straub, S., Baumgartner, L.P., and John, T. (2017). SIMS chlorine isotope analyses in melt inclusions from arc settings. *Chemical Geology, 449,* p. 112-122.

Marques, A.F.A., Scott, S.D., Gorton, M.P., Barriga, F.J.A.S., and Fouquet, Y. (2009). Pre-eruption history of enriched MORB from the Menez Gwen (37 degrees 50 " N) and Lucky Strike (37 degrees 17 " N) hydrothermal systems, Mid-Atlantic Ridge. *Lithos, 112,* p. 18-39.

Marques, A.F.A., Scott, S.D., and Guillong, M. (2011). Magmatic degassing of ore-metals at the Menez Gwen: input from the Azores plume into an active Mid-Atlantic Ridge seafloor hydrothermal system. *Earth and Planetary Science Letters, 310,* p. 145-160.

Marques, A.F.A., Relvas, J.M.R.S., Scott, S.D., Rosa, C., and Guillong, M. (2020). Melt inclusions in quartz from felsic volcanic rocks of the Iberian Pyrite Belt: Clues for magmatic ore metal transfer towards VMS-forming systems. *Ore Geology Reviews, 126,* 103743.

Marquis, P., Hubert, C., Brown, A.C., and Rigg, D.M. (1990a). Overprinting of early, redistributed Fe and Pb-Zn mineralization by late-stage Au-Ag-Cu deposition at the Dumagami mine, Bousquet district, Abitibi, Quebec: Canadian Journal of Earth Sciences, v. 27, p. 1651−1671.

Marquis, P., Hubert C., Brown, A.C., and Rigg, D.M. (1990b). An evaluation of genetic models for gold deposits of the Bousquet district, Quebec, based on their mineralogical,

geochemical and structural characteristics. Canadian Institute of Mining and Metallurgy Special volume 24, p. 383−399.

Marquis, P., Brown, A.C., Hubert, C., and Rigg, D.M. (1990c). Progressive alteration associated with auriferous massive sulfide bodies at the Dumagami Mine, Abitibi greenstone belt, Quebec: *Economic Geology, v. 85*, p. 746-764.

Marshall, B., and Gilligan, L. (1987) An introduction to remobilization: Information from ore-body geometry and experimental considerations, *Ore Geology Reviews, 2,* p. 87-131.

Marshall, B. and Gilligan, L. (1993). Remobilization, syn-tectonic processes and massive sulphide deposits, *Ore Geology Reviews, 8,* p. 39-64.

Marshall, B., Vokes, F.M., and Larocque, A.C.L. (2000). Regional metamorphic remobilization: Upgrading and formation of ore deposits, *Reviews in Economic Geology, 11,* p. 19-38.

Martin, H. (1999). Adakitic magmas: modern analogues of Archaean granitoids. *Lithos, 46(3),* p. 411 – 429.

Marumo, K. (1989). Genesis of kaolin minerals and pyrophyllite in Kuroko deposits of Japan: implications for the origins of the hydrothermal fluids from mineralogical and stable isotope data. *Geochim Cosmochim Acta 53*, p. 2915–2924.

Mathieu, L. (2018). Quantifying hydrothermal alteration: A review of methods. *Geosciences, 8(7),* 245 p.

Matthews, N.E., Huber, C., Pyle, D.M., and Smith, V.C. (2012). Timescales of Magma Recharge and Reactivation of Large Silicic Systems from Ti Diffusion in Quartz. *Journal of Petrology, 53(7),* p.1385–1416.

Maughan, D.T., Keith, J.D., Christiansen, E.H., Pulsipher, T., Hattori, K., and Evans, N.J. (2002). Contributions from mafic alkaline magmas to the Bingham porphyry Cu–Au–Mo deposit, Utah, USA. *Mineralium Deposita, 37,* p. 14–37.

Maulana, A., Watanabe, K., Imai, A., and Yonezu, K. (2013). Origin of magnetite- and ilmenite-series granitic rocks in Sulawesi, Indonesia: Magma genesis and regional metallogenic constraint. Procedia Earth and Planetary Science, 6, p. 50-57.

McDonough W.F. and Ireland T.R., (1993). Intraplate origin of komatiites inferred from trace elements in glass inclusions: *Nature, v. 365,* p. 432–434.

McDonough, W.F. and Sun, S.-S. (1995). Composition of the Earth. *Chemical Geology, 120,* p. 223-253.

McInnes, B., and Cameron, E., (1994). Carbonated alkaline hybridizing melts from a sub-arc environment: Mantle wedge samples from the Tabar-Feni-Lihir-Tanga-Feni Arc, Papua New Guinea: Earth and Planetary Science Letters, v. 122, p. 125–141.

McNicoll, V., Goutier, J., Dubé, B., Mercier-Langevin, P., Ross, P-S., Dion, C., Monecke, T., Legault, M., Percival, J., and Gibson, H. (2014). U-Pb geochronology of the Blake River Group, Abitibi greenstone belt, Quebec, and implications for base metal exploration. Economic Geology, 109, p. 27–59.

Mercier-Langevin, P. (2005). Geologie du gisement de sulfures massifs volcanogenes auriferes LaRonde, Abitibi, Quebec. Unpublished Ph.D. thesis, Quebec, Canada, Institut National de la Recherche Scientifique, Centre Eau, Terre et Environnement, 689.

Mercier-Langevin, P., Dubé, B., Hannington, M.D., Davis, D.W., and Lafrance, B. (2004). Contexte geologique et structural des sulfures massifs volcanogenes auriferes du Gisement LaRonde, Abitibi. Ministere des Ressources naturelles, de la Faune et des Parcs, Quebec, Report ET 2003-03, 47.

Mercier-Langevin, P., Dubé, B., Lafrance, B., Hannington, M., Galley, A., Moorhead, J., and Gosselin, P. (2007a). Metallogeny of the Doyon-BousquetLaRonde mining camp, Abitibi greenstone belt, Quebec, *in* Goodfellow, W.D., ed., Mineral deposits of Canada: A synthesis of major deposit-types, district metallogeny, the evolution of geological provinces, and exploration methods: Mineral Deposits Division, Geological Association of Canada, Special Publication no. 5, p. 673–701.

Mercier-Langevin, P., Dubé, B., Hannington, M.D., Davis, D.W., Lafrance, B., and Gosselin, G. (2007b). The LaRonde Penna Au-rich volcanogenic massive sulfide deposit, Abitibi greenstone belt, Quebec: Part 1 - Geology and geochronology. Economic Geology, 102, p. 585−609.

Mercier-Langevin, P., Dubé, B., Hannington, M.D., Richer-Lafleche, M., and Gosselin G. (2007c). The LaRonde Penna Au-rich volcanogenic massive sulfide deposit, Abitibi greenstone belt, Quebec: Part 2 - Lithogeochemistry and paleotectonic setting. Economic Geology, 102, p. 611−631.

Mercier-Langevin, P., Dubé, B., LaFrance, B., Hannington, M.D., Galley, A., Marquis, R., Moorhead, J., and Davis, D.W. (2007d). A group of papers devoted to the Laronde Penna Au-rich volcanogenic massive sulfide deposit, Eastern Blake River Group, Abitibi Greenstone Belt, Quebec: Preface. *Economic Geology, 102,* p. 577-583.

Mercier-Langevin, P., Ross, P.-S., Lafrance, B., and Dubé, B. (2008). Volcaniclastic rocks of the Bousquet scoriaceous tuff units north of the LaRonde Penna mine, Doyon-Bousquet-LaRonde mining camp, Abitibi greenstone belt, Quebec. Geological Survey of Canada Current Research Paper 2008-11, 19.

Mercier-Langevin, P., Wright-Holfeld, A., Dubé, B., Bernier, C., Houle, N., Savoie, A., and Simard, P. (2009). Stratigraphic setting of the Westwood-Warrenmac ore zones, Westwood project, Doyon-Bousquet-LaRonde mining camp, Abitibi, Quebec. Geological Survey of Canada Current Research Paper 2009-03, 20.

Mercier-Langevin, P., Hannington, M., Dubé, B., and Bécu, V. (2011a). The gold content of volcanogenic massive sulfide deposits. Mineralium Deposita, 46, p. 509-539.

Mercier-Langevin, P., Goutier, J., Ross, P.-S., McNicoll, V., Monecke, T., Dion, C., Dubé, B., Thurston, P., Becu, V., Gibson, H., Hannington, M., and Galley, A., (2011b). The Blake River Group of the Abitibi greenstone belt and its unique VMS and gold-rich VMS endowment. Geological Survey of Canada Open File Report 6869, 61 p.

Mercier-Langevin, P., Hannington, M., Dubé, B., McNicoll, V., Goutier, J., and Monecke, T., 2011c, Geodynamic influences on the genesis of Archean world-class gold-rich VMS deposits: examples from the Blake River Group, Abitibi greenstone belt, Canada: *Let's Talk Ore Deposits, Proceeding of the 11th Biennial SGA Meeting Volume I*, p. 85–87.

Mercier-Langevin, P., McNicoll, V., Allen, R.L., Blight, J.H.S., and Dubé, B. (2013). The Boliden gold-rich volcanogenic massive sulfide deposit, Skellefte district, Sweden: new U–Pb age constraints and implications at deposit and district scale. Mineralium Deposita, 48, p.485-504.

Mercier-Langevin, P., Lafrance, B., Bécu, V., Dubé, B., Kjarsgaard, I., and Guha, J. (2014). The Lemoine Auriferous Volcanogenic Massive Sulfide Deposit, Chibougamau Camp, Abitibi Greenstone Belt, Quebec, Canada: Geology and Genesis. Economic Geology, v. 109, p. 231-269.

Mercier-Langevin, P., Dubé, B., Blanchet, F., Pitre, D., and Laberge, A. (2017). Chapter 7: The LaRonde Penna Au-Rich Volcanogenic Massive Sulfide Deposit. *Reviews in Economic Geology, v. 19,* p. 225–245.

Mercier-Langevin, P., Lawley, C.J.M., and Castonguay, S., (ed.) (2020). Targeted Geoscience Initiative 5: Contributions to the Understanding of Canadian Gold Systems; *Geological Survey of Canada, Open File 8712,* 328 p.

Métrich, N., Schiano, P., Clocchiatti, R., and Maury, R.C. (1999). Transfer of sulfur in subduction settings: an example from Batan Island (Luzon volcanic arc, Philippines). *Earth Planet. Sci. Lett. 167,* p. 1–14.

Métrich, N., and Wallace, P.J. (2008). Volatile abundances in basaltic magmas and their degassing paths tracked by melt inclusions. Reviews in Mineralogy and Geochemistry, 69, p. 363-402.

Meyer, C., and Hemley, J.J. (1967). Wall rock alteration, in Barnes, H.L., ed., Geochemistry of hydrothermal ore deposits: New York, Holt, Rinehart, and Winston, Inc., p. 166–235.

Meyer, C., Shea, E.P., Goddard, C.C., Jr., and staff (1968). Ore deposits at Butte, Montana, in Ridge, J.D., ed., Ore deposits of the United States, 1933–1967 (Graton-Sales volume): New York, American Institute of Mining, Metallurgical, and Petroleum Engineers, p. 1373–1416.

Mining Data Online (2020). *Bingham Canyon Mine*, 23/09/2020, <https://miningdataonline.com/property/357/Bingham-Canyon-Mine.aspx>.

Mittlefehldt, D.W. (1998) Cesium. In: Geochemistry. Encyclopedia of Earth Science. Springer, Dordrecht.

Molina, J.F., and Poli, S. (2000). Carbonate stability and fluid composition in subducted oceanic crust: an experimental study on H2O–CO2-bearing basalts. *Earth and Planetary Science Letters, 176,* p. 295–310.

Morteani, G. and Preinfalk, C. (1996). REE distribution and REE carriers in laterites formed on the alkaline complexes of Araxá and Catal o (Brazil). In Rare Earth Minerals: Chemistry, Origin and Ore Deposits. Mineralogical Society Series 7,
p. 227–255.

Mortensen, J.K. (1993). U-Pb geochronology of the eastern Abitibi subprovince. Part 2: Noranda-Kirkland Lake area. *Canadian Journal of Earth Sciences, v. 30*, p. 29−41.

Morton, R.L., and Franklin, J.M. (1987). Two-fold classification of Archean volcanic-associated massive sulfide deposits: *Economic Geology, v. 82,* p. 1057–1063.

Moss, R., Scott, S.D., and Binns, R.A. (1997). Concentrations of gold and other ore metals in volcanics hosting the PACMANUS sea-floor sulfide deposit: JAMSTEC *Journal of Deep Sea Research, v. 13,* p. 257–267.

Moss, R., Scott, S.D., and Binns, R.A. (2001). Gold Content of Eastern Manus Basin Volcanic Rocks: Implications for Enrichment in Associated Hydrothermal Precipitates. Economic Geology, 96, p. 91-107.

Moyen, J.-F. (2009). High Sr/Y and La/Yb ratios: The meaning of the “adakitic signature”. *Lithos, 112,* p. 556-574.

Mueller, W.U., Daigneault, R., Mortensen, J.K., and Chown, E.H. (1996). Archean terrane docking: Upper crust collision tectonics, Abitibi greenstone belt, Quebec, Canada. Tectonophysics, 265, p. 127-150.

Mustard, R., Ulrich, T., Kamenetsky, V.S., and Mernagh, T. (2006). Gold and metal enrichment in natural granitic melts during fractional crystallization. *Geology, 34(2),* p. 85–88.

Natural Resources Canada (2019). *Targeted Geoscience Initiative: Increasing Deep Exploration Effectiveness,* Natural Resources Canada, February 10, 2020, < https://www.nrcan.gc.ca/targeted-geoscience-initiative-increasing-deep-exploration-effectiveness/10907>

Nekvasil, H. (1992). Ternary feldspar crystallization in high-temperature felsic magmas. *American Mineralogist, 77(5-6),* p. 592-604.

Newton, R.C. (1986). Fluids of granulite facies metamorphism. In: Walther, J.V., Wood, B.J. (Eds.), Fluid–Rock Interactions During Metamorphism. Springer-Verlag, New York, pp. 36–59.

Neyedley, K., Hanley, J.J., Zajacz, Z., and Fayek, M. (2021). Accessory mineral thermobarometry, trace element chemistry, and stable O isotope systematics, Mooshla Intrusive Complex (MIC), Doyon-Bousquet-LaRonde mining camp, Abitibi Greenstone Belt, Québec. *TGI-5 Special Paper, 2020.*

Nielsen, R.L., Crum, J., Bourgeois, R., Hascall, K., Forsythe, L.M., Fisk, M.R., and Christie, D.M. (1995). Melt inclusions in high-An plagioclase from the Gorda Ridge: an example of the local diversity of MORB parent magmas. *Contrib. Mineral. Petrol. 122,* 34–50.

Nielsen, R.L., Michael, P.J., and Sours-Page, R. (1998). Chemical and physical indicators of compromised melt inclusions. Geochimica et Cosmochimica Acta, 62, p. 831 – 839.

Nielsen, T.F.D., Solovova, I.P., and Veksler, I.V. (1997). Parental melts of melilitolite and origin of alkaline carbonatite: Evidence from crystallised melt inclusions, Gardiner complex. *Contributions to Mineralogy and Petrology, 126,* p. 331-344.

Nikanorov, A. (2009). The Oddo-Harkins rule and distribution of chemical elements in freshwater ecosystems. *Doklady Earth Sciences, 426,* p. 600–604.

Ohmoto, H., and Skinner, B.J. (1983). eds., The Kuroko and related volcanogenic massive sulfide deposits: Economic Geology Monograph 5, 604.

Ohmoto, H. (1996). Formation of volcanogenic massive sulfide deposits: The Kuroko perspective. *Ore Geology Reviews, 10,* p. 135-177.

Palme, H. and Jones, A. (2004). Solar system abundances of the Elements. *In: Treatise on Geochemistry. Holland, H.D. and Turekian, K.K. (Editors), Elsevier, Amsterdam.* 41-61.

Pan, Y., and Stauffer, M.R. (2000). Cerium anomaly and Th/U fractionation in the 1.85 Ga Flin Flon Paleosol: Clues from REE- and U-rich accessory minerals and implications for paleoatmospheric reconstruction. American Mineralogist, 85, p. 898–911.

Patten, C.G.C., Pitcairn, I.K., Teagle, D.A.H., and Harris, M. (2016). Mobility of Au and related elements during the hydrothermal alteration of the oceanic crust: implications for the sources of metals in VMS deposits. *Mineralium Deposita, 51*, p. 179-200.

Pearce, J. (1996). A User's Guide to Basalt Discrimination Diagrams. *Geol. Assoc. Canada Short Course Notes, 12*, 79-113.

Pearce, J.A., and Cann, J.R. (1975). Tectonic setting of basic volcanic rocks determined using trace element analysis. *Earth and Planetary Science Letters 19,* p. 290 300.

Pearce, J.A., Harris, N.B.W., and Tindle, A.G. (1984). Trace element discrimination diagrams for the tectonic interpretation of granitic rocks. *Journal of Petrology, 25,* 956-983.

Péloquin, A.S., Potvin, R., Laflèche, M.R., Verpaelst, P., and Gibson, H.L. (1990). The Blake River Group, Rouyn-Noranda area, Quebec: A stratigraphic synthesis, in Rive, M., Verpaelst, P., Gagnon, Y., Lulin, J.-M., Riverin, G., and Simard, A., eds., The northwestern Quebec polymetallic belt: A summary of 60 years of mining exploration, *CIM Special Volume 43,* p. 107–118.

Perfit, Michael R., Ridley, W. Ian, and Jonasson, Ian R. (1999). Geologic, petrologic, and geochemical relationships between magmatism and massive sulfide mineralization along the eastern Galapagos spreading center: Reviews in Economic Geology, v. 8, p. 75–100.

Pettke, T., Halter, W.E., Webster, J.D., Aigner-Torres, M., and Heinrich, C.A. (2004). Accurate quantification of melt inclusion chemistry by LA-ICPMS A comparison with EMP and SIMS and advantages and possible limitations of these methods. Lithos, 78(4), p. 333-361.

Piercey, S.J., Murphy, D.C., Mortensen, J.K., and Paradis, S. (2001a). Boninitic magmatism in a continental margin setting, Yukon-Tanana terrane, southeastern Yukon, Canada: Geology, v. 29, p. 731-734.

Piercey, S.J., Paradis, S., Murphy, D.C., and Mortensen, J.K. (2001b). Geochemistry and paleotectonic setting of felsic volcanic rocks in the Finlayson Lake volcanic-hosted massive sulfide (VHMS) district, Yukon, Canada; Economic Geology, v. 96, p. 1877-1905.

Piercey, S.J. (2009). Lithogeochemistry of volcanic rocks associated with volcanogenic massive sulphide deposits and applications to exploration, in Submarine Volcanism and Mineralization: Modern through Ancient, (eds.) B. Cousens and S.J. Piercey; Geological Association of Canada, Short Course 29-30 May 2008, Quebec City, Canada, p. 15-40.

Piercey, S.J. (2011). The setting, style, and role of magmatism in the formation of volcanogenic massive sulfide deposits. *Mineralium Deposita, 46,* p. 449-471.

Pitcairn, I.K. (2011). Background concentrations of gold in different rock types. *Applied Earth Science, 120*, p. 31–38.

Pitcher, W.S. (1983) in K.J. Hsü. *Mountain building processes*, London; New York: Academic Press.

Pitcher, W.S. (1993). *The Nature and origin of granite* (1st ed.), Netherlands: Springer.

Plank, T., and Langmuir, C.H. (1993). Tracing trace elements from sediment input to volcanic output at subduction zones. *Nature, 362,* p. 739–743.

Pokrovski, G.S., Kokh, M.A., Guillaume, D., Borisova, A.Y., Gisquet, P., Hazemann, J.-L., Lahera, E., Del Net, W., Proux, O., Testemale, D., Haigis, V., Jonchière, R., Seitsonen, A.P., Ferlat, G., Vuilleumier, R., Saitta, A.M., Boiron, M.-C., and Dubessy, J. (2015). Sulfur radical species form gold deposits on Earth. *Proceedings of the National Academy of Sciences of the United States of America, 112(44),* 13484 – 13489.

Poli, S., Franzolin, E., Fumagalli, P., and Crottini, A., (2009). The transport of carbon and hydrogen in subducted oceanic crust: an experimental study to 5 GPa. *Earth and Planetary Science Letters, 278,* p. 350–360.

Poulsen, K.H., and Hannington, M.D., (1996). Volcanic-associated massive sulphide gold, in Eckstrand, O.R., Sinclair, W.D., and Thorpe, R.I., eds., Geology of Canadian Mineral Deposit Types: Geology of Canada, v. 8, p. 183-196.

Poulsen, K.H., Robert, F., and Dubé, B. (2000). Geological classification of Canadian gold deposits: Geological Survey of Canada, Bulletin 540, 106.

Powell, W.G., Carmichael, D.M., and Hodgson, C.J. (1995). Conditions and timing of metamorphism in the southern Abitibi greenstone belt, Quebec: *Canadian Journal of Earth Sciences, v. 32, p.* 787–805.

Prokin V.A., and Buslaev F.P. (1999). Massive copper-zinc sulphide deposits in the Urals. *Ore Geology Review, 14,* p.1–69.

Rapien, M.H., Bodnar, R.J., Simmons, S., Szabó., CS., Wood, C.P. and Sutton, S.R. (2003). Melt inclusion study of the embryonic porphyry copper system at White Island, New Zealand. *Society of Economic Geologists Special Publication, 10,* p. 41–59.

Reed, M.H., and Palandri, J. (2006). Sulfide mineral precipitation from hydrothermal fluids, in Vaughan, D.J., ed., Sulfide mineralogy and geochemistry: Mineralogical Society of America, *Reviews in Mineralogy and Geochemistry 61,* p. 609–631.

Richards, J.P., and Kerrich, R. (2007). Special paper: Adakite-like rocks: Their diverse origins and questionable role in metallogenesis. *Economic Geology, 102,* p. 537-576.

Richardson, C., Cann, J., Richards, H., and Cowan, J. (1987). Metal-depleted root zones of the Troodos ore-forming hydrothermal systems, Cyprus. *Earth and Planetary Science Letters, 84,* p. 243–253.

Richter, F.M. (1986). Simple models for trace element fractionation during melt segregation. *Earth and Planetary Science Letters, 77(3-4),* p. 333-344.

Rickard, D.T., and Zweifel, H. (1975). Genesis of Precambrian sulfide ores, Skellefte district, Sweden: *Economic Geology, v.70,* p. 225-274.

Roedder, E., (1965). Liquid CO_2 inclusions in olivine-bearing nodules and phenocrysts from basalts. *American Mineralogist, 50,* p. 1746–1782.

Roedder, E. (1979). Origin and significance of magmatic inclusions. *Bulletin de Minéralogie, v. 102,* p. 487-510.

Roedder, E. (1984). Volume 12: Fluid inclusions. Mineralogical Society of America. *In* ed. Ribbe, P.H., *Reviews in Mineralogy, vol. 12,* p. 1–646.

Roedder, E. (1992). Fluid inclusion evidence for immiscibility in magmatic differentiation. *Geochimica et Cosmochimica Acta, 56,* p. 5-20.

Roggensack K. (2001). Unraveling the 1974 eruption of Fuego volcano (Guatemala) with small crystals and their young melt inclusions. *Geology, 29(10),* p. 911-914.

Rona, P.A., and Scott, S.D. (1993). Preface to special issue on sea-floor hydrothermal mineralization: new perspectives. *Economic Geology, 88,* p. 1933-1976.

Rona, P.A., Hannington, M.D., Raman, C.V., Thompson, G., Tivey, M.K., Humphris, S. E., Lalou, C., and Petersen, S. (1993). Active and relict seafloor hydrothermal mineralization at the TAG hydrothermal field, Mid-Atlantic Ridge: *Economic Geology, v. 88,* p. 1989–2017.

Rooney, T.O., Franceschi, P., and Hall, C.M. (2011). Water-saturated magmas in the Panama Canal region: a precursor to adakite-like magma generation? *Contributions to Mineralogy and Petrology, 161 (3),* p. 373-388.

Ross, P.-S., and Bédard, J.H. (2009). Magmatic affinity of modern and ancient subalkaline volcanic rocks determined from trace-element discriminant diagrams. *Canadian Journal of Earth Sciences, 2009, 46(11),* p. 823-839.

Rosso K.M. and Bodnar R. J. (1995). Microthermometric and Raman spectroscopic detection limits of CO_2 in fluid inclusions and the Raman spectroscopic characterization of CO_2. Geochimica et Cosmochimica Acta, 59, p. 3961-3975.

Roth, T., Thompson, J.F.H., and Barrett, T.J. (1999). The precious metal-rich Eskay Creek deposit, northwestern British Columbia. *Reviews in Economic Geology, 8,* p. 357–373.

Rusk, B. G., Reed, M. H., Dilles, J. H. and Kent, A. J. R. (2006). Intensity of quartz cathodoluminescence and trace-element content in quartz from the porphyry copper deposit at Butte, Montana. *American Mineralogist, 91,* 1300–1312.

Rusk, B.G., Lowers, H.A., and Reed, M.H. (2008a). Trace elements in hydrothermal quartz: relationships to cathodoluminescent textures and insights into vein formation. Geology, 36, p. 547.

Rusk, B.G., Reed, M.H., and Dilles, J.H. (2008b). Fluid inclusion evidence for magmatic-hydrothermal fluid evolution in the porphyry copper–molybdenum deposit at Butte, Montana. Economic Geology, 103, p. 307–334.

Sales, R.H., and Meyer, C. (1948). Wall rock alteration at Butte, Montana: American Institute of Mining and Metallurgical Engineers Transactions, v. 178, p. 9–35.

Sangster, D., and Scott, S.D. (1976). Precambrian strata-bound massive Cu-Zn-Pb sulfide ores of North America, in Wolf, K.H., ed., *Handbook of strata-bound and stratiform ore deposits: Amsterdam, Elsevier,* p. 129–222.

Savoie, A., Trudel, P., Sauvé, P., and Perrault, G. (1990). Géologie de la mine Doyon, Cadillac, Québec; in The northwestern Québec polymetallic belt: a summary of 60 years of mining exploration, (ed.) M. Rive, P. Verpaelst, Y. Gagnon, J.-M. Lulin, G. Riverin, and A. Simard; Canadian Institute of Mining, Metallurgy and Petroleum, Special Volume 43, p. 401-411.

Savoie, A., Trudel, P., Sauve, P., Hoy, L., and Lao, K. (1991). Geologie de la mine Doyon (region de Cadillac). Ministere de l'Energie et des Ressources, Quebec, Report ET 90-05, 80.

Sawkins, F.J. (1976). Massive sulphide deposits in relation to geotectonics: *Geological Association of Canada Special Paper 14,* p. 221-240.

Sawkins, F.J. (1990). Integrated tectonic-genetic model for volcanic-hosted massive sulfide deposits: *Geology, v. 18,* p. 1061–1064.

Schiano, P. (2003). Primitive magmas recorded as silicate melt inclusions in igneous minerals. Earth Science Reviews, 63, p. 121-144.

Schiano, P. & Clocchiatti, R. (1994): Worldwide occurrence of silica-rich melts in sub continental and suboceanic mantle minerals. *Nature, 368,* p. 621-624.

Schiano, P., Clocchiatti, R., Joron, J.L. (1992): Melt and fluid inclusions in basalts and xenoliths from Tahaa Island, Society archipelago: evidence for a metasomatized upper mantle. *Earth Planet. Sci. Lett., 111,* p. 69-82.

Schiffman, P., Bettison, L., and Smith, B. (1987). Mineralogy and geochemistry of epidosites from the Solea graben, Troodos ophiolite, Cyprus. In: Ophiolites: oceanic crustal analogues: proceedings of the symposium "Troodos": p. 673-683.

Schwindinger, M., Weinberg, R.F., and White, R.W. (2020). The Fate of Accessory Minerals and Key Trace Elements During Anatexis and Magma Extraction. *Journal of Petrology, 31.*

Scott, S.D. (1997). Submarine hydrothermal systems and deposits, in Geochemistry of Hydrothermal Ore Deposits, 3rd Edition, (ed.) H.L. Barnes; John Wiley and Sons Ltd., New York, p. 797-875.

Scott, S.D., and Binns, R.A. (1995). Hydrothermal processes and contrasting styles of mineralization in the western Woodlark and eastern Manus Basins of the western Pacific. P. 473–205 in Hydrothermal Vents and Processes. L.M. Parson, C.L. Walker, and D.R. Dixon, eds, Geological Society of London Special Publications.

Seaman, S.J. (2000). Crystal Clusters, Feldspar Glomerocrysts, and Magma Envelopes in the Atascosa Lookout Lava Flow, Southern Arizona, USA: Recorders of Magmatic Events. *Journal of Petrology, 41(5),* p. 693-716.

Severs, M.J., Beard, J.S., Fedele, L., Hanchar, J.M., Mutchler, S.R., and Bodnar, R.J. (2009). Partitioning behavior of trace elements between dacitic melt and plagioclase, orthopyroxene, and clinopyroxene based on laser ablation ICPMS analysis of silicate melt inclusions. *Geochimica et Cosmochimica Acta, 73,* p. 2123-2141.

Shanks, W.C., Bischoff, J.L. and Rosenbauer, R.J. (1981). Sea-water sulfate reduction and sulfur isotope fractionation in basaltic systemsinteraction of sea-water with fayalite and magnetite at 200-350 C. *Geochimica Cosmochimica Acta, 45,* p. 1977-1995.

Shanks, W.C.P. (2012). Hydrothermal alteration in volcanogenic massive sulfide occurrence model. Scientific Investigations Report 2010-5070-C, p. 169-180.

Sharpe, R., and Gemmell, J.B. (2002). The Archean Cu-Zn magnetite-rich Gossan Hill volcanic-hosted massive sulfide deposit, Western Australia; genesis of a multistage hydrothermal system: *Economic Geology, v. 97,* p. 517-539.

Shaw, D.M. (1970). Trace element fractionation during anatexis. *Geochimica Cosmochimica Acta, 34,* p. 237-243.

Sherlock, R.L., Roth, T., Spooner, E.T.C., and Bray, C.J. (1999). The origin of the Eskay Creek precious metal-rich volcanogenic massive sulfide deposit: fluid inclusion and stable isotope data. *Economic Geology, 94,* p. 803–824.

Shimizu, K., Komiya, T., Hirose, K., Shimizu, N., and Maruyama, S. (2001). Cr-spinel, an excellent micro-container for retaining primitive melts - implications for a hydrous plume origin for komatiites, *Earth and Planetary Science Letters, 189,* p. 177-188.

Shimizu, K., Shimizu, N., Komiya, T., Suzukia, K., Maruyama, S., and Tatsumi, Y. (2009). CO_2-rich komatiitic melt inclusions in Cr-spinels within beach sand from Gorgona Island, Colombia. *Earth and Planetary Science Letters, 288(1-2),* p. 33-43.

Shinohara, H., Kazahaya, K., and Lowenstern, J.B. (1995). Volatile transport in a convecting magma column: implications for porphyry Mo mineralization. Geology, 23, p. 1091–1094.

Sillitoe, R.H., Hannington, M.D., and Thompson, J.F.H. (1996). High sulfidation deposits in the volcanogenic massive sulfide environment. *Economic Geology, 91,* p. 204–212.

Simon, A. C. Frank, M. R., Pettke, T., Candela, P. A., Piccoli, P. M., and Heinrich C. A (2005). Gold partitioning in melt-vapor-brine systems. *Geochimica Cosmochimica Acta, 69,* p. 3321–3335.

Sisson, T.W. and Bacon, C.R. (1992). Garnet High-Silica Rhyolite Trace-Element Partition-Coefficients Measured by Ion Microprobe. *Geochimica et Cosmochimica Acta 56(5),* p. 2133-2136.

Sittner, J., and Götze, J. (2018). Cathodoluminescence (CL) Characteristics of Quartz from Different Metamorphic Rocks within the Kaoko Belt (Namibia). *Minerals, 8(5),* 190.

Sneeringer, M.A., and Watson, E.B (1985). Milk cartons and ash cans: two unconventional welding techniques. American Mineralogist, 70, p. 200-201.

Sobolev, A.V., and Kostyuk, V.P. (1975). Magmatic crystallisation based on a study of melt inclusions. Proc. Coffi 9, 182–235.

Sobolev, A.V. (1996). Melt inclusions in minerals as a source of principle petrological information. Petrology 4, 228–239.

Sobolev, A.V., and Shimizu, N. (1993). Ultra-depleted primary melt included in an olivine from the Mid-Atlantic Ridge. *Nature 363,* p. 151–154.

Sobolev, A.V., and Chaussidon, M. (1996). H_2O concentrations in primary melts from island arcs and mid-ocean ridges: implications for H_2O storage and recycling in the mantle. *Earth Planet. Sci. Lett. 137,* 45–55.

Sobolev, A.V., Hofmann, A.W., and Nikogosian, I.K. (2000). Recycled oceanic crust observed in 'ghost plagioclase' within the source of Mauna Loa lavas. Nature 404, 986–990.

Solomon, M. (1976). Volcanic massive sulphide deposits and their host rocks: A review and an explanation, in Wolf, K.H., ed., Handbook of strata-bound and stratiform ore deposits, II: Regional studies and specific deposits: Amstedam, Elsevier, p. 1307–1328.

Solomon, M. and Walshe, J.L. (1979). The formation of massive sulfide deposits on the seafloor. *Economic Geology, 74:* p. 797-813.

Sparks R. S. J. (2003). Dynamics of magma degassing. *Geological Society of London, Special Publication, 213,* 5–22.

Spear, F.S., and Wark, D.A. (2009). Cathodoluminescence imaging and titanium thermometry in metamorphic quartz. Journal of Metamorphic Geology, 27, p.187-205.

Spilliaert, N., Métrich, N., and Allard, P., (2006a). S-Cl-F degassing pattern of water-rich alkali basalt: modelling and relationship with eruption styles on Mount Etna volcano. *Earth and Planetary Science Letters, 248,* p. 772–786.

Spilliaert, N., Allard, P., and Metrich, N. (2006b). Melt inclusion record of the conditions of ascent, degassing, and extrusion of volatile-rich alkali basalt during the powerful 2002 flank eruption of Mount Etna (Italy). *Journal of Geophysical Research, 111.*

Stanton, R. (1990). Magmatic evolution and the ore type-lava type affiliations of volcanic exhalative ores. *Australian Institute of Mining and Metallurgy Proceedings, 15,* p. 101–107.

Stanton, R. (1994). Ore elements in arc lavas. *In* Oxford: Clarendon Press; New York: Oxford University Press, 1994, 391.

Stavast, W.J.A., Keith, J.D., Christiansen, E.H., Dorais, M.J., Larocque, A., and Evans, N. (2006). The fate of magmatic sulfides during intrusion or eruption, Bingham and Tintic districts, Utah. Economic Geology, 101, p. 329–345.

Stoiber, R.E., and Rose, W.I. (1974). Fumarole incrustations at active central american volcanoes. *Geochimica et Cosmochimica Acta, 38(4),* p. 495-516.

Stone, W.E. (1990). Archean volcanism and sedimentation in the Bousquet gold district, Abitibi greenstone belt, Quebec: Implications for stratigraphy and gold concentration: *Geological Society of America Bulletin, v. 102,* p. 147–158.

der Straaten, F. V., Halama, R., John, T., Schenk, V., Hauff, F., and Andersen, N. (2011). Tracing the effects of high-pressure metasomatic fluids and seawater alteration in blueschist-facies overprinted eclogites: Implications for subduction channel processes, *Chemical Geology*.

Student J.J., and Bodnar R.J. (1996) Melt inclusion microthermometry: petrologic constraints from the H_2O-saturated haplogranite system. *Petrology, 4,* p. 291-306.

Student, J.J., and Bodnar, R.J. (2004). Silicate melt inclusions in porphyry copper deposits: Identification and homogenization behavior. *The Canadian Mineralogist, 42,* p. 1583-1599.

Swinden, H.S. (1991). Paleotectonic settings of volcanogenic massive sulfide deposits in the Dunnage Zone, Newfoundland Appalachians; Canadian Institute of Mining and Metallurgy Bulletin, v. 84, p. 59-89.

Syme, E.C., Lucas, S.B., Bailes, A.H., and Stern, R.A. (1999). Contrasting arc and MORB-like assemblages in the Paleoproterozoic Flin Flon Belt, Manitoba, and the role of intra-arc extension in localizing volcanic-hosted massive sulfide deposits; Canadian Journal of Earth Sciences, v. 36, p. 1767-1788.

Szabo, C, Bodnar, R.J., and Sobolev, A.V. (1996). Metasomatism associated with subduction-related, volatile-rich silicate melt in the upper mantle beneath the Nograd-Gomor Volcanic Field, Northern Hungary / Southern Slovakia: Evidence from silicate melt inclusions. *Eur. J. Mineral, 8,* p. 881-899.

Taran, Y.A., Hedenquist, J.W., Korzhinsky, M.A., Tkachenko, S.I., and Shmulovich, K.I. (1995). Geochemistry of magmatic gases from Kudryavy volcano, Iturup, Kuril Islands. Geochimica et Cosmochimica Acta, 59(9), p. 1749-1761.

Taunton, A.E., Welch, S.A., Santelli, C.M., Fournelle, J., and Banfield, J.F. (1998). Apatite weathering and cerium fractionation; possible microbial influences. *Geological Society of America, Abstracts with Programs, 30,* 304.

Taylor, S.R., and McLennan, S.M. (1985). *The continental crust: its composition and evolution*. Geoscience texts. Blackwell, Oxford. 312 pp.

Taylor, B.K., Crook, A.W., Sinton, J.M., and Petersen, L. (1991). Manus Basin, Papua New Guinea, SeaMARC II sidescan sonar imagery and bathymetry, in South Pacific Seafloor Atlas, SOPAC Region, Sheets 1-7, Hawaii Institute of Geophysics, Honolulu.

Teasdale, N., Brown, A.C., and Tourigny, G., 1996, Gîtologie de la mine Bousquet 2: Ministère des Ressources naturelles, Québec, Report MB 96-37, 43.

Thomas, J.B., Watson, E.B., Spear, F.S., Shemella, P.T., Nayak, S.K., and Lanzirotti, A. (2010). TitaniQ under pressure: the effect of pressure and temperature on the solubility of Ti in quartz. *Contributions to Mineralogy and Petrology, 160,* p. 743-759.

Thomas, R., and Klemm, W. (1997). Microthermometric Study of Silicate Melt Inclusions in Variscan Granites from SE Germany: Volatile Contents and Entrapment Conditions. *Journal of Petrology, 38(12),* p. 1753-1765.

Thomas, R., Förster, H.-J., and Heinrich, W. (2003). The behaviour of boron in a peraluminous granite-pegmatite system and associated hydrothermal solutions: a melt and fluid-inclusion study. *Contributions to Mineralogy and Petrology, 144,* p. 457-472.

Thompson, A.B., Aerts, Maarten, and Hack, A.C. (2007). Liquid Immiscibility in Silicate Melts and Related Systems. *Reviews in Mineralogy & Geochemistry, 65,* p. 99-127.

Thurston, P.C., Ayer, J.A., Goutier, J., and Hamilton, M.A. (2008). Depositional gaps in Abitibi Greenstone Belt stratigraphy: A key to exploration for syngenetic mineralization. *Economic Geology, 103*(6), p. 1097-1134.

Titley, S.R., and Hicks, C.L., eds. (1966). Geology of the porphyry copper deposits—Southwestern North America: Tucson, Ariz., University of Arizona Press, 287 p.

Tomkins, H.S., Powell, R., and Ellis, D.J. (2007). The pressure dependence of the zirconium-in-rutile thermometer. Journal of Metamorphic Geology, 25, p. 703-713.

Tourigny, G., Brown, A.C., Hubert, C., and Crépeau, R. (1989a). Synvolcanic and syntectonic gold mineralization at the Bousquet Mine, Abitibi greenstone belt: *Economic Geology, v. 84*, p. 1875-1890.

Tourigny, G., Hubert, C., Brown, A.C., and Crépeau, R. (1989b). Structural control on gold mineralization at the Bousquet mine, Abitibi, Quebec: *Canadian Journal of Earth Sciences, v. 26*, p. 157–175.

Tourigny, G., Brown, A.C., Hubert, C., and Crépeau, R. (1990). Syn-volcanic and syn-tectonic gold mineralization at the Bousquet Mine, Abitibi greenstone belt, Quebec: *Economic Geology, v. 85,* p. 1875-1890.

Tourigny, G., Doucet, D., and Bourget, A. (1993). Geology of the Bousquet 2 mine: An example of a deformed, gold-bearing polymetallic sulfide deposit: *Economic Geology, v. 88*, p. 1578–1597.

Tremblay, A., Tourigny, G., and Machado, N., (1995). Zircon U/Pb age constraints on deformation and gold mineralization of the Mooshla intrusive complex, southern Abitibi belt, Canada [abs.]: Geological Society of America Annual Meeting, New Orleans, Abstracts with Programs.

Tropper, P., and Manning, C.E. (2007). The solubility of corundum in H_2O at high pressure and temperature and its implications for Al mobility in the deep crust and upper mantle. Chemical Geology, 240, p. 54-60.

Trudel, P., Sauve, P., Tourigny, G., Hubert, C., and Hoy, L. (1992). Synthese des caracteristiques geologiques des gisements de la region de Cadillac (Abitibi). Ministere des Ressources naturelles, Quebec, Report MM 91-01, 106.

Urabe, T. (1987). Kuroko deposits modeling based on magmatic hydrothermal theory: Mining Geology, v. 37, p. 159–176.

Urabe, T., Yuasa, M., and Nakao, S. (1987). Hydrothermal sulfides from a submarine caldera in the Shichito-Iwojima Ridge, northwestern Pacific. Marine Geology, 74, p. 295–299.

Urabe, T., and Marumo, K. (1991). A new model for Kuroko-type deposits of Japan, Episodes, 14, p. 246-251.

Valliant, R.I., and Hutchinson, R.W. (1982). Stratigraphic distribution and genesis of gold deposits, Bousquet region, northwestern Quebec. Canadian Institute of Mining and Metallurgy Special Volume 24, p. 27−40.

van Staal, C.R., Wilson, R.A., Rogers, N., Fyffe, L.R., Langton, J.P., McCutcheon, S.R., McNicoll, V., and Ravenhurst, C.E. (2003). Geology and tectonic history of the Bathurst Supergroup, Bathurst Mining Camp, and its relationships to coeval rocks in southwestern New Brunswick and adjacent Maine - a synthesis, in Goodfellow, W.D., McCutcheon, S.R., and Peter, J.M., eds., Massive Sulfide Deposits of the Bathurst Mining Camp, New Brunswick and Northern Maine: Economic Geology Monograph 11, p. 37-60.

van Staal, C.R., Whalen, J.B., Valverde-Vaquero, P., Zagorevski, A. and Rogers, N. (2009). Pre-Carboniferous, episodic accretion-related, orogenesis along the Laurentian margin of the northern Appalachians. *Geological Society, London, Special Publications, 327*, p. 271-316.

Vasyukova, O., and Williams-Jones, A. (2020). Partial melting, fractional crystallisation, liquid immiscibility and hydrothermal mobilisation – A 'recipe' for the formation of economic A-type granite-hosted HFSE deposits. *Lithos, 356 – 357,* 105300.

Vearncombe, S., Barley, M.E., Groves, D.I., McNaughton, N.J., Mikucki, E.J., and Vearncombe, J.R. (1995). 3.26 Ga Black smoker-type mineralization in the Strelley Belt, Pilbara-Craton, Western-Australia. *Journal of the Geological Society, 152*, p. 587-590.

Veksler, I.V., Nielsen, T.F.D., and Sokolov, S.V. (1998). Mineralogy of Crystallized Melt Inclusions from Gardiner and Kovdor Ultramafic Alkaline Complexes: Implications for Carbonatite Genesis. Journal of Petrology, 39(11-12), p. 2015-2031.

Van Westrenen, W., Blundy, J.D., and Wood, B.J. (2001). High field strength element/rare earth element fractionation during partial melting in the presence of garnet: Implications for identification of mantle heterogeneities. *Geochemistry, Geophysics, and Geosystems, 2*, 19 p.

Von Damm, K.L., 2000, Chemistry of hydrothermal vent fluids from 9°-10°N, East Pacific Rise: "Time zero", the immediate posteruptive period. *Journal of Geophysical Research, v. 105,* p. 11,203–11,222.

Wallace, P.J. (2003). From Mantle to Atmosphere: Magma Degassing, Explosive Eruptions, and Volcanic Volatile Budgets, *In* Melt inclusions in volcanic systems: methods, applications, and problems (B. De Vivo & R.J. Bodnar, Eds). *Developments in Volcanology 5, Elsevier, Amsterdam,* p. 105-127.

Wallace, M.E., and Green, D.H. (1988). An experimental determination of primary carbonatite magma composition. Nature, 335, p. 343-346.

Walter, M.J., and Presnall, D.C. (1994). Melting behavior of simplified lherzolite in the system CaO-MgO-Al2O3-SiO2-Na2O from 7 to 35 kbar. Journal of Petrology, 35, p. 329-359.

Wark, D. A. and Spear, F. S. (2005). Ti in quartz: cathodoluminescence and thermometry. *Goldschmidt 2005, 15.* Geochemical Society, Moscow, Idaho, A592.

Watson, E., Wark, D., Price, J., and Van Orman, J. (2002). Mapping the thermal structure of solid-media pressure assemblies. Contributions to Mineralogy and Petrology, 142, p. 640-652.

Watt, G.R., Wright, P., Galloway, S., and McLean, C. (1997). Cathodoluminescence and trace element zoning in quartz phenocrysts and xenocrysts. *Geochimica et Cosmochimica Acta, 61(21),* p. 4337-4348.

Warren, M.R., Hanley, J.J., Ames, D.E., and Jackson, S.E. (2015). The Ni–Cr–Cu content of biotite as pathfinder elements for magmatic sulfide exploration associated with mafic units of the Sudbury Igneous Complex, Ontario, Canada. *Journal of Geochemical Exploration, 153,* p. 11 – 29.

Webber, A.P., Roberts, S., Taylor, R.N., and Pitcairn, I.K. (2013). Golden plumes: substantial gold enrichment of oceanic crust during ridge-plume interaction. *Geology, 41*, p. 87–90.

Webster, J.D. (1997). Exsolution of magmatic volatile phases from Cl-enriched mineralizing granitic magmas and implications for ore metal transport. *Geochimica et Cosmochimica Acta, 61(5),* p. 1017-1029.

Webster, J.D., Congdon, R.D., and Lyons, P.C. (1995). Determining preeruptive compositions of late Paleozoic magma from kaolinized volcanic ashes: Analysis of glass inclusions in quartz microphenocrysts from Tonsteins. Geochimica et Cosmochimica Acta, v. 59, p. 711-720.

Webster, J.D., and Thomas, R. (2006). Silicate melt inclusions in felsic plutons: a synthesis and review. In Melt Inclusions in Plutonic Rocks (J. D. Webster, ed.) Mineralogical Association of Canada, Short Course, 36, p. 1-26.

Weill, D.F., and Drake, M.J. (1973). Europium Anomaly in Plagioclase Feldspar: Experimental Results and Semiquantitative Model. *Science, 8,* p. 1059-1060.

White, W.M., and Patchett, P.J. (1984). Hf–Nd–Sr isotopes and incompatible element abundances in island arcs: implications for magma origins and crust–mantle evolution. *Earth and Planetary Science Letters, 67,* p. 167–185.

Williams, C.T. (1978). Uranium-Enriched Minerals in Mesostasis Areas of the Rhum Layered Pluton. *Contributions to Mineralogy and Petrology, 66,* p. 29-39.

Winter, J.D. (2001). *An Introduction to Igneous and Metamorphic Petrology* (1st ed.). Pearson.

Woodruff, L. G. and Shanks, W. C. (1988). Sulfur isotope study of chimney minerals and vent fluids from 21 N, East Pacific Rise-hydrothermal sulfur sources and disequilibrium sulfate reduction. *Journal of Geophysical Research, 93,* p. 4562-4572.

Wright-Holfeld, A., Mercier-Langevin, P., and Dubé, B. (2010). Contrasting alteration mineral assemblages associated with the Westwood deposit ore zones, Doyon-Bousquet-LaRonde mining camp, Abitibi, Quebec. Geological Survey of Canada Current Research Paper 2010-9, p. 1-25

Wright-Holfeld, A., Mercier-Langevin, P., and Dubé, B. (2011). Mass changes and element mobility associated with the Westwood deposit ore zones, Doyon-Bousquet-LaRonde mining camp, Abitibi, Quebec. Geological Survey of Canada Current Research Paper 2011-8, 15.

Yamamoto J. and Kagi H. (2006). Extended micro-Raman densimeter for CO_2 applicable to mantle-originated fluid inclusions. Chemistry Letters, 35 (6), 610-611.

Yamamoto J., Kagi H., Kaneoka I., Lai Y., Prikhod'ko V.S. and Arai S. (2002). Fossil pressures of fluid inclusions in mantle xenoliths exhibiting rheology of mantle minerals: implications for the geobarometry of mantle minerals using micro-Raman spectroscopy. Earth Planetary Science Letters, 198 (3-4), 511-519.

Yang, K., and Scott, S.D. (1996). Possible contribution of a metal-rich magmatic fluid to a sea-floor hydrothermal system. *Nature, 383,* p. 420-423.

Yang, K., and Scott, S.D. (2002). Magmatic degassing of volatiles and ore metals into a hydrothermal system on the modern seafloor of the Eastern Manus back-arc basin, western Pacific. *Economic Geology, 97,* 1079-1100.

Yang, K., and Scott, S.D. (2003). Geochemical relationships of felsic magmas to ore metals in massive sulfide deposits of the Bathurst mining camp, Iberian Pyrite Belt, Hokuroko district and the Abitibi belt. Economic Geology Monograph, 11, p. 457-478.

Yang, K., and Scott, S.D. (2005). Vigorous exsolution of volatiles in the magma chamber beneath a hydrothermal system on the modern sea floor of the eastern Manus back-arc basin, western Pacific: evidence from melt inclusions. *Economic Geology, 100*, p. 1085-1096

Yang, K., and Scott, S.D. (2006). Magmatic fluids as a source of metals in seafloor hydrothermal systems. *Geophysical Monograph Series, 166,* p. 1-23.

Yang, W.-B., Niu, H.-C., Li, N.-B., Hollings, P., Zurevinski, S., and Xing, C.-M. (2020). Enrichment of REE and HFSE during the magmatic-hydrothermal evolution of the Baerzhe alkaline granite, NE China: Implications for rare metal mineralization. *Lithos, 358 – 359,* 105411.

Yardley, B.W.D., and Bodnar, R.J. (2014). Fluids in the continental crust. Geochemical Perspectives, 3 (1).

Yardley, B.W.D., and Cleverley, J.S. (2015). The role of metamorphic fluids in the formation of ore deposits. From: Jenkin, G. R. T., Lusty, P. A. J., McDonald, I., Smith, M. P., Boyce, A. J. and Wilkinson, J. J. (eds) 2015. Ore Deposits in an Evolving Earth. Geological Society, London, Special Publications, 393, p. 117–134.

Yaxley, G. M., Ghosh, S., Kiseeva, E. S., Mallik, A., Spandler, C., Thomson, A. R. and Walter, M. J. (2019) CO_2-Rich Melts in Earth, *in* Orcutt, B.N., Daniel, I. & Dasgupta, R. (eds.) Deep Carbon: Past to Present. Cambridge: *Cambridge University Press*, pp. 129-162

Yeats, C.J., and Groves, D.I. (1998). The Archean Mount Gibson gold deposits, Yilgarn craton, Western Australia: Products of combined synvolcanic and syntectonic alteration and mineralisation: *Ore Geology Reviews, v. 13*, p. 103-129.

Yergeau, D. (2015). Géologie du gisement synvolcanique aurifère atypique Westwood, Abitibi, Québec. Unplublished Ph.D. thesis, Quebec, Canada, Canada, Institut National de la Recherche Scientifique, Centre Eau, Terre et Environnement, 671.

Yergeau, D., Mercier-Langevin, P., Dubé, B., Jackson, S., Malo, M., Bernier, C., and Simard, P. (2014). Synvolcanic Au-Ag±Cu-Zn-Pb massive sulphides, veins and disseminations of the Westwood deposit, Abitibi greenstone belt, Québec. *Geological Survey of Canada, Open File 7482*, 54 p.

Yergeau, D., Mercier-Langevin, P., Dubé, B., Malo, M., McNicoll, V.J., Jackson, S.E., Savoie, A., and La Rochelle, F. (2015). The Archean Westwood Au deposit, southern Abitibi: Telescoped Au-rich VMS and intrusion-related Au systems, In: Targeted Geoscience Initiative 4: Contributions to the Understanding of Precambrian Lode Gold Deposits and Implications for Exploration, (ed.) B. Dubé and P. Mercier-Langevin; *Geological Survey of Canada, Open File 7852*, p. 177–191.

Yuan, C., Sun, M., Xiao, W., Wilde, S., Li, X., Liu, X., Long, X., Xia, X., Ye, K., and Li, J. (2009). Garnet-bearing tonalitic porphyry from East Kunlun, Northeast Tibetan Plateau: implications for adakite and magmas from the MASH Zone. *International Journal of Earth Science (Geol Rundsch), 98*, p. 1489–1510.

Zajacz, Z., Halter, W., Malfait, W.J., Bachmann, O., Bodnar, R.J., Hirschmann, M.M., Mandeville, C.W., Morizat, Y., Müntener, O., Ulmer, P., and Webster, J.D. (2005). A composition-independent quantitative determination of the water content in silicate glasses and silicate melt inclusions by confocal Raman spectroscopy. *Contributions to Mineralogy and Petrology, 150*, p. 631 – 642.

Zajacz, Z., and Halter, W. (2007). LA-ICPMS analyses of silicate melt inclusions in co-precipitated minerals: Quantification, data analysis and mineral/melt partitioning. *Geochimica et Cosmochimica Acta, 71(4)*, p. 1021-1040.

Zajacz, Z., Halter, W.E., Pettke, T. and Guillong, M. (2008) Determination of fluid/melt partition coefficients by LA-ICPMS analysis of co-existing fluid and silicate melt inclusions: Controls on element partitioning. *Geochimica Et Cosmochimica Acta, 72*, p. 2169-2197.

Zajacz, Z., Candela, P., Piccoli, P., Wälle, M., and Sanchez-Valle, C. (2012). Gold and copper in volatile saturated mafic to intermediate magmas: Solubilities, partitioning, and implications for ore deposit formation. *Geochimica et Cosmochimica Acta., 91*. 10.1016/j.gca.2012.05.033.

Zellmer, G. F., Edmonds, M. & Straub, S. M. (eds) *The Role of Volatiles in the Genesis, Evolution and Eruption of Arc Magmas.* Geological Society, London, Special Publications, 410.

Zhang, Q.,Machado, N., Ludden, J., andMoore, D. (1993). Geotectonic constraints from U-Pb ages for the Blake River Group, the Kinojévis Group and the Normétal mine area, Québec: *Geological Association of Canada – Mineralogical Association of Canada, Joint Annual Meeting, Program and Abstracts, v. 18,* p. A-114.

Zhang, R.Y., Zhai, S.M., Fei, Y.W., and Liou, J.G. (2003). Titanium solubility in coexisting garnet and clinopyroxene at very high pressure: the significance of exsolved rutile in garnet. Earth and Planetary Science Letters, 216, p. 591-601.

Zhang, Z., Fedortchouk, Y., and Hanley, J. J. (2015). Evolution of diamond resorption in a silicic aqueous fluid at 1-3 GPa: Application to kimberlite emplacement and mantle metasomatism. Lithos, 227, p. 179-193.

Zhang, D. and Audétat, A. (2018). Magmatic-Hydrothermal Evolution of the Barren Huangshan Pluton, Anhui Province, China: A Melt and Fluid Inclusion Study. *Economic Geology, 113,* p. 803-824.

Zhao, J., Brugger, J., and Pring, A. (2019). Mechanism and kinetics of hydrothermal replacement of magnetite by hematite. *Geoscience Frontiers, 10(1),* p. 29 – 41.

Chapter 3: Conclusions, limitations, and future work

3.1 Key conclusions

The results of this study show that Bousquet Formation SMI are well preserved and contain important information regarding magmatic evolution, metal tenor, volatile content, and P-T conditions. The key findings of this study are:

(i) In the Bousquet Formation, only two volcanic lithologies contain appropriate SMI acceptable for thorough study: SMI inside magmatic quartz phenocrysts of units 2.0 [quartz feldspar porphyry (QFP) rhyolite sills] and 5.3 rhyolite sills] (QFP rhyolite flows). Primary SMI are protected in phenocrysts despite recrystallization and have bulk compositions that are chemically and mineralogically compatible with trapped silicate liquids. Based on petrographic and compositional criteria, careful evaluation of each melt inclusion assemblage is required to distinguish true SMI from hourglass-type inclusions and to evaluate contamination by accidental saturated phase entrapment or alteration by post-entrapment modification. To do this robustly, a combination of cathodoluminescence imaging, inclusion and host petrography (SEM, optical, Raman) and scrutiny of LA-ICP-MS data after single inclusion analysis is required. Dissemination of trace elements based on LA-ICP-MS data suggests that unit 2.0 SMI has ORG or WPG (anorogenic) tectonic settings, while unit 5.3 SMI is consistent with the classification of syn-COLG or VAG. Nonetheless, no SMI has trace element (Sr-Y-La-Yb) features consistent with Archean TTG,

indicating major compositional alteration prior to trapping (e.g., by substantial plagioclase fractionation and crustal contamination).

(ii) The spectrum of major and trace elements, like ore metals, is much broader in the SMI, although the bulk compositions of the SMI and bulk rocks are similar and have comparable tectonic affinity classifications. This represents a mixture of many processes: differentiation (prior to entrapment and eruption), aggregation of crystals (diluting incompatible melt constituents in rhyolites), possibly degassing/interaction at depth with carbonic volatiles, and alteration/metamorphism post-solid. In this geological environment, metal concentrations in bulk rocks assayed are *not* indicative of the composition of the initial magmatic liquids.

(iii) Comparative study of apatite, SMI, and bulk rock data reveals that SMI and coeval apatite record the crystallization of large quantities of plagioclase, K-feldspar, and apatite at depth prior to eruption-emplacement. SMI reported substantial rhyolite differentiation (at least 70-75% crystallization) over its history of entrapment, suggesting a long phenocryst residence at depth in a staging chamber or deeper source area. SMI were trapped in quartz phenocrysts at P = 10 - 13.5 kbar based on preliminary constraints from SMI homogenization experiments combined with Ti-in-quartz thermometry, consistent with the expected range of early paragenesis for the magmas of the Mooshla Intrusive Complex. Homogenized SMI suggests that there was co-entrapment of an immiscible carbonic fluid (CO2-dominant), implying that at the time of entrapment in the phenocrysts, the melt was saturated in CO2. Due to their advanced age, the presence of CO2 in the SMI of the Bousquet rhyolites indicates that any SMI trapped in a magmatic system may potentially have CO2 as a

saturated phase. CO2-bearing fluids were continuously received from an external source by the Bousquet magmatic system, were CO2 saturated, and underwent constant fractionation iterations with degassing causing early removal of H2O metal-bearing fluids. Mixing silicate melt with immiscible CO2 (e.g., derived from wall rocks) could have separated some ore metals from the magma prior to SMI entrapment.

(iv) Unit 5.3 SMI range from 6 ppb Au (1st quartile) to 159 ppb Au (3rd quartile; n = 10) while unit 2.0 SMI range from 5 ppb Au (1st quartile) to 24 ppb Au (3rd quartile; n = 14); at these Au concentrations, a minimum of 0.5-15 km3 and 4-19 km3 rhyolitic magma would be needed, respectively, to obtain the Au by leaching or devolatilization in the LaRonde Penna VMS deposits. A conservative estimate of the volume of the Bousquet Formation's Upper Member is approximately ~7.5 km3. It is therefore possible that the rhyolitic units of the Bousquet Formation delivered magmatic Au to the VMS deposits (with an efficiency correction). However it is important to note that while these metal concentrations are well above upper crustal concentrations, when compared to younger, felsic magmas in arc and transitional ore-forming environments, the Bousquet Formation rhyolitic melts were not exceptionally evolved or enriched in ore metals.

(v) The existence in the SMI of both Units 5.3 and 2.0 of co-entrapped carbonic liquid and very low water content may mean that the ore metal content in the SMI is a minimum value. The lack of correlation between very strongly incompatible elements e.g., Cs) and ore metals (in SMI) is consistent with the disruption by immiscible or exsolving fluid phases of the original metal contents of the SMI. On

the other hand, selected metal ratios between the SMI and the LaRonde Penna deposit ore bodies for elements consistently enriched in the SMI (Cu/Au, Cu/As, Au/As, Sb/Bi) overlap, and this is unlikely to be a coincidence, indicating that these ore metal ratios are conservative even in the presence of saturated volatiles. In comparison to the Mouska, Doyon and Westwood deposits, both the SMI and ore bodies are distinguished by low Au/As and Cu/As ratios. The overlap between the LaRonde Penna ore and SMI in metal ratios is an indication that the volcanic rocks had some direct influence on the ore metal content of the LaRonde Penna VMS system, either by active degassing or passive leaching.

3.2 Limitations and future work

(i) The compositional difference between melt inclusion and bulk rock geochemistry may be due to a method of mixing magma in either a closed system (i.e., compositionally zoned magma chamber) or an open system (i.e. mixing of two separate magma batches; Dietrich et al., 2000). These are possibilities which could be explored in future studies.

(ii) The variability in SMI compositions found in the same unit can be directly linked to the trapping of SMI at different times in quartz phenocrysts that were crystallised long before the eruption. Future work to account for this variability would be to take note of SMI shapes, as they may gradually shift from irregular in late-formed crystals to mature negative-crystal shapes in early-formed crystals (Manley, 1996; Frezzotti, 2001).

(iii) If the SMI devitrified, there must be assurance that the H_2O peaks came from a glass and not from a microcrystalline K-feldspar that was devitrified. If a K-feldspar was

shot, a water band would be very tiny, since there is no water in a K-feldspar. This is more work which can be done in future studies.

(iv) With other techniques, like infrared, the amount of CO_2 in the inclusions could be measured.

(v) Laser ablation data for zircons is complimentary to Ti in quartz because if the Ti values are unmixed from the host and the zircon then a pressure for the phenocryst can be calculated. This will allow the potential estimate of a very precise depth for the magma chamber from which the phenocryst came. However, there are only two good zircon signals collected for the current data set. Also, a different internal standard needs to be chosen for the zircons found in units 2.0 and 5.3. Besides Zr, Hf is the other major element that is present in zircon in quite high concentrations. Unfortunately, Hf was not present in the laser ablation element menu when the zircons were studied. Going forward, there needs to be a timely way that will allow estimates on the entrapment depth for the samples. However, zircon grains in quartz phenocrysts were not nearly as prevalent as other accessory minerals, like apatite.

(vi) Thomas et al. (2010) presented a diagram that makes use of several minerals when determining an exact pressure. On the diagram, there are calibration lines that represent values of Zr in rutile. The calibration lines intersect with lines representing Ti in quartz. Zirconium would not accumulate in quartz because it is quite incompatible in most rock-forming minerals (Burnham, 2018). The Zr concentrations in rutile would be a good constraint; however, the rutile needles in unit 2.0 and 5.3 samples are too small to isolate and therefore difficult to get an accurate reading. However, measuring Ti in zircons is an

alternative option because there are large zircon grains present in units 2.0 and 5.3. There are still many samples left from these units, so a search for zircons can be conducted; even so, it will take time to map the grains and should be considered for future work. When more zircons have been mapped in the samples, Hf will be included in the laser ablation menu list and an internal standard for Hf can be established on the probe at Dalhousie University.

(vii) Zircon fractionation did not progress throughout the evolution of the magma as can be seen by the lack of correlation with Zr and Cs (Figure 26F). Further study looking at the Zr/Hf ratios of zircons in quartz diorites and gabbros of the MIC could give a better idea of whether there is another mineral that is fractionating U. Any mineral that fractionates U would result in a change in Zr/Hf ratios because Zr would be removed proportionally with U (Lovering and Wark, 1974; Frondel, 1975; Pearce and Cann, 1975; Williams, 1978).

(viii) Collection of more SEM-EDS analyses of unit 5.3 exposed types I and II SMI (homogenized and non-homogenized), and analyses of type III inclusions with a distinction made between melt + accidentally trapped minerals and hourglass inclusions. This distinction will allow for accidentally trapped mineral phases to be catalogued for both units 2.0 and 5.3.

(ix) Future mass-balance work: An in-depth quantitative study on the efficiency of Au precipitation in this type of environment and whether this volume of magma could provide enough Au to the LaRonde Penna VMS deposits.

(x) Investigate whether the Au content of the Bousquet Formation magma was incorporated into CO_2.

Appendix 2A - LA-ICP-MS analyses of unit 2-2 SMI

Sample (unit: 2.0)	23Na20 Ind.%I	25MgO	27Al2O3	29SiO2	31P2O5	39K2O	44CaO	47TiO2	51MnO	54FeO	118(ppm)	45Sc	51V	53Cr	59Co	62Ni	65Cu	75As	85Rb	88Sr	89Y	90Zr	93Nb	95Mo	107Ag	118Sn	121Sb	133Cs	137Ba	139La	140Ce	141Pr	146Nd	147Sm	151Eu	157Gd	159Tb	163Dy	165Ho	167Er	169Tm	172Yb	175Lu	178Hf	181Ta	182W	197Au	208Pb	209Bi	232Th	238U
3Bb-28-177-phenz-mat02	1.68678364	0.85776	15.3389	70.002	<DLT	4.63345	0.21186	0.76016	0.0747	3.89518	39.9693328	51.855	11.4272	<5|6	1.37187	<83	74.3606	106.456	90.162	133.68	17.5232	677.056	35.8715	<1.00	16.0993	28.401	3.95492	7.24892	744.234	5.99237	114.4746	1.76872	8.99105	2.1653	0.23807	0.67593	1.05394	10.3342	2.60296	8.09451	1.09504	8.77332	1.52123	23.3363	3.02783	0.62867	<0.68	75.4622	3.86749	4.24728	0.72227
3Bb-28-177-phenz-mat03	0.42973701	0.19457	18.7363	70.0016	0.04137	1.43344	0.13526	0.19737	0.03341	1.77672	13.2207266	12.5979	<0.32	<6.45	0.55663	<4.9	124.873	30.658	87.6253	66.2923	51.1743	261.443	14.3175	1.2723	4.54827	1.622366	<0.86	2.6199	494.838	33.0903	74.4737	9.29638	39.2644	10.2335	0.7187	8.62492	1.36507	8.30701	1.78691	5.72778	0.89918	7.3044	1.0753	8.11163	0.79552	<0.21	<0.24	14.1966	0.54572	4.58906	1.16072
3Bb-28-177-phenz-mat03	0.24964647	0.13406	15.1729	70.0069	0.01791	1.63912	0.86175	0.21112	0.02407	2.48415	21.9373552	7.4772	0.11207	<0.50	1.07582	<1.91	<0.995	3.9684	21.1525	201.007	41.3008	470.38	20.4197	1.60765	0.82463	1.78733	0.16002	0.46213	295.188	7.81939	17.7869	2.22073	9.04962	2.49745	0.54976	2.86629	0.49414	4.4841	1.44383	0.52903	1.2296	0.79119	1.74671	0.14424	0.9808	0.842	<0.014	8.13273	0.06069	0.53799	1.41954
3Bb-28-177-phenz-mat04	4.06522787	0.19707	7.27454	70.0028	0.02572	2.31558	0.68656	0.25535	0.03979	1.18643	14.0023249	15.1993	0.66151	<0.73	0.68741	<1.86	0.23829	19.339	50.6811	129.824	114.836	439.803	17.8658	1.03868	1.55966	2.7456	0.41788	1.28232	567.107	42.5513	94.3367	12.2248	51.8533	12.5921	1.7026	14.5831	2.54549	17.7913	4.15637	12.5602	1.93282	14.1234	2.23165	12.6837	0.90986	0.33411	<0.017	59.5359	0.24633	6.65145	1.76215
3Bb-28-177-phenz-mat07	1.44708358	0.1464	14.4597	70.0024	0.01494	3.0186	1.11136	0.21833	0.02247	2.54684	17.2741923	n.a.	n.a.	n.a.	0.1321	21.096	n.a.	n.a.	n.a.	305.192	n.a.	1.49827	2.3551	2.36137	0.55112	1.28961	n.a.	n.a.	n.a.	n.a.	n.a.	n.a.	n.a.	n.a.	n.a.	n.a.	n.a.	n.a.	n.a.	n.a.	n.a.	n.a.	n.a.	n.a.	0.25519	n.a.	n.a.
3Bb-28-188-S-phenz-mat03	0.71947521	0.55	17.6975	70.0055	<0.028	1.66911	0.10523	0.1303	0.02529	2.09289	33.5247586	15.3102	1.55216	<10.3	1.10344	<9.4	1900.76	21.64	90.4985	36.85382	0.87025	259.465	5.90371	<0.49	4.36315	2.86119	1.07999	3.68137	782.029	<0.070	0.1086	<0.022	0.28186	<0.15	0.04896	<0.44	0.189	1.9392	0.69664	2.41313	0.32792	3.83405	0.62788	13.0341	0.49129	<0.23	<0.29	207.112	5.01305	3.91643	0.25176
3Bb-28-188-S-phenz-mat04	5.82705604	0.23522	11.7766	70.0019	0.02647	0.88645	3.1088	0.16454	0.01846	1.55262	7.38753088	11.6859	0.18469	<2.33	0.94707	<5.35	<0.43	37.857	37.3255	365.576	114.14	329.833	15.4667	1.50022	0.51311	1.92708	0.37432	3.75917	1.90707	46.9378	108.585	14.6109	60.1825	15.6883	1.45056	17.4725	3.11707	20.4268	5.06065	13.3109	2.23813	17.919	2.62587	13.2237	1.03613	0.3706	<0.096	87.1276	1.16336	9.05644	2.30438
3Bb-28-188-S-phenz-mat05	0.31979991	1.15226	16.3202	69.9889	0.02324	1.74868	0.40809	0.17729	0.02527	2.82629	41.1046823	9.67185	0.44882	<5.16	1.9403	<8.76	<0.66	16.396	128.758	20.6887	62.1061	468.734	18.6795	1.0036	<0.30	2.86166	0.66268	4.11993	745.96	23.2175	50.8402	6.17683	26.5003	6.95506	0.99962	5.30083	0.92201	8.06565	2.31143	8.65188	1.70518	11.4143	2.08674	15.4096	1.66653	0.63095	<0.15	38.9863	0.58244	8.28697	1.90165
3Bb-28-188-S-phenz-mat06	0.31677618	0.51917	17.4188	70.0018	0.04109	1.80732	0.51863	0.21821	0.04136	2.10352	33.0377449	12.2347	0.68761	<1.95	0.84019	<2.61	<0.23	12.159	68.1209	98.4276	6.52367	397.11	12.3387	<0.083	<0.0022	3.52496	0.76641	3.70846	409.643	13.0598	34.2327	4.80123	19.9077	4.15598	0.38535	2.25395	0.31091	1.75427	0.41622	1.62222	0.25604	2.05227	0.31475	0.95978	0.19959	0.3289	<0.038	48.4368	2.38279	8.11761	0.82175
3Bb-28-188-S-phenz-mat07	5.58843753	0.20256	15.9262	70.0001	<0.15	0.36104	3.68484	0.20171	0.02233	0.92177	<48.0	6.10411	<2.03	<48.3	<1.22	<84.5	<7.68	49.439	15.6186	501.553	124.025	241.348	3.92866	1.72722	<3.31	<9.03	<6.98	<1.76	41.0617	11.9775	113.569	16.0671	69.3737	18.2868	3.07209	25.5476	3.3381	20.2666	5.4328	9.66648	2.33119	11.6579	1.31643	13.9798	2.29379	<0.54	<1.95	120.063	<1.60	9.73926	2.36726
3Bb-28-188-S-phenz-mat08	6.0101763	0.1755	15.4001	70.0006	0.04179	0.96158	3.20967	0.18134	0.02312	1.39773	<14.0	n.a.	n.a.	n.a.	0.8225	81.6383	335.475	n.a.	n.a.	1.1898	<0.34	<1.77	<0.12	1.43153	n.a.	67.5296	n.a.	n.a.	n.a.	n.a.	n.a.	n.a.	n.a.	n.a.	n.a.	n.a.	n.a.	n.a.	n.a.	n.a.	n.a.	n.a.	13.0359	n.a.	13.7748	0.4211	<0.26	<0.065	n.a.	<0.56	n.a.	n.a.
3Bb-28-188-S-phenz-mat14-mt01	4.26775696	0.15939	15.8661	70.0035	0.01595	2.67645	1.99405	0.17369	0.01832	2.08438	32.3705466	n.a.	n.a.	n.a.	n.a.	n.a.	n.a.	n.a.	n.a.	227.419	101.16	335.526	n.a.	1.07644	0.41791	2.03113	0.40988	2.60071	n.a.	45.1318	n.a.	n.a.	n.a.	n.a.	n.a.	n.a.	n.a.	n.a.	n.a.	n.a.	n.a.	n.a.	13.6304	n.a.	11.387	1.12489	0.40181	0.00482	n.a.	0.66058	n.a.	n.a.
3Bb-28-188-S-phenz-mat14-mt02	3.81834726	0.21634	16.1592	69.996	0.01177	2.3641	1.87938	0.18898	0.01842	1.69436	31.2226577	n.a.	n.a.	n.a.	n.a.	n.a.	n.a.	n.a.	n.a.	225.27	100.99	337.6	n.a.	1.04758	0.41953	2.70124	0.4017	2.63112	n.a.	37.0265	n.a.	n.a.	n.a.	n.a.	n.a.	n.a.	n.a.	n.a.	n.a.	n.a.	n.a.	n.a.	12.1313	n.a.	12.2627	0.87342	0.32971	<0.024	n.a.	0.81954	n.a.	n.a.
3Bb-28-188-S-phenz-mat14-mt03	5.20476308	0.18685	16.1105	70.0054	0.02009	1.37588	2.60506	0.18511	0.01649	1.28992	33.2385524	n.a.	n.a.	n.a.	n.a.	n.a.	n.a.	n.a.	n.a.	320.838	101.243	347.935	n.a.	0.62598	0.3954	<1.18	<0.75	1.5643	n.a.	32.5208	n.a.	n.a.	n.a.	n.a.	n.a.	n.a.	n.a.	n.a.	n.a.	n.a.	n.a.	n.a.	13.8962	n.a.	12.7564	1.00416	<0.20	<0.029	n.a.	0.60358	n.a.	n.a.
3Bb-28-188-S-phenz-mat14-mt04	0.32449626	0.01888	16.6158	69.9999	0.01432	1.68069	0.05798	0.2006	0.03439	3.11261	50.2636169	n.a.	n.a.	n.a.	n.a.	n.a.	n.a.	n.a.	n.a.	22.0569	46.1464	327.811	n.a.	1.57407	0.03831	1.44684	<0.47	3.48946	n.a.	7.68574	n.a.	n.a.	n.a.	n.a.	n.a.	n.a.	n.a.	n.a.	n.a.	n.a.	n.a.	n.a.	7.61907	n.a.	12.1314	1.16159	0.22202	<0.018	n.a.	0.32318	n.a.	n.a.
3Bb-28-188-S-phenz-mat14-mt05	6.32365937	0.22773	15.3848	70.002	0.02522	0.3035	3.20377	0.23092	0.0572	1.28122	14.2145526	n.a.	n.a.	n.a.	n.a.	n.a.	n.a.	n.a.	n.a.	384.55	107.561	348.683	n.a.	1.54744	0.28282	<0.71	<0.48	3.6075	n.a.	47.1688	n.a.	n.a.	n.a.	n.a.	n.a.	n.a.	n.a.	n.a.	n.a.	n.a.	n.a.	n.a.	14.4832	n.a.	12.9272	1.08169	0.28889	<0.018	n.a.	0.5961	n.a.	n.a.
3Bb-28-188-S-phenz-mat14-mt06	5.10196902	0.23479	15.9168	69.9962	0.027	1.3669	0.21157	0.16462	0.03614	1.58081	13.4626775	n.a.	n.a.	n.a.	n.a.	n.a.	n.a.	n.a.	n.a.	295.767	84.6004	299.865	n.a.	<0.23	0.28597	1.03857	<0.43	2.28439	n.a.	38.4453	n.a.	n.a.	n.a.	n.a.	n.a.	n.a.	n.a.	n.a.	n.a.	n.a.	n.a.	n.a.	10.895	n.a.	9.98344	0.82437	0.14388	<0.017	n.a.	0.76189	n.a.	n.a.
3Bb-28-188-S-phenz-mat07	6.77279734	0.0984	16.165	69.969	0.02157	0.31103	2.95373	0.11434	0.02243	0.51327	<9.01	n.a.	n.a.	n.a.	348.829	110.683	334.585	n.a.	1.32417	0.2419	<0.74	<0.68	1.36727	n.a.	46.1579	n.a.	n.a.	n.a.	n.a.	n.a.	n.a.	n.a.	n.a.	n.a.	n.a.	n.a.	n.a.	n.a.	n.a.	n.a.	n.a.	n.a.	13.657	n.a.	11.9679	0.93908	<0.12	<0.016	n.a.	0.31187	n.a.	n.a.
3Bb-29-218-phenz-mat01	6.98688892	0.2333	15.3511	69.9979	<0.025	0.64942	1.45811	0.17169	0.05118	2.08188	<7.90	5.21704	0.55099	<6.26	2.23169	<5.1	3.28094	<6.96	30.3623	81.9699	97.0989	261.091	11.5882	2.07565	0.98933	<1.07	<0.87	1.97175	285.864	11.2186	117.156	14.2764	58.8708	14.7324	1.47342	17.3039	2.66447	17.7441	3.51751	10.1015	1.73351	9.97912	1.41053	8.82616	0.62865	<0.19	<0.23	18.4517	0.29633	8.24475	1.95728
3Bb-28-218-phenz-mat02	7.29080429	0.19611	15.1263	70.0008	<0.011	0.52736	1.82125	0.17072	0.0506	1.81348	9.2070728	6.56538	0.55673	<2.72	1.7203	<6.81	9.38862	<2.81	28.1166	104.106	134.292	292.536	19.8931	1.68461	0.38267	<0.51	<0.42	2.38783	396.842	68.7904	177.925	18.8072	82.4643	19.7411	1.64431	22.111	3.86763	23.8652	4.83735	14.5768	2.17872	13.6059	2.0088	3.11023	1.02584	0.26768	<0.10	24.3558	0.99216	9.73762	2.35935
3Bb-28-218-phenz-mat03	7.46318567	0.1667	15.2323	70.0053	0.01672	0.609	1.5317	0.12118	0.04727	1.99978	6.15627825	7.77614	0.68634	<2.08	1.20817	<5.8	18.683	1.2779	34.571	67.9905	95.7293	260.092	20.7517	1.45053	0.54385	1.49566	0.27185	2.49479	174.756	42.6215	94.7229	12.1788	51.8533	13.2554	1.07565	14.6668	2.44558	16.0407	3.48843	10.5183	1.54856	10.6599	1.64527	8.43172	0.59586	0.29028	<0.032	20.8656	0.92881	5.06856	1.56116
3Bb-28-218-phenz-mat04	6.69327428	0.19177	15.5308	69.9963	<0.040	0.34787	2.49822	0.17902	0.0429	1.58798	<3.6	1.83666	<0.61	<10.8	1.53621	<22.7	15.2179	<7.55	22.6374	134.906	91.797	355.747	8.14759	1.36053	0.851	<1.79	<1.39	2.01536	124.291	45.2603	103.261	12.7656	55.5585	14.0018	1.47359	16.712	2.4837	17.636	3.51174	9.18663	1.65421	11.8923	1.73627	10.8866	0.49964	<0.36	<0.34	26.3224	<0.36	6.79861	1.58054
3Bb-28-218-phenz-mat05	6.66130107	0.22792	15.2756	69.9993	<0.0068	0.53853	1.95123	0.20695	0.05142	2.0852	6.15638317	n.a.	n.a.	n.a.	1.55907	1.1949	n.a.	n.a.	n.a.	299.853	n.a.	1.22397	0.45624	0.88834	<0.48	1.57023	n.a.	n.a.	n.a.	n.a.	n.a.	n.a.	n.a.	n.a.	n.a.	n.a.	n.a.	n.a.	n.a.	n.a.	n.a.	n.a.	n.a.	9.99858	0.75212	0.27598	<0.017	n.a.	0.36492	n.a.	n.a.
3Bb-28-218-phenz-mat06	6.33882498	0.17174	15.7263	69.9931	<0.015	0.49767	2.40952	0.16892	0.05109	1.63815	9.30320358	5.44051	0.28435	<2.27	2.33167	<8.99	29.2246	<2.40	29.453	120.754	107.276	241.973	19.2063	1.80696	0.56478	1.05606	<0.63	2.04596	126.163	54.2673	122.261	15.4076	65.2491	15.0407	0.82796	15.4186	2.67873	18.4897	3.74998	10.8895	1.73039	11.3902	1.79407	8.48751	1.03311	0.31325	<0.13	15.2232	0.28065	7.36767	1.76772
3Bb-28-218-phenz-mat07	7.80457416	0.03186	15.8168	69.9969	<0.0078	0.19462	1.80118	0.08764	0.03182	0.83271	6.67426369	7.32188	0.18695	<1.85	0.38199	<2.32	7.01971	1.395	16.4819	87.0566	107.599	278.273	17.9931	2.40501	0.17253	0.26458	0.08739	2.14143	229.088	51.6145	139.288	15.987	64.4645	16.003	0.78933	16.6593	2.83737	20.3008	4.00714	11.9661	1.87289	12.1825	1.868	9.87087	0.81546	0.27455	<0.043	13.4897	0.67085	7.84324	1.79904
3Bb-28-218-phenz-mat08	1.20422295	0.50162	16.2092	69.998	0.05369	0.90258	0.37847	0.43496	0.0748	3.14253	38.2005173	n.a.	n.a.	n.a.	54.5092	<2.34	n.a.	n.a.	n.a.	948.566	n.a.	0.22306	1.33211	2.49398	0.70568	3.85757	n.a.	n.a.	n.a.	n.a.	n.a.	n.a.	n.a.	n.a.	n.a.	n.a.	n.a.	n.a.	n.a.	n.a.	n.a.	n.a.	n.a.	n.a.	24.5551	1.10788	0.63552	<0.016	n.a.	0.40856	n.a.	n.a.
3Bb-28-278-phenz-mat01	3.74736426	0.25628	15.3869	69.9929	0.01618	0.33642	0.27161	0.07722	0.04228	0.76123	<6.0	n.a.	n.a.	n.a.	0.33394	3.6056	n.a.	n.a.	n.a.	1.8385	381.967	n.a.	0.77774	0.41599	0.46154	0.07079	1.88183	n.a.	n.a.	n.a.	n.a.	n.a.	n.a.	n.a.	n.a.	n.a.	n.a.	n.a.	n.a.	n.a.	n.a.	n.a.	n.a.	n.a.	16.4653	1.98782	0.28885	0.03535	<0.03	n.a.	n.a.	n.a.
3Bb-28-278-phenz-mat02	0.17747874	0.37524	17.5509	70.0012	<0.023	0.38273	0.31675	0.30767	0.09068	1.97708	21.7487777	20.4018	1.15265	<8.09	0.41662	<4.0	31.5289	<8.82	94.4184	22.3131	134.119	380.423	12.3092	2.03068	<0.51	5.05775	<0.81	1.33121	1883.85	64.725	158.142	19.3638	82.5946	18.7957	2.90205	21.3886	3.95582	30.6792	6.45563	17.5089	2.39157	16.3715	2.35328	15.3657	0.51278	0.439	<0.21	3.90887	<0.35	12.8576	2.82416
3Bb-28-278-phenz-mat03	0.39348232	0.26215	18.0446	70.0027	0.01743	0.30162	0.21117	0.28728	<0.16	0.89177	14.6393	<22.2	1.04642	<8.6	0.31279	<3.7	77.8805	65.4546	80.0092	455.876	17.2321	<2.05	<0.57	<0.62	<0.13	1.85158	1091.51	67.8886	162.913	17.7576	76.3905	20.1147	1.88218	17.2542	3.40523	19.9307	4.19657	10.3141	1.58652	9.22943	1.29702	10.2902	0.92727	0.37985	<0.45	22.7726	<0.82	<0.035	0.50981
3Bb-28-278-phenz-mat04	0.15608764	0.26783	18.0285	70.0002	<0.083	0.98687	0.51316	0.28273	0.05251	2.16559	<29.6	7.5189	<3.01	<25.5	0.88724	<8.2	31.5092	19.924	74.2999	80.8164	84.1042	351.453	12.5496	<2.08	<1.30	<0.72	<2.66	1.63899	178.41	51.1163	134.81	14.4291	63.0883	15.5751	1.81011	19.5475	2.65623	18.4757	2.15851	7.91803	1.38599	8.49682	1.87379	16.175	0.2664	<0.66	<0.92	26.641	<0.77	9.90531	1.7862
3Bb-28-278-phenz-mat05	2.38134733	0.14699	15.2479	69.9977	<0.013	0.17463	2.55081	0.25327	0.04156	1.56152	7.08848751	4.65092	0.74222	<0.56	1.29098	<7.88	11.6962	0.48697	270.452	1.63625	1.94624	<0.29	1.03157	<0.63	0.69185	56.102	15.3488	194.954	16.2629	71.1525	17.4399	1.80152	18.7725	2.12092	20.1176	4.16769	11.1078	1.38908	9.29261	1.41782	10.4074	1.56478	<0.12	<0.077	23.0262	<0.11	9.62327	1.89643
3Bb-28-278-phenz-mat02	0.26391656	0.41268	17.7986	69.9951	<0.093	0.52422	0.54294	0.22284	0.04588	2.22406	<36.7	7.80479	<1.03	<33.1	<0.98	<50.6	<0.29	<20.8	81.3224	19.7453	167.995	429.003	25.6584	<0.94	<2.29	<5.27	<3.13	<1.08	1693.66	77.3176	178.248	24.136	112.152	26.4985	2.35158	29.1039	3.85589	30.8569	6.50987	23.7908	2.93031	21.0916	3.04946	19.3117	1.34623	<0.84	<0.96	16.9316	<0.87	15.5784	2.90504
3Bb-28-278-phenz-mat05	0.14919328	0.04967	16.7585	70.0004	<0.12	0.15468	2.08661	0.07585	0.02586	0.78087	<8.07	4.41134	<2.91	<49.5	<1.20	<9.3	31.6458	6.1663	12.2124	640.013	242.975	11.7432	<2.82	<0.85	<0.76	<0.71	<0.84	1.88436	1565.61	<0.19	0.4122	<0.16	<0.91	<1.46	<0.02	<0.26	<0.61	<0.16	0.58298	0.36869	0.97858	0.18168	<0.66	<0.13	1.33283	<1.14	2.05127	2.86687
3Bb-28-278-phenz-mat01	0.52696738	0.28311	17.2898	69.9937	<0.010	0.90424	1.26121	0.2716	0.06311	2.44496	20.109403	9.02525	1.06912	<2.85	1.02533	<6.51	9.10725	1.0557	64.0997	62.467	130.142	351.591	18.1798	1.31788	0.57397	3.03326	<0.28	1.50846	572.452	128.231	16.457	69.4808	16.9734	1.92047	18.9555	3.23516	21.5611	4.718	13.9842	2.03201	13.5818	1.94973	10.4727	0.99763	0.39556	<0.085	17.3088	0.41467	8.90649	2.10033
3Bb-28-278-phenz-mat06	1.58746727	0.07087	16.7729	69.9965	<0.027	0.22228	2.30876	0.0153	0.06868	0.84476	<8.26	0.75192	<0.37	<7.19	0.79534	<2.3	10.7795	<4.28	5.51247	202.962	21.7854	248.843	8.02816	1.51551	<0.49	<1.24	<0.75	<0.18	12.2392	57.6267	75.6186	8.75901	33.3748	6.31854	<0.11	1.942	0.32268	1.97564	0.66053	2.48256	0.45266	0.82792	0.9793	0.33768	0.09673	<0.096	<0.25	1.74745	<0.21	4.23122	1.36177
3Bb-28-282-phenz-mat01	1.64109519	0.1012	16.2062	69.998	0.01588	0.28533	3.17709	0.26619	0.02133	1.99557	5.14680722	11.6461	0.68009	<1.37	1.09431	<9.66	51.2325	0.8512	6.95036	169.675	118.957	183.888	11.3777	2.26124	0.91555	4.03272	<0.15	0.48313	13.9965	65.3403	146.581	18.2269	77.6919	18.774	1.50884	22.3647	3.74149	24.2782	4.99751	13.3265	1.82311	11.5879	1.63171	5.9721	0.65759	<0.038	<0.041	3.4627	<0.034	9.85786	1.8059
3Bb-28-282-phenz-mat02	0.98857207	0.14663	17.1997	70.0066	0.02599	0.54982	0.23161	0.08776	0.03986	1.46252	17.0166191	n.a.	n.a.	n.a.	0.47063	<2.6	<0.77	10.9756	25.294	272.186	178.17	22.04	<0.83	<0.67	2.75996	<0.75	1.73833	742.328	128.911	310.006	34.5707	139.419	28.8942	2.62227	43.7562	7.42623	46.8942	11.2821	22.9054	3.08651	20.3408	3.0053	22.7092	3.4997	0.49888	<0.13	23.2031	<0.23	20.3491	3.6026
3Bb-28-282-phenz-mat03	2.03951165	0.26776	16.3673	70.0041	<0.0018	1.26293	0.29518	0.27611	0.05921	2.32088	187.6426645	10.4308	0.38575	<0.43	1.39276	<1.24	166.516	7.787	56.3872	61.1881	3.48693	435.432	25.2349	0.71889	0.84808	3.42167	0.76409	2.37946	242.445	4.73031	0.49986	1.52632	0.31998	0.95835	0.36412	0.07565	0.68203	0.14223	0.47041	0.09053	0.95405	0.08104	17.1101	1.59424	0.02966	<0.017	14.0211	0.11346	1.22271	0.49431
3Bb-28-282-phenz-mat04	3.62389753	0.16948	15.2467	70	<0.0014	1.64168	0.23191	0.28075	0.04868	2.18268	108.7547185	5.6462	0.75418	<0.37	1.23811	<9.98	687.925	5.2535	61.6858	80.7275	11.4185	390.65	13.5734	0.63317	7.57266	2.16987	0.63107	2.27393	867.765	0.98055	3.1216	0.96822	1.80778	0.16949	0.23769	1.02851	0.12864	1.59736	0.38782	1.44924	0.27656	2.10108	0.28024	0.41109	0.18911	0.03046	<0.067	11.4623	0.11368	0.84978	0.59764
3Bb-28-282-phenz-mat05	5.64948172	0.12081	15.2012	70.006	<0.018	0.38961	3.88196	0.20014	0.04646	1.46538	6.39046321	2.81607	0.50523	<2.42	1.6961	<2.0	<0.66	6.1318	19.3387	113.736	110.827	264.468	8.55235	1.55464	<0.43	2.77602	<1.05	0.9896	45.2259	56.7116	120.096	15.1818	65.9844	16.6153	1.54884	17.5103	2.75763	19.4032	3.71774	11.0673	1.25564	8.23275	0.74319	0.1208	<0.19	16.4958	0.27097	8.89161	0.51558
3Bb-28-282-phenz-mat06	0.47478358	0.22168	17.2988	69.9999	<0.0124	0.44965	1.16972	0.13481	0.05132	2.645	13.5195381	7.82853	0.50894	<3.44	1.19408	<8.48	<0.62	<0.39	74.2566	61.6291	112.016	269.01	23.2601	1.52114	0.57605	2.31811	0.57973	1.89014	1077.119	51.0357	120.312	14.6348	57.6498	13.2988	1.44853	18.2803	3.10887	19.6152	4.08796	12.3113	1.98586	13.8649	2.16576	14.0184	0.98676	0.16406	<0.12	18.7263	0.26177	7.80917	2.00388
3Bb-28-282-phenz-mat07	5.24673785	0.20849	16.4119	69.985	0.00585	1.47632	2.52577	0.1695	0.03299	0.99294	24.1659778	6.25328	0.67733	<0.36	0.60455	<1.08	26.0956	1.2789	25.4812	89.9667	113.507	279.493	23.0976	1.3907	0.23517	1.47496	0.2123	0.85553	100.843	8.64497	9.54735	1.39774	4.50689	1.34006	0.16727	2.50196	1.13782	13.9851	4.14137	15.1706	2.40121	16.7786	2.394	9.68337	1.67407	0.16616	0.01486	5.71063	0.06022	14.2034	2.50807
3Bb-28-282-phenz-mat08	3.47787264	0.11972	16.799	70.0007	0.01561	0.26013	2.66331	0.14541	0.01986	0.91665	10.2427998	8.84157	0.62438	<0.45	1.34654	<4.48	1.27392	0.5312	18.6463	94.6417	118.701	257.876	26.182	1.87479	0.57319	3.36101	0.72156	1.99148	558.127	56.2522	125.231	16.1079	66.9973	16.0161	1.44085	17.706	2.99841	19.1805	4.26176	13.0696	1.88121	12.9193	1.98637	8.8357	1.4477	0.4087	<0.017	9.79092	0.80027	8.37755	1.85252
3Bb-28-282-phenz-mat14	3.78708769	0.19681	15.7215	69.993	0.00617	2.50428	1.95882	0.17863	0.06112	2.65254	52.9366677	11.4527	0.56238	<0.25	1.39741	<0.65	0.10689	1.9897	55.7099	60.9381	176.728	327.157	31.6898	2.43168	2.18557	4.56681	0.56197	2.79687	455.375	71.0243	168.83	20.5781	86.6562	21.42	1.32498	23.9354	4.10742	28.637	6.39276	18.7243	3.

Appendix 2B - LA-ICP-MS analyses of unit S-3 SMI

Sample (unit S-3)	23Na20 Ant.%)	25MgO	27Al2O3	29SiO2	31P2O5	39K2O	44CaO	47TiO2	55MnO	56FeO	118(ppm)	45Sc	51V	53Cr	59Co	62Ni	65Cu	75As	85Rb	88Sr	89Y	90Zr	93Nb	95Mo	107Ag	118Sn	121Sb	133Cs	137Ba	139La	140Ce	141Pr	146Nd	147Sm	151Eu	157Gd	159Tb	163Dy	165Ho	167Er	169Tm	172Yb	175Lu	178Hf	181Ta	182W	197Au	208Pb	209Bi	232Th	238U
121S-161-493-phenc1-met01	0.516876337	0.65172	17.5347	70.0047	<0.018	5.13137	1.7694	0.28881	0.03142	1.23081	33.1876788	0.75114	4.62062	<0.95	0.50618	<3.2	<0.90	5.00698	120.425	94.9503	30.2783	146.281	10.7622	0.91959	<0.43	<0.95	<0.67	2.06393	1720.74	66.4766	122.559	12.2027	40.348	6.42196	0.99923	5.24764	0.56288	4.43041	1.14311	4.26539	0.72843	4.66454	0.68142	1.25106	0.61179	0.83377	<0.21	10.5892	0.33613	20.1225	5.11469
121S-161-493-phenc1-met02	0.109413458	0.574603	17.8866	69.9934	<0.023	5.7336	1.00218	0.36116	0.01704	1.12582	60.98505073	3.10187	3.81754	<7.27	0.76785	<6.1	<1.24	<8.84	159.723	56.3392	45.9951	125.15	8.5701	2.52473	<0.40	1.44663	<0.81	2.17697	1786.62	82.5699	149.978	15.4011	51.1261	8.57339	1.34738	6.43121	0.80437	6.49578	1.74734	5.12318	0.94026	6.02828	0.73197	1.45005	0.64798	0.54038	<0.21	10.4952	0.49406	23.6484	5.64571
121S-161-493-phenc2-met01	0.860974766	0.640803	17.9414	70.0039	0.03714	4.65672	1.97548	0.25207	0.02215	1.01728	35.4929361	n.a.	n.a.	n.a.	n.a.	n.a.	n.a.	174.054	n.a.	1.92278	<0.097	0.44368	<0.44	2.26456	n.a.	n.a.	n.a.	n.a.	n.a.	n.a.	n.a.	n.a.	n.a.	n.a.	n.a.	n.a.	n.a.	n.a.	n.a.	n.a.	n.a.	n.a.	n.a.	0.80461	0.65426	0.5166	<0.016	n.a.	0.22567	n.a.	n.a.
121S-161-493-phenc2-met11	0.130786416	0.849916	17.9434	69.9934	0.0054	6.33643	0.12889	0.14569	0.01275	0.43405	43.42473158	2.04653	4.51911	<1.59	0.42992	<3.56	0.46157	2.5672	146.633	18.8419	21.872	254.643	4.72413	2.07679	<0.13	0.73933	<0.17	8.49924	1573.62	74.1333	156.122	15.5838	50.5095	8.55858	1.17203	6.04399	0.8455	6.31976	0.90637	2.65451	0.68953	3.55691	0.55949	7.84407	1.7046	0.11331	0.11537	3.90296	<0.042	0.45126	4.24284
121S-161-493-phenc2-met03	0.131477384	0.457157	17.5161	70.0027	0.01175	5.71547	1.36123	0.2595	0.02007	1.02191	35.71645132	4.09679	4.75046	<0.97	0.29742	<1.74	0.26272	1.84868	132.061	92.7924	12.0102	107.772	15.1447	1.71797	<0.096	1.1907	<0.10	16.15	1695.3	94.8476	183.873	17.5892	56.974	8.3502	1.47117	6.53106	1.04518	7.44258	1.94052	6.43614	1.12133	7.95598	1.13365	3.79992	1.02102	0.90401	<0.018	13.8522	0.44807	27.54	7.99703
121S-161-493-phenc2-met12	0.573402403	0.497539	18.1218	69.9947	<0.0073	5.24883	1.20952	0.3372	0.03108	1.03018	36.09140366	2.88298	4.57992	<2.24	0.27473	<5.12	<0.29	20.0169	121.162	89.1633	25.4458	130.163	15.2166	<0.069	<0.17	1.06071	<0.24	3.18582	1745.41	55.1931	101.796	10.5377	32.2215	6.91818	0.84586	3.50839	0.52334	4.03361	0.87976	2.70338	0.44885	3.65193	0.47281	6.64324	0.84938	0.6328	<0.081	16.188	0.11012	15.7077	4.65957
121S-161-493-phenc3-met01	1.455374303	0.36512	17.5798	69.9961	<0.014	4.19949	2.30861	0.2658	0.01155	0.81681	44.9977361	2.60968	3.55008	<4.43	0.33823	<1.6	<0.72	26.1167	97.1995	166.83	27.9118	181.294	11.8359	<0.34	<0.26	<0.74	<0.55	2.08576	1352.55	64.6378	118.957	11.1958	38.0248	5.86298	1.00516	4.68682	0.86672	4.61599	1.0288	3.00868	0.44936	3.60961	0.53071	6.14662	0.81692	0.6724	<0.10	23.9765	0.37402	17.9326	4.31287
121S-161-493-phenc4-met01	1.296891661	0.36524	17.0422	70.0035	<0.029	3.91054	3.06009	0.2341	0.01467	1.03588	44.2209631	0.79206	3.83654	<11.4	<0.364	<18.3	3.80891	<6.47	93.3956	197.614	40.2462	168.747	10.3915	2.78288	<0.72	<1.67	<0.99	1.89326	1334.21	99.5416	182.628	18.6166	62.048	11.0747	1.51607	6.76933	0.8593	7.77321	1.45832	5.69138	0.91227	5.5721	0.99688	8.55111	0.85693	0.65791	<0.29	18.8966	<0.33	31.2651	7.07133
121S-161-493-phenc4-met02	0.735518817	0.443837	17.3778	70.0015	0.02918	4.94146	2.08548	0.26753	0.01363	1.0246	36.87626142	0.59928	3.53625	<9.53	<0.204	<7.5	<1.06	<5.98	114.018	127.798	23.037	137.083	13.3866	1.98179	<0.62	<1.37	<0.98	1.55779	1711.68	51.5316	100.944	9.66495	32.7029	4.96457	0.72449	3.72513	0.47828	3.46584	0.78653	2.64803	0.47448	3.5196	0.61061	5.84631	1.0773	0.62206	<0.22	16.7562	<0.27	15.9461	4.19125
121S-161-493-phenc4-met03	0.072384536	0.58321	17.6254	69.9943	<0.064	6.16458	0.85348	0.3385	0.01467	1.36859	62.7331354	<1.13	2.25963	<27.1	<0.630	<62.8	<2.62	<15.5	136.667	50.5571	25.2466	<15.7	6.57102	1.00103	<1.67	<3.65	<2.58	2.16816	1782.55	63.3936	116.217	12.2489	40.6824	2.58095	0.60391	4.86012	0.82907	4.22307	1.38688	2.47529	0.50842	4.37084	0.55707	6.09033	0.4157	<0.64	<0.60	7.92168	<0.72	21.5427	3.88406
121S-161-492(2-phenc1-met01	0.425846884	0.47769	18.1766	69.9986	0.00456	4.54586	1.83418	0.28821	0.01367	1.02218	27.2376334	n.a.	n.a.	n.a.	n.a.	n.a.	n.a.	103.249	24.0768	169.348	n.a.	2.15678	<0.14	<0.61	<0.49	1.62161	n.a.	51.5136	n.a.	n.a.	n.a.	n.a.	n.a.	n.a.	n.a.	n.a.	n.a.	n.a.	n.a.	n.a.	n.a.	n.a.	n.a.	1.28045	n.a.	4.75478	0.74391	0.4261	<0.037	n.a.	0.18231	n.a.	n.a.
121S-161-492(2-phenc1-met02	0.108533562	0.59116	18.4758	69.9986	0.04796	5.4853	0.6646	0.40415	0.01279	1.21109	<24.2	n.a.	n.a.	n.a.	n.a.	n.a.	n.a.	n.a.	36.4176	32.0124	136.336	n.a.	1.72314	<0.70	<3.32	<2.44	2.28752	n.a.	60.9396	n.a.	n.a.	n.a.	n.a.	n.a.	n.a.	n.a.	n.a.	n.a.	n.a.	n.a.	n.a.	n.a.	n.a.	n.a.	3.88861	n.a.	4.49396	0.30027	<0.55	0.41457	n.a.	<0.57	n.a.	n.a.
121S-161-492(2-phenc2-met01	0.186287523	0.651187	17.7429	69.9938	0.0254	5.85713	0.87733	0.31033	0.02117	1.33373	37.8769401	n.a.	n.a.	n.a.	n.a.	n.a.	n.a.	n.a.	61.6669	39.2619	121.328	n.a.	1.30568	<0.12	0.94853	0.56838	2.68777	n.a.	85.3939	n.a.	n.a.	n.a.	n.a.	n.a.	n.a.	n.a.	n.a.	n.a.	n.a.	n.a.	n.a.	n.a.	n.a.	n.a.	2.72767	n.a.	3.92915	0.7539	0.76517	0.31048	n.a.	<0.11	n.a.	n.a.
121S-161-492(2-phenc2-met04	1.072963628	0.410157	18.0285	70.0015	0.03527	3.71199	2.67862	0.27434	0.00925	0.78534	20.61157739	n.a.	n.a.	n.a.	n.a.	n.a.	n.a.	n.a.	173.28	26.5587	135.782	n.a.	1.7346	<0.18	<0.95	<0.59	1.26965	n.a.	56.1884	n.a.	n.a.	n.a.	n.a.	n.a.	n.a.	n.a.	n.a.	n.a.	n.a.	n.a.	n.a.	n.a.	n.a.	n.a.	2.73235	n.a.	3.93783	0.67706	0.22862	<0.026	n.a.	<0.17	n.a.	n.a.
121S-161-492(2-phenc2-met05	0.100486765	0.6891	17.5311	69.9964	0.00435	5.42764	1.55034	0.31184	0.01514	1.33057	33.6141719	n.a.	n.a.	n.a.	n.a.	n.a.	n.a.	n.a.	58.7644	1.80642	125.436	n.a.	1.87714	<0.41	<2.08	<1.36	2.28718	n.a.	3.6219	n.a.	n.a.	n.a.	n.a.	n.a.	n.a.	n.a.	n.a.	n.a.	n.a.	n.a.	n.a.	n.a.	n.a.	n.a.	0.83137	n.a.	2.06636	0.94408	0.30777	<0.056	n.a.	<0.37	n.a.	n.a.
121S-161-492(2-phenc2-met08	0.111963716	0.583053	18.4187	70.0014	<0.025	5.46551	0.86578	0.32987	0.01448	1.1863	<18.3	n.a.	n.a.	n.a.	n.a.	n.a.	n.a.	n.a.	50.1223	36.1448	168.237	n.a.	0.99265	<0.38	<2.11	<1.37	2.0623	n.a.	62.534	n.a.	n.a.	n.a.	n.a.	n.a.	n.a.	n.a.	n.a.	n.a.	n.a.	n.a.	n.a.	n.a.	n.a.	n.a.	4.81696	n.a.	5.91909	0.96066	0.60283	<0.052	n.a.	<0.38	n.a.	n.a.
121S-161-493(6)-phenc1-met01	0.978644522	0.381	17.1022	70.0003	0.0533	4.75765	2.09886	0.24106	0.01872	1.11993	81.6131106	n.a.	n.a.	n.a.	n.a.	n.a.	n.a.	n.a.	123.728	38.012	151.198	n.a.	2.02176	0.13786	1.12677	0.61478	2.64643	n.a.	94.2583	n.a.	n.a.	n.a.	n.a.	n.a.	n.a.	n.a.	n.a.	n.a.	n.a.	n.a.	n.a.	n.a.	n.a.	n.a.	7.07517	n.a.	6.63186	1.55605	0.88084	<0.0075	n.a.	0.45759	n.a.	n.a.
121S-161-493(6)-phenc1-met02	0.141945286	1.38544	16.4153	70.003	0.03113	4.03844	0.41853	0.22477	0.02047	2.311	75.9156942	n.a.	n.a.	n.a.	n.a.	n.a.	n.a.	n.a.	18.9266	9.10979	135.113	n.a.	2.46156	0.00364	0.95075	<0.15	5.37191	n.a.	14.5205	n.a.	n.a.	n.a.	n.a.	n.a.	n.a.	n.a.	n.a.	n.a.	n.a.	n.a.	n.a.	n.a.	n.a.	n.a.	1.95068	n.a.	6.14246	1.17313	0.45024	0.00442	n.a.	<0.045	n.a.	n.a.
121S-161-493(6)-phenc1-met03	0.364381595	0.4974	17.2931	69.9962	<0.076	4.61751	2.2142	0.27085	0.01514	1.70496	<18.2	n.a.	n.a.	n.a.	n.a.	n.a.	n.a.	n.a.	114.07	164.125	95.2923	n.a.	4.72573	<1.17	<5.63	<3.94	2.50752	n.a.	355.75	n.a.	n.a.	n.a.	n.a.	n.a.	n.a.	n.a.	n.a.	n.a.	n.a.	n.a.	n.a.	n.a.	n.a.	n.a.	20.723	n.a.	5.03133	0.68845	<0.67	<0.14	n.a.	<1.29	n.a.	n.a.
121S-161-493(6)-phenc1-met04	0.642894421	0.47738	17.8032	70.0065	0.08236	5.27815	1.29888	0.2634	0.01072	1.11155	52.2306987	n.a.	n.a.	n.a.	n.a.	n.a.	n.a.	n.a.	88.3704	23.5029	243.013	n.a.	1.55987	<0.36	<2.17	<1.45	1.9141	n.a.	52.6133	n.a.	n.a.	n.a.	n.a.	n.a.	n.a.	n.a.	n.a.	n.a.	n.a.	n.a.	n.a.	n.a.	n.a.	n.a.	4.83652	n.a.	10.3562	2.03688	1.00357	<0.050	n.a.	<0.41	n.a.	n.a.
121S-161-493(6)-phenc1-met05	1.275677878	0.64762	18.5714	70.0062	0.06137	4.2097	1.10268	0.27173	0.00858	0.85545	58.6636286	n.a.	n.a.	n.a.	n.a.	n.a.	n.a.	n.a.	133.385	<0.051	161.907	n.a.	1.59453	<0.20	<1.27	<0.73	2.05815	n.a.	<0.053	n.a.	n.a.	n.a.	n.a.	n.a.	n.a.	n.a.	n.a.	n.a.	n.a.	n.a.	n.a.	n.a.	n.a.	n.a.	1.15149	n.a.	7.1185	1.42683	0.84257	<0.030	n.a.	<0.25	n.a.	n.a.
121S-161-493(6)-phenc1-met06	1.919225102	0.328838	17.8053	69.9963	<0.015	3.47	2.47159	0.26272	0.01072	0.76816	48.61004535	n.a.	n.a.	n.a.	n.a.	n.a.	n.a.	n.a.	205.702	23.1721	100.874	n.a.	2.20668	0.14076	<1.21	<0.73	1.74708	n.a.	58.6156	n.a.	n.a.	n.a.	n.a.	n.a.	n.a.	n.a.	n.a.	n.a.	n.a.	n.a.	n.a.	n.a.	n.a.	n.a.	3.9197	n.a.	4.70316	0.72813	0.62712	<0.027	n.a.	<0.23	n.a.	n.a.
121S-161-493(6)-phenc1-met07	0.09888275	1.81074	14.9737	70.0025	0.02372	5.00148	2.1842	0.22364	0.00585	2.60358	49.45896002	n.a.	n.a.	n.a.	n.a.	n.a.	n.a.	n.a.	23.553	3.12181	179.871	n.a.	1.80775	<0.10	<1.17	<0.79	1.09818	n.a.	38.102	n.a.	n.a.	n.a.	n.a.	n.a.	n.a.	n.a.	n.a.	n.a.	n.a.	n.a.	n.a.	n.a.	n.a.	n.a.	1.72559	n.a.	7.67532	0.99441	0.22719	<0.026	n.a.	<0.24	n.a.	n.a.
121S-161-493(6)-phenc1-met08	0.145634874	0.73018	17.7489	69.9963	0.07013	6.03206	0.66121	0.26537	0.01553	1.31672	73.7599433	n.a.	n.a.	n.a.	n.a.	n.a.	n.a.	n.a.	18.1835	8.77349	220.887	n.a.	<0.047	<0.069	0.57037	0.2564	2.80559	n.a.	206.715	n.a.	n.a.	n.a.	n.a.	n.a.	n.a.	n.a.	n.a.	n.a.	n.a.	n.a.	n.a.	n.a.	n.a.	n.a.	2.73038	n.a.	10.1611	1.15426	0.51691	<0.0090	n.a.	<0.081	n.a.	n.a.
121S-161-493(6)-phenc1-met09	1.198802229	0.32568	17.2451	69.9951	0.06076	3.79173	2.05626	0.21915	0.02054	1.10159	36.8121391	n.a.	n.a.	n.a.	n.a.	n.a.	n.a.	n.a.	176.912	42.0511	120.972	n.a.	<0.098	<0.059	0.79667	0.39976	1.83457	n.a.	97.3724	n.a.	n.a.	n.a.	n.a.	n.a.	n.a.	n.a.	n.a.	n.a.	n.a.	n.a.	n.a.	n.a.	n.a.	n.a.	6.11542	n.a.	4.08051	0.87747	0.84384	<0.0078	n.a.	0.31458	n.a.	n.a.
121S-161-493(6)-phenc1-met10	1.077429304	0.39955	17.2227	70.001	0.06038	3.89239	3.06327	0.24796	0.01631	1.04212	30.2091641	n.a.	n.a.	n.a.	n.a.	n.a.	n.a.	n.a.	180.971	36.3481	151.502	n.a.	1.67177	<0.10	0.81271	0.34079	1.44652	n.a.	74.5429	n.a.	n.a.	n.a.	n.a.	n.a.	n.a.	n.a.	n.a.	n.a.	n.a.	n.a.	n.a.	n.a.	n.a.	n.a.	5.76718	n.a.	6.01845	0.82083	0.87478	<0.013	n.a.	0.28979	n.a.	n.a.
121S-161-493(6)-phenc1-met11	1.005290599	0.40087	17.7359	69.9971	0.03882	4.62151	1.78017	0.27724	0.01637	1.0887	38.1875381	n.a.	n.a.	n.a.	n.a.	n.a.	n.a.	n.a.	113.207	30.0514	156.581	n.a.	2.07383	3dl	0.61542	0.44119	1.77966	n.a.	76.5336	n.a.	n.a.	n.a.	n.a.	n.a.	n.a.	n.a.	n.a.	n.a.	n.a.	n.a.	n.a.	n.a.	n.a.	n.a.	3.8717	n.a.	4.62868	1.3422	0.85895	<0.014	n.a.	0.26254	n.a.	n.a.
121S-161-493(6)-phenc2-met01	1.114329576	0.418805	17.6484	69.9989	0.08537	3.62511	2.8135	0.26932	0.01914	1.01386	28.99109843	n.a.	n.a.	n.a.	n.a.	n.a.	n.a.	n.a.	179.679	32.4688	219.648	n.a.	1.04134	<0.25	<1.61	<0.95	1.4358	n.a.	120.985	n.a.	n.a.	n.a.	n.a.	n.a.	n.a.	n.a.	n.a.	n.a.	n.a.	n.a.	n.a.	n.a.	n.a.	n.a.	6.84372	n.a.	8.67206	0.91805	0.62866	<0.035	n.a.	<0.31	n.a.	n.a.
121S-161-493(6)-phenc2-met02	0.816311684	0.47302	17.2224	70.0037	0.02756	4.4576	2.49059	0.25953	0.01562	1.13075	26.91535052	n.a.	n.a.	n.a.	n.a.	n.a.	n.a.	n.a.	138.814	27.8862	132.477	n.a.	2.19892	<0.13	1.5084	<0.46	1.74797	n.a.	59.7772	n.a.	n.a.	n.a.	n.a.	n.a.	n.a.	n.a.	n.a.	n.a.	n.a.	n.a.	n.a.	n.a.	n.a.	n.a.	4.11769	n.a.	3.32394	0.60506	0.54032	<0.016	n.a.	<0.14	n.a.	n.a.
121S-161-493(6)-phenc2-met03	1.061561509	0.37513	17.3468	70.0028	0.03308	4.22273	2.62227	0.22368	0.02135	1.09061	43.25105561	n.a.	n.a.	n.a.	n.a.	n.a.	n.a.	n.a.	151.938	42.7459	131.422	n.a.	1.69407	0.00075	0.91926	0.38242	1.75269	n.a.	106.183	n.a.	n.a.	n.a.	n.a.	n.a.	n.a.	n.a.	n.a.	n.a.	n.a.	n.a.	n.a.	n.a.	n.a.	n.a.	5.85059	n.a.	6.65157	0.93022	0.73558	<0.0052	n.a.	0.30621	n.a.	n.a.
121S-161-493(6)-phenc2-met04	1.167555747	0.38388	17.4506	69.9993	0.04109	3.56962	3.31271	0.25833	0.02062	0.84986	35.19879416	n.a.	n.a.	n.a.	n.a.	n.a.	n.a.	n.a.	209.416	34.8776	147.572	n.a.	2.39547	<0.16	<1.61	<1.05	1.41069	n.a.	82.8705	n.a.	n.a.	n.a.	n.a.	n.a.	n.a.	n.a.	n.a.	n.a.	n.a.	n.a.	n.a.	n.a.	n.a.	n.a.	5.88027	n.a.	5.58562	0.55626	0.72287	<0.042	n.a.	<0.33	n.a.	n.a.
121S-161-493(6)-phenc2-met07	0.105282271	0.55737	17.747	70.0033	0.06632	5.83209	0.96982	0.29777	0.01603	1.40493	48.1864147	n.a.	n.a.	n.a.	n.a.	n.a.	n.a.	n.a.	59.7832	40.5252	75.9383	n.a.	0.93019	<0.37	<2.48	<1.37	2.41269	n.a.	85.9629	n.a.	n.a.	n.a.	n.a.	n.a.	n.a.	n.a.	n.a.	n.a.	n.a.	n.a.	n.a.	n.a.	n.a.	n.a.	7.34301	n.a.	6.73491	0.73743	0.77031	<0.058	n.a.	<0.49	n.a.	n.a.
121S-161-493(6)-phenc2-met08	0.787038686	0.41978	17.3576	70.0007	0.06096	4.32209	2.70892	0.23749	0.01944	1.10593	37.1918736	n.a.	n.a.	n.a.	n.a.	n.a.	n.a.	n.a.	144.644	43.8454	181.407	n.a.	2.54288	<0.068	0.61422	0.2883	1.51195	n.a.	99.4525	n.a.	n.a.	n.a.	n.a.	n.a.	n.a.	n.a.	n.a.	n.a.	n.a.	n.a.	n.a.	n.a.	n.a.	n.a.	6.28456	n.a.	5.99014	0.88763	0.82844	<0.010	n.a.	0.24809	n.a.	n.a.
711-7200-US-(6)-phenc1-met01	3.615586842	0.195515	14.4137	69.9932	0.06511	6.80869	0.49121	0.1834	0.02172	1.23277	93.60401033	n.a.	n.a.	n.a.	n.a.	n.a.	n.a.	n.a.	575.034	22.4849	114.97	n.a.	1.54147	0.22335	1.12797	1.88619	5.92905	n.a.	56.817	n.a.	n.a.	n.a.	n.a.	n.a.	n.a.	n.a.	n.a.	n.a.	n.a.	n.a.	n.a.	n.a.	n.a.	n.a.	1.82451	n.a.	5.26867	1.88079	0.74034	0.00185	n.a.	0.27332	n.a.	n.a.
711-7200-US-(6)-phenc1-met02	4.567359241	0.21571	14.9764	69.9973	0.06016	5.55235	0.32722	0.18543	0.02162	1.15426	108.648736	n.a.	n.a.	n.a.	n.a.	n.a.	n.a.	n.a.	382.732	19.3796	154.797	n.a.	1.93719	2.8678	1.16092	2.26519	5.56	n.a.	63.6314	n.a.	n.a.	n.a.	n.a.	n.a.	n.a.	n.a.	n.a.	n.a.	n.a.	n.a.	n.a.	n.a.	n.a.	n.a.	1.69805	n.a.	5.0658	1.78878	0.81565	<0.012	n.a.	0.15751	n.a.	n.a.
711-7200-US-(6)-phenc1-met03	4.630890473	0.185231	14.6716	69.997	0.03271	5.99864	0.38164	0.20582	0.01648	0.87969	93.39390104	n.a.	n.a.	n.a.	n.a.	n.a.	n.a.	n.a.	359.64	19.4951	123.257	n.a.	2.06083	0.14006	1.19301	1.84381	5.69727	n.a.	57.3172	n.a.	n.a.	n.a.	n.a.	n.a.	n.a.	n.a.	n.a.	n.a.	n.a.	n.a.	n.a.	n.a.	n.a.	n.a.	1.88636	n.a.	5.7572	1.98022	0.76162	<0.010	n.a.	0.24362	n.a.	n.a.
711-7200-US-(6)-phenc2-met01	0.12507006	0.29885	13.5659	69.9995	0.04418	11.7212	0.08016	0.14128	0.02019	1.80356	28.01203898	n.a.	n.a.	n.a.	n.a.	n.a.	n.a.	n.a.	122.815	14.8267	109.049	n.a.	1.77168	<0.44	<2.92	<1.66	4.47008	n.a.	45.2161	n.a.	n.a.	n.a.	n.a.	n.a.	n.a.	n.a.	n.a.	n.a.	n.a.	n.a.	n.a.	n.a.	n.a.	n.a.	3.05144	n.a.	4.75493	0.1144	<0.17	<0.10	n.a.	<0.51	n.a.	n.a.
711-7200-US-(6)-phenc2-met02	0.1299016	0.2639	13.8971	70.0016	0.06399	11.5539	0.14982	0.13094	0.01558	0.78536	<18.6	n.a.	n.a.	n.a.	n.a.	n.a.	n.a.	n.a.	212.878	10.9119	104.869	n.a.	1.55355	<0.36	<2.34	<1.33	3.55632	n.a.	47.2836	n.a.	n.a.	n.a.	n.a.	n.a.	n.a.	n.a.	n.a.	n.a.	n.a.	n.a.	n.a.	n.a.	n.a.	n.a.	2.06144	n.a.	5.87242	0.95941	0.19846	<0.051	n.a.	<0.44	n.a.	n.a.
711-7200-US-(6)-phenc3-met01	1.336706505	0.49953	12.1892	69.9979	0.05065	9.67033	0.4637	0.3562	0.02814	2.49456	57.745902	n.a.	n.a.	n.a.	n.a.	n.a.	n.a.	n.a.	405.153	29.027	146.615	n.a.	3.22413	0.34639	1.57351	1.85383	3.00386	n.a.	176.925	n.a.	n.a.	n.a.	n.a.	n.a.	n.a.	n.a.	n.a.	n.a.	n.a.	n.a.	n.a.	n.a.	n.a.	n.a.	3.94334	n.a.	6.56054	1.40714	1.80542	0.16158	n.a.	0.06679	n.a.	n.a.
711-7200-US-(6)-phenc3-met02	0.296254477	0.18603	13.7263	69.9975	0.04197	11.9522	0.08306	0.01758	0.01241	0.48672	51.3976075	n.a.	n.a.	n.a.	n.a.	n.a.	n.a.	n.a.	171.189	15.3525	98.4915	n.a.	1.74394	0.14628	<1.08	1.19623	4.6267	n.a.	49.8893	n.a.	n.a.	n.a.	n.a.	n.a.	n.a.	n.a.	n.a.	n.a.	n.a.	n.a.	n.a.	n.a.	n.a.	n.a.	2.24114	n.a.	3.49988	0.32888	0.25924	<0.028	n.a.	<0.320	n.a.	n.a.
711-7200-US-(6)-phenc3-met03	0.531490473	0.2488	13.4616	70.002	0.0641	11.4667	0.11158	0.17503	0.01477	0.921	42.7756739	n.a.	n.a.	n.a.	n.a.	n.a.	n.a.	n.a.	198.128	17.8961	115.304	n.a.	1.67245	<0.38	<2.32	<1.34	5.67473	n.a.	47.2362	n.a.	n.a.	n.a.	n.a.	n.a.	n.a.	n.a.	n.a.	n.a.	n.a.	n.a.	n.a.	n.a.	n.a.	n.a.	2.25106	n.a.	4.67541	1.32168	0.22852	<0.049	n.a.	<0.44	n.a.	n.a.
711-7200-US-(6)-phenc3-met04	0.251838413	0.32935	13.5164	69.997	0.04877	11.4688	0.13624	0.13614	0.02185	1.09304	39.13668809	n.a.	n.a.	n.a.	n.a.	n.a.	n.a.	n.a.	173.433	15.7012	140.619	n.a.	1.67981	<0.33	<1.68	<1.13	3.89443	n.a.	61.9089	n.a.	n.a.	n.a.	n.a.	n.a.	n.a.	n.a.	n.a.	n.a.	n.a.	n.a.	n.a.	n.a.	n.a.	n.a.	2.59712	n.a.	4.99737	0.54127	0.18634	<0.045	n.a.	<0.332	n.a.	n.a.
711-7200-US-(6)-phenc4-met01	0.323372286	0.22926	13.3737	69.9988	0.04396	11.6982	0.19371	0.19577	0.02815	0.93495	77.44051107	n.a.	n.a.	n.a.	n.a.	n.a.	n.a.	n.a.	420.179	16.8047	99.6624	n.a.	1.89507	0.10499	0.9472	1.56613	5.94071	n.a.	64.3214	n.a.	n.a.	n.a.	n.a.	n.a.	n.a.	n.a.	n.a.	n.a.	n.a.	n.a.	n.a.	n.a.	n.a.	n.a.	2.83574	n.a.	4.27774	1.49703	0.54403	<0.031	n.a.	0.16364	n.a.	n.a.
711-7200-US-(6)-phenc4-met02	0.805154283	0.10875	13.6082	69.9968	0.05655	11.5109	0.22676	0.10048	0.00634	0.58375	71.66898408	n.a.	n.a.	n.a.	n.a.	n.a.	n.a.	n.a.	398.696	22.8754	113.391	n.a.	<0.093	<0.15	1.45484	<0.50	6.10921	n.a.	72.0987	n.a.	n.a.	n.a.	n.a.	n.a.	n.a.	n.a.	n.a.	n.a.	n.a.	n.a.	n.a.	n.a.	n.a.	n.a.	3.68475	n.a.	4.96649	1.10373	0.22165	0.02356	n.a.	<0.16	n.a.	n.a.
711-7200-US-(6)-phenc4-met03	2.104077685	0.18203	13.7717	69.9992	0.04937	9.00632	0.10483	0.17225	0.02209	1.14625	54.6407238	n.a.	n.a.	n.a.	n.a.	n.a.	n.a.	n.a.	626.734	25.0817	88.8054	n.a.	1.81495	0.09303	0.97558	1.30084	4.65256	n.a.	81.7461	n.a.	n.a.	n.a.	n.a.	n.a.	n.a.	n.a.	n.a.	n.a.	n.a.	n.a.	n.a.	n.a.	n.a.	n.a.	2.95189	n.a.	3.8308	1.30831	0.81963	0.00485	n.a.	0.17906	n.a.	n.a.
711-7200-US-(6)-phenc4-met04	1.132451

Appendix 3A - LA-ICP-MS analyses of titanium in quartz phenocrysts of unit 2.0

Sample	47Ti (ppm)	aT (°C)	bT (°C)
3086-19-278-pC-ap1	80.2	653	809
3086-29-177-pheno1-melt1	42.9	595	741
3086-29-177-pheno2-melt1	202	754	927
3086-29-177-pheno2-melt2	86.6	660	818
3086-29-177-pheno2-melt3	61.7	628	780
3086-29-177-pheno2-melt4	97.7	673	832
3086-29-177-pheno3-melt1	98.8	674	834
3086-29-177-pheno3-melt2	75.4	647	802
3086-29-177-pheno3-melt3	85.0	659	816
3086-29-177-pheno4-melt1	123	697	861
3086-29-177-pheno4-melt2	123	697	860
3086-29-188.5-pheno13-melt1	80.2	653	809
3086-29-188.5-pheno13-quartz	80.0	653	809
3086-29-188.5-pheno14-melt1	92.8	667	826
3086-29-188.5-pheno14-melt2	83.7	657	814
3086-29-188.5-pheno14-melt3	89.3	664	822
3086-29-188.5-pheno14-melt4	86.2	660	817
3086-29-188.5-pheno14-melt5	99.0	674	834
3086-29-188.5-pheno14-melt6	87.9	662	820
3086-29-188.5-pheno14-melt7	92.9	668	826
3086-29-188.5-pheno14-quartz	84.0	657	814
3086-29-188.5-pheno14-quartz2	86.5	660	818
3086-29-188.5-pheno1-melt1	70.1	640	794
3086-29-188.5-pheno1-melt2	64.3	632	784
3086-29-188.5-pheno1-melt3	46.8	603	750
3086-29-188.5-pheno3-melt2	122	697	860
3086-29-188.5-pheno3-melt3	119	694	857
3086-29-188.5-pheno4-melt1	72.3	643	797
3086-29-188.5-pheno4-melt2	73.6	644	799
3086-29-188.5-pheno5-melt1	65.2	633	786
3086-29-188.5-pheno6-melt1	75.4	647	802
3086-29-188.5-pheno6-melt2	69.7	639	793
3086-29-188.5-pheno7-melt1	62.6	629	781
3086-29-188.5-pheno7-melt2	86.0	660	817
3086-29-188.5-pheno8-melt1	72.9	644	798
3086-29-188.5-pheno8-melt2	119	694	857
3086-29-188.5-pheno8-quartz	87.0	661	818
3086-29-188.5-pheno9-melt1	107	682	843
3086-29-188.5-pheno9-quartz	100	675	835
3086-29-218-pheno1-melt1	87.5	661	819
3086-29-218-pheno1-melt2	99.9	675	835
3086-29-218-pheno1-melt3	75.8	647	803
3086-29-218-pheno1-melt4	94.4	669	828
3086-29-218-pheno2-melt1	107	682	844
3086-29-218-pheno3-melt1	112	687	849
3086-29-218-pheno4-melt1	84.0	657	814
3086-29-218-pheno4-melt2	73.5	644	799
3086-29-218-pheno5-melt1	133	705	870
3086-29-278-pA-ap1	140	711	877
3086-29-278-pB-ap1	140	712	878
3086-29-278-pD-ap1	75.2	647	802
3086-29-278-pheno1-melt1	70.0	640	794
3086-29-278-pheno1-melt2	67.1	636	789
3086-29-278-pheno2-melt1	105	680	841
3086-29-278-pheno2-melt2	86.5	660	818
3086-29-278-pheno3-melt1	94.6	669	828
3086-29-278-pheno4-melt1	26.5	555	695
3086-29-278-pheno4-melt2	96.2	671	830
3086-29-278-pheno4-melt3	67.2	636	789
3086-29-282.7-pA-a1	119	693	856
3086-29-282.7-pB-a1	95.2	670	829
3086-29-282-pheno1-melt1	101	676	836
3086-29-282-pheno1-melt2	81.2	654	810
3086-29-282-pheno1-melt4	111	686	848
3086-29-282-pheno1-melt6	107	682	843
3086-29-282-pheno2-melt1	65.0	633	785
3086-29-282-pheno2-melt2	66.7	635	788
3086-29-282-pheno2-melt3	84.1	658	815
3086-29-282-pheno3-melt1	83.5	657	814
3086-29-282-pheno3-melt2	103	678	838
3086-29-282-pheno4-melt1	69.7	639	793
3086-29-282-pheno4-melt2	79.9	652	809
3215-166.131.8-pheno10-quartz	95.3	670	829
3215-166-131.8	92.2	667	825
3215-166-131.8-pheno10-melt1	103	678	839
3215-166-131.8-pheno12-melt1	92.0	667	825
3215-166-131.8-pheno12-quartz	84.4	658	815
3215-166-131.8-pheno13-melt1	121	695	858
3215-166-131.8-pheno13-melt2	106	681	842
3215-166-131.8-pheno13-quartz	98.4	673	833
3215-166-131.8-pheno13-quartz2	96.5	671	831
3215-166-131.8-pheno14-melt3	85.5	659	816
3215-166-131.8-pheno14-quartz	80.0	653	809
3215-166-131.8-pheno14-quartz2	78.7	651	807
3215-166-131.8-pheno1-melt1	63.9	631	783
3215-166-131.8-pheno1-melt2	79.8	652	808
3215-166-131.8-pheno2-melt1	69.6	639	793
3215-166-131.8-pheno2-melt2	88.2	662	820
3215-166-131.8-pheno2-melt3	91.1	666	824
3215-166-131.8-pheno3-melt1	92.0	667	825
3215-166-131.8-pheno3-melt2	82.4	655	812
3215-166-131.8-pheno3-melt3	91.8	666	825
3215-166-131.8-pheno4-melt1	70.4	640	794
3215-166-131.8-pheno4-melt2	56.2	619	770
3215-166-131.8-pheno5-melt1	71.2	641	795
3215-166-131.8-pheno6-melt1	79.4	652	808
3215-166-131.8-pheno7-melt1	1.80	386	497
3215-166-131.8-pheno8-melt1	72.1	642	797
3215-166-131.8-pheno8-melt2	73.2	644	799
3215-166-131.8-pheno8-melt3	57.2	621	771
3215-166-131.8-pheno9-melt1	88.0	662	820
3215-166-131.8-pheno9-melt2	114	688	851
3215-166-131.8-pheno9-melt3	87.3	661	819
3215-166-131.8-pheno9-quartz	92.5	667	826
3215-166-79.3-pheno1-melt1	65.7	634	786
3215-166-79.3-pheno1-melt2	80.7	653	810
3215-166-79.3-pheno1-melt3	59.9	625	776
3215-166-79.3-pheno1-melt4	79.3	652	808
3215-166-79.3-pheno2-melt2	77.9	650	806
3215-166-79.3-pheno2-melt3	69.5	639	793
3215-166-79.3-pheno3-melt2	69.7	639	793
3215-166-79.3-pheno4-melt2	64.7	632	785
3215-166-79.3-pheno4-melt3	60.6	626	778
3215-166-79.3-pheno5-melt1	50.3	609	758
3215-166-79.3-pheno5-melt2	7.87	469	594
3215-166-79.3-pheno6-melt1	65.3	633	786
3215-166-79.3-pheno6-melt3	50.3	609	758
3215-166-79.3-pheno6-melt4	68.8	638	791
731-9061-U2(3)-p1-ap1	93.0	668	826
731-9061-U2(3)-p1-zr1	74.6	646	801
731-9061-U2(3)-p1-zr2	74.4	645	800
731-9061-U2(3)-p2-ap1	100	675	835
731-9061-U2(3)-p3-ap1	97.8	673	832
731-9061-U2(3)-p3-ap2	84.5	658	815
731-9061-U2(3)-p3-ap3	64.4	632	784
731-9061-U2(3)-p4-ap1	84.4	658	815
731-9061-U2(3)-p5-ap1	83.8	657	814
731-9061-U2(3)-p6-ap1	97.6	673	832
731-9061-U2(3)-p7-ap1	81.0	654	810
731-9061-U2(4)-pA-zr1	92.8	667	826
731-9061-U2(4)-pB-ap1	87.7	662	819
731-9061-U2(4)-pB-ap2	83.6	657	814
731-9061-U2(4)-pC-ap1	94.1	669	828
731-9061-U2(4)-pD-quartz	92.1	667	825
731-9061-U2(4)-pE-ap1	98.0	673	833
731-9061-U2(4)-pF-ap2	86.1	660	817
731-9061-U2.0(4)-pheno1-melt1	88.9	663	821
731-9061-U2.0(4)-pheno2-melt1	73.8	645	800
731-9061-U2.0(4)-pheno2-melt2	69.7	639	793
731-9061-U2.0(4)-pheno2-melt3	81.7	655	811
731-9061-U2.0(4)-pheno2-quartz	80.0	653	809
731-9061-U2.0(4)-pheno3-melt2	67.2	636	789
731-9061-U2.0(4)-pheno3-quartz	72.5	643	797
731-9061-U2.0(4)-pheno4-melt1	76.0	647	803
731-9061-U2.0(4)-pheno4-quartz	95.1	670	829
731-9061-U2.0(4)-pheno5-melt1	75.5	647	802
731-9061-U2.0(4)-pheno5-melt2	81.4	654	811
731-9061-U2.0(4)-pheno5-melt3	60.1	625	777
731-9061-U2.0(4)-pheno5-quartz	80.4	653	809
731-9061-U2.0(4)-pheno6-melt1	73.8	645	799
731-9061-U2.0(4)-pheno6-melt2	72.2	643	797
731-9061-U2.0(4)-pheno6-melt3	75.9	647	803
731-9061-U2.0(4)-pheno6-melt4	58.0	622	773
731-9061-U2.0(4)-pheno6-melt5	59.5	624	776
731-9061-U2.0(4)-pheno6-quartz	68.7	638	791
731-9061-U2.0(4)-pheno6-quartz2	75.0	646	801
731-9061-U2.0(5)-pheno1-melt1	94.9	670	829
731-9061-U2.0(5)-pheno1-quartz	91.6	666	825
731-9061-U2.0(5)-pheno2-melt1	81.1	654	810
731-9061-U2.0(5)-pheno2-melt2	75.0	646	801
731-9061-U2.0(5)-pheno2-quartz	71.8	642	796
731-9061-U2.0(5)-pheno2-quartz2	82.2	655	812
731-9061-U2.0(5)-pheno3-melt1	77.8	650	805
731-9061-U2.0(5)-pheno3-melt2	77.1	649	804
731-9061-U2.0(5)-pheno3-melt3	85.9	660	817
731-9061-U2.0(5)-pheno3-quartz	78.4	651	806
731-9061-U2.0(5)-pheno4-melt1	78.1	650	806
731-9061-U2.0(5)-pheno4-melt2	76.4	648	803
731-9061-U2.0(5)-pheno4-melt3	81.9	655	811
731-9061-U2.0(5)-pheno4-quartz	87.1	661	819
731-9061-U2.0(5)-pheno5-melt1	86.9	661	818
731-9061-U2.0(5)-pheno5-melt2	68.6	638	791
731-9061-U2.0(5)-pheno5-melt3	36.5	581	725
731-9061-U2.0(5)-pheno5-quartz	82.6	656	812
quartz-pheno1-3086-29-188.5	86.8	661	818
quartz-pheno2-3086-29-218	101	676	836
quartz-pheno2-3086-29-278	102	677	837
quartz-pheno2-3086-29-282	102	677	838
quartz-pheno3-3086-29-177	80.1	653	809
quartz-pheno3-3086-29-177	82.0	655	812
quartz-pheno4-3086-29-177	103	678	839
quartz-pheno4-3086-29-188.5	70.3	640	794

a At 6.5 kbar.
b At 13.5 kbar.

Appendix 3C - LA-ICP-MS analyses of titanium in quartz phenocrysts of unit 5.3

Sample	47Ti (ppm)	aT (°C)	bT (°C)	Sample	47Ti (ppm)	aT (°C)	bT (°C)
3215-161-493(2)-pheno1-melt1	149	718	885	3215-161-493-pheno4-melt2	87.9	662	820
3215-161-493(2)-pheno1-melt2	160	726	895	3215-161-493-pheno4-melt3	94.4	669	828
3215-161-493(2)-pheno2-melt1	138	710	875	711-7200(2)-p1-a1	89.5	664	822
3215-161-493(2)-pheno2-melt2	138	709	875	711-7200(2)-p1-quartz	72.4	643	797
3215-161-493(2)-pheno2-melt4	125	699	863	711-7200(2)-p2-a1	138	709	875
3215-161-493(2)-pheno2-melt6	119	693	856	711-7200(2)-p2-quartz	125	699	863
3215-161-493(2)-pheno2-melt8	119	694	857	711-7200(2)-p3-a1	105	680	841
3215-161-493(2)-pheno2-melt9	164	729	898	711-7200(2)-p4-quartz	117	691	854
3215-161-493(3)-p1-a1	15.5	515	648	711-7200(2)-p5-a1	78.8	651	807
3215-161-493(3)-p2-a1	117	691	854	711-7200(2)-p5-quartz	106	681	842
3215-161-493(3)-p3-a1	118	692	855	711-7200(3)-p1-a1	116	691	854
3215-161-493(3)-p3-quartz	118	692	855	711-7200(3)-p1-quartz	126	700	864
3215-161-493(6)-pheno1-melt1	104	679	840	711-7200(3)-p2-a1	108	683	844
3215-161-493(6)-pheno1-melt2	90.8	665	824	711-7200(3)-p3-a1	173	735	905
3215-161-493(6)-pheno1-melt3	97.8	673	832	711-7200(3)-p4-a1	141	712	878
3215-161-493(6)-pheno1-melt3	124	698	862	711-7200(3)-p5-a1	125	699	863
3215-161-493(6)-pheno1-melt4	109	684	845	711-7200(3)-p5-quartz	134	706	871
3215-161-493(6)-pheno1-melt6	106	681	842	711-7200(3)-p6-a1	164	729	898
3215-161-493(6)-pheno1-melt7	88.1	662	820	711-7200(3)-p7-a1	148	718	885
3215-161-493(6)-pheno1-melt8	93.3	668	827	711-7200(4)-pheno1-melt2	122	696	859
3215-161-493(6)-pheno2-melt1	106	681	842	711-7200(4)-pheno1-melt3	111	686	848
3215-161-493(6)-pheno2-melt2	121	695	859	711-7200(4)-pheno1-quartz	110	686	847
3215-161-493(6)-pheno2-melt3	123	697	861	711-7200(4)-pheno2-melt1	87.0	661	818
3215-161-493(6)-pheno2-melt4	128	701	865	711-7200(4)-pheno2-melt2	105	681	841
3215-161-493(6)-pheno2-melt5	121	695	858	711-7200(4)-pheno2-melt3	112	687	849
3215-161-493(6)-pheno2-melt6	141	712	878	711-7200(4)-pheno2-quartz	107	682	843
3215-161-493(6)-pheno3-melt1	94.5	669	828	711-7200(4)-pheno2-quartz2	110	685	846
3215-161-493(6)-pheno3-melt2	96.2	671	830	711-7200(4)-pheno3-melt1	103	678	839
3215-161-493(6)-pheno3-melt3	103	678	839	711-7200(4)-pheno3-melt2	107	682	843
3215-161-493(6)-pheno4-melt1	103	679	839	711-7200(4)-pheno3-melt3	104	680	840
3215-161-493(7)-p1-a1	116	691	853	711-7200(4)-pheno3-quartz	108	683	844
3215-161-493(7)-p2-quartz	122	696	859	711-7200(4)-pheno3-quartz2	107	682	843
3215-161-493(7)-p3-a1	101	677	837	711-7200(4)-pheno4-melt1	110	685	847
3215-161-493-pheno1-melt1	104	679	840	711-7200(4)-pheno4-melt2	119	693	856
3215-161-493-pheno1-melt2	98.4	673	833	711-7200(4)-pheno4-melt3	118	693	855
3215-161-493-pheno1-melt4	119	693	856	711-7200(4)-pheno4-melt4	112	687	849
3215-161-493-pheno2-melt1	114	689	851	711-7200(4)-pheno4-melt5	106	681	842
3215-161-493-pheno2-melt2	130	703	868	711-7200(4)-pheno4-melt6	98.2	673	833
3215-161-493-pheno2-melt3	114	689	851	711-7200(4)-pheno4-melt7	114	689	851
3215-161-493-pheno3-melt2	131	704	869	711-7200(4)-pheno4-quartz	83.0	656	813
3215-161-493-pheno3-melt3	101	677	837	quartz-pheno4-3215-161-493	104	679	840
3215-161-493-pheno4-melt1	101	676	836				

a At 6.5 kbar.

b At 13.5 kbar.